NSTX-U FY2016 Year End Report

J. Menard, M. Ono, and the NSTX-U Team

October 6, 2016 – Version 14

Table of contents

Executive Summary of NSTX-U Year-End Report for FY2016

• Executive Summary for FY2016 Notable Outcomes

- *Notable 1 - Objective 1.2: "Perform experimental research on NSTX Upgrade to address key spherical torus issues at magnetic field, plasma current, and pulse length beyond that achieved in NSTX, after completion of CD-4 for the NSTX-U project."*

  - NSTX-U researchers completed commissioning of all magnetic diagnostics needed for equilibrium reconstruction and plasma control, established reliable plasma shape control, and began implementation of a new inboard gap control for improved control of early H-mode access. NSTX-U researchers completed key profile diagnostics for ion and electron density and temperature, and developed long-pulse L-mode scenarios and high-performance H-mode scenarios in support of transport, stability, and energetic particle experimental proposals.

  - L-mode scenarios were developed with toroidal field magnitude and plasma pulse duration simultaneously exceeding the highest values achieved on NSTX in either L-mode or H-mode at any heating power. NSTX-U researchers also developed 1MA H-mode plasmas matching the longest-duration 1MA H-mode plasma performance achieved in NSTX. Follow-on experiments were planned to surpass NSTX maximum current values, but the PF1AU coil internal fault forced premature cessation of NSTX-U operations for FY2016 and plasma currents surpassing NSTX maximum values were not achieved.

  - The new more tangential 2nd NBI of NSTX-U rapidly yielded important physics results for Alfven Eigenmode stability. In particular, when any NBI 2 source was added to a plasma with one or more NBI line 1 sources, it was observed that the addition of more beam power could completely suppress the counter-propagating Global Alfven Eigenmode (GAE). The capability to suppress the GAE with the substitution of sources at the same neutral beam power, or by adding more NBI power, will prove to be a useful tool for understanding the role of GAE in electron heat transport previously observed on NSTX.

- *Notable 2 - Objective 1.2: ""Conduct NSTX-U experiments and data analysis to support the FES joint research target on detecting and minimizing the consequences of disruptions in present and future tokamaks, including ITER."*

  - NSTX-U made substantial progress in FY2016 toward identifying impending disruptions and in ramping down the plasma when disruptions can no longer be avoided. In support of this research, a new "Shutdown State Machine" was implemented in the Plasma Control System (PCS). Such a rapid controlled ramp to zero current can reduce electromagnetic loads on in-vessel components. The development of plasma shutdown methods, both during normal operations and during off-normal events, is critical for the ultimate development and protection of ITER and future tokamak/ST devices.

  - Disruption prevention and avoidance is also an important operational goal for future devices, and the disruption event characterization and forecasting (DECAF) code is under development at NSTX-U in order to facilitate a comprehensive framework for disruption prevention through forecasting and avoidance. Progress on the development of DECAF was made in three areas during FY2016: (1) identification of rotating MHD modes, (2) characterization of a set of resistive wall mode (RWM) disruptions, and (3) the development of a reduced kinetic model for RWM stability.

- NSTX-U began deployment of three Massive Gas Injection (MGI) valves that are very similar to the double flyer plate design being considered for ITER. NSTX-U will be the first device to operate this valve design in plasma discharges. In FY2016, these valves were tested off-line and shown to deliver the required amount of gas to support NSTX-U experiments. Planned experiments will provide new MGI data by studying gas assimilation efficiencies for MGI gas injection from different poloidal locations (at the same toroidal location), with emphasis on injection into the private flux region. Two of the three valves were tested on NSTX-U for full operation in nitrogen, helium, and neon at the full operating pressure of 10,000 Torr, and the final testing of the third valve will be completed during the FY17 outage.

- A novel fast-triggering disruption mitigation system based on the rail-gun concept was designed, components fabricated and the system fully assembled. This device - referred to as an Electromagnetic Particle Injector (EPI) - is fully electromagnetic and has no mechanical moving parts which ensures high reliability after a period of long standby. In addition to responding on the required fast time scale, EPI performance substantially improves when operated in the presence of high magnetic fields. Thus, an EPI system is also suitable for installation in close proximity to a fusion reactor. Laboratory-based experimental test results from the operation of this system will be presented at the 2016 IAEA Fusion Energy Conference.

• Executive Summary for Facility and Diagnostics

➢ Facility and Diagnostic Milestones

- **Milestone F(16-1) –** NSTX-U operated for 10.06 run weeks with 1066 plasma shots to commission the upgraded facility and perform research operations. 31 experimental machine proposals related to the commissioning of the facility including diagnostics systems were performed.

- **Milestone F(16-2)** – Following the completion of the final engineering design review in March 2016, procurement and fabrication of all high-Z tile components was completed. High-Z tiles are available for installation during the FY2017 outage.

- **Milestone F(16-3**) – The Conceptual Design Review for the NSTX-U Divertor Cryo-pump project was held on August 3rd, 2016. This integrated, system level review covered all aspects of the project including the cryo-pump, divertor, liquid helium delivery, as well as impacts to NSTX-U, safety, cost and schedule. The review panel, consisting of PPPL, GA and MIT staff, deemed the review successful.

- **Milestone F(16-4) –** Engineering conceptual design of the ECH/EBW system was successfully completed. This includes a detailed design of the gyrotron room layout, high voltage power supply specification, and transmission line layout details. Cost and schedule estimates were also developed. As a part of the design activity, collaboration with the Tsukuba group was initiated to characterize the prototype gyrotron for use on NSTX-U.

- **Milestone F(16-5)** – A successful engineering conceptual design of the Non-axisymmetric Control Coils (NCC) was completed. This includes a detailed design of the NCC system taking into account possible thermal and electromagnetic forces. A bottoms-up project estimation of costs, schedule and risks was presented. The required testing and characterization of the sample conductors was also performed. A Systems Requirements Document (SRD) was also prepared.

- **Milestone D(16-1)** – A bolometer system to measure the radiated power in the NSTX-U divertor region was designed and fabricated and is being prepared during the FY17 outage. This system will allow the strongly radiating regions of the divertor to be identified for various operational scenarios and will provide measurements of the total power radiated from the divertor region.

Operations, Heating Systems, and other Diagnostics

- The NSTX-U digital coil protection system implementation and testing was completed and supported NSTX-U coil testing and plasma operations.

- The poloidal field and flux measurements are used to constrain both off-line and real-time equilibrium reconstructions. All integrators were calibrated with a dedicated test setup. All sensors were calibrated via single coil test shots, and their spurious pickup corrected. These gains and pickup corrections were successfully validated against LRDFIT simulations.

- All six NBI sources were conditioned up to the full voltage of 90 keV.

- All six RF sources for the high-harmonic fast wave heating system were readied and all twelve antennas have been vacuum conditioned readied for plasma operations.

- A large number of research tools and diagnostics have been installed and commissioned including Boronization, Massive Gas Injector, Granular Injector, Lithium Evaporators, Multi-pulse Thomson Scattering System, Real-time Velocity Diagnostic, MSE-LIF, Material Analysis and Particle Probe, Fast Ion D-Alpha diagsnotic,.

Executive Summary of Research Results – FY16 Milestones

R(16-1): Assess H-mode energy confinement, pedestal, and SOL characteristics with higher BT, Ip and NBI heating power

- H-mode plasmas were developed in NSTX-U over a limited range of plasma current, and thermal confinement times were seen to be at the H98y,2 level or greater, as compared to L-mode plasmas, where this confinement enhancement factor was < 1. In these H-mode plasmas, the electron thermal diffusivity was about a factor of two to three lower than that in L-mode discharges.

- L-mode parametric scans were carried out with: (1) varied plasma current at fixed heating power and line averaged density, and (2) varied heating power at fixed plasma current and line-average density. No strong current dependence emerged from this scan. There is a slightly positive dependence of thermal confinement time on current which is weaker than is found in conventional aspect ratio L-mode studies, but which also has a high statistical uncertainty. Using a preliminary and small collection of L-mode discharges, a power degradation of $P^{-2/3}$ is observed and is consistent with previous non-ST L-mode results.

- Initial measurements of the turbulence in L-mode and H-mode NSTX-U plasmas have been conducted using the upgraded 2D BES system. Broadband turbulence is observed up to 150 kHz in the pedestal region and up to 100 kHz several cm inside of the pedestal. Across the L-H transition, fluctuation levels drop by a factor of six in the pedestal region and a factor of three inward of the pedestal top. These results pave the way for future detailed studies of the turbulence across L-H transitions.

➢ *R(16-2): Assess the effects of NBI parameters on the fast ion distribution function and neutral beam driven current profile*

- All fast-ion diagnostics used to characterize the distribution function and its time evolution were successfully commissioned. Data from neutron detectors, FIDA and ssNPA systems were routinely available during the run. Preparation for the installation and commissioning of a Charged Fusion Product Array also made progress, although the premature end of the FY-16 Run prevented initial tests during plasma operations. Unfortunately, q-profile measurements through MSE were not available due to the premature end of the run due to the PF1AU coil failure, thus hampering NB current drive studies that rely on MSE-constrained equilibria for reliable and quantitative TRANSP analysis of the non-inductive current fraction.

- It was observed that at high NB injection energy (Vinj~85keV), the neutron rise and decay rate of four available neutral beam sources agree reasonably well with TRANSP classical modelling which suggests that beams ions are well confined. However, at low NB injection energy (Vinj~65keV), the measured neutron rise is lower and the measured decay rate is faster than TRANSP modelling predictions. The reason for the discrepancy at low injection energy is under investigation. Potential reasons for the discrepancy are uncertainties in the measured Zeff or in the beam species mix between full, half and third NB energy components at low beam injection voltage. Spectroscopic data was obtained at the end of the FY2016 run to further study the beam species mix dependence on injection voltage.

➢ *R(16-3): Develop the physics and operational tools for obtaining high-performance discharges in NSTX-U*

- Plasma current and outboard gap control were established, real-time EFIT was commissioned, and ISOFLUX control of plasma radial and vertical position was established.
- New vertical position control sensors and algorithms were added and commissioned.
- Error field correction and plasma facing component conditioning methods were implemented.
- A plasma shutdown algorithm based on a state-machine was defined and utilized.
- Operational scenarios within the new Digital Coil Protection System limits were developed.
- The above improvements all contributed to the development of ST-record L-mode plasma durations at high current and in the re-establishment of high-performance H-mode discharges.
- Real-time resistive wall mode (RWM) sensor and control codes were re-commissioned, but RWM/EF active feedback was not used during operations due to runtime limitations.

Executive Summary for Additional Research Highlights

Boundary Science

➢ Summary of Research Highlights for Pedestal Structure and Control

- The energy exchange dynamics across the low-to-high-confinement (L-H) using gas-puff imaging (GPI) has been investigated in NSTX discharges. Analysis using velocity fields shows that the production term, which is a proxy for the transfer of the energy from mean flows to turbulence or vice-versa, is systematically negative just prior to the L-H transition, which indicates that turbulence depletion mechanism may not be playing an important role in the transition to the H-mode.

- Highly-shaped, high-performance NSTX H-mode discharges have been extensively studied on three fronts. SOLPS was used to quantify the edge transport change with lithium coatings. The electron particle diffusivity decreased by 10-30x, while the electron thermal diffusivity decreased by 4x just inside the top of the pedestal, but increased by up to 5x very near the separatrix, generally similar to analysis of weakly-shaped H-modes. Next, linear gyrokinetic predictions of micro-instabilities have been performed to show that micro-tearing modes are stabilized in lithiated discharges at the pedestal top, which is a consequence of the electron temperature pedestal extending further inwards, as observed experimentally. Third, using ELITE and M3D-C^1, it was shown that the highly-shaped, boronized, ELMy (no lithium reference) discharges are stable to ideal MHD modes, but could be unstable to resistive modes of low toroidal mode number.

- Good progress was made in commissioning diagnostics and analysis tools for pedestal studies in NSTX-U. The BES system was upgraded for optimum coverage of the pedestal. In addition, significant progress was made in the development of the pulse burst laser system that will enable examination of the pedestal structure formation mechanisms. Finally, the first inter-ELM fits of the density and temperature profiles have been performed for NSTX-U H-modes, showing pedestal structure similar to NSTX.

➢ Summary of Research Highlights for Divertor and Scrape-off Layer

- Progress was made in relating blob/turbulence properties with divertor heat fluxes. Comparison of experimental edge turbulence parameters with theoretical estimates for drift-interchange turbulence and SOLT simulations suggested that turbulence mechanisms were not negligible in determining the heat flux width. Also, filament footprints in the divertor were studied in L-modes, with large correlation to upstream blobs observed in the far SOL, progressively decaying towards the separatrix. New diagnostics capabilities in NSTX-U enabled the study of near-separatrix filaments in the inner and outer divertor legs.

- The behavior of ELM heat flux profiles was investigated via experiments and MHD simulations in NSTX and DIII-D. While the NSTX ELMs were primarily on the kink-peeling side, and generally showed contraction of the heat flux width, ELMs in DIII-D demonstrated both broadening and contraction, depending on the pedestal collisionality. Linear MHD stability simulations indicate that the broadening observed at high collisionality was associated to the pedestal operating point moving towards the ballooning side. A non-linear MHD simulation of ELM heat flux with JOREK found that the magnetic energy perturbation was closely related to the formation of homoclinic tangles, largely affecting the heat flux profiles in the near SOL region, while kinetic energy perturbation was the main contributor to the filament formation, mainly affecting the heat flux profiles in the far SOL region.

- Studies of NSTX-U snowflake divertor configurations were performed with UEDGE and EMC3-EIRENE. UEDGE studies were enabled by a new advanced grid generator for various snowflake geometries. The effect of n=3 magnetic perturbations on snowflake divertors was studied with M3D-C^1. More striations in the particle and heat flux target profiles, leading to a larger wetted area and smaller peak heat fluxes onto the PFCs, are expected in the snowflake configuration.

Summary of Research Highlights for Materials and Plasma Facing Components

- The Material Analysis and Particle Probe (MAPP) diagnostic has operated on NSTX-U taking detailed measurements of material evolution during plasma operations. These measurements are able to quantitatively evaluate the plasma-facing component composition identifying, even, the chemical compounds developed on the surface. The measurements are opening the door to understanding the chemical mechanisms underlying performance improvement as a result of wall conditioning schemes such as boronization and, eventually, lithium application.

- Detailed characterization of the plasma-response to changing wall conditions is evaluated with optical emission spectroscopy and filtered camera images of the divertor. These measurements characterize the evolution of the plasma-material interactions coupled to the material changes monitored with MAPP. The data highlight the importance of controlling oxygen and water vapor with wall conditioning and provide an important link between material characterization and plasma response.

- Preparations for the NSTX-U high-Z divertor upgrade have continued with procurement of the high-Z tiles after a lengthy design process as well as novel diagnostic and modeling developments. Implanted depth markers have been developed to characterize campaign-integrated erosion from high-Z material to a high degree of accuracy. Whole machine modeling and improved spectroscopic coverage will enable improved understanding of the evolution of the entire tokamak during future experimental campaigns.

Core Science

➢ Summary of Research Highlights for Macroscopic Stability

- EFIT equilibrium reconstructions relying only on magnetic measurements have been available from the first shots of NSTX-U, and "partial kinetic" EFIT reconstructions have also been successfully utilized in NSTX-U.

- A variety of low-n MHD activity has been observed in NSTX-U, including sawteeth, 1/1 helical core modes, 2/1 modes, and 3/2 modes and the behavior of these modes was found to be strongly affected by differences in beam injection.

- Error fields due to a time-dependent tilt of the TF coil as it interacted with stray fields produced by the OH leads which were present in NSTX have been designed out of NSTX-U. Compass scan experiments resulted in optimized error field correction, which lead to improved performance of NSTX-U discharges. The results also showed that the optimal correction likely varies during the shot, implying that there may be more than one error field source. Candidate sources include the out-of-round nature of the main vertical field coil, induced currents that flow in the vessel wall during ramp-up, and a static tilt of the TF center rod with respect to the vertical axis of the PF-5 coil. The effect of these potential sources on the plasma has been modeled using VALEN, IPEC, and M3D-C1.

- The MARS-F code and the newly developed resistive DCON code were applied to investigate n=1 tearing instability in NSTX-U. Both codes showed that the n=1 tearing mode can be naturally unstable in NSTX-U L-mode discharges depending on the operational conditions, and also interestingly, the tearing instability may be driven by m>2, n=1 modes, instead of the typically expected m=2, n=1 mode.

- Calculations with the DCON stability code confirm that NSTX-U H-mode discharges have achieved operation above the ideal no-wall stability limit. Additionally, a composite no-wall limit model that was developed for NSTX which includes internal inductance, pressure peaking, and aspect ratio does a good job at predicting the NSTX-U no-wall limit.

- Capability of the disruption event characterization and forecasting (DECAF) code has been greatly expanded. The code provides quantitative statistical characterization of the chains of events which most often lead to disruption of plasmas and is being updated to provide forecasts which integrate with a disruption avoidance system and are utilized in real-time during a device's operation.

- A DECAF module has been developed to identify existence of rotating MHD modes, to determine the mode frequency with a fast Fourier transform (FFT), and to track characteristics that lead to disruption, such as rotation bifurcation and mode locking.

- DECAF was used to characterize a set of NSTX discharges with unstable resistive wall modes (RWM). It was found that a simple threshold on low frequency poloidal magnetic sensors usually gave RWM timings near the disruption time unless there were minor disruptions and statistics on the disruption event chains provided insight into the typical sequences of NSTX disruptions.

- A reduced kinetic model for RWM stability which calculates the projected growth rate based upon plasma quantities which may be measurable in real-time has been implemented in DECAF and tested on NSTX discharges. This approach has the potential to anticipate unstable resistive wall modes and use real-time rotation control to steer the plasma to more favorable profiles.

- Halo current studies have been advanced on two fronts: (1) the ITPA database of non-axisymmetric and rotating halo currents has been extended to include substantial data sets from each of NSTX, DIII-D, C-Mod, and ASDEX Upgrade, with the primary effort this fiscal year going toward gathering AUG data and furthering the database analysis; and (2) initial NSTX-U halo current data was collected from shunt tiles located both in the lower divertor and on the center stack.

- Nonlinear, three-dimensional disruption modeling of NSTX plasmas with M3D-C1 has been carried out in order to quantify wall forces during the current quench phase of vertical displacement events (VDEs) and to inform plans for future Halo current diagnostics on NSTX-U.

- Massive Gas Injection (MGI) valves, very similar to the double flyer plate design being considered for ITER to rapidly quench the discharge after an impending disruption is detected, have been tested and installed in NSTX-U. NSTX-U will be the first device to operate this valve design in plasma discharges. Additionally, a fast-acting electromagnetic particle accelerator has also been designed and assembled.

- Progress has been made on a conceptual design for possible upgrades to the 3D magnetic field diagnostics on NSTX-U. Ongoing study of the expected plasma response structure in NSTX-U at high plasma pressure as predicted by the MARS-K code has identified the top and bottom of the machine as favorable locations where relatively large radial and poloidal field perturbations are especially expected when applied fields couple strongly to the plasma.

- The Nyquist analysis, as a powerful tool in stability theory, has been applied to probe and better understand the multi-mode aspects in 3D plasma response in tokamaks. This new MHD spectroscopy has been successfully tested on DIII-D using MARS-F, indicating potential advantage in optimizing the coil phasing and frequency in ELM suppression experiments, and will be applied to various devices including EAST and NSTX-U with available magnetic sensors and 3D coils.

- The newly developed code, GPEC, has been successfully applied to predict NCC capability of NTV optimization in NSTX-U. GPEC provides (1) self-consistent solutions across equilibrium and neoclassical transport, and (2) NTV torque matrix, by which NCC configuration can by systematically optimized with eigenvectors and eigenvalues of the torque matrix.

- Detailed field line integration simulations of the M3D-C1 plasma response needed for comparing the structure of magnetic islands produced by the NCC in NSTX-U to those produced by the DIII-D I-coil have been completed. Results from this comparison shows that the m/n = 9/3 magnetic island screening factor in DIII-D is 75% large than in NSTX-U while the kink response near the q = 3 surface in the two machines is significantly stronger in NSTX-U.

Summary of Research Highlights for Transport and Turbulence

- Long (~2 second), steady L-mode plasmas were successfully developed during commissioning of NSTX-U, spanning a range of plasma current, density, heating power and NBI source tangency all at toroidal field (0.65T) larger than NSTX. In addition to supporting future planned core and boundary experiments, L-mode discharges will support a multi-institutional validation effort of global gyrokinetic turbulence simulations.

- Initial transport analysis of NSTX-U L and H-mode plasmas was successfully accomplished. Power degradation of the L-mode energy confinement was recovered (τ_E~$P^{-0.66}$), in accord with previous tokamak results. Ion transport was found to be near neoclassical levels in at least some of the L-mode plasmas. H-mode energy confinement with $H_{98,y2}$~1 was demonstrated for many energy confinement times, with electron thermal diffusivities 2-3× smaller than L-mode.

- BES turbulence measurements (collaboration with U-Wisconsin) were acquired in the NSTX-U L-mode plasmas showing substantial normalized fluctuations (1-4%) in the outer third of the plasma, which will be used to validate gyrokinetic simulations. Ion scale fluctuations were also observed to decrease across the L-H transition.

- Initial linear gyrokinetic simulations of the NSTX-U L-mode plasmas indicate both ion temperature gradient (ITG) and microtearing mode (MTM) instabilities are unstable, but often weaker than the large E×B shearing rates. Electron temperature gradient (ETG) instability was also predicted unstable in the outer half of the plasma. Predictive modeling using the Rebut-Lallia-Watkins MTM transport model gives surprisingly good agreement with measured Te profiles.

- Global gyrokinetic simulations of ion-scale turbulence using the PPPL Theory GTS code reproduce ion transport in an NSTX H-mode plasma where a large density gradient was previously predicted to suppress electron-scale ETG turbulence. However, the predicted ion-scale electron transport is still much smaller than the experimental analysis, indicating missing transport contributions that may depend either on electromagnetic effects or residual electron scale turbulence (e.g. via multi-scale coupling) not included in the code.

- Using a previously established database of NSTX discharges, a significant correlation is found between normalized wavenumber and frequency based on the compressional (CAE) and global Alfven eigenmode (GAE) resonance conditions, $\omega_{ci} = \omega - k_{||}v_{b||}$, expected to be important in determining their stability (collaboration with UCLA). A weaker correlation is also identified between the measured amplitude-weighted CAE & GAE mode number (or frequency) and peak electron temperature, supporting the hypothesis that at sufficiently high total amplitude, these modes can impact the electron energy balance.

- Neural net analysis of core transport in NSTX H-mode plasmas (collaboration with Seoul National University) has been used to identify parameters which are most sensitively correlated with local electron and ion heat fluxes at different regions in the plasma.

- Refined analysis of perturbative momentum transport experiments in MAST (collaboration with CCFE) that allow for time dependent transport coefficients (proportional to the ion thermal diffusivity, χ_φ, $V_\varphi \sim \chi_i$) indicate a much weaker momentum pinch than inferred previously. Initial quasi-linear gyrokinetic simulations also predict a weak momentum pinch.

- **Summary of Research Highlights for Energetic Particles**

  - Experiments have begun to assess the dependence of the fast ion distribution function on Neutral Beam injection from 1^{st} vs 2^{nd} NB lines. Preliminary results indicate the more tangential (co-passing) fast ion population forming during NB line 2 injection. Analysis from neutron rate evolution following "NB blips" suggests a discrepancy at low NB injection energy with respect to "classical" expectations, which is presently being investigated.

  - Initial observations of Alfvénic instabilities in NSTX-U scenarios indicate the possibility of suppressing high-frequency Global Alfvén eigenmodes (GAE) through injection from NB line 2. This is thought to be caused by the different fast ion distribution resulting from NB line 2 vs. NB line 1 injection, with more co-passing particles providing a less efficient drive (or even stabilizing) GAEs.

  - Measurements of magnetic perturbations up to the ion-cyclotron frequency suggest that Ion Cyclotron Emission (ICE) has been measured. ICE appears to originate from the plasma edge. Work is in progress to understand the correlation between the measured ICE spectrum and properties of the fast ion distribution.

  - Several numerical tools have been developed to investigate the physics of Compressional and Global AEs (CAE/GAEs), including codes to compute expected eigenmodes for a given plasma scenario and non-linear CAE/GAE simulations. Comparison between numerical results and NSTX/NSTX-U experiments is in progress.

  - Modeling tools have been validated to provide an accurate description of the fast ion evolution in the presence of instabilities such as toroidal Alfvén eigenmodes (TAEs). Focusing on a specific NSTX L-mode scenario with unstable TAEs, a hybrid version of the ORBIT code has been used to compute the expected mode saturation amplitudes. Fast ion transport for the same scenario has been studied through a "critical gradient model" and a reduced model implemented in TRANSP. Results from the two models are in reasonable agreements.

  - An improved criterion for the onset of "bursting/chirping" regime for Alfvénic instabilities has been developed and tested against NSTX plasmas. The criterion can correctly predict the regime of AE instabilities. One notable result is that micro-turbulence can play a significant role in the onset of bursting/chirping AEs, even if macroscopic fast ion transport by turbulence is negligible.

Integrated Scenarios

➢ Summary of Research Highlights for Solenoid-Free Start-up and Ramp-up

- Initial progress towards the design of non-inductive current ramp-up scenarios in the National Spherical Torus Experiment Upgrade (NSTX-U) has been made through the use of TRANSP predictive simulations. The strategy involves, first, ramping the plasma current with high harmonic fast waves (HHFW) to about 400 kA, and then further ramping to 900 kA with neutral beam injection (NBI).

- Numerical simulations (NIMROD code) have for the first time been shown to generate a high-fraction of closed flux surfaces during transient CHI operation. The ratio of the closed poloidal flux to the injector flux is over 70% (similar to experimental observations).

- The large closed flux fraction was obtained using constant in time coil currents, which bodes well for transient CHI application to a ST-FNSF or a reactor with superconducting coils.

- A paper describing the transient CHI concept for a ST-FNSF was published.

- In an effort lead by the NSTX-U CHI Team during the past year, all necessary systems needed for initiating transient CHI on QUEST were commissioned. This includes the NSTX sized CHI capacitor bank, voltage snubbers, fast gas injection systems, and fast voltage monitors. The first CHI experiments on QUEST are planned for later in 2016.

- The NSTX-U CHI capacitor bank is ready to support plasma operations on NSTX-U.

➢ Summary of Research Highlights for Wave Heating and Current Drive

- The HHFW system was recommissioned with many improvements to the crowbar circuit, breakers, and relays. Vacuum conditioning raised the stand-off voltage to least 19 kV for each sub-system, and the entire system is ready for plasma conditioning.

- Coupling HHFW power to the plasma depends strongly on the outer gap size, and we have initiated studies both on how the outer gap and loading resistance varies in NSTX-U during start-up and in response to changes in plasma heating.

- 2D AORSA full wave simulations and a sensitivity analysis on the artificial collisional damping (used as a proxy to represent the real, and most likely nonlinear, damping processes) in the scrape-off layer have been performed for NSTX/NSTX-U and "conventional" tokamaks with higher aspect ratios, such as the DIII-D, Alcator C-Mod, and EAST devices.

- A special class of modes, dubbed “annulus resonances,” conduct a large fraction of the total wave power in the edge plasma of a cylindrical model and have a half radial wavelength into the edge plasma region. These results corroborate results drawn from the full-wave code AORSA, namely that cavity-like modes are driving the SOL losses on NSTX.

- The extension of the full wave code TORIC to include non-Maxwellian ion effects in the minority and high harmonic heating regimes has been implemented and completed.

- RF rectification, studied as a function of injected HHFW power, deviates from the expected dependence, perhaps due to an onset of elevated plasma potential to offset the rapidly increasing rectified electron current. This is important both for SOL losses of HHFW power in NSTX and for the EAST ICRF system, which also produces bands of light on the lower divertor and changes in floating potential in divertor Langmuir probes, similar to NSTX.

➢ Summary of Research Highlights for Advanced Scenarios and Control

- Breakdown and current ramp scenarios were developed for both the 8 kA and 20 kA OH pre-charge scenarios.

- rtEFIT was commissioned for NSTX-U, with many improvements including a multi-threading option which allows more extensive calculations without sacrificing computation time. Further, the ISOFLUX shape control algorithms were fully commissioned for NSTX-U, including X-point and/or strikepoint location control and a new inner-gap control algorithm.

- An automated discharge shutdown algorithm was introduced, based on a state machine formulation.

- The vertical position control system was expanded with both new sensors and new algorithms.

- High-β H-mode discharges were recovered, exceeding the n=1 no-wall limit.

- Modeling of profile and snowflake divertor control is laying the foundation for future high-priority experiments on NSTX-U.

Performance of FY2016 Notable Outcomes:

Notable 1 - Objective 1.2: *"Perform experimental research on NSTX Upgrade to address key spherical torus issues at magnetic field, plasma current, and pulse length beyond that achieved in NSTX, after completion of CD-4 for the NSTX-U project."*

FY2016 was a productive first year of operations and research for NSTX-U as described in subsequent sections of this report. All magnetic diagnostics needed for off-line and real-time equilibrium reconstructions were commissioned, and the real-time EFIT reconstructions and the ISOFLUX plasma boundary shape control algorithm were commissioned. Key profile diagnostics were commissioned including multi-point Thomson Scattering (MPTS) and Charge Exchange Recombination Spectroscopy (CHERS). Long-pulse L-mode scenarios were developed for transport studies and intrinsic error-field detection and correction, and high-performance H-mode plasmas operating near and slightly above the n=1 no-wall stability limit were also developed. More details on scenario development are provided below in the report for FY2016 Research Milestone R(16-3): *"Develop the physics and operational tools for obtaining high-performance discharges in NSTX-U"*. Further, several transport, stability, and energetic particle physics experiments were carried out as described in the milestone and highlights sections in this report.

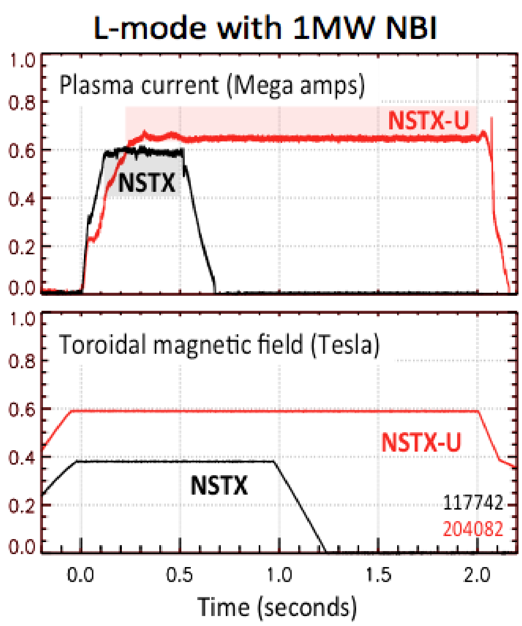

Fig. NO16-1-1*: Comparison of NSTX and NSTX-U L-mode discharges.*

Figure NO16-1-1 shows comparisons of NSTX (black) and NSTX-U (red) L-mode plasmas each heated with 1MW of NBI heating. The significantly larger (factor of 3) ohmic solenoid flux available in NSTX-U combined with 50% higher toroidal field resulted in a factor of 4 increase in L-mode pulse duration for otherwise similar plasma conditions. Reproducible sawtoothing plasmas were achieved in NSTX / NSTX-U for the first time, and this enabled new studies of tearing-mode stability and triggering not previously accessible in NSTX. Figure NO16-1-1 shows plasma current sustained past t=2.0s, and this plasma duration exceeds the record pulse duration achieved in NSTX in any confinement regime (L-more or H-mode) and any heating power. Further, Figure NO16-1-1 also shows toroidal field of 0.6T sustained with a flat-top exceeding 2s, and this toroidal field exceeds the maximum field achievable on NSTX (0.55T) for a factor of 3-4 times longer than in NSTX. Thus, in a single plasma discharge, Figure NO16-1-1 demonstrates toroidal field magnitude and flat-top and plasma pulse duration simultaneously exceeding the highest values achieved on NSTX.

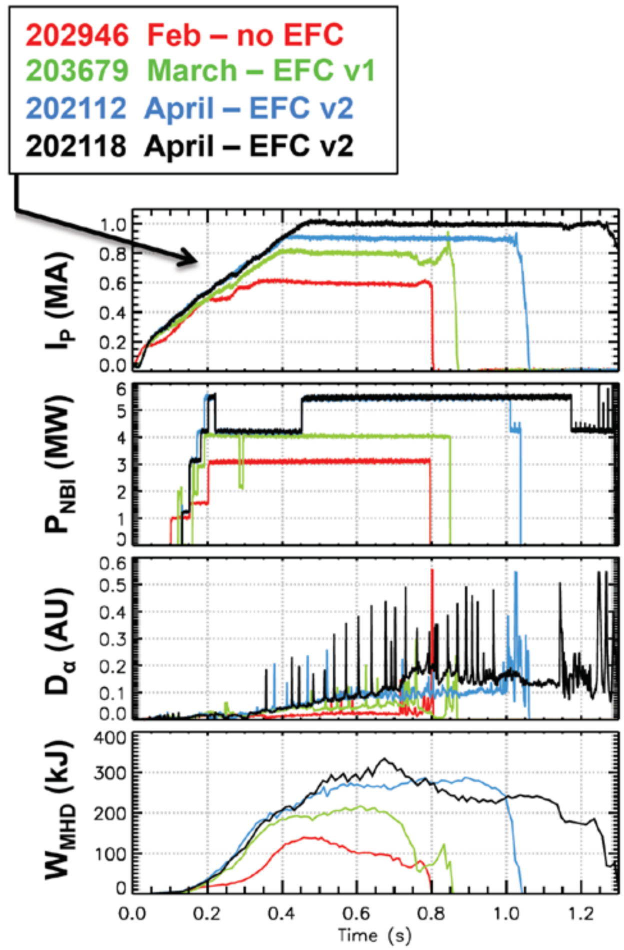

***Fig. NO16-1-2**: H-mode scenario progression during FY16 run.*

While H-mode access was obtained relatively rapidly in NSTX-U (within the first two weeks of post-bake-out operation), long-pulse H-mode operation required significantly more development than the relatively rapid L-mode development described above and in the summary of milestone R16-3. Critical elements of MHD-stable long-pulse H-mode operation with boronization on NSTX and NSTX-U include sufficient heating power to sustain regular ELMs, adequate error-field correction, and the utilization of early H-mode access, i.e. H-mode access during the plasma current ramp-up. Such early H-mode access plays an important role in increasing the plasma temperature and the off-axis bootstrap current – both of which slow the current penetration, significantly lower the plasma internal inductance, allow increased early elongation, and help maintain an elevated safety factor profile in the plasma core. In both NSTX and NSTX-U high current scenarios, lack of early H-mode access often resulted in triggering of m/n=2/1 tearing modes that can slow and lock if intrinsic error fields are too high.

Figure NO16-1-2 shows a sample of the progression of H-mode plasma scenarios obtained in NSTX-U - see the R16-3 milestone report for more details. As is evident in the figure, the early H-mode plasma shot 204118 sustained a plasma current flat-top of 1MA lasting until t=1.25s. This matches the end time of the longest-duration 1MA H-mode plasma flat-top achieved in NSTX. The maximum plasma current and length of discharge steadily increased through the run as the available neutral beam heating power increased, the axisymmetric control of the plasma shape was refined, and the identification and correction of error fields progressed. Experiments underway at the conclusion of the run were advancing the neutral beam heating, plasma shape control, and error field correction to the levels needed to increase the NSTX-U plasma current up to 1.5 MA at an on-axis toroidal field of 0.65 T. The NSTX record for plasma current sustained for ~1-2 current redistribution times is 1.3MA sustained to t = 0.8s, and transient (~1 energy confinement time) plasma currents up to 1.4MA were also achieved at 0.55T. However, NSTX-

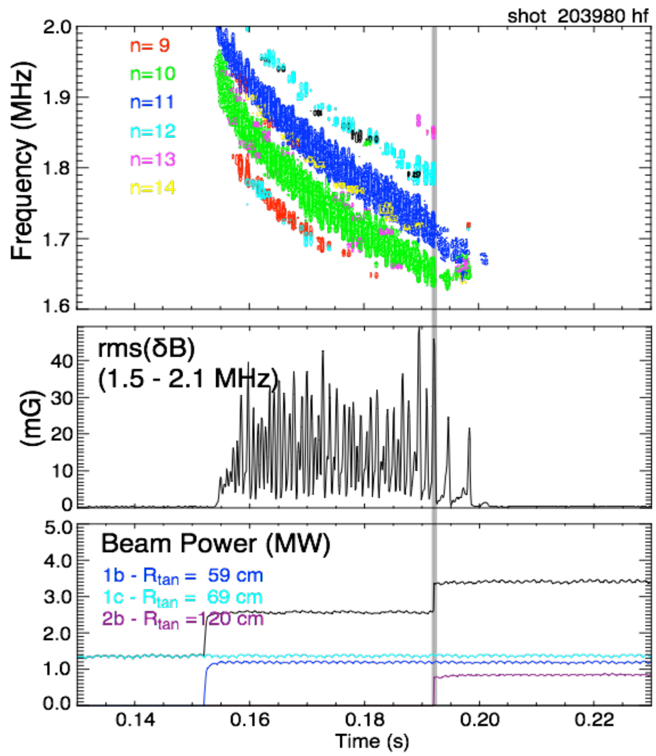

***Figure NO16-1-3**: (a) spectrogram showing GAE modes. (b) Root-mean-square fluctuation level of GAE. (c) Injected NB power: black-total, colors represent the power injected from each individual source.*

U researchers were unable to access currents above 1MA before the PF1AU coil internal fault forced cessation of NSTX-U operations for FY2016. Thus, NSTX-U achieved higher toroidal field and pulse durations than NSTX and matched 1MA NSTX H-mode performance levels in only 10 weeks of commissioning and operations, but was unable to surpass NSTX maximum plasma current values due to insufficient scenario development time.

While NSTX-U has not yet exceeded the highest NSTX plasma current levels, the new more tangential 2nd NBI of NSTX-U rapidly yielded important results for Alfven Eigenmode stability. In particular, it was found early in the FY16 run that the original NSTX beam sources, with tangency radii inside the magnetic axis, would excite a similar spectrum of instabilities to those commonly seen on NSTX. Nearly all operation of NSTX-U has been at a nominal toroidal field of 6.5 kG, higher than NSTX could reach, and the plasma densities tended to be lower than was seen on NSTX. As the new neutral beam (NB) line 2 sources became operational, it was quickly noted that use of these sources was anti-correlated with the presence of Global Alfven Eigenmodes (GAE). Further, when any NB 2 source was added to a plasma with one or more NB line 1 sources and it was seen that the addition of more beam power could completely suppress the counter-propagating GAE (see Figure NO16-1-3). This observation is qualitatively consistent with a theory of GAE instability developed by Gorelenkov where the drive/damping of resonant fast ions was dependent on the Larmor radius and changes in the fast-ion distribution function. The capability to suppress the GAE with the substitution of sources at the same neutral beam power, or by adding more NB power, will prove to be a useful tool for understanding the role of GAE in electron heat transport. New research results enabled by the new beamline are described in more detail below in the summary of Research Milestone R(16-2) and in the Energetic Particle research highlights.

<u>Notable 2 - Objective 1.2:</u> *"Conduct NSTX-U experiments and data analysis to support the FES joint research target on detecting and minimizing the consequences of disruptions in present and future tokamaks, including ITER."*

The full text of the Joint Research Target (JRT) for FY2016 is:

"Conduct research to detect and minimize the consequences of disruptions in present and future tokamaks, including ITER. Coordinated research will deploy a disruption prediction/warning algorithm on existing tokamaks, assess approaches to avoid disruptions, and quantify plasma and radiation asymmetries resulting from disruption mitigation measures, including both pre-existing and resulting MHD activity, as well as the localized nature of the disruption mitigation system. The research will employ new disruption mitigation systems, control algorithms, and hardware to help avoid disruptions, along with measurements to detect disruption precursors and quantify the effects of disruptions."

NSTX-U made substantial progress in FY2016 toward identifying impending disruptions and in ramping down the plasma when disruptions can no longer be avoided. Key to this progress was the implementation of a new "Shutdown State Machine" in the Plasma Control System (PCS). There are several motivations for implementing such a system. First, the largest forces on the coils and their support structures in NSTX often occurred during transients while trying to control an already-disrupting plasma. By accepting that the plasma is disrupting and attempting instead to control it rapidly to zero current, these transient loads can be reduced. Secondly, the development of plasma shutdown methods, both during normal operations and during off-normal events, is critical for the ultimate development of ITER and future tokamak/ST devices.

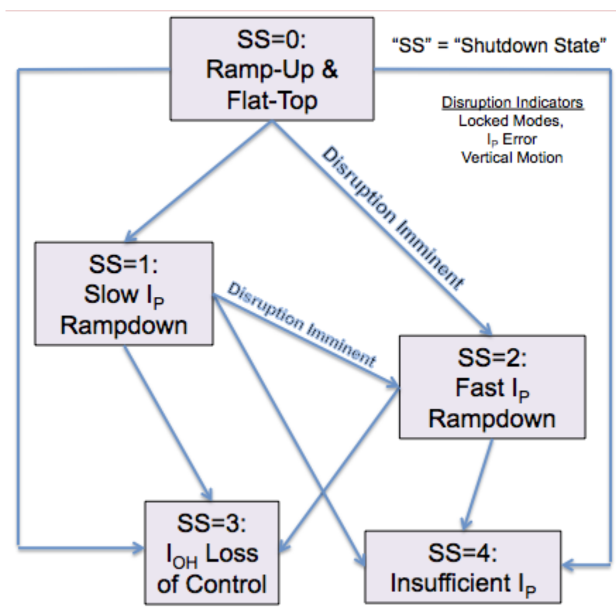

Fig. NO16-2-1*: State machine architecture in NSTX-U PCS*

This shutdown code is based on a state machine formalism, described by Fig. NO16-2-1. In this system, the plasma is initiated in the SS=0 state, for ramp-up and flat-top control. There are two terminal states: SS=3 occurs when the OH current has exceeded a final threshold, which implies an imminent loss of OH current control and therefore plasma current control, while SS=4 corresponds to the case where the plasma current has vanished (either due to being ramped down or a disruption). In either of these terminal states, all gas injection is stopped, the neutral beams are turned off, and all coil currents are returned to zero. In between the two terminal states and the initial SS=0 state reside the two plasma rampdown sequences. SS=1 contains a slow rampdown, which is intended to be entered when the plasma is in a normal state. Only i) an operator waveform, ii) the OH current dropping beneath an initial threshold, or iii) the OH coil approaching an I^2t limit could drive this transition. The fast rampdown state, on the other hand, is intended to cover cases where the plasma has entered an unhealthy state, and needs to be quickly ramped down. The present code allows transitions to the fast rampdown state when any of the following occur: large n=1 modes are detected by the Resistive Wall Mode sensors, excessive vertical motion was detected by the vertical position observer, the fractional plasma current error exceeded a threshold, or the plasma current dropped beneath a threshold. Additional details of this state machine are described in the Research Milestone R16-3 report below.

The shutdown state machine described above has already proven to be very effective at identifying major losses of plasma confinement and/or control and ramping down the plasma. Disruption prevention and avoidance is also an important operational goal for future devices, and the disruption event characterization and forecasting (DECAF) code was written at NSTX-U in order to facilitate a comprehensive framework for disruption prevention through forecasting and avoidance, or prediction and mitigation of the detrimental consequences. The ultimate goal of such an approach is to provide forecasts, which integrate with a disruption avoidance system and are utilized in real-time during a device's operation. Previously reported DECAF work focused on the first step: quantitative statistical characterization of the chains of events which most often lead to disruption of plasmas. Progress on the development of DECAF was made in three areas during FY2016 (see the Macroscopic Stability TSG highlights in this report for more details). The 3 areas include: (1) identification of rotating MHD modes, (2) characterization of a set of resistive wall mode (RWM) disruptions, and (3) the development of a reduced kinetic model for RWM stability. The identification of rotating MHD modes in DECAF is provided as an example new capability in this Notable Outcome report.

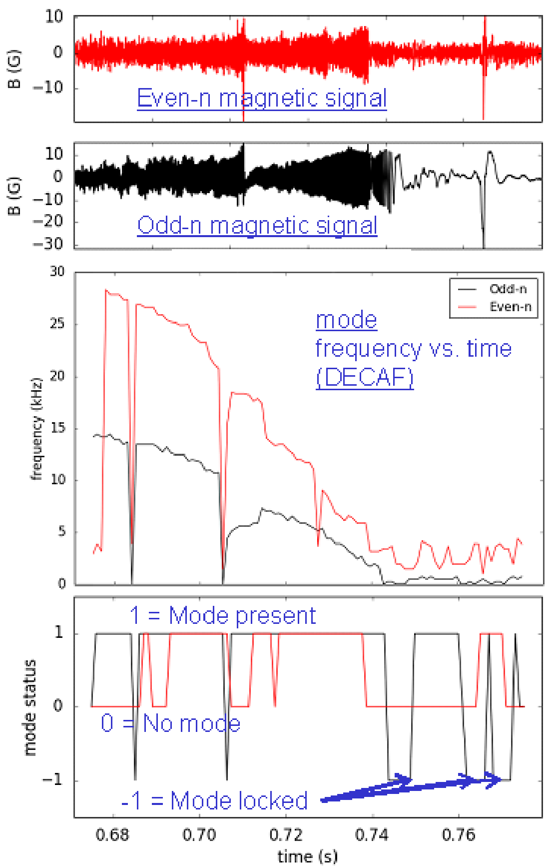

Figure NO16-2-2: *Identification of rotating MHD in DECAF for NSTX-U discharge 204202.*

An essential step for DECAF analysis of tokamak data is identification of rotating MHD activity, such as neoclassical tearing modes. The initial goals were for the code to identify existence of rotating MHD modes and to track characteristics that lead to disruption, such as rotation bifurcation and mode locking. The approach taken was to apply a fast Fourier transform (FFT) analysis to determine the mode frequency and bandwidth evolution. Figure NO16-2-2 shows the even-n and odd-n magnetic signals for NSTX-U discharge 204202, the mode frequencies determined by DECAF and the mode status, showing odd-n locking late in the discharge. Such real-time analysis could potentially provide much earlier warning of possible mode locking and disruption than is presently achievable with the low-frequency RWM/EF sensors already included in the PCS state-machine. Activities are already underway to specify and then implement a real-time rotating MHD identification algorithm for NSTX-U.

Methods to rapidly quench the discharge after an impending uncontrolled disruption is detected are essential to protect the in-vessel components of ITER and any future ST-based devices. In support of this activity, NSTX-U will employ three Massive Gas Injection (MGI) valves that are very similar to the double flyer plate design being considered for ITER. NSTX-U will be the first device to operate this valve design in plasma discharges. In FY2016, these valves were tested off-

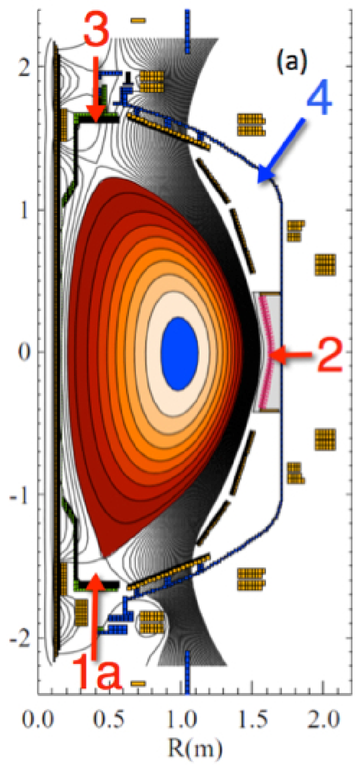

Figure NO16-2-3: *Existing (Red) and Planned (Blue) MGI valve locations on NSTX-U.*

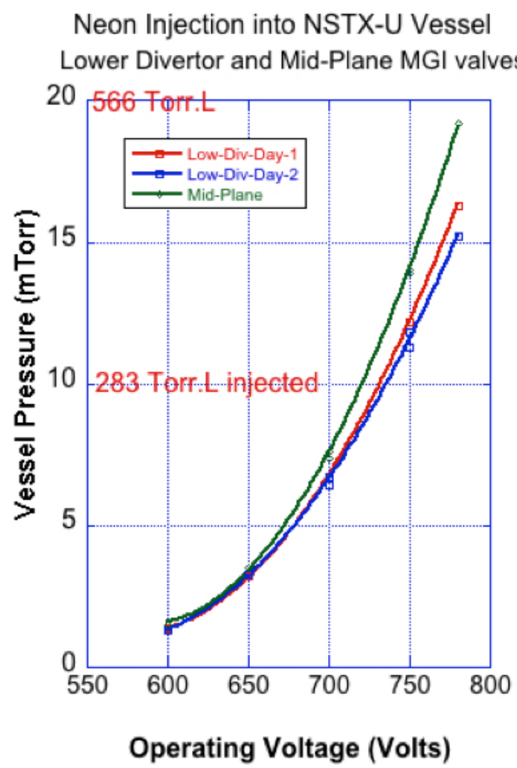

Figure NO16-2-4: *Vessel pressure increase as a function of operation voltage for the valves located at positions 1a and 2.*

line and shown to deliver the required amount of gas (~ 200 – 400 Torr.L) to support NSTX-U experiments. These experiments which will provide new MGI data by studying gas assimilation efficiencies for MGI gas injection from different poloidal locations (at the same toroidal location), with emphasis on injection into the private flux region. The valve has also been successfully operated in external magnetic fields of 1 T, and a recently published journal paper describes the results obtained from these off-line tests.

Three of these valves were installed on NSTX-U. These correspond to locations 1a, 2 and 3 in Fig. NO16-2-3. In preparation for FY16 MGI experiments, the goal of which was to conduct a comparison of the mid-plane to lower divertor injection locations, the lower-divertor and mid-plane valves were commissioned and prepared for full operational capability. The capacitor based power supplies needed to operate these valves were operated at 1kV, which is more than the ~800V needed for injecting 400 Torr.L of neon into NSTX-U. Both these valves were then tested for full operation in nitrogen, helium, and neon at the full operating pressure of 10,000 Torr. Figure NO16-2-4 is a plot of the amount of neon injected as the operating voltage is increased. These valves are now ready to support plasma operation and would have been used in MGI experiments in the FY16 run if more experimental run time had been available. During the FY17 NSTX-U outage the upper MGI valve will be commissioned and prepared for full operational capability.

Finally, while the MGI system may be adequate for most disruptions, the warning time for the onset of some disruptions could be much less than the MGI system response time. To address this important issue, a novel system based on the rail-gun concept was designed, components fabricated and the system fully assembled. The system consists of a 1m long rail gun powered by a 20mF, 2kVcapacitor bank. The capacitor bank parameters are essentially the same as that used for the transient CHI experiments on NSTX. The device referred to as an Electromagnetic Particle Injector (EPI) is fully electromagnetic, with no mechanical moving parts, which ensures high reliability after a period of long standby, and is described in a recent journal publication. In addition to responding on the required fast time scale, its performance substantially improves when operated in the presence of high magnetic fields. The system is also suitable for installation in close proximity to the reactor vessel. Experimental results from the operation of this system will be presented at the 2016 IAEA Fusion Energy Conference.

NSTX-U FY2016 Year End Report: Facility and Diagnostics

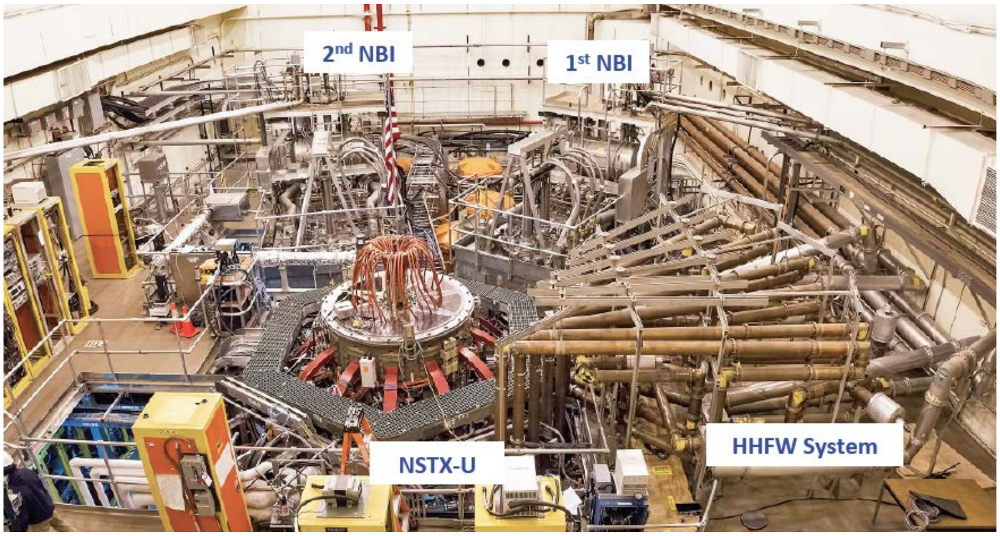

Fig. FD-1 *- Aerial view of the NSTX-U Test Cell. The newly commissioned 2nd NBI beam box can be seen in the background.*

In FY 2016, NSTX-U operated for 10.06 run weeks with 1066 plasma shots to commission the upgraded facility and perform research operations. 31 experimental machine proposals related to the commissioning of the facility including diagnostics systems were performed. After an extensive high temperature bake-out of vacuum vessel, plasma operation started on Dec. 18, 2015. CD-4-like discharges were achieved on the first day, and the current was quickly ramped up to 700 kA on Dec. 22, 2015. After the new year, boronizations were performed and with NBI injection into the plasma, H-mode was accessed in plasmas on Jan. 13, 2016. H-mode access is now routine, and experimental machine proposals (XMPs) have been performed and a number of experimental proposals (XPs) have begun. A NSTX-U Test Cell aerial view taken in Feb. 2016 is shown in Fig. FD-1. The installation and commissioning for the modifications to the Multi-Pulse Thomson Scattering (MPTS) diagnostic required for the NSTX-U were completed in FY2015 and the MPTS is now supporting research operations. On June 28, the PF-1A upper coil developed an internal short. After performing various tests, it was decided that the coil was indeed damaged and required replacement. After completing post-run diagnostic calibrations and TF joint electrical measurements, the PF-1A upper coil was removed for further examination on August 24, 2016. A coil shop has been set up at PPPL to fabricate the replacement PF-1A coil. To provide capabilities needed to carry out NSTX-U scientific research, the NSTX Team identified high priority facility and diagnostic enhancements for post upgrade operations as the part of the successful DOE NSTX-U Five Year Plan Review. These included diagnostics and physics capabilities provided by NSTX Research Team members from U.S. laboratories other than PPPL as shown in Fig. FD-2. Those capabilities being currently implemented are indicated by the green dots. The red circles are the longer-term significant enhancements, i.e., divertor cryo-pump (DCP), non-axisymmetric control coil (NCC), and electron cyclotron heating (ECH), and conceptual engineering designs completed in FY 2016.

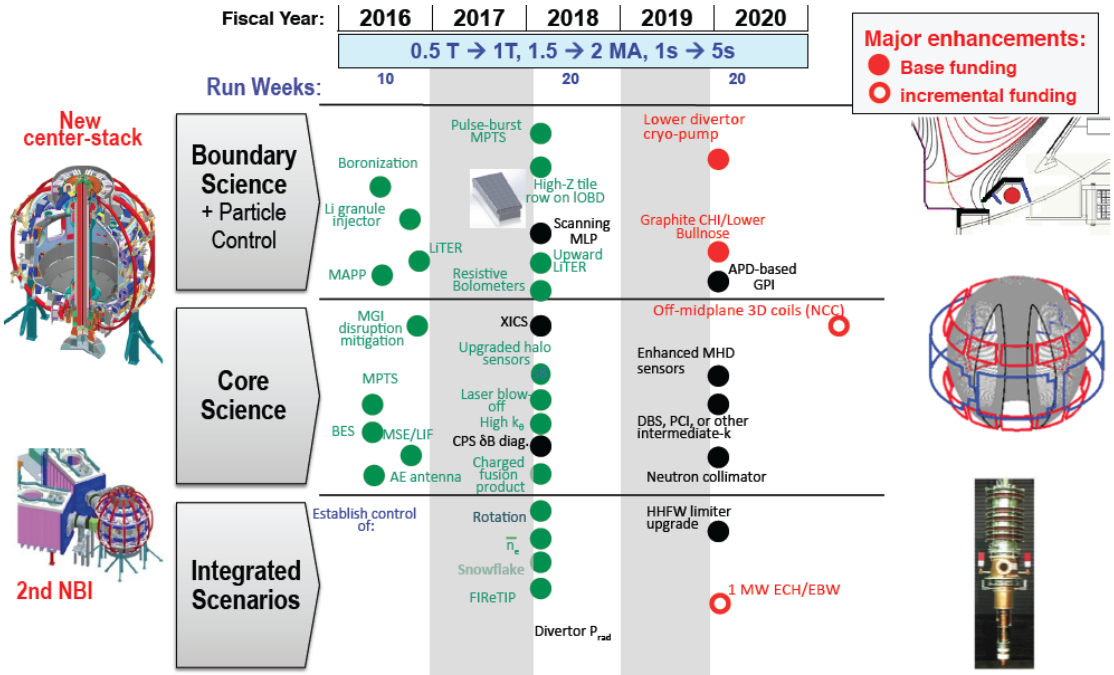

Fig. FD-2 - Overview of the NSTX-U Facility Plan

Facility and Diagnostic Milestones for FY2016

Facility Milestone F(16-1): Complete FY 2016 NSTX-U research operation. (September 2016)

Description: With base funding, the NSTX Upgrade Project is expected to continue its run through the 3^{rd} quarter of FY 2016, before going into the FY 2016 outage in the 4^{th} quarter to install the high-Z tiles and prepare for the higher field and current operations.

Report: NSTX-U has operated for 10.06 run weeks with 1066 plasma shots to commission the upgraded facility and performed research operations. 31 experimental machine proposals related to the commissioning of the facility including diagnostics systems were performed. The plasma operations were performed mostly at B_T = 6.5 kG up to 2.2 sec. which significantly exceeded that of NSTX of up to B_T = 5.5 kG up to 1 sec. The plasma operation was interrupted due to the PF-1AU coil failure. All of the NBI sources were conditioned up to the full 90 kV. HHFW antennas were vacuum conditioned with all of the six rf sources. A large number of diagnostics were installed and commissioned.

Facility Milestone F(16-2): Complete high-Z tile fabrication and prepare for installation. (September 2016)

Description: With the completion of the engineering design in March 2016, procurement and fabrication of high-Z tile components should be completed by Sept. 2016 so that they are available for installation in FY 2017 during the outage. The NSTX-U long-range plan calls for a gradual change in PFC material from the existing graphite tiles to high-Z surfaces. This change is motivated by surface-science and linear-device studies indicating that the lithium behavior on metallic substrates is significantly different from behavior on graphitic surfaces. There is little expectation that a power reactor will feature graphite surfaces leading to the need for complex and subtle interpretations of current experiments with respect to plans for future reactors. A gradual upgrade to high-Z PFCs will provide the NSTX-U program with two major benefits: first high-Z PFC performance and impact on core scenarios can be assessed in their own right and studies of lithium-coated and flowing-Li systems can be assessed with an integrated core scenario.

Report: The NSTX-U completed a design and has nearly completed fabrication of a complete set of high-Z tiles for the outboard divertor. The design was intended to replace, nearly one-for-one, divertor tiles in the outboard divertor of NSTX-U so as to minimize in-vessel modifications and changes to mounting hardware. In order to increase the allowable heat-flux to the front-surface, a castellated design was utilized. This design separates the location of peak temperature and peak stress which is advantageous as TZM rapidly weakens at elevated temperatures. The PFCs are rated for heat-flux impact factors of 10 $MJm^{-2}s^{-1/2}$, or nominally $10MWm^{-2}$ for a full second. This will minimize the impact on operations and provide a reference point for future designs in other high-heat flux regions of the machine. The tile fabrication job is nearing completion and the full set of divertor tiles are expected at PPPL by September 2016. The first-article receipt inspection was completed in late June and Fig. FD-3 shows the first tile fabricated by the selected vendor. The fabrication method utilized is electro-discharge-machining, or wire-EDM. This fabrication method is useful for fine-feature work in molybdenum, but also in bulk tungsten components. Experimental tiles include a tungsten tile to support experiments as well as a highly-shaped tile that will further mitigate heat fluxes and extend the usefulness of future components composed of high-Z metals. A plan for installation has been laid out during the design process for the high-Z tiles and was included in the Final Design Review for the tiles held in February, 2016. The installation procedure will be formalized prior to actual installation in the machine.

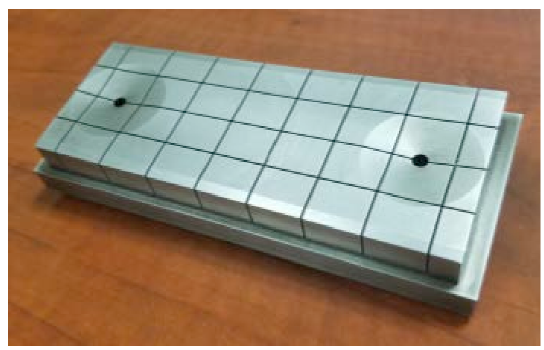

Figure FD-3. First-article high-Z tile provided to PPPL for inspection

Facility Milestone F(16-3): Complete divertor cryo-pump engineering conceptual design. (September 2016)

Description: Complete engineering conceptual design of lower divertor cryo-pump. This includes a detailed design of the divertor cryo-ring and the divertor cryo-pump chamber layout taking into account possible thermal and electromagnetic forces. The cost and schedule should be also developed.

Report: The Conceptual Design Review for the NSTX-U Divertor Cryo-pump project was held on August 3rd, 2016. A schematic of the Cryo-pump is shown in Fig. FD-4. This integrated, system level review covered all aspects of the project including the cryo-pump, divertor, liquid helium delivery, as well as impacts to NSTX-U, safety, cost and schedule. The review panel, consisting of PPPL, GA and MIT staff, deemed the review successful. The review material can be found at http://w3.pppl.gov/cpd/index.htm.

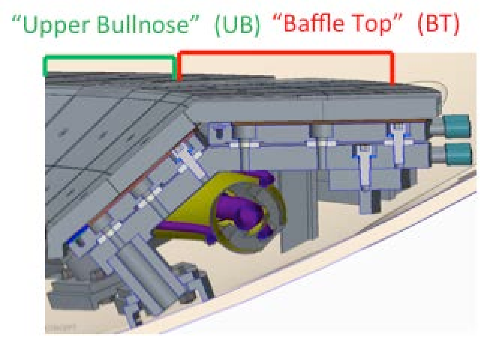

Fig. FD-4. A schematic of the NSTX-U Divertor Cryo-pump layout

Facility Milestone F(16-4): Complete electron cyclotron heating / electron Bernstein wave (ECH/EBW) system engineering conceptual design. (September 2016)

Description: Complete engineering conceptual design of the ECH/EBW system. This includes a detailed design of the gyroton room layout, the high voltage power supply specification, the transmission line layout details. The cost and schedule should be also developed. As a part of the design activity, collaborate with the Tsukuba group to characterize the proto-type gyrotron and assess the viability of its use on NSTX-U.

Report: Engineering conceptual design of the ECH/EBW system was successfully completed. This includes a detailed design of the gyrotron room layout, the high voltage power supply specification, and the transmission line layout details. The preliminary cost and schedule was also developed. As a part of the design activity, collaboration was initiated with the Tsukuba group to characterize the proto-type gyrotron and assess the viability of its use on NSTX-U.

Facility Milestone F(16-5): Complete non-axisymmetric control coil (NCC) engineering conceptual design. (September 2016)

Description: Complete engineering conceptual design of NCC. This includes a detailed design of the NCC system taking into account possible thermal and electromagnetic forces. The cost and schedule should be developed and the required testing and characterization of the sample conductors should be also performed. The NCC are intended to satisfy a number of physics criterion including magnetic breaking, error field control, fast Resistive Wall Mode (RWM) control and ELM stabilization.

Report: Successful engineering conceptual design of NCC was complete. This includes a detailed design of the NCC system taking into account possible thermal and electromagnetic forces as shown in Fig. FD-5. A bottom-up project estimation of costs, schedule and risks was presented. The required testing and characterization of the sample conductors were also performed. A Systems Requirements Document (SRD) was also prepared. A total of 21 chits were generated from the design review and the review was declared as acceptable.

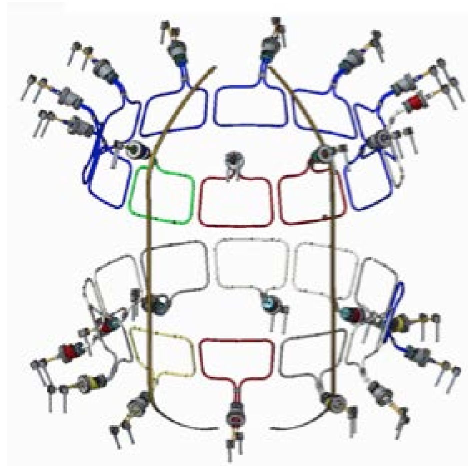

Fig. FD-5. The NCC configuration with 12 upper and 12 lower coils.

Diagnostic Milestone D(16-1): Complete fabrication of divertor resistive bolometers and prepare for installation (September 2016)

Description: A bolometer system to measure the radiated power in the NSTX-U divertor region will be designed, fabricated, and prepared for installation during the shutdown following the FY16 run. The system will consist of two views, one looking down into the divertor region from a top port at bay J and the other viewing the divertor region horizontally from a lower port at Bay I. Both views will have eight channels of metal-foil resistive bolometer sensors, for a total of 16 channels. Shutters and active cooling will be provided to protect the sensors during NSTX-U bakeout. This system will allow the strongly radiating regions of the divertor to be identified for various operational scenarios and will provide measurements of the total power radiated from the divertor region.

Report: Conceptual and final design reviews for the divertor resistive bolometer installations at Bays I and J were held in FY2016. Procurement of the long-lead time sensors and data acquisition system were completed and these items have been delivered to PPPL. A final solid model of the Bay I installation was developed and fabrication drawings were produced. The final solid model for the Bay J installation has also been completed and the fabrication drawings are in production. Fabrication of components will start in September 2016, followed assembly and testing of the systems. Both resistive bolometer systems will be installed during the 2016-2017 NSTX-U outage.

Plasma Control System support of research plasma operations – The NSTX-U plasma control system reliably supported both power system testing and plasma operations. The new real-time Linux computers, which used a new serial FPDP interface replacing the previously employed parallel FPDP interface, operated reliably with minimal downtime. The realtime data stream functioned with very high reliability. New plasma control algorithms introduced include:

- updates to rtEFIT, including a new parallelized options,
- updates to ISOFLUX shape control, the option for direct control of the inner plasma-wall gap, and expanded gap control algorithms for basic shape control of limited discharges in ramp up and ramp down
- updates to the vertical control codes, including additional sensors,
- updates to PCS NBI control algorithms, and PCS control of center-stack gas injection
- development of an integrated discharge shut-down system, and
- improvements to the realtime RWM sensor compensations.

See the R16-3 milestone report for more details on these new algorithms.

Digital Coil Protection System support of research plasma operations - The NSTX-U digital coil protection system supported NSTX-U coil testing and plasma operations. This system uses the measured coil currents to compute forces, torques, and stresses, and then compares the computations to predefined limit values. Exceeding a limit value results in the power supplies going into a safe state. See the R16-3 milestone report for more details on the DCPS support of the research campaign.

Magnetics For Equilibrium Reconstruction, Boundary Control, and RWM Suppression – There are many more magnetic sensors in NSTX-U than NSTX, largely due to the increase in the number of sensors on the newly fabricated center column. This system was fully commissioned during FY-16 to support research operations.

The poloidal field and flux measurements are used to constrain both off-line and realtime equilibrium reconstructions. All integrators were calibrated with a dedicated test setup. All sensors were calibrated via single coil test shots, and their spurious pickup corrected. These gains and pickup corrections were checked against the LRDFIT code, and found to be quite good. Those LRDFIT comparisons also revealed an anomaly in the data during current ramps, which was traced to a set of copper tubes in the CS casing that were not previously included in the conducting structure model. Once these were included, good agreement was found between the LRDFIT predictions and the poloidal field & flux measurements, both during current ramps and steady state phases.

The capability for a diamagnetic flux measurement was restored. The diamagnetic flux in NSTX-U is measured via a return lead of the plasma current rogowski sensor; this measurement, however, is dominated by the flux from the TF coil. Therefore, in FY-15, a rogowski sensor was installed on one the TF outer legs, allowing a direct measurement of the time-derivative of the TF current. By combining these measurement in FY-16, it is possible to get a clean diamagnetic flux signal. This system was commissioned in the first weeks of the FY-16 run, and was used as a constraint in all EFIT02 reconstructions. It is also available in realtime.

The resistive wall mode (RWM) sensor signals were examined during the initial magnetics calibration shots in December, and further cabling errors resolved. All integrators were calibrated. The software calibration routines from NSTX were resurrected, updated, and used to develop a new set of calibration coefficients. The RWM sensors were then used to deduce resistive wall modes and locked modes for the majority of the NSTX-U run campaign.

Finally, the plasma current measurement system was brought into full functionality. It was found during operations in December 2015 that the plasma current measurement was contaminated by large current ripple from the PF-1a coils. In particular, while the rogowski did not detect that current ripple directly, the ripple appeared in some vessel current segments as computed by the hardware I_P calculator, and therefore appeared in the final plasma current calculation. This was remedied by placing low-pass filters on the analog outputs of the key vessel current calculation channels. In this way, the plasma current measurement system supported research operations in FY-16.

PF-1A Upper Coil Failure - On June 28, 2016, the PF-1A Upper (PF-1AU) coil developed an internal short. Plasma operations were stopped when the PF-1AU coil cooling water flow indicator showed an inadequate flow rate. The cooling water path was indeed clogged, and during an attempt to unclog the water path, a small droplet-shaped copper piece came out of the water line. This suggested that the coil could be shorted internally and melted locally. The internal turn-to-turn short was confirmed by the observation of induced internal currents when a neighboring coil was energized. Further detailed analyses of the coil impedance history revealed that the PF-1AU coil was degrading over a three-month period prior to its failure, as shown by blue dots in Fig. FD-6. In contrast, the PF-1A Lower (PF-1AL) coil impedances, shown by red points, showed no sign of degradation. Further tests of the PF-1AU coil showed an indication of multiple turn-to-turn shorts. On July 20, it was decided to terminate FY 2016 plasma operations. After completing post-run diagnostic calibrations and TF joint measurements, the PF-1AU coil was removed for further examination on August 24, 2016. A forensic team was formed to analyze the damaged coil and determine the likely cause of the coil failure. A PF-1A coil design team was also formed to incorporate any findings from the forensic effort. A number of coil improvements were already identified and incorporated into the design, including eliminating sharp jogs, increasing insulation thickness, using a continuous conductor to eliminate in-line

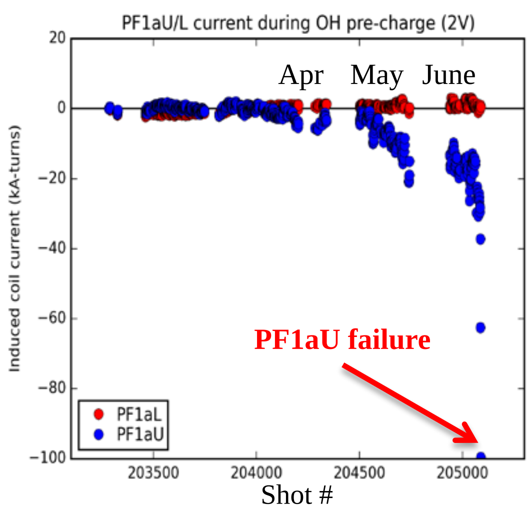

Fig. FD-6 *- PF-1A coil inductance time evolution. PF-1AU shows inductance degradation over a period of three months* braze joints, and a softer conductor to ease the coil winding process. A coil shop was set up at PPPL to manufacture possibly multiple PF-1A coils in FY 2017.

Preparation toward full operational capability – With the PF-1A coil issues identified and other technical information obtained during FY 2016 plasma operations, we are formulating an operational plan toward full operational capability for NSTX-U. A priority is to bring the device capability to its full design capability as soon as possible. During the outage planned in FY 2017, improvements will be made that include TF joint lead extension replacement, passive plate structure enhancement, improved PF-1A coils, and PF coil flex bus support enhancements. The coil monitoring systems will be also upgraded. Prior to the start of the plasma operations in FY 2018, we plan to test the NSTX-U coils to its full capability. In FY2017, the goal will be to bring the TF coils to 1 T for 5 s and the PF coils to the full values needed for 2 MA operations.

Neutral Beam Injection (NBI) Systems – After completion of the NSTX-U center-stack and NBI upgrade (KPP firing one ion source at 45 kV into armor May 10, 2015), the beam hardware was inspected and evaluated to bring all 6 ion sources into service at experimentally useful accelerating voltage and neutral beam power. The NBI systems comprised of power supplies, controls, cryogenics, beam-lines, services, and sources required extensive effort and attention to detail to achieve the mission of 6 sources at 90 kV for plasma heating experiments. The cryogenics system had been made operational for the BL2 KPP shots and it stayed in service to support startup.

After inspections and during startup a number of sources experienced attrition due to a range of problems including an internal water leak, external water leak, a vacuum leak, and shorted arc chamber components. Sources were removed from the beam-lines in the NTC and taken to the Source Shop for evaluation and remedy. Multiple sources were repaired this year and once again installed to achieve a full complement of ion sources on both beam lines prior to plasma operation demand. The Source Shop refurbishment facility resumed daily and weekend operations to accomplish this effort after dormancy during the upgrade construction years. The Source Shop continued to operate throughout the fiscal year to generate additional sources to cover early operation attrition and to make fully tested spares. The run period was completed with 6 sources operable and in service on BL1 and 2. Three source refurbishments are in progress in the shop to become spares.

Additional effort was required to improve the productivity of the shop. The optical qualifier used for grid and accelerator alignment had repeated problems so a new unit large enough to handle the size and weight of the sources was sought, identified, and purchased. The humidity in the Mockup Building is subject to outside air make-up and therefore hipot testing is often postponed until high voltage leakage current is within allowed bounds. An engineered solution was identified and implemented to control local humidity on the hipot stand. Finally, the source grids have experienced the most attrition during and since TFTR operation so the source grids are the pacing item for how many total sources we can still build from the 15 original units. Source grid module end caps were requisitioned and a vendor eventually supplied 20 acceptable units that will allow the fabrication of 10 additional grid modules

The Cryogenics plant which had made a full start in November of 2014 in preparation for the NBI KPP run continued 24/7 operations throughout the FY 15 year and FY16 run period with both beam lines at LHe temperatures. After 15 months of continuous operation, some degradation of performance was noticed and investigated. Trends in readings were identified that pointed to a Cold Box Helium leak. A Cold Box warmup and entry was performed; leak checking identified one large leak and a much smaller leak that was masked by the large one. Both leaks were repaired and the Cold Box was promptly returned to service. The LHe Refrigerator operated at full capacity after the repair.

In light of this critical cryogenics need and single point failure and the impact on schedule that a cryogenics problem in the Cold Box could have on the NSTX-U program, a new initiative was started to update the LHe Refrigerator with a new unit located closer to the NTC. This project is working in close collaboration with the cryo-pump divertor project to supply liquid Helium for it also.

In addition to cryogenics, both beam lines needed deionized water, vacuum, gas injection, Sulfur Hexaflouride, and pneumatic services all of which were made operational and reliable for daily use throughout the FY16 run period. The newly rebuilt SF6 skid and controls performed many operations due to the high demand for maintenance evolutions on high voltage equipment. The system continued to work well and minimize the release of SF6 to the environment. The vacuum systems and beam-line controls were called upon to perform weekly cryopanel regenerations to remove effluent Deuterium. The regenerations were routinely performed on weekends without impact on NSTX-U or NBI operations.

Each ion source requires 6 different power supplies to produce an experimentally useful neutral particle beam for plasma injection. Concerted effort was devoted to qualifying each power supply for use. Each power supply required pre-operational testing, extensive tuning, and interlock checks to return to service. Each Modulator/Regulator required local exerciser, dummy load, and source operation testing and tuning to make all necessary adjustments. The NBI team began conditioning sources early in FY16 when the NTC could be locked and beam enable and arm permits allowed in conjunction with machine operations. By January 7 2016, the first neutral beam was injected into NSTX-U plasmas at modest levels. By the end of March, all 6 sources were operational and conditioning into calorimeters and injecting power up to about 1 MW per source when requested.

After the first few weeks of conditioning, BL2 sources began experiencing operating ceilings due to faulting. After extensive high voltage system troubleshooting, it was discovered that transmission line problems were limiting voltage levels. The transmission line problems stemmed from the very tight space into which the TFTR transmission lines were installed for NSTX-U BL2. Repairs undertaken during maintenance weeks and weekends were successful and conditioning levels increased accordingly. The transmission line repairs required NTC access so repairs were staged on weekends and during extended maintenance periods. An Auto-Transformer in the NB Switchyard was found to have a fault and was replaced by a spare assembled by AC Power from two other units.

After the Cold Box repair mentioned above, the transmission line repairs, and the auto-transformer replacement, all 6 sources were conditioned to 90 kV and 2 MW each for a total of 12 MW available by the end of the run period. Neutral Beam Injection proceeded according to approved experimental plans as needed. After the completion of the plasma operations, the NBI and HHFW systems were shut down according to procedures.

HHFW Heating and Current Drive Systems – In parallel with NSTXU startup in the Fall of 2015, the High Harmonic Fast Wave systems were returned to service with pre-operational testing, dummy load testing to 1 MW each, and interlock checks. These systems were dormant for the entire 5 year span of the upgrade and returned to service this year with lesser priority than upgrade work. All 6 HHFW systems were operational by the Holiday break and ready for antenna conditioning.

In January 2016, on the first day of attempts to put voltage on RF antennae, a breaker trip failure caused an arc in HHFW#5 crowbar cabinet. Damage was limited to the cabinet. An RF Recovery team was formed. The arc fault was investigated and extent of condition determined. A Corrective Action Plan was prepared, approved, and implemented. The breaker trip technology was upgraded. The HHFW cabinet was repaired. The systems were hardened against the recurrence of a fault. The RF and AC feeder breaker coordination was vastly improved. The CAP was completed in a matter of several months. All 6 systems were returned to service with pre-operational tests, dummy load testing, and then antenna conditioning on the machine to approximately 20 kV. All six systems were ready for plasma experiments when the run period was curtailed. The ECH PI system was made operational for the NSTX-U first plasma KPP run and then returned to service to support all of the plasma shots for FY16 with no issues.

Significant HHFW related diagnostic upgrades have been performed in FY 2016. Two arrays of divertor Langmuir probes were installed in the NSTX-U vessel specifically for HHFW studies. Circuitry is being built to directly measure the RF (30 MHz) component of the collected current to determine the process underlying the SOL loss of HHFW power. Recent analysis suggests that RF rectification is driving the heat flux to the surface. Measuring the RF voltage at the divertor, along with a new wide-angle IR-camera view provided by ORNL, will test this hypothesis in great detail. ORNL performed diagnostic tests on the microwave electronics for the SOL reflectometer. The system is ready to acquire raw data. A mid-plane probe shaft, situated in the middle of the HHFW antenna, is being fitted with two Langmuir probes and double-Langmuir probe designed by ORNL. Coaxial Helicity Injection (CHI) System - Recent NIMROD simulations in the NSTX-U geometry have shown very high levels of closed flux for CHI initiation in the NSTX-U geometry. Three new individuals are now certified in the CHI capacitor bank operating procedures. The resistive voltage divider network was installed, and work is in progress to finish installation of two Ross Electronics based fast voltage monitors. These systems monitor the NSTX-U vessel voltage during CHI operations. Work related to the final connections of the gas lines to the CHI gas injection valves are in progress. Initial testing of the CHI system into a plasma load will begin after these activities are completed.

Resistive Wall Mode (RWM) control system - While NSTX-U is a modification of NSTX, changes to the device conducting structure (e.g., new 2nd NBI port structure), mid-plane RWM control coils, and equilibria require re-computation of n = 1 active RWM control performance using proportional gain, and RWM state space control. The upgrade also adds new capability, such as independent control of the 6 RWM coils. This new capability, combined with the upgrade of the RWM state space controller will also allow simultaneous n = 1 and n = 2 active control, along with n = 3 dynamic error field correction. Finally, the active control performance of the proposed off-mid-plane non-axisymmetric control coils (NCC) also needs to be evaluated, and a significant increase in controllable β_N is expected with the RWM state space control in NSTX-U, as was found for NSTX.

Disruption Mitigation Systems - Predicting and controlling disruptions is an important and urgent issue for ITER. Methods to rapidly quench the discharge after an impending disruption is detected are also essential to protect the vessel and internal components of an ST-FNSF. In support of this activity, NSTX-U will employ three Massive Gas Injection (MGI) valves that are very similar to the double flyer plate design being considered for ITER. NSTX-U will be the first device to operate this valve design in plasma discharges. Three of these valves are now installed on NSTX-U. These correspond to the upper divertor, lower divertor and mid-plane locations on NSTX-U. In preparation for FY16 MGI experiments, the goal of which was to conduct a comparison of the mid-plane to lower divertor injection locations, the lower-divertor and mid-plane valves were commissioned and prepared for full operational capability. The capacitor-based power supplies needed to operate these valves were operated at 1kV, which is more than the ~800V needed for injecting 400 Torr.L of neon into NSTX-U. Both these valves were then tested for full operation in nitrogen, helium, and neon at the full operating pressure of 10,000 Torr on NSTX-U. An important aspect of the NSTX-U MGI system is that the piping configuration between the valve and the vessel for the configurations being compared is nearly identical. In off-line tests, the valve was operated in a 1T external magnetic field and at a pressure of 15,000 Torr.

Electromagnetic Particle Injector (EPI) - The shattered pellet injector being considered for ITER uses the MGI valve to propel the frozen pellet. This will limit its velocity to about 300-400m/s and thus limit its response time since the pellets will be launched many meters away from the plasma. The penetration depth of the shattered fragments into ITER grade plasmas is unknown. To address this important issue, a novel system based on the rail-gun concept was designed, components fabricated and the system fully assembled. The system consists of a 1m long rail gun powered by a 20mF, 2kVcapacitor bank. The capacitor bank parameters are essentially the same as that used for the transient CHI experiments on NSTX. The device referred to as an Electromagnetic Particle Injector (EPI) is fully electromagnetic, with no mechanical moving parts, which ensures high reliability after a period of long standby. In addition to responding on the required fast time scale, its performance is projected to substantially improve when operated in the presence of a high magnetic field. The system is also suitable for installation in close proximity to the reactor vessel. Experimental results from the operation of this system will be presented at the 2016 IAEA Fusion Energy Conference.

Fueling Tools - NSTX-U plasma operations will require the capability for gas injection from numerous locations. The gas injection systems on NSTX were not adequate to meet the physics program needs of NSTX-U as improvements are needed in the area of divertor heat flux mitigation, and increased levels of gas injection from high-field side to meet the up to 10s discharge pulses planned for in NSTX-U. The legacy gas injection code from NSTX, while functional, had reached a state where maintenance and upgrades were difficult. Therefore, the control algorithms were redesigned and rewritten to improve its clarity, consistency and the ability to introduce new capabilities (such as density or radiation feedback) that employ the NSTX-U gas injectors. A number of the gas lines and vessel pressure measurements were changed or upgraded during the outage, and these systems were brought on-line and calibrated in support of CD-4 operations and the subsequent research operations. Note that unlike NSTX, all gas injectors are now programmed from the PCS.

Boronization – Boronization is a conditioning technique for reducing oxygen applied to NSTX-U plasma-facing components after bakeout and helium glow discharge cleaning (GDC). The boronization process involves GDC with a mixture of 95% helium and 5% deuterated trimethylborane (dTMB) which is followed by another period of helium GDC. During the past year, a new dTMB system was installed on NSTX-U. A PLC is used to control the flow of dTMB through coaxial lines from a specially-designed gas cabinet inside the NSTX-U Test Cell to the vacuum vessel. The boronization system was used regularly for wall conditioning in support of plasma operations in FY16~~.~~

Granule Injector for Investigation of Multi-species Particle Injection and ELM Control – The assembly and testing was completed for the NSTX-U granule injector (GI). The new control system for remote GI operation was made operational. The initial motivation for the GI was to inject lithium granules for ELM control (“ELM pacing”). This was successfully demonstrated on EAST and DIII-D, and ELM pacing experiments with lithium injection are planned for NSTX-U. The granule injector was commissioned An outstanding question is the effect of other granule materials on plasmas, and this will be investigated in the future NSTX-U run.

Lithium Evaporator – The NSTX lithium evaporator (LITER) system will be reused on NSTX-U. Each LITER is a temperature controlled stainless steel container filled with liquid lithium (LL), with a nozzle to direct the lithium vapor for coating PFCs at desired locations. As on NSTX, the nozzle will be aimed on NSTX-U toward the middle of the inner divertor to maximize the lithium deposition on the divertor plates. The LITER passes through a PFC gap in the upper divertor region. The LITERs have been remounted and made operational. The liquid lithium filler for LITER (LIFTER) was also prepared for filling the LITERs in the NSTX-U South High Bay.

Liquid lithium technology development – Surviving the extended NSTX-U bake-out is a critical feature needed for any pre-loaded liquid lithium tile targets for the NSTX-U. Initial testing of a method for surviving the nearly 3-weeks at 350C with significant partial pressures of water and carbon dioxide have recently been tested in collaboration with the University of Illinois at Urbana-Champaign. In these tests, a porous sample was loaded with a macroscopic amount of liquid lithium and then coated with a thin (200nm) layer of molybdenum metal using physical vapor deposition techniques commonly used for semi-conductor fabrication. These samples were then placed into a chamber and heated to 350C and then exposed to a 250mTorr gas pressure environment. The bubbler chamber used to introduce the gas consisted of 80C liquid water with CO2 flowing through which should yield a ~0.3 mole fraction of water vapor with the balance being CO2. At this pressure, the equivalent gas exposure as during the 2010 NSTX-U bake-out is achieved in only 7 minutes. During this exposure, *no reactions were observed*. Subsequent tests with plasma exposure were characterized by optical emission spectroscopy and indicated a much larger Li-to-O line ratio than with reference samples of Li that were completely reacted with air. These tests seem to indicate a proof-of-principle for protecting a Li target via an eroding surface layer of molybdenum.

NSTX-U Diagnostic System Status and Plans - Diagnostic installation continued during FY2016, with the focus on completing ex-vessel diagnostic installations that were not completed in FY2015. A list of the existing diagnostic systems which were installed and commissioned in FY2016 is shown in Table FD-1. These systems obtained useful data during the FY2016 experimental campaign. Over half of those diagnostic systems are provided by collaborators, with installation support provided by PPPL. The status of these key systems as of the end of FY2016 is briefly summarized below.

Installed

- Magnetics for equilibrium reconstruction
- *Halo current detectors*
- *High-n and high-frequency Mirnov arrays*
- RWM / Locked-mode sensors
- MPTS (42 ch, 60 Hz)
- T-CHERS: $T_i(R)$, $V_\phi(r)$, $n_C(R)$, $n_{Li}(R)$, (51 ch)
- P-CHERS: $V_\theta(r)$ (71 ch)
- Edge Rotation Diagnostics (T_i, V_ϕ, V_{pol})
- *Beam Emission Spectroscopy (48 ch)*
- *Midplane ME-SXR (200 ch)*
- *SAMI edge field pitch diagnoistc*
- Midplane tangential AXUV bolometer array (40 ch)
- Ultra-soft x-ray arrays – multi-color
- *Fast Ion D_α profile measurement (perp + tang)*
- Solid-State neutral particle analyzer
- Neutron measurements
- *Charged Fusion Product*
- *Fast IR camera (two color)*
- *Material Analysis and Particle Probe*
- AXUV-based Divertor Bolometer
- Tile temperature thermocouple array
- Fast visible cameras
- Visible bremsstrahlung radiometer
- *Visible and UV survey spectrometers*
- *VUV transmission grating spectrometer*
- *Visible filterscopes (hydrogen & impurity lines)*
- Wall coupon analysis
- *1-D CCD H_α cameras (divertor, midplane)*
- *2-D divertor fast visible cameras (4)*
- *Two-color intensified 2D cameras TWICE (2)*
- *Edge neutral density diagnostic ENDD*
- IR cameras (30Hz) (3)
- Dust detector
- Edge Deposition Monitors
- Scrape-off layer reflectometer
- Edge neutral pressure gauges
- Fast lost-ion probe (energy/pitch angle resolving)
- Microwave Reflectometer
- *MSE-CIF (18 ch)*
- *MSE-LIF (20 ch)*
- *Divertor VUV Spectrometer (SPRED)*
- *Gas-puff Imaging (500kHz)*
- *Langmuir probe array*
- *Divertor fast eroding thermocouple*

Ready next run year

- FIReTIP interferometer
- *Laser blow-off system*
- *Poloidal FIR high-k scattering*
- *Midplane metal foil bolometer*
- *Metal foil divertor bolometer*

New capability,
Enhanced capability

***Table FD-1** – Status of Initial NSTX-U Diagnostic Systems*

Good progress was made on design and fabrication of several major diagnostics planned for installation during the shutdown following the FY2016 run. These include the poloidal FIR high-k scattering system, the resistive bolometer systems that view both the core plasma and the divertor region, and the Pulse Burst Laser System upgrade to the Multi-Pulse Thomson Scattering System. These are described in more detail below.

Multi-Pulse Thomson Scattering (MPTS) – The modification of the MPTS system required to reorient the laser beams to accommodate the larger diameter of the new center stack was completed in FY2015. In FY2016, the system was calibrated and operated reliably, providing electron temperature and density profiles to a variety of experiments. The only part of the MPTS upgrade that was not installed before the start of the FY2016 run is the calibration probe used to measure changes in the transmission of the light collection window due to deposition during operation. In FY2016, the calibration probe was fabricated and installation was planned for the summer of 2016 before the run ended. The calibration probe will be installed during the FY2016-2017 outage.

CHERS – The following charge-exchange recombination spectroscopy (CHERS) diagnostics operated reliably during the FY2016 run and provided data to a number of experiments: CHERS (toroidal and poloidal), Edge Rotation Diagnostic (ERD, toroidal and poloidal) and Real-Time Velocity (RTV). Good progress was made on developing beam-notching scenarios to allow the toroidal CHERS diagnostic to provide reliable measurements of the ion temperature and toroidal rotation velocity in discharges in which the second neutral beam, which is in the field of view of the toroidal CHERS background view, is used. An upgrade of the CHERS CCD detectors to detectors capable of higher frame rates and will be implemented during the FY2016-17 outage.

Commissioning and initial operation of the NSTX-U Real-Time Velocity diagnostic

On NSTX-U, available actuators for future implementation of plasma rotation control are neutral beam injection (NBI) and plasma braking through active magnetic coils. Measurements of plasma velocity to feed back on vφ are provided by a dedicated Real Time Velocity (RTV) diagnostic based on active charge exchange recombination spectroscopy. Actions of observers and actuators will be coordinated through the Plasma Control System (PCS).

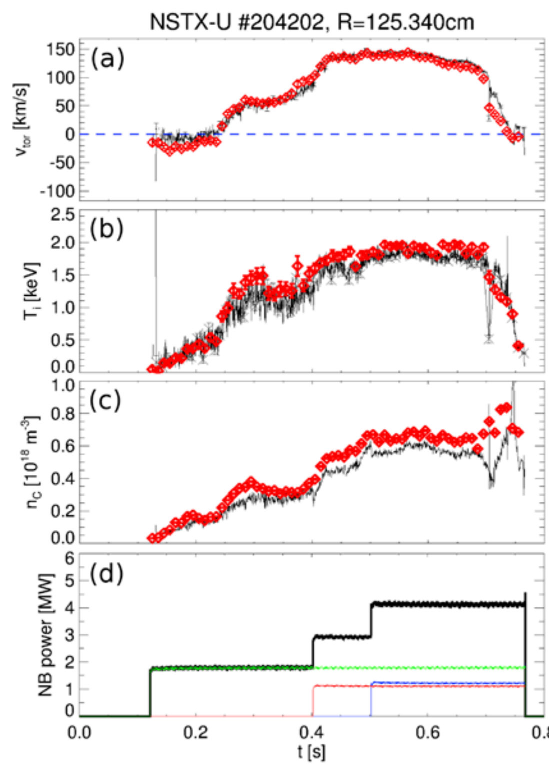

Figure FD-7: *Comparison of (a) velocity, (b) ion temperature and (c) carbon density at R = 125 cm from RTV and regular CHERS. (d) Waveforms of the injected NB power from the three sources of NB injection line 1.*

The RTV system has been optimized for high throughput and high sampling rate, up to 5 kHz. Although a sampling rate ~0.5 kHz is adequate for vφ control implementation, higher rates are useful for physics studies requiring measurements of vφ dynamics with submillisecond time resolution. Initial operation of the RTV system during the FY-16 Run confirmed the achievement of the design goals.

The RTV control and acquisition software has been developed to provide two main functions: (i) acquire and store data for offline (post-discharge) analysis, and (ii) analyze data in real time and send velocity data to PCS. Offline analysis tools have been also developed. RTV results are available in-between shots and for physics studies.

RTV complements the main active charge-exchange recombination spectroscopy diagnostic CHERS with high temporal resolution at four radial locations, spanning from the plasma center to the edge. An example of offline RTV results for NSTX-U discharge #204202 is shown in Fig. FD-7 for the view aimed at R = 125 cm, corresponding to mid-radius for typical NSTX-U plasmas, and compared with CHERS results. Results from the two systems compare well, although large discrepancies >50% in the inferred carbon density are sometimes observed (likely due to RTV absolute calibration issues).

A comparison between vφ and ion temperature results from post- discharge vs. real-time analysis of RTV data is shown in Fig. FD-8. Considering the simplifications introduced in the real-time analysis, the results compare well. Real-time results have larger uncertainties, caused by the simplified fitting method and imperfect removal of spurious contributions to the spectra, e.g. from "plume" emission. Overall, the temporal evolution of both vφ and temperature is well recovered in real-time, as required to implement rotation control.

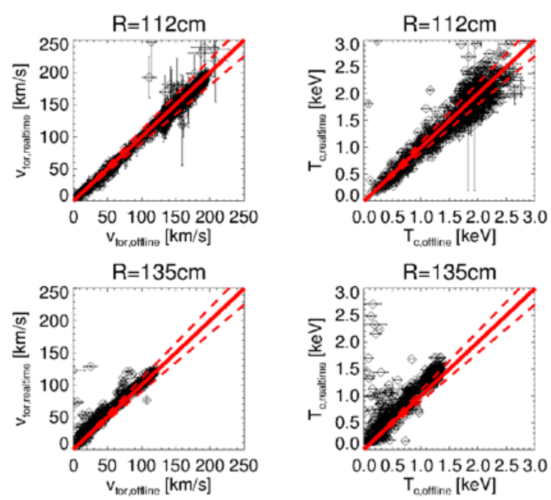

Figure FD-8: *Comparison of velocity and ion temperature from post-discharge and real-time analysis of RTV spectra (shown in black and red, respectively). Direct comparison for v_φ and T_C from core (R~112cm) and an edge (R~135cm) channels shows good overall agreement. Results from the real-time fit have larger uncertainties as a result of the simplifications introduced in the fitting algorithm compared to offline analysis.*

At present, real-time results of vφ and associated uncertainty are output as analog voltages. The latter are acquired by PCS and made available for implementing rotation control. Algorithms for real time rotation control are under development [and will be tested during the next NSTX-U campaign.

Far Infrared Tangential Interferometer/Polarimeter – UC-Davis is in the process of reconfiguring and upgrading the Far Infrared Tangential Interferometer/Polarimeter (FIReTIP) on NSTX-U. The seven-channel FIReTIP system employed previously on NSTX is being reconfigured into a three-chord system. Chord #1 will be employed for core plasma density monitoring as well as density feedback control and density calibration of the Thomson scattering system, while subsequent channels (as additional vacuum windows and retro-reflectors are installed) will monitor core and edge fluctuations. The FIReTIP lasers have been placed just outside the NSTX-U test cell. The waveguide to transport the FIReTIP beams to Bay G and the enclosure with the launching optics have been delivered to PPPL. They will be installed on NSTX-U in FY2017, along with the optics, phase comparator electronics, digitizers etc. that make up the full system. Chord #1 is expected to be operational for research plasmas in early 2017, with additional chords to follow in succeeding years.

Soft X-Ray Diagnostics – The Johns Hopkins University group completed installation and commissioning of the following soft x-ray diagnostics: the core and edge tangential Multi-energy Soft X-ray system (ME-SXR) for high time resolution measurements of the electron temperature, the mid-plane tangential Transmission Grating Imaging Spectrometer (TGIS) for impurity studies, and the poloidal Ultrasoft X-ray arrays (USXR) for MHD mode detection. These systems obtained initial data during the FY2016 run.

Motional Stark Effect – Collisionally Induced Fluorescence (MSE-CIF) – The MSE-CIF system was operational for the FY2016 campaign. By the end of the run, the energy of the neutral beam viewed by the system increased to the target value of 90 keV for tuning the interference filters.

Motional Stark Effect – Laser Induced Fluorescence (MSE-LIF) – The MSE-LIF will provide measurements of the field line pitch angle profile without requiring injection of the heating neutral beam needed for the present MSE-CIF system on NSTX-U, and combined measurements from the MSE-LIF and MSE-CIF diagnostics will allow radial profiles of the radial component of the electric field and the pressure to be measured. The system was installed and commissioned prior to the NSTX upgrade outage and utilizes a small diagnostic neutral beam (DNB) and a laser to excite the fluorescence. The laser and DNB were re-commissioned and the DNB was conditioned to operate at its target operating energy. The system was not able to obtain plasma data before the FY2016 run ended but measurements to validate its performance were made using field-only shots.

Synthetic Aperture Microwave Imaging (SAMI) – The SAMI diagnostic that was previously installed on MAST in the UK is now installed and operating on NSTX-U. The SAMI diagnostic can image mode-converted electron Bernstein wave emission and perform 2-D Doppler backscattering. Both techniques allow the measurement of the radial profile of the field pitch, and hence the current density, in the plasma edge. The diagnostic can also measure edge flows and turbulence characteristics. The initial results from NSTX-U was presented in an invited talk "Measuring edge pitch angle using 2-D microwave Doppler backscattering on MAST and NSTX-U" at the 2016 High Temperature Plasma Diagnostic Conference.

Turbulence Diagnostics - For turbulence diagnostics systems, the high-k scattering system detector array presently located at Bay K had to be relocated to Bay L after the 2nd NBI installation at Bay K. By re-aiming the microwave beam, it is possible to measure both the radial and poloidal components of the high-k turbulence. The existing 290 GHz microwave-based system is being replaced by a 693GHz laser-based system (see below). The higher frequency system is designed to improve high-k resolution and SNR. For low-k turbulence, the beam emission spectroscopy (BES) system with a new generation of BES detectors has been developed by the University of Wisconsin group. For magnetic fluctuations, a promising diagnostic appears to be the cross polarization system presently being tested on DIII-D. A preliminary feasibility study is planned on NSTX-U. For the edge region, the existing gas puff imaging (GPI) diagnostic for edge turbulence studies on NSTX-U has been upgraded for FY16. This camera-based GPI system will now have a new optical zoom capability with ~1 mm spatial resolution to image turbulence below the ion gyroradius for the first time (near the ETG range).

High-k Scattering System – The 290 GHz high-k tangential scattering system of NSTX is being replaced by a 693 GHz poloidal scattering system for NSTX-U, thereby considerably enhancing planned turbulence physics studies by providing a measurement of the k_θ-spectrum of both ETG and ITG modes. The probe beam in this case will enter the plasma from Bay G while a tall exit window located on Bay L will be employed to collect the radially- and poloidally-scattered beams and image them onto an array of waveguide mixers. The design for the mounting structure for the mixers has been finalized. It will be fabricated and installed in FY17, along with low loss corrugated waveguides to bring the FIR beam to launch optics on Bay G. A high power CO_2 laser will pump a 693 GHz FIR laser both of which are to be housed in the three-level table that also supports in four FIReTIP lasers in the "mezzanine" area just outside the NSTX test cell. The high-k scattering system is scheduled to be operational for the FY17-18 run.

Beam Emission Spectroscopy - The Beam Emission Spectroscopy (BES) diagnostic on NSTX-U is based upon observing the D_α emission of collisionally-excited neutral beam atoms and provides spatially-resolved measurements of longer wavelength density fluctuations in the plasma core. These measurements play a key role in elucidating the physics of ion transport and MHD instabilities. In FY15, BES sightlines were reconfigured for 2D measurements spanning the outer plasma and pedestal region. The 2D fiber assembly was designed and fabricated by U. Wisconsin with support from PPPL, and the new configuration contains 54 sightlines in an approximate 9x7 grid. The new 2D configuration opens scientific opportunities for multi-field turbulence measurements with flow fields from velocimetry techniques. Flow field observations can shed light on E×B flow and shear flow, zero-mean-frequency zonal flows, and geodesic acoustic mode (GAM) zonal flows. Also, turbulence-induced particle transport can be directly inferred from 2D BES measurements of density and flow field. Finally, the U. Wisconsin collaboration completed a 16-channel expansion of the BES detection system for a total of 48 detection channels available for the FY2016 campaign.

Foil-based bolometry diagnostics – During FY16, the NSTX-U team underwent design, procurement and testing activities led by ORNL collaborators to equip NSTX-U with foil-based bolometry diagnostics. This includes systems using conventional resistive bolometers (RB) and a prototype InfraRed Video Bolometer (IRVB), both of which measure plasma radiation based on temperature changes of metallic absorbers which is proven to be more accurate than present NSTX-U systems which use AXUV diodes. On other machines, AXUV diodes have been shown to significantly underestimate radiated power.

Resistive bolometers (RB) - As a result of collaboration with ORNL, good progress was made on the design of resistive bolometers to accurately measure radiative losses in NSTX-U. Two installations that view the divertor are planned: an eight-channel system that views the divertor region horizontally from a port at Bay I and an eight-channel system that views the divertor from a top port at Bay J. The data from these systems will allow the dominant regions of radiation in the divertor to be identified. A 24-channel resistive bolometer to provide detailed spatial profiles of the core plasma radiation from Bay G is also planned. Conceptual, preliminary, and final design reviews for all three systems were held in FY2016. Long lead-time components including thin-foil sensors and data acquisition hardware were procured. Final solid CAD models of the systems were developed and fabrication drawings for the Bay I installation are complete. Fabrication drawings for the Bay G and Bay J installations are in progress. Fabrication and installation of the three system will occur during the FY2016-17 outage. They will utilize a new FPGA-based analyzer system which enables improved calibration, a reduced cost-per-channel and a substantially reduced rack footprint.

Infrared Video Bolometer (IRVB) - IRVB measures the radiated power by using a high-resolution IR camera to observe the infrared emission from a thin platinum foil heated by the plasma emission. This technique has been demonstrated on fusion experiments in LHD and JT-60U. On-site collaborators from NIFS (Japan) and ORNL, along with PPPL, performed laboratory testing and completed the design and fabrication of an infrared imaging bolometer to view the lower divertor of NSTX-U. The system was installed during the FY2016 run but was unable to obtain data before the run ended. It will be tested at Alcator C-Mod in September 2016 and then re-installed on NSTX-U during the FY2016-17 outage to be available for the FY2017-18 run. If the initial results are favorable, a system with an optimized view of the divertor could be designed for NSTX-U.

Boundary Physics Diagnostics - The NSTX facility has been investing strongly in boundary physics related diagnostics in the past several years, and a major activity has been to insure that port space is available on NSTX-U to accommodate them. There are over 20 boundary physics diagnostic systems on NSTX-U and additional ones are being readied. They include Gas-Puff Imaging (500kHz), a new poloidal Langmuir probe array, Edge Rotation Diagnostics (T_i, V_ϕ, V_{pol}), 1-D CCD H_α cameras (divertor and midplane), 2-D fast visible cameras for divertor and overall plasma imaging, divertor bolometer, IR cameras (30Hz), fast IR camera (two color), tile temperature thermocouple array, divertor fast eroding thermocouples, dust detector, Quartz Microbalance Deposition Monitors, scrape-off layer reflectometer, edge neutral pressure gauges, Material Analysis and Particle Probe (MAPP), Divertor Imaging Spectrometer, Lyman Alpha (Ly_a) Diode Array, visible bremsstrahlung radiometer, visible and UV survey spectrometers, VUV transmission grating spectrometer, visible filterscopes (hydrogen & impurity lines), and wall coupon for post-run analysis. Major upgraded boundary physics diagnostics are described in more detail below.

Materials Analysis and Particle Probe (MAPP) - Understanding plasma-wall interactions is critical to the development of controlled thermonuclear fusion. The MAPP diagnostic provides unique data toward this goal through exposing first-wall materials to tokamak discharges, and analyzing them without compromising any time-sensitive chemistry-dependent surface information. This is accomplished by withdrawing samples into a separate chamber under vacuum, where their surfaces can be probed with X-rays and low energy ions to characterize them. The MAPP system was installed on NSTX-U as a collaborative effort by the University of Illinois at Urbana-Champaign (UIUC) and PPPL, and has already been used to study the effects of surface conditioning techniques on plasma-facing components. The X-ray photoelectron spectroscopy (XPS) system on the MAPP was used to provide a baseline characterization of samples prior to their insertion into the NSTX-U vacuum vessel. The samples have been positioned so that their faces are flush with the divertor plasma-facing surface, and are subject to wall conditioning techniques that include glow discharge cleaning and boronization. Samples of plasma-facing component materials were exposed during boronization using MAPP. They are made of ATJ graphite, which matches the composition of the outboard divertor tiles. The samples have been removed for study using a variety of surface analysis techniques at the University of Illinois at Urbana-Champaign (UIUC). The results will have a key role in interpreting data from MAPP samples exposed to plasmas during NSTX-U operations in a UIUC-PPPL collaboration. A research highlight on the MAPP appeared in the March 31, 2016 Monthly Newsletter of the U.S. Burning Plasma Organization (USBPO).

SOL and divertor diagnostic development for NSTX-U - Two new diagnostics are being developed by LLNL to support radiative divertor feedback control. In conceptual form, both spectroscopic diagnostics would provide a semi-localized electron temperature estimate in the divertor in real time, which can be used in the plasma control system to control the gas seeding rate. These diagnostics are the divertor SPRED vacuum ultraviolet spectrometer and the divertor imaging Balmer line spectrometer (DIBS). The divertor SPRED spectrometer will use real-time carbon or nitrogen spectral line intensities as proxies for radiated power, as well as boron-like, beryllium-like, and lithium-like line intensity ratios that are highly sensitive to electron temperature in the range 1-10 eV. The DIBS diagnostic will provide a multi-chordal coverage of the divertor legs. Temperature-sensitive high-n Balmer line intensity ratios (n=6-12) will be used in real-time for electron temperature evaluation. Both diagnostics are being installed on NSTX-U for initial testing in FY2016.

Upper and lower divertor fast visible cameras - Full poloidal/toroidal coverage of impurity emission from the plasma facing components (PFCs) was achieved in NSTX-U via bandpass-filtered two-dimensional fast cameras viewing the upper and lower PFCs. Two wide-angle fast visible cameras (Bay E and Bay J top) were used in NSTX for the full toroidal imaging of the lower divertor. These cameras were re-installed in NSTX-U and were complemented with a symmetric view of the upper divertor from Bay H bottom. In the initial NSTX-U experimental campaign, the wide angle cameras were dedicated to deuterium and carbon emission measurements. A new fast camera with higher sensitivity and optimized throughput was installed at Bay J midplane and enabled imaging of divertor turbulence via C III emission.

TWICE diagnostic for NSTX-U - Two dual-wavelength imaging system TWICE-I and TWICE-II (Two Wavelength Imaging Camera Equipment), developed by LLNL, based on a charge injection device (CID) radiation-hardened intensified camera complemented fast cameras imaging capabilities with the ability to image weaker visible lines and a custom-built two-color system for the simultaneous imaging of different wavelengths. Intensified camera views in NSTX-U included high-resolution views of the lower divertor from Bay I-top and from Bay J-top. In the initial NSTX-U experimental campaign, TWICE-I and TWICE-II were dedicated to the monitoring of oxygen, boron and molecular carbon emission from the PFCs.

Extreme Ultraviolet Spectrometers – Installation of three LLNL high spectral resolution extreme ultraviolet (EUV) grating spectrometers on a midplane port at Bay E was completed. Data from these instruments will be used to infer impurity densities in the plasma core and pedestal. The two previously existing spectrometers, the X-ray and Extreme Ultraviolet Spectrometer (XEUS) and the Long-Wavelength and Extreme Ultraviolet Spectrometer (LoWEUS) and the new spectrometer, the Metal Monitor and Lithium Spectrometer Assembly (MonaLisa), have been calibrated on the Livermore EBIT facility to cover the wavelength range between 5 – 440 Å. The spectrometers cover overlapping wavelength ranges to ensure no gaps in impurity monitoring (XEUS, 5 – 65 Å; MonaLisa, 50 – 220 Å; LoWEUS, 190 – 440 Å). All three spectrometers were commissioned and obtained useful data during the FY2016 run. Implementation of improvements to the spectrometer vacuum system is planned for the FY2016-17 outage

Laser blow-off impurity injection system – The LLNL group worked with PPPL on developing and installing a laser blow-off impurity injection system on NSTX-U. It will be used for low- and high-Z impurity transport studies in the core, pedestal, and edge of NSTX-U plasmas. The system is comprised of a 10-Hz, 1 J laser, beam delivery optics, and a target chamber that will be mounted on the NSTX-U vacuum vessel. A new laser room location has been chosen and will be built on the mezzanine above the South Bay entrance. The laser room specifications have been worked out and a vendor has been identified. Installation is planned for early FY17.

Pulse Burst Laser System – Good progress was made on fabrication and testing of the Pulse Burst Laser System (PBLS) being implemented as an upgrade to the MPTS diagnostic under a DOE Early Career Research Project. This work is nearly complete and delivery of the laser system to PPPL is expected in September 2016. Preparations for integration of the laser into the MPTS diagnostic have started. The area that will house the power supplies is being prepared and fdopperAn optical system to combine the beams from the two existing lasers into one beam was prototyped and found to work well. This approach allows the PBLS laser beam to be combined onto the same path without modifying the remainder of the system. The high time resolution measurements enabled by this capability will allow detailed exploration of H-mode pedestal and ELM physics.

Energetic Particle Diagnostics – Both vertical and tangential Fast Ion D-Alpha (FIDA) diagnostics by UCI were reinstalled on NSTX-U at the end of FY2015. Both FIDA diagnostics were commissioned and have routinely taken data in plasma experiments in FY16 run. A new and multi-view ssNPA system by UCI, which uses stacks arrays of silicon diodes with different foil thickness to get spatial profile measurements and some energy information, has been installed and successfully commissioned. Arrays mounted at different ports around the NSTX-U vessel provide both radial and tangential views to enable measurements of the fast ion distribution at different values of radius, energy and pitch. The ssNPA system is also capable of measuring fluctuations up to 120 kHz, which is suitable to study fast ion driven instabilities and transport. The ssNPA system was fully operational and has obtained useful data in the FY2016 run. During the FY2016-2017 outage, a few individual detectors will be added to work in pulse-counting mode to get fine energy spectrum, which is crucial for the study of the acceleration of fast ions by high-harmonic fast wave heating.

Neutron Diagnostics – Three fission chamber neutron detectors and four scintillator detectors were installed on NSTX in FY2015. The absolute calibration of the fission chambers was determined through use of a Cf-252 neutron source in the vessel. This source is one that PPPL obtained from ANL to replace an old TFTR-era source that had become too weak to provide in-vessel calibrations within an operationally acceptable amount of time. These fission chamber detectors were operational for the NSTX-U first plasma KPP. A transfer of the fission chamber calibrations to a higher range of neutron rates was performed early in the FY2016 campaign and it is anticipated the calibration will be extended to a yet higher range in the FY17-18 campaign.

A scintillator-based Fast Lost Ion probe (sFLIP) contributes to the NB characterization by providing energy and pitch resolved spectra of lost fast ions, e.g. from prompt losses, as the NB tangency radius is varied. sFLIP is being upgraded with a faster CCD detector capable of frame rates up to 100 kHz. A set of photo-multiplier tubes is also being installed on sFLIP for energy and pitch integrated measurements at rates up to 250 kHz from 6-10 sub-regions of the sFLIP scintillator plate. Major modifications to the vacuum vessel and two large diagnostic ports to accommodate the new neutral beam lines for NSTX-U has resulted in displacement of sFLIP from the port it had used during NSTX operations. A suitable alternate port for this diagnostic was identified, and that port was enlarged and substantially reinforced to accommodate the diagnostic. The in-vessel part of this diagnostic was then installed at the new location, while at the same time extending its range of pitch angle acceptance. This latter change should allow for additional beam ion loss information in the forthcoming campaigns.

Charged Fusion Product (CFP) Diagnostic – The fusion rate profile diagnostic (also known as the ‘proton detector’ or ‘PD’) has been designed by collaborators at Florida International University (FIU). It provides direct measurements of the fusion reactivity profile. Because both the 3 MeV protons and 1 MeV tritons produced by DD fusion reactions are largely unconfined for NSTX-U parameters, they quickly escape the plasma. When these ions are measured by the PD detector array, their orbits can be tracked backward into the plasma. Such orbits are equivalent to curved sightlines for each detector, so that multiple signals can be inverted to infer a radial profile of the high-energy fast ions. A 4-channel CFP prototype has been tested in FY2013 on the MAST device (see the Energetic Particle Research Section). The 3 MeV protons and 1 MeV tritons produced by DD fusion reactions in MAST have been clearly observed. Given the successful observations on MAST, a similar system for with 6 channels) has passed its final design review. Construction of the approximately half of the probe drive support structure was accomplished in FY16. The data obtained on NSTX-U in FY17 will enable assessment of the signal-to-noise ratio of this diagnostic. Funding for a 16-channel system for NSTX-U has been approved, and exploration of configurations for the ten additional channels is underway. The FIU group has been approached about designing a similar system for MAST-U, as the results obtained from the four channel version of this diagnostic on MAST were regarded as interesting and valuable.

Energetic-Particle-Induced Mode Diagnostics - The UCLA 16-channel comb quadrature reflectometry system will be utilized to study the eigenmode structure of fast-ion driven Alfven as well as other MHD modes. In the past this system and its predecessors have provided a wealth of additional information including investigation of three-wave coupling processes and identification of the potential role of Compressional Alfven Eigenmodes (CAEs) in contributing to core anomalous transport. The reinstallation (after the upgrade outage) system at Bay-J was completed. First plasma data was obtained and all 16 quadrature channels worked properly. Clear evidence of high frequency coherent mode activity (~1.8 MHz) was observed during neutral beam heating consistent with GAE activity. This 16-channel system will be complemented by a new four-channel reflectometer/Doppler backscattering system enabling fluctuation measurements up to densities of 9.2 x $10^{19}m^{-3}$.

Similarly to NSTX, several arrays of high-frequency Mirnov coils will provide routine measurements of the fluctuations spectrum on NSTX-U. Two sets of coils are toroidally displaced to enable the computation of the toroidal mode number of the modes from the phase of the complex spectrum. A reduced set of coils is displaced poloidally to provide information on the poloidal mode structure. The bandwidth of the magnetic fluctuation measurements will be extended on NSTX-U from the present 2-2.5 MHz up to 4 MHz, to account for the expected frequency up-shift of the modes as the toroidal field is increased. The fast Mirnov sensors were also brought into full functionality. The newly reconfigured high-f array was digitized with a new high-speed DTACq digitizer, while the legacy high-n array was digitized with a PC as in NSTX. Both systems functioned reliably, detecting both low frequency kink/tearing modes and higher frequency *AE modes.

A quantity of great relevance for EP studies is the radial structure of *AE (i.e., all types of Alfven eigen-modes). Several complementary systems will be available to this end on NSTX-U, including beam emission spectroscopy (BES) arrays, reflectometers, interferometers, polarimeters, and X-ray detectors. A proposal for installing a Doppler back-scattering (DBS) system will be also considered based on the resource availability (see below). The BES system will provide low-k density fluctuation measurements near the mid-plane for normalized radii 0.1 $< r/a < 1$. The number of channels will be increased from 32 up to 64 to simultaneously sample a wide region of the plasma. The measurement region will extend poloidally to cover a ~10 cm broad strip along the mid-plane. Further improvements may include a toroidally-displaced set of viewing channels, possibly limited to the edge region, to measure background emission (in the absence of the 2nd NB source) or the toroidal mode number of the instabilities. Density fluctuations are also derived from a multi-channel reflectometer system. The 16 channels available on NSTX will be complemented by 8 new channels at higher frequency, which will enable fluctuation measurements up to densities ~10^{20} m^{-3}. Line-integrated measurements of density fluctuations will also be available from 3-4 far-infrared interferometer with sampling frequency ~4 MHz. Beside density fluctuations, other quantities such as magnetic field and velocity fluctuations are important for a thorough identification and characterization of the different instabilities.

Reflectometry / Doppler Backscattering / Cross-polarization scattering

The reinstallation (after the upgrade outage) of the 16-channel UCLA reflectometer system at Bay-J was completed in early CY2016. First plasma data was obtained with all 16 quadrature channels working properly. Clear evidence of high frequency coherent mode activity (~1.8 MHz) was observed in neutral beam heated NSTX-U plasmas consistent with GAE activity. Data from the UCLA 16-channel reflectometry system provided radial structure and amplitude measurements of fast-ion driven Alfvén and other MHD modes. In addition to this 16-channel reflectometer system UCLA has fabricated and lab tested a new four channel reflectometry/Doppler backscattering system. This W-band system complements and extends the current 16 spatial channel UCLA reflectometer system providing the ability to measure mode structures to the core of high-density (8.2 to 9.2 x $10^{19} m^{-3}$) NSTX-U H-mode plasmas. It is planned to install this system on NSTX-U in the early FY2017 time period. The unique system design allows either fluctuation reflectometry or Doppler backscattering (DBS) to be performed using the same RF probe frequencies and optics. It is fully remotely controlled and able to switch between DBS and reflectometry on a shot to shot basis. Configured as a reflectometer, the system adds four channels to the existing 16-channel reflectometer capability resulting in 20 simultaneous spatial positions.

Doppler backscattering (DBS) has significant measurement capabilities and is able to measure intermediate wavenumber density fluctuations (with $k_\theta \rho_s$ in the range 1 – 10 or higher depending upon local temperature and magnetic field, spatial and temporal resolutions $\Delta r \leq 1$ cm and $\Delta t \leq 1 \mu s$), flow, GAM and zonal flows, intrinsic rotation, ELM and EHO activity. The measured flows will include the intrinsic $\tilde{\boldsymbol{E}} \times \boldsymbol{B}$ flows of Alfvén eigenmodes, potentially providing a novel direct measurement of AE $\tilde{\boldsymbol{E}}$. DBS may also prove sensitive to kinetic Alfvén wave ($k_r \rho_s \gtrsim 1$), which are believed to be commonly excited by linear mode conversion of AEs and may significantly contribute to energy transport. The DBS intermediate-k measurement will fill a gap in wavenumber space between lower-k BES and higher-k forward scattering measurements. In addition to this, a completely new measurement capability will be added – cross-polarization scattering (CPS) – to measure internal, localized magnetic fluctuations. Cross-polarization scattering (CPS) has significant capabilities being able to measure internal magnetic fluctuations over a broad wavenumber range $k_\theta \rho_s \sim 0.2–17$ with high time and space resolutions (Δr of order 1 cm and $\Delta t = 1 \mu s$). CPS may also prove sensitive to kinetic Alfvén waves. Internal magnetic fluctuation measurements will be especially important at the higher plasma betas in NSTX-U as electromagnetic effects are predicted to become increasingly important as beta increases. The CPS system will be integrated into the DBS system in the FY2017 timeframe.

NSTX-U FY2016 Year End Report: Research Results

In FY2016, the NSTX-U research team contributed experimental data and analysis in support of the 2016 DOE Joint milestone*:*

"Conduct research to detect and minimize the consequences of disruptions in present and future tokamaks, including ITER. Coordinated research will deploy a disruption prediction/warning algorithm on existing tokamaks, assess approaches to avoid disruptions, and quantify plasma and radiation asymmetries resulting from disruption mitigation measures, including both pre-existing and resulting MHD activity, as well as the localized nature of the disruption mitigation system. The research will employ new disruption mitigation systems, control algorithms, and hardware to help avoid disruptions, along with measurements to detect disruption precursors and quantify the effects of disruptions."

The NSTX-U research contributions to the 2016 Joint Milestone are described in a separate report, and the NSTX-U contributions to *"Conduct NSTX-U experiments and data analysis to support the FES joint research target on detecting and minimizing the consequences of disruptions in present and future tokamaks, including ITER"* are summarized above.

Summary descriptions of the results of research milestones are provided below. Descriptions of additional selected research highlights are also provided in subsequent sections.

FY2016 Research Milestone R(16-1): Assess H-mode energy confinement, pedestal, and scrape off layer characteristics with higher B_T, I_P and NBI heating power **(Target - September 2016. Initiated – September 2016)**

Milestone Description: *Future ST devices such as ST-FNSF will operate at higher toroidal field, plasma current and heating power than NSTX. To establish the physics basis for future STs, which are generally expected to operate in lower collisionality regimes, it is important to characterize confinement, pedestal and scrape off layer trends over an expanded range of engineering parameters. H-mode studies in NSTX have shown that the global energy confinement exhibits a more favorable scaling with collisionality ($B\tau_E \sim 1/\nu^*_e$) than that from ITER98y,2. This strong ν^*_e scaling unifies disparate engineering scalings with boronization ($\tau_E \sim I_p^{0.4} B_T^{1.0}$) and lithiumization ($\tau_E \sim I_P^{0.8} B_T^{-0.15}$). In addition, the H-mode pedestal pressure increases with $\sim I_P^2$, while the divertor heat flux footprint width decreases faster than linearly with I_P. With double B_T, double I_P and double NBI power with beams at different tangency radii, NSTX-U provides an excellent opportunity to assess the core and boundary characteristics in regimes more relevant to future STs and to explore the accessibility to lower collisionality. Specifically, the relation between H-mode energy confinement and pedestal structure with increasing I_P, B_T and P_{NBI} will be determined and compared with previous NSTX results, including emphasis on the collisionality dependence of confinement and beta dependence of pedestal width. Coupled with low-k turbulence diagnostics and gyrokinetic simulations, the experiments will provide further evidence for the mechanisms underlying the observed confinement scaling and pedestal structure. The scaling of the divertor heat flux profile with higher I_P and P_{NBI} will also be measured to characterize the peak heat fluxes and scrape off layer widths, and this will provide the basis for eventual testing of heat flux mitigation techniques. Scrape-off layer density and temperature profile data will also be obtained for several divertor configurations, flux expansion values, and strike-point locations to validate the assumptions used in the FY2012-13 physics design of the cryopump to inform the cryo-pump engineering design to be carried out during FY2016.*

Milestone R(16-1) Report:

The results of studies that address the above Research Milestone are described below. They include, L- and H-mode Confinement and Transport characteristics, low-k turbulence measurements during the L-phase and across the L-H transition, and developing tools for Pedestal and SOL studies.

L- and H-mode confinement

Confinement and transport analyses for both L- and H-modes produced in NSTX-U were carried out using the TRANSP code. This initial analysis of the data relies on imperfect input in the sense of assumptions for Z_{eff} and neutral density at the boundary. An assumption for Z_{eff} is necessary because of low signal in the CHERS diagnostic at low beam power, as well as lack of available background emission measurements when the second neutral beam was fired. For the results presented here, a flat Z_{eff}=2 profile was assumed. This value was chosen based on some available CHERS data, although there is some measurements (FIDA) and modeling (TRANSP) that suggest the value could be higher.

TRANSP analysis incorporated measured electron and ion kinetic profile data, magnetic equilibria as computed by kinetic EFIT, and functions of time such as plasma current, neutron production rate, toroidal magnetic field, etc. The fast ion contribution is modeled using the NUBEAM module in TRANSP. New in this calculation is the use of a feedback algorithm that adjusts the Anomalous Fast Ion Diffusivity (AFID) during the calculation in order to bring the calculated and measured neutron rates into agreement. This AFID feedback algorithm is essential for the rapid completion of BEtween and Among Shots TRANSP (BEAST) runs during experimental operations, results of which can feed into preparation for subsequent discharges. It was found, especially for lower density discharges and discharges with obvious MHD activity, that up to 50% of the fast ion density/power could be lost through shine-thru, orbits leaving the main plasma and intersecting material surfaces or charge-exchange with thermal neutrals. A more rigorous validation of the NUBEAM calculation against FIDA and ssNPA measurements is a necessary future task.

H-mode plasmas were also produced in NSTX-U, and the thermal confinement times were seen to be at the $H98_{y,2}$ level or greater, as compared to L-mode plasmas, where this confinement enhancement factor was <1 (Fig. R16-1-1). In these H-mode plasmas, the electron thermal diffusivity was about a factor of two to three lower than that in L-mode discharges.

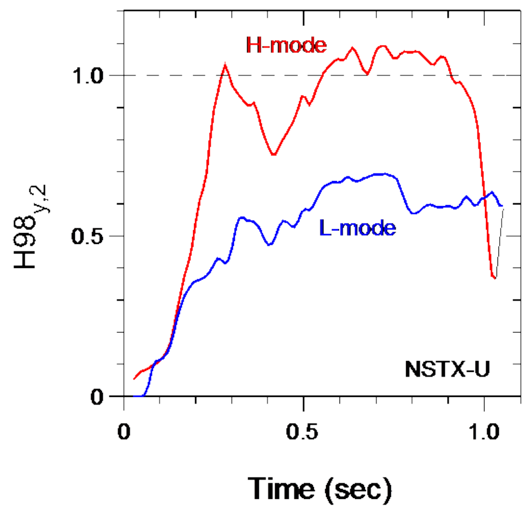

Fig. 16-1-1: Confinement enhancement factors as a function of time for an H-mode and an L-mode NSTX-U discharge.

Limited parameter variation studies of the dependence of the thermal energy confinement time were possible only with L-mode plasmas, where controlled scans were conducted. No controlled scans were as yet conducted for H-mode plasmas. The L-mode parametric scans consisted of changing plasma current at fixed heating power and line averaged density, and changing heating power at fixed plasma current and line averaged density. At fixed heating power in the range from P_{heat}=2.4 – 3.1 MW and line averaged densities from 4.75 to 5.25 x 10^{19} m^{-3}, a plasma current scan from 0.8 to 1.0 MA was performed. No strong current dependence emergef from this scan. There is a slightly positive dependence of thermal confinement time on current ($I_p^{0.38}$), which is weaker than is found in conventional aspect ratio L-mode studies, but which also has a high statistical uncertainty.

The power dependence of the L-mode thermal confinement time was taken from a scan of discharges with Ip=0.8 MA, B_T=0.65 T and line averaged densities within the range of 3.8 – 4.7 x 10^{19} m^{-3}. The range of neutral beam plus ohmic heating power is approximately 1.1 to 3.9 MW. There is a clear clustering of discharges in the 2 to 2.5 MW range, and the fit through the points is highly leveraged by single minimum and maximum power points. With these caveats, this small collection of discharges, however, shows a power degradation of $P^{-2/3}$, consistent with previous non-ST L-mode results [R16-1-1].

The local transport in selected L-mode discharges has been assessed through local power balance calculations in TRANSP, and the results indicate that the electron thermal diffusivity is very high and anomalous, ~7 – 20 m^2/s in the outer half of the plasma, consistent with previous NSTX results and indicating that the electron channel dominates the energy loss. Ion transport is lower, with χ_i ~ 1- 5 m^2/s in the outer portion of the plasma, and at or above the neoclassical level there.

Predictive calculations showed that the Rebut-Lallia-Watkins (RLW) model for microtearing-induced transport [R16-1-2] does an excellent job in predicting electron temperature profiles that agree with measured ones in at least one of these L-mode discharges. The result is seen in Fig. R16-1-2. The RLW was shown to predict T_e profiles accurately in high collisionality NSTX H-mode discharges [R16-1-3], consistent with gyrokinetic result showing the dominance of this low-k mode. For the NSTX-U L-mode, gyrokinetic simulations show that microtearing is present but is limited in space as the dominant mode. Linear gyrokinetic studies indicate that both ITG modes (at low $k_\theta\rho_s$<1) and ETG modes (high $k_\theta\rho_s$ >1) are predicted to be the dominant microinstabilities outside the midradius, r/a=0.5-0.8. Microtearing is predicted to be dominant at low $k_\theta\rho_s$ inside of r/a=0.5. These linear results, however, do not reveal the strength of the subdominant instabilities, and it is conceivable that microtearing is unstable even where the ITG is dominant. Additional and more in depth gyrokinetic studies are needed to assess better the role of microtearing in these discharges.

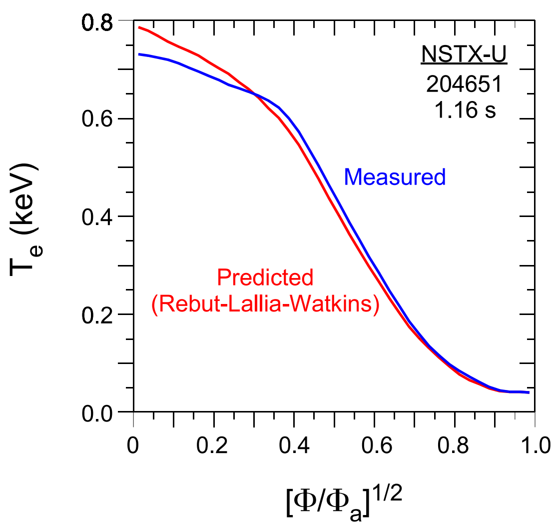

Fig. 16-1-2: The measured electron temperature profile (red) vs that predicted by the Rebut-Lallia-Watkins microtearing-induced electron transport model in an NSTX-U L-mode discharge.

Turbulence measurements

Turbulence studies were initiated during FY16 operations using the Beam Emission Scattering system. This initial shakedown period, along with the installation of the High-k Scattering system during this outage and expected results, gives confidence in the ability to start to resolve sources of turbulence and transport during FY17 operations.

The U-Wisconsin beam emission spectroscopy (BES) system has been used to measure ion scale turbulence fluctuations in a number of NSTX-U L-mode plasmas. Fig. R16-1-3(a) shows the power spectra of the normalized density fluctuations (assumed to be proportional to the BES intensity, $\delta n/n \sim \delta I/I$) in a 2.6 MW L-mode. The spectra are measured at five adjacent radial positions between ~138-148 cm (corresponding to normalized radii r/a~0.7-0.95) and illustrate broadband frequency fluctuations up to ~200 kHz. The strength, frequency-integrated over 2-200 kHz, is quite substantial increasing from ~1% at the inner channel to >4% at the outer channel, suggesting the presence of strong ion scale turbulence. The 2D BES measurements will be used for future validation of gyrokinetic turbulence predictions.

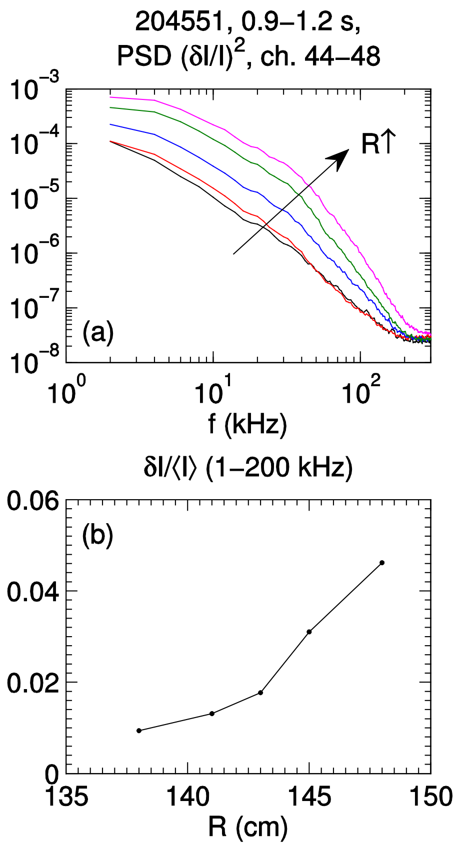

Fig. R16-1-3: (a) Power spectra of normalized density fluctuations from BES at different radii. (b) Radial profile of fluctuation amplitude (f=2-200 kHz).

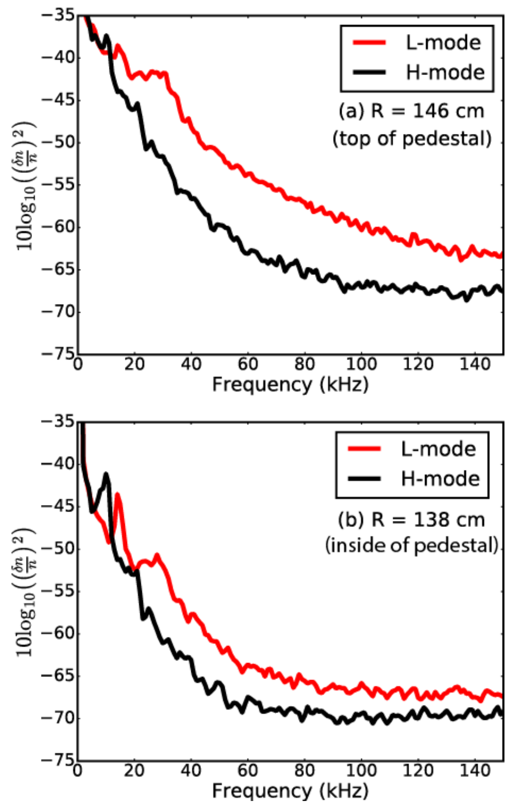

Figure R16-1-4: Autopower spectra of normalized density fluctuations across the L-H transition at (a) top of the pedestal, and (b) ~7 cm inward of the pedestal. Peaks in the spectrum below 15 kHz are MHD modes. Shot 204990, Ip = 0.65 MA, PNB = 1 MW.

Initial measurements of the turbulence in L-mode and H-mode NSTX-U plasmas have been conducted using the upgraded 2D BES system [R16-1-4]. Fig. R16-1-4 compares the density fluctuation spectra before and after an L-H transition at two locations. Broadband turbulence is observed up to 150 kHz in the pedestal region and up to 100 kHz several cm inside of the pedestal. Across the L-H transition, fluctuation levels drop by a factor of six in the pedestal region and a factor of three inward of the pedestal top. These results pave the way for future detailed studies of the turbulence across L-H transitions.

Theoretical work to understand the dynamics of the L-H transition and the turbulence changes at the transition has recently been published. The work [RL16-1-5] addresses a popular model for the L-H transition, in which the energy in turbulent fluctuations is directly depleted via Reynolds-stress-induced energy transfer to the zonal flows. Previous experimental attempts to validate this model have used energy balance between zonal flows and nonzonal (turbulent) ExB velocities, concluding that the mechanism was viable. However, the new article demonstrates that parallel electron force balance couples the nonzonal velocities with the free energy carried by the electron density fluctuations, replenishing the turbulent ExB energy until the sum of the two turbulent free energies is exhausted. Since that sum is typically two orders of magnitude larger than the energy in turbulent ExB flows alone, the Reynolds-stress-induced energy-transfer mechanism is likely to be much too weak to explain the rapid turbulence suppression at the L-H transition.

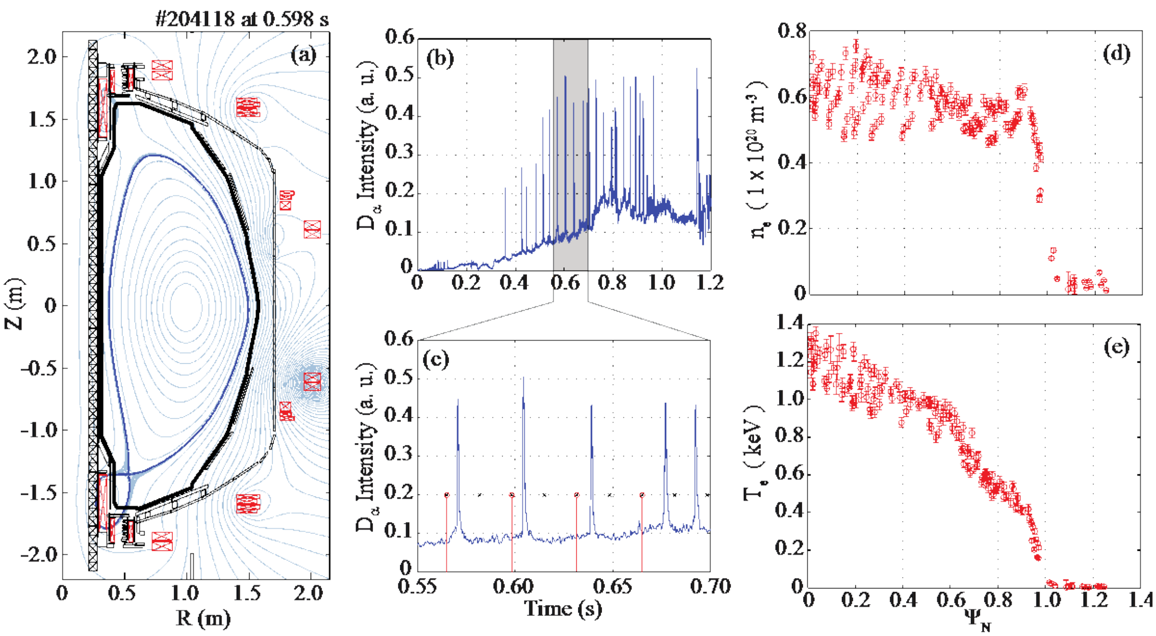

Figure R16-1-5: (a) Example of equilibrium reconstruction of the NSTX-U H-mode discharge. (b) – (c) D□ emission from the lower divertor showing ELMs. (d) Example of ELM-sync'ed density profile from Thomson scattering. (e) Example of ELM-sync'ed temperature profile from Thomson scattering.

Pedestal and SOL physics

Pedestal and SOL physics studies in FY16 were operationally limited. However, tools to address important aspects of these studies have been developed.

Understanding the underlying physics that controls the H-mode pedestal in tokamak plasmas is an important issue due to its strong impact on the overall plasma performance. A key element for the plasma edge stability and pedestal structure analysis on NSTX is a Pedestal Analysis toolkit, developed by T. Osborne from GA. This toolkit has been updated to allow analysis of NSTX-U plasmas, which is already being used to analyze NSTX-U H-mode plasmas. As an example, Figure R16-1-5 (a) shows the equilibrium reconstruction of an NSTX-U H-mode discharge with I_P = 1.0 MA, P_{NBI} = 5.5 MW, κ = 2.1 δ_L = 0.68 and δ_U = 0.35. Panels (b) and (c) show ELMs in the D_α emission from the lower divertor. Panels (d) and (e) show the electron density and temperature profiles from Thomson scattering measurements corresponding to the times indicated panel (c). Providing support on the use of this toolkit is an important component of collaboration between GA.

The pedestal physics, specifically the MHD stability and pedestal profiles, will be studied using the toolkit described above, in conjunction with the ideal MHD code ELITE and the two-fluid resistive MHD code M3D-C^1.

References

[R16-1-1] Kaye, S.M., et al. Nucl. Fusion **37** 1303 (1997).
[R16-1-2] Rebut, P.H. and M. Brusati, Plasma Phys. Cont. Fusion **28** 113 (1986), Rebut, P.H., et al., in Proc. Of the 12th IAEA Conference on Plasma Physics and Controlled Nuclear Fusion Research, Nice, France, paper IAEA-CN-50/D-4-1 (1988).
[R16-1-3] Kaye, S.M., et al., Phys. Plasmas **21** 082510 (2014).
[R16-1-4] Smith, D.R. et al., Rev. Sci. Instrum **83**, 10D502 (2012).
[R16-1-5] Stoltzfus-Dueck, T., Phys. Plasmas **23** 054505 (2016).

FY2016 Research Milestone R(16-2): Assess the effects of neutral beam injection parameters on the fast ion distribution function and neutral beam driven current profile **(Target - September 2016. Initiated – September 2016)**

Milestone Description: *Accurate knowledge of neutral beam (NB) ion properties is of paramount importance for many areas of tokamak physics. NB ions modify the power balance, provide torque to drive plasma rotation and affect the behavior of MHD instabilities. Moreover, they determine the non-inductive NB driven current, which is crucial for future devices such as ITER, FNSF and STs with no central solenoid. On NSTX-U, three more tangentially-aimed NB sources have been added to the existing, more perpendicular ones. With this addition, NSTX-U is uniquely equipped to characterize a broad parameter space of fast ion distribution, Fnb, and NB-driven current properties, with significant overlap with conventional aspect ratio tokamaks. The two main goals of the proposed Research Milestone on NSTX-U are (i) to characterize the NB ion behavior and compare it with classical predictions, and (ii) to document the operating space of NB-driven current profile. Fnb will be characterized through the upgraded set of NSTX-U fast ion diagnostics (e.g. fast-ion D-alpha: FIDA, solid-state neutral particle analyzer: ssNPA, scintillator-based fast-lost-ion probe: sFLIP, and neutron counters) as a function of NB injection parameters (tangency radius, beam voltage) and magnetic field. Well controlled, single-source scenarios at low NB power will be initially used to compare fast ion behavior with classical models (e.g. the NUBEAM module of TRANSP) in the absence of fast ion driven instabilities. Diagnostics data will be interpreted through the "beam blip" analysis technique and other dedicated codes such as FIDASIM. Then, the NB-driven current profile will be documented for the attainable NB parameter space by comparing NUBEAM/TRANSP predictions to measurements from Motional Stark Effect, complemented by the vertical/tangential FIDA systems and ssNPA to assess modifications of the classically expected Fnb. As operational experience builds up during the first year of NSTX-U experiments, additions to the initial Fnb assessment will be considered for scenarios where deviations of Fnb from classical predictions can be expected. The latter may include scenarios with MHD instabilities, externally imposed non-axisymmetric 3D fields, and additional High-Harmonic Fast Wave (HHFW) heating.*

Milestone R(16-2) Report

With the beginning of NSTX-U operations in FY-16, incremental progress has been made on Milestone R16-2. All the fast ion diagnostics used to characterize the distribution function and its time evolution have been succesfully commissioned (cf. Section on NSTX-U Diagnostics). Data from neutron detectors, FIDA and ssNPA systems were routinely available during the Run – thus completing Experimental Machine Proposals (XMP) 107 and 110 on diagnostics checkout. Preparation for the installation and commissioning of a Charged Fusion Product Array also made progress, although the premature end of the FY-16 Run prevented initial tests during plasma operations. Unfortunately, q-profile measurements through MSE have not been available during the Run, thus hampering NB current drive studies that rely on MSE-constrained equilibria for reliable and quantitative TRANSP analysis of the non-inductive current fraction.

XP/XMP	*Title*	*Goals*
110	FIDA/ssNPA/sFLIP checkout	Commissioning of main fast ion diagnostics. Test background subtraction techniques for FIDA. Compare phase space response of different systems. Test sFLIP diagnostic.
107	Neutron diagnostic calibration	Obtain low-NB-power plasmas with low neutron count rate. Transfer calibration from pulse-counting to current-counting mode for fission chamber counter. Transfer calibration to scintillators.
1522	Beam ion confinement of 2nd NB line	Checkout confinement properties of fast ions from 2nd NB line in quiescent conditions. Investigate confinement vs. beam source, injection energy, plasma current, toroidal field. Compare with classical predictions from NUBEAM/TRANSP.
1523	Characterization of 2nd NB line	Assess operating regimes achievable with combinations of 1st + 2nd NB lines. First characterization of NB-CD with 2nd NB line. Dedicated discharges will explore pressure profile modifications vs. NB source mix. This XP complements the Ip/Bt scan XP by Kaye et al.
1524	AE critical gradient	Explore applicability of "critical gradient" model for fast ion profile in the presence of instabilities. Validate numerical models. Characterize EP transport vs. NB power, fast ion pressure with unstable AE modes.

Table R16-2-1: *Summary of approved XMPs and XPs targeting Milestone R16-2.*

Among the experiments originally planned to address the Milestone (see Table R16-2-1), only XP-1522 on “Beam ion confinement of 2nd NB line” received run time. The experiment was not completed due to unavailability of NB sources from all NB lines. Other experiments were deferred awaiting for MSE availability. Nonetheless, initial data from NSTX-U plasmas with injection from both 1st and 2nd NB lines have been collected and are being analyzed to provide further guidance for future experiments. For example, data are available for sawtoothing L-mode scenarios, whose analysis in terms of fast ion distribution modification and effects on NB-CD will provide complementary data to results from conventional aspect ratio device.

For an initial assessment of beam ion confinement from the different NB sources, short (20ms) beam “blips” from neutral beam line 1 and 2 were alternatively injected into center-stack limited L-mode plasmas. Since the neutron rate signal is dominated by beam-target reactions in these neutral beam heated plasmas, the neutron rise during neutral beam injection is proportional to the number of confined beam ions and the neutron decay following beam turn-off depends on the slowing-down and losses. It has been observed that at high NB injection energy (V_{inj}~85keV), the neutron rise and decay rate of four available neutral beam sources agree reasonably well with TRANSP classical modelling (see Table R16-2-1), which suggests that beams ions are well confined. However, at low NB injection energy (V_{inj}~65keV), the measured neutron rise is lower and the measured decay rate is faster than TRANSP modelling predictions (Table R16-2-2). The reason for the discrepancy at low injection energy is under investigation. Potential reasons for the discrepancy are uncertainties in the measured Z_{eff} or in the beam species mix between full, half and third NB energy components at low beam injection voltage. It should be mentioned that experiments at the lower injection energy were performed early in the FY-16 Run, when tuning of the NB sources was still progressing towards “nominal” operating conditions.

Source (E_{inj}=85keV)	Neutron Rise (Exp/TRANSP)	Neutron Decay Rate (Exp/TRANSP)
1B (R_{tan} 60cm)	0.82+-0.10	1.01+-0.14
1C (R_{tan} 50cm)	1.05+-0.07	1.05+-0.13
2A (R_{tan} 130cm)	1.04+-0.06	1.04+-0.11
2C (R_{tan} 110cm)	0.83+-0.09	0.94+-0.17

***Table R16-2-1**: Neutron rate response to short NB "blips" with NB injection voltage of 85kV.*

Source (E_{inj}=65keV)	Neutron Rise (Exp/TRANSP)	Neutron Decay Rate (Exp/TRANSP)
1B (R_{tan} 60cm)	0.48	1.01
1C (R_{tan} 50cm)	0.52+-0.02	0.84+-0.27
2A (R_{tan} 130cm)	0.47+-0.02	0.94+-0.04
2C (R_{tan} 110cm)	0.49+-0.02	0.77+-0.09

***Table R16-2-2**: Neutron rate response to short NB "blips" with NB injection voltage of 65kV.*

NB "blip" experiments also provided a first indication of the effects of NB injection from the different sources on the fast ion distribution. The multi-view SSNPA system [R16-2-1] can separate the response of passing and trapped particles. The setup geometry determines that the active charge-exchange signals of t-SSNPA and r-SSNPA are sensitive to passing and trapped particles, respectively. Fig. [R16-2-1] show the SSNPA signals in a beam "blips" experiment in which ~20 ms pulses of NB source 1C, 2A, and 2C are alternatively injected. When 1C from NB line #1 is injected, r-SSNPA signals immediately increase, and then decays after the beam is turned off. Similarly, t-SSNPA signals jump up when NB 2A or 2C from NB line #2 is employed. Since the p-SSNPA system intersects with neither NB line #1 nor #2, the signals are purely passive signals, and they are weakly affected by the NB modulation.

Development and validation of numerical tools to understand the evolution of the fast ion distribution function and correlate it with fast ion driven instabilities made substantial progress in FY-16. Although more validation work is required for the new NSTX-U scenarios, these tools are ready for comprehensive studies related to Milestone R16-2. The models provide accurate description of the fast ion evolution (e.g. in TRANSP) and of the correlation between fast ion driven instabilities and fast ion profiles, thus enabling more reliable predictions of the NB drivent current.

A new module has been developed for the ORBIT code to compute self-consistently the evolution of instabilities and fast ion distribution [R16-2-2]. Mode amplitude and phase are evolved based on the energy exchanged with fast ions, whose unperturbed distribution is taken from the NUBEAM module of TRANSP. Growth rates, mode saturated amplitudes and relaxed fast ion profiles are thus computed consistently. Validation of the "critical gradient model" CGM has also progressed in FY-16, including the comparison between results obtained with perturbative vs non-perturbative treatment of the modes [R16-2-3]. The model has been applied to NSTX and DIII-D cases, showing reasonable agreement with experimental data, e.g. in terms of predicted vs. measured neutron rate deficit. Finally, the reduced "kick model" for fast ion transport implemented in TRANSP has been validated against NSTX and DIII-D data [R16-2-4] [R16-2-5]. Results also compare well with predictions from the CGM model. Since FY-15, the kick model has been further improved by including the effects of a finite electrostatic potential, which is important for plasmas with large rotation such as NSTX/NSTX-U. More details on each of the models and the main results during FY-16 can be found in the "Energetic Particles Research Highlights" Section.

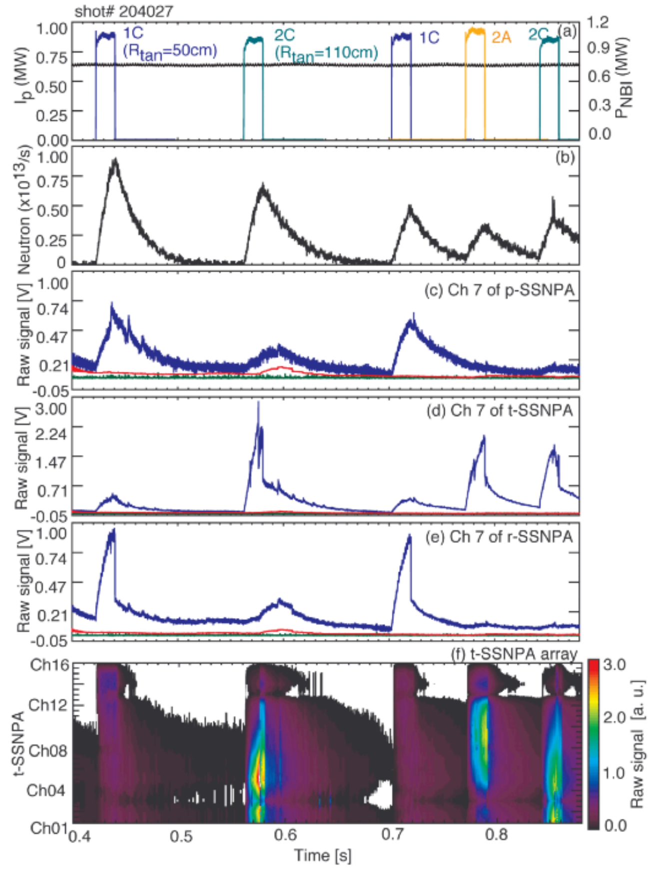

Figure R16-2-1: *Temporal evolution of (a) plasma current and injected NB power, (b) neutron rate, (c) channel 7 of p-SSNPA, (d) channel 7 of t-SSNPA, (d) channel 7 of f-SSNPA, and (f) one array of t-SSNPA. The "blind" detector signal and estimation of x-ray induced noise are also shown in (c)-(e) with green and red curves, respectively. (Figure from Ref. [R16-2-1]).*

References

[R16-2-1] D. Liu et al., Rev. Sci. Instrum. **87**, 11D803 (2016)
[R16-2-2] R. B. White et al., Plasma Phys. Control. Fusion (in press 2016)
[R16-2-3] N. Gorelenkov et al., Nucl. Fusion **56**, 112015 (2016)
[R16-2-4] M. Podestà et al., Nucl. Fusion **56**, 112005 (2016)
[R16-2-5] M. Podestà et al., Phys. Plasmas **23**, 056106 (2016

FY2016 Research Milestone R(16-3): *Develop the physics and operational tools for obtaining high-performance discharges in NSTX-U* **(Target - September 2016. Completed – September 2016)**

Milestone Description: *Steady-state, high-beta conditions are required in future ST devices, such as a FNSF/CTF facility, for increasing the neutron wall loading while minimizing the recirculating power. NSTX-U is designed to provide the physics knowledge for the achievement of such conditions by demonstrating stationary, long pulse, high non-inductive fraction operation. The ultimate toroidal field (1.0 T) and plasma current (2.0MA) capability of NSTX-U is twice that in NSTX. NSTX-U has a capability for >5 second discharges, and it has an additional beamline which doubles the available heating power and provides much greater flexibility in the beam current drive profile. The aim for studies during the first year of operation of NSTX-U is to lay the foundation for the above operational scenario goals by developing needed physics and operational tools, using toroidal fields up to ~0.8 T, plasma currents up to ~1.6 MA, improved applied 3D field capabilities from additional power supplies, a variety of plasma facing component (PFC) conditioning methods, and advanced fueling techniques. As an example of the latter, supersonic gas injection provides higher fueling efficiency, and will be used to develop reliable discharge formation with minimal gas loading. Differing PFC conditioning techniques, including boronization and lithium coatings, will be assessed to determine which are most favorable for longer pulse scenarios. Impurity control techniques, an example of which is ELM pacing, will be developed for the reduction of impurity accumulation in otherwise ELM-free lithium-conditioned H-modes. The higher aspect ratio, high elongation ($2.8 < \kappa < 3.0$) plasma shapes anticipated to result in high non-inductive fraction in NSTX-U will be developed, and the vertical stability of these targets will be assessed, with mitigating actions taken if problems arise. An initial assessment of low-n error fields will be made, along with expanding the RWM control and dynamic error field correction strategies using both proportional and state-space $n \geq 1$ feedback schemes, taking advantage of the spectrum flexibility provided by the 2^{nd} SPA power supply. Resonant field amplification measurements, ideal MHD stability codes, and kinetic stability analysis will be used to evaluate the no-wall and disruptive stability limits in these higher aspect ratio and elongation scenarios. These physics and operational tools will be combined to make an initial assessment of the non-inductive current drive fraction across a range of toroidal field, plasma density, boundary shaping, and neutral beam parameters.*

Milestone R(16-3) Report:

Operations leading up to and during FY16 campaign made significant progress in developing the operational tools for high-performance discharges. Plasma current and outboard gap control were established (Section R16-3-1). The Real-time EFIT (rtEFIT) code was recommissioned, and many new features were added (Section R16-3-2). ISOFLUX control of the plasma radius and vertical position was established (Section R16-3-3). New vertical position control sensors and algorithms were added (Section R16-3-4). Error field correction strategies (Section R16-3-5) and plasma facing component conditioning (section R16-3-6) methods were assessed. A plasma shutdown algorithm, based on a state-machine, was defined (Section R16-3-7), and operations within the new Digital Coil Protection System was defined (Section R16-3-8). These improvements were manifest in the re-establishment of high-performance H-mode discharges, as shown in the three sub-sections of Section R16-3-9. Additionally, the realtime resistive wall mode (RWM) sensor and control codes were established (Section R16-3-10), though RWM feedback was not used during plasma discharges. Other relevant improvements to the realtime plasma control system are described in Section R16-3-11.

These achievements lay the foundation for continued development of high-performance discharge scenarios, and thus fulfill the present milestone.

Section R16-3-1: Initial Plasma Formation, Current and Position Control

In initial NSTX-U operations, the plasma breakdown and current ramp was established. The Centerstack "Key Performance Parameter" (KPP) plasmas of August 2015 were made with an 8 kA Ohmic precharge. This was chosen to match the approximate leakage flux of the NSTX OH coil, so that the PF-3 fields required to form the field null would be similar (the NSTX-U solenoid has approximately three times the enclosed flux, and leakage flux, such that the 24 kA NSTX pre-charge is roughly matched by an 8 kA NSTX-U pre-charge). These were successful in the initial commissioning of the machine.

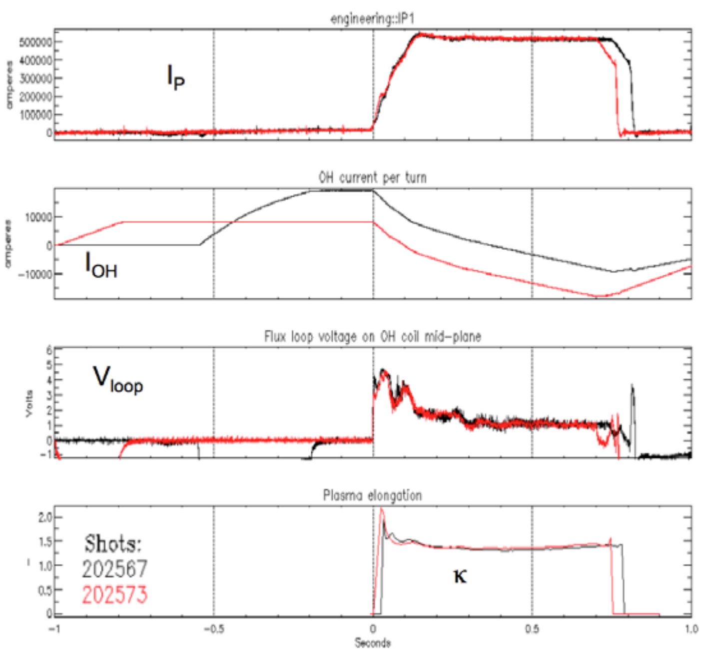

Fig. R16-3-1: *Example of early helium Ohmic discharges with 8 kA and 20 kA Ohmic pre-charge levels.*

While the first NSTX-U discharges used the 8 kA pre-charge, run time was rapidly allocated to developing 20 kA pre-charge scenarios. These cases, with larger amounts of Ohmic flux, are needed for the longer plasma scenarios. As shown in Fig. R16-3-1, similar 8 kA and 20 kA helium discharges were developed. In this particular case, the two 600 kA discharges have similar plasma current evolution. The case in red has an 8 kA precharge, while the case in black has the 20 kA precharge. The two cases have similar loop voltage evolution, except in the few ms following breakdown; the 20 kA case has a smaller field null, and thus requires more initial loop voltage to generate the breakdown avalanche.

These discharges use a simple outboard gap control algorithm based on a limited number of magnetic sensors [R16-3-1]. This "PCC" algorithm (a legacy name meaning "Position and Current Control") is loosely based on an algorithm used on NSTX [R16-3-2], but with substantial upgrades. These include the following: i) elimination of unphysical inner-gap request, which complicated the algorithm with no tangible benefit, ii) control of the gap between the plasma and the secondary passive plates using the PF3 coils was added to the algorithm. This is in addition to the existing control capability of the gap between the plasma and the primary passive plates using the PF5 coil, which provides rudimentary elongation control, iii) elimination of the vertical position control term in favor of a dedicated vertical control algorithm, and vi) adding a compensation term proportional to the ohmic solenoid current so that the X-point location can be held constant using this shape control algorithm as the Ohmic coil flux swings. The control of the PF3 coils using gap control (item 2 in the list) generalizes the control scheme of these coils such that it is valid over a wide variety of ramp up and ramp down scenarios. Item 3 in the list (vertical control improvements) will be discussed in a separate section. The benefits if item 4 are visible in Fig. R16-3-2, where the magnetic equilibria from a single discharge, but two different times separated by greater than a second, are shown. The OH flux changes substantially over this time duration, and the PF-1a and PF-2 currents decrease to maintain the same triangularity (at the expense of a change in the strikepoint location and flux expansion).

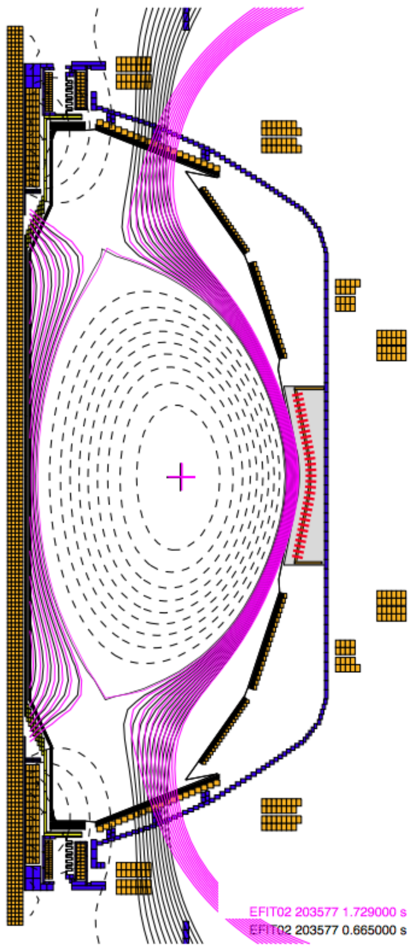

Fig. R16-3-2: *Constant shape held as the OH flux evolves, using the PCC shape control algorithm*

Note that this shape control scheme can be viewed as intermediate in two senses. First, it was the workhorse shape control scheme during the early phase of the campaign before ISOFLUX control was qualified. Once ISOFLUX was commissioned, this scheme continued to be used for the early, low current phase of the shot before rtEFIT is well converged. It also is used for gap control during the controlled ramp down of a discharge. See the next sections for more detail on rtEFIT and ISOFLUX.

Section R16-3-2: EFIT and Real-time EFIT

A common description of the plasma is given by the Grad-Shafranov equation, a second order PDE describing a toroidally symmetric MHD equilibrium. The code EFIT solves this equation, finding the solution most consistent with available diagnostic data. Two versions of this code are automatically run after each NSTX-U discharge [R16-3-3], with different constraint sets. On NSTX and NSTX-U, these are labeled EFIT01, relying only on external magnetic measurements, and the "partial kinetic" EFIT02, which augments the magnetic data with a diamagnetic flux constraint and a pressure profile constraint.

Creating and verifying an accurate model of the conducting structures and coils in the upgrade of NSTX was a significant endeavor to produce high fidelity equilibrium reconstructions. This work is also critical to enable accurate real-time EFIT reconstructions for NSTX-U (more detail given on rtEFIT results below). As is normal, the effort is presently an iterative process between the modeling and reconstruction analysis, and the diagnosticians that supply input to the analysis. This was a multi-month effort, with several key details identified that were required in the model to produce accurate equilibria. Many new details were added to NSTX-U reconstructions compared to NSTX. The two most significant alterations required for the model are presently:

(i) Modeling of the wall currents in the NSTX-U center stack is essential for accurate equilibria, especially through the plasma startup phase and into the plasma current flattop phase, while inductively-generated wall currents are strong. Greater than 0.42 MA total vessel current has been reconstructed using NSTX-U EFIT. These currents are accentuated in NSTX-U compared to NSTX due to the thicker center stack sleeve regions above/below the device midplane. Currents in these regions are significant enough to shape the inner side of the plasma during start-up. Knowledge of this shaping, which changes as the inductive wall currents dissipate, was important to NSTX-U machine operators in understanding how to develop research-grade plasmas from the initial start-up plasma created in the device.

(ii) As well as the magnitude of the vessel current, the poloidal distribution of the vessel current is essential for accurate equilibria. After the careful construction and first multi-week iteration steps taken to verify the NSTX-U EFIT vessel and coil model, it was found that the reconstructed poloidal distribution of the significant current at the upper and lower ends of the NSTX-U center stack was not consistent with the magnetic diagnostics to the expected accuracy. The difference implied a reduction of the vessel resistance in the two end regions by a factor of two. The puzzle was solved by realizing that the significant number of copper cooling tubes within the two end sleeves of the center stack had not been included in the conducting structure model. Their inclusion explained the reduced resistance implied by the magnetics data.

During FY16 run campaign, the EFIT code was used to analyze over 2300 plasma and vacuum shots, and related tests using two different tests of constraints and diagnostics. EFIT01 reconstructions have been available to the NSTX-U Team from the very first shots of the campaign, while EFIT02 [R16-3-4] became available once the MPTS and diamagnetic flux data was routinely available immediately after the shot. Due to the longer pulse lengths in NSTX-U compared to NSTX, a larger number of equilibria were run per shot than for NSTX. Approximately 600,000 NSTX-U EFIT analysis timeslices were run in FY16, which gives an average of about 190 timeslices per shot.

Beyond post-shot analyses, the Grad-Shafranov equation can also be used for real-time control. In this case, the real-time EFIT, or rtEFIT, code is run within the PCS framework. rtEFIT was used on NSTX [R16-3-2] in the past, but a number of updates were done in preparing for NSTX-U operations [R16-3-1]. These include i) new vessel conducting structure definitions, ii) new Greens tables for the computation of flux and field at various locations, iii) increasing the number of magnetic diagnostics used to constrain the equilibrium, iv) adoption of the same profile parameterization as in the off-line EFIT, and v) increasing the spatial grid from 33x33 to 65x65.

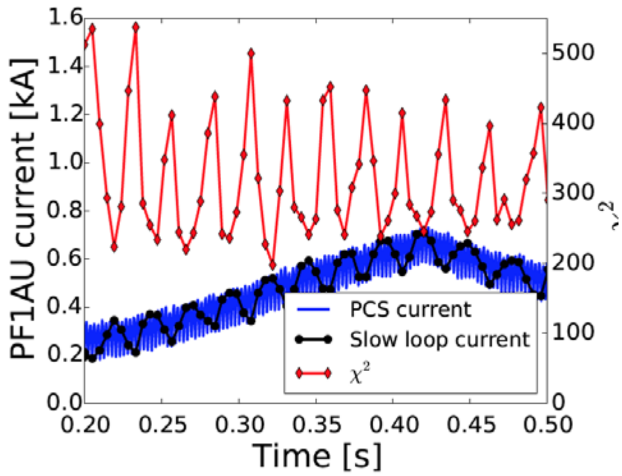

Fig. R16-3-3: *Aliased PF-1aU coil current (black), and its impact on the reconstructed χ^2 (blue).*

With the basic computation of only the Grad-Shafranov equilibrium, cycle times of 3.4 ms were achieved, sufficient for the ISOFLUX shape control described in the next section. However, when additionally fitting the vessel currents and computing quantities like β_N, l_i, or the q-profile, the cycle time became too slow. To overcome this limitation, the multithreading option for rtEFIT was used for the first time in NSTX(-U). Scans were performed to optimize the distribution of threads amongst the code branches, and an optimal mix was found that allowed 44 vessel and coil currents to be fit and the additional quantities calculated, while keeping the equilibrium calculation time below 5 ms.

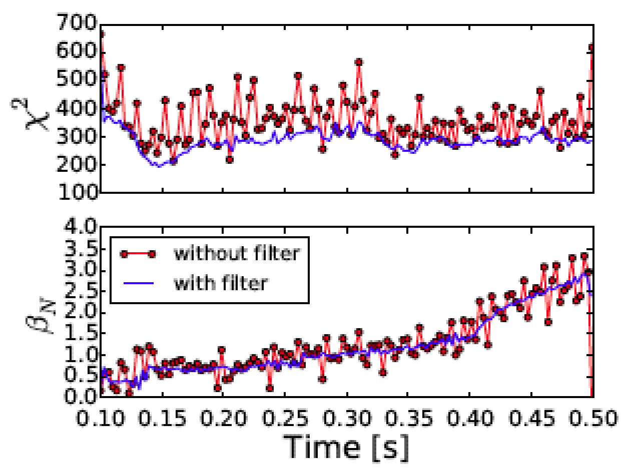

Fig. R16-3-4: Comparison of χ^2(top) and β_N (bottom), both with (blue) and without the anti-aliasing filter.

While the NSTX-U raw data stream and base computations are clocked at $200\mu s$, the slower rtEFIT computation time presents the possibility of aliasing between the data and the reconstructions. In NSTX-U, some divertor coils have a rather large current ripple due to their low effective inductance and the pulsed nature of the 6-pulse thyristor rectifier. As shown in Fig. R16-3-3, this results in their current being aliased in the rtEFIT code: the measured PF-1aU current (blue) was undersampled by the slow loop, creating the current trace in black. This then resulted in large oscillations in the χ^2goodness of fit parameter and in the calculated quantities β_N and l_i.

In order to resolve this issue, a second order digital butterworth filter was written into PCS, applied to the 200 μs sampled data before it is provided to the rtEFIT equilibrium solver. It was found that a corner frequency equal to one half of the rtEFIT computation frequency was sufficient to eliminate these oscillations. This is shown in Fig. R16-3-4, where the χ^2 values are reduced and the fluctuations largely eliminated by the addition of the input data filter.

R16-3-3: ISOFLUX shape and divertor control

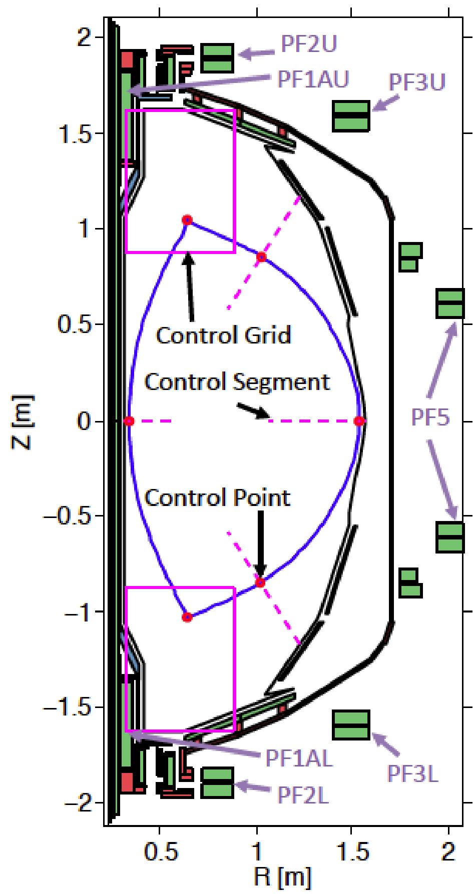

Fig. R16-3-5: *NSTX-U coils and low elongation plasma boundary, the ISOFLUX X-point search grid, and control segments and control points.*

Once rtEFIT was commissioned, it became available for use in ISOFLUX shape control [R16-3-5]. In this algorithm, the flux at a series of control points is controlled to match the flux at a reference location (this is the so called reference flux). The control points are defined as the intersection of the operator-programmed desired plasma boundary with a set of predefined line segments. The reference flux can be defined as either the flux at the limiter (for limited discharges) or at the X-point (for diverted discharges); see Fig. R16-3-5 for illustrations of the line segment locations and search grids. During operations, flux-errors at the control points and X-point position errors are computed, and a PID operator applied to that error. The column vector of these PID values is then multiplied by the M-matrix, which maps the PID values to voltage requests for the various coils.

The ISOFLUX algorithm was run on NSTX [R16-3-2], with separate algorithms for the control of limited and diverted discharges. However, numerous code improvements were made to support NSTX-U operations [R16-3-1]. For instance, before the campaign started, the code was rewritten to make use of the PCS code-generator capability, improving maintainability and making future improvements easier to implement. The number of lines in the code for controlling diverted plasmas was reduced by 75% in this manner, while adding additional features. Another improvement was the addition of a transition smoothing feature to the code, which prevents large discontinuities in the coil voltage request across changes to the ISOFLUX configuration. Additionally, in the diverted plasma control algorithm (ISODNULL), the code has been updated to automatically switch between using the X-point flux and the limiter flux when defining the reference flux. This assists in recovering and maintaining a diverted configuration following plasma transients that momentarily cause the inner gap to close. Finally a new dr-sep control algorithm was commissioned, and an inner gap control method was defined. The latter will be described in more detail at the end of this section.

The first ISOFLUX algorithm commissioned was the so-called ISOELONG algorithm, used to control limited discharges. This algorithm uses the PF-3 and PF-5 coils to control points along the large major radius side of the plasma. This algorithm is used through the complete discharge for inner wall limited plasmas. An example result from this algorithm is shown in Fig. R16-3-6. It can be seen that the distance errors along the outboard control segments and the lower outer control segment have some initial oscillations, which are damped out. The errors then approach zero as the integral gain terms take effect.

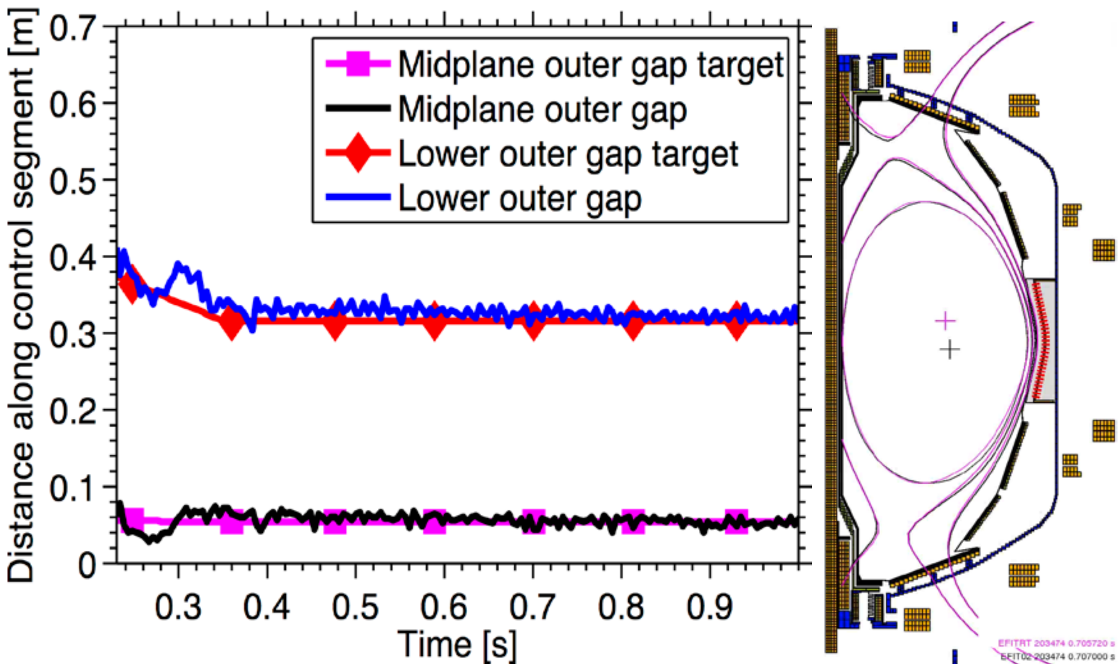

Fig. R16-3-6: *(left) Time evolution of two of the error quantities (midplane outer gap and lower outer gap) for an inboard limited discharge (203474). Note that the PCS internally computes errors in units of flux, but these are plotted as distance errors for clarity. (right) EFIT02 (black) and rtEFIT (purple) comparisons of the equilibrium at t=0.707 seconds. The SOL lines are spaced by 3 cm at the outboard midplane.*

Following this work, the ISOFLUX algorithm was extended to control diverted discharges using the ISODNULL algorithm, including control of the X-point and/or strikepoint locations. In these cases, the PF-5 and PF-3 coils continue to control points on the large major radius side of the plasma, while the PF-1a and PF-2 coils control the X-point and/or strike-point quantities. NSTX had developed strikepoint control, with each divertor coil linked to a separate quantity. NSTX-U has developed a multi-input-multi-output (MIMO) controller, accounting for the interacting effect of the coils within the control law. An example use of this controller is shown in Fig. R16-3-7. The quantities shown are the requested and achieved upper X-point radius and upper X-point height; good tracking is observed for both quantities. Note that the data presented in the figure was filtered with a 5 ms time constant to remove small oscillations due to the rtEFIT aliasing effect noted in the previous section (this plasma was made before the anti-aliasing filter was introduced); in the real-time calculation, a low-pass filter was applied to the error signals to remove noise and oscillations from the control loop.

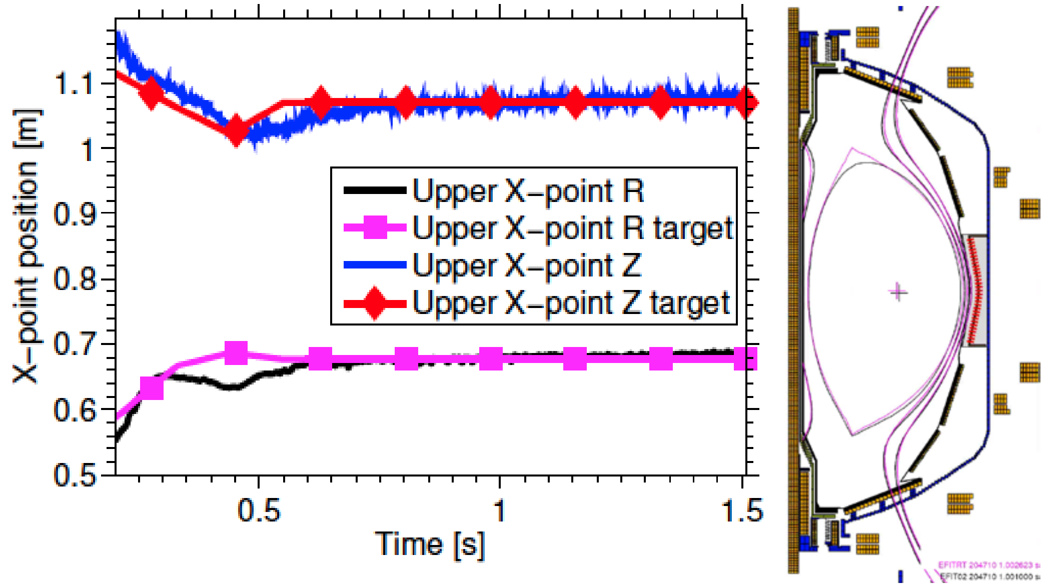

Fig. R16-3-7: *(left) Time evolution of two of the error quantities (Upper X-point R & Z) for diverted discharge 204710. (right) EFIT02 (black) and rtEFIT (purple) comparisons of the equilibrium at t=1.001 seconds. The SOL lines are spaced by 3 cm at the outboard midplane.*

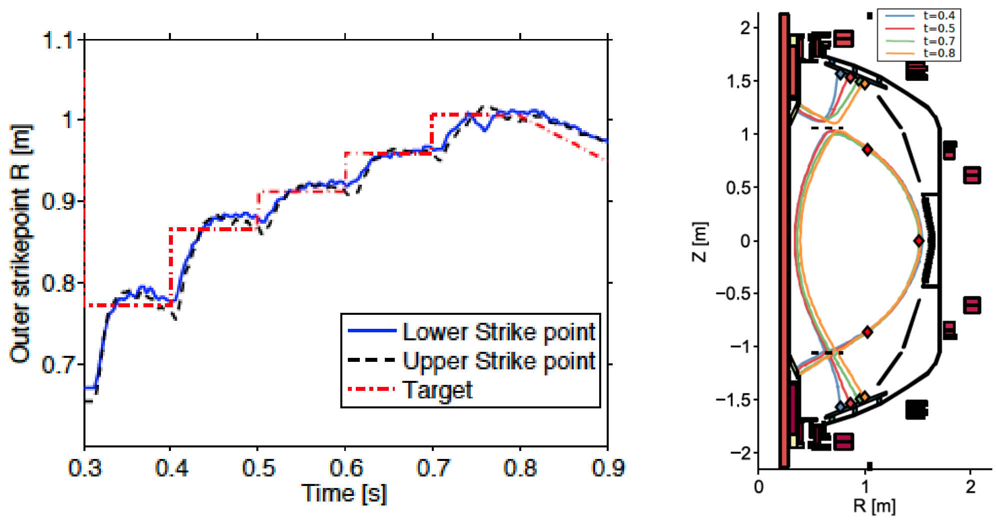

Fig. R16-3-8: *(left) Evolution of the requested and achieved outer strikepoint radius (as calculated by rtEFIT) as a function of time, and (right) rtEFIT magnetic equilibria at selected times, for shot 203879*

Related control schemes have been used to control the outer strike-point in similar discharges. This is shown in Fig. R16-3-8, where a series of four steps is made in the outer strike point request; note that this is an up-down symmetric request. The rtEFIT reconstruction shows good tracking of the request, indicating that the control scheme is working well [R16-3-6].

This excellent control of the outer strike point has also been confirmed by non-magnetic diagnostics. In particular, the lower-divertor CII emission is plotted as a function of radius and time in Fig. R16-3-9. The emission of singly ionized carbon light is localized to just above the

PFC surface, and so is a good indicator of the strikepoint location. We can see that the emission tracks the steps in the EFIT strikepoints, which in Fig. R16-3-8 were shown to track the PCS operator request.

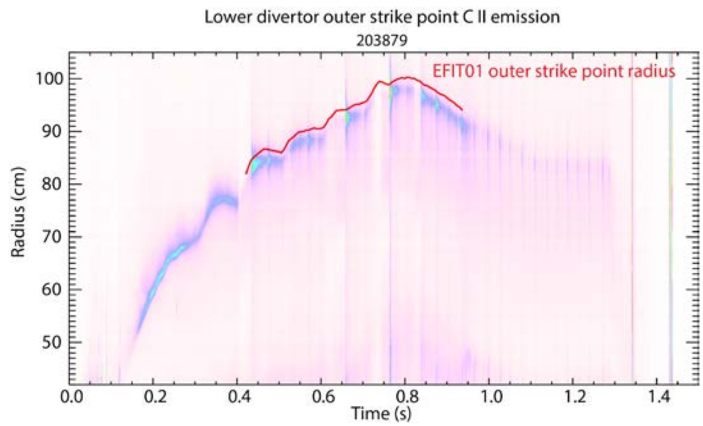

Fig. R16-3-9: *(left) Contour plot of the C II light on the outboard divertor, as a function of time and major radius. The EFIT01 strikepoint radius is also shown.*

In the course of developing H-mode scenarios, it was determined that more precise control of the diverting time was required. This translated into the desire for closed loop inner gap control. This is a challenging requirement in an ST like NSTX-U, which has no inner PF-coils to directly control this quantity. Further, all coils on NSTX-U had already been assigned to other control tasks (gaps, X-point positions, strikepoint positions). Therefore, a novel control scheme was developed to make this control a reality.

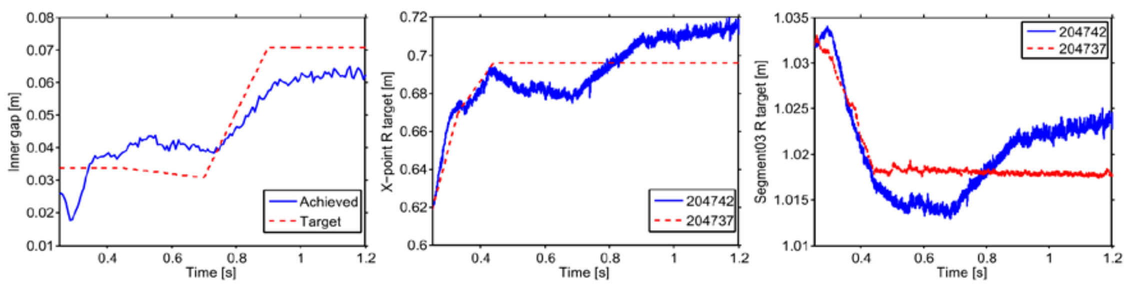

Fig. ***R16-3-11****: (left) The achieved and target values for the inner gap, for a discharge (204742) with closed loop control. The center and right frames show the X-point radius and lower outer control point position for shot without inner-gap control (red) and with inner gap control (blue). The target tracking is achieved by modifying the (center) X-point and segment 3 (right) target requests (blue), compared to a similar shot with inner-gap control turned off (red).*

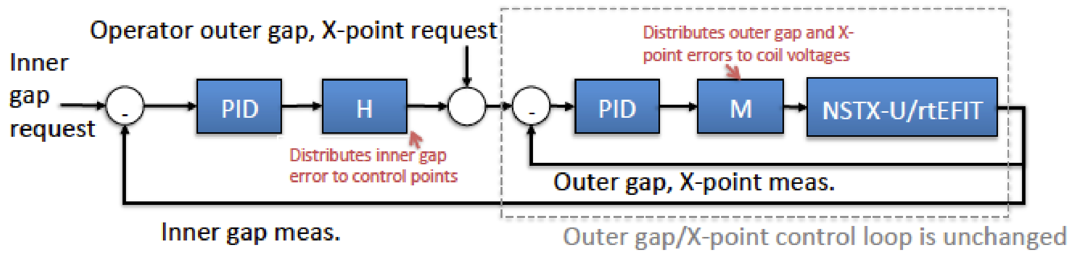

Fig. R16-3-10: *Schematic of the inner gap control algorithm*

The inner gap control scheme is described in Fig. R16-3-10. The inner flux error is computed on the far left, and a PID operator is applied to this. The output of this calculation is then used to modify in real-time positions of the control points associated with the previously defined control, via the weighting matrix H. For instance, if the inner gap is found to be too small in real-time, then depending on the values in the H-matrix, the target radius of the X-points is increased, or the upper & lower outer control points are moved out. The control of outer gaps and X-points then follows based on the new control point locations, as described above.

Fig. R16-3-11 shows an example of this control in use. The left frame shows the requested of the inner gap, as well as the achieved gap evolution. Good tracking is clearly achieved. The center and right frames show the X-point radius and lower outer control point position for shot without inner-gap control (red) and with inner gap control (blue). The target tracking is achieved by modifying the (center) X-point and segment 3 (right) target requests (blue), compared to a similar shot with inner-gap control turned off (red).

With the results presented in Sections R16-3-3 and R16-3-2, it is clear that NSTX-U has made great strides in plasma shape control, and is positioned to use these advances to support plasma scenario development.

R16-3-4: Vertical position control

Beyond shape control, it is also necessary to assess and control the fast vertical motion of the plasma. This is especially critical when pursuing operations at high elongation, as is required to meet the NSTX-U programmatic goals. Hence, vertical position control as a topic received critical attention leading up to, and during, the FY16 run campaign.

The first step in establishing vertical position control is to determine both the position (Z_P), and vertical velocity (dZ_P/dt), of the plasma. This was accomplished in NSTX-U by increasing the number of sensors used compared to NSTX [R16-3-6]. As shown on the left side of Fig. R16-3-12, NSTX used two flux loop sensors, mounted symmetrically around the midplane on the passive plates, to estimate I_PZ_P and I_PdZ_P/dt based on the differences in flux $(\psi_U - \psi_L)$ and the difference in voltage $(V_U - V_L)$ respectively [R16-3-2]. In NSTX-U, we have dramatically increased the number of flux-loop pairs, allowing many more sensors to be used for this estimation. Note that the voltage loop differences are taken in hardware, so that the quantity

$V_{U,i} - V_{L,i}$ is digitized directly, but the flux differences $\psi_{U,i} - \psi_{L,i}$ are taken in software, after digitization of the individual fluxes.

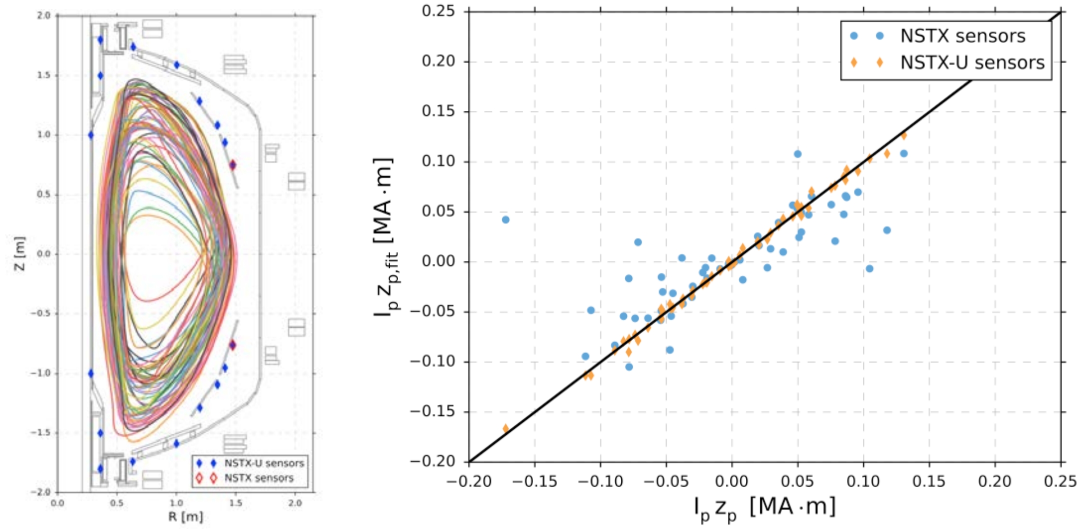

***Fig. R16-3-12**: (left) Vertical position sensors in NSTX-U, and (right) fits of the sensors to model data. See text for details.*

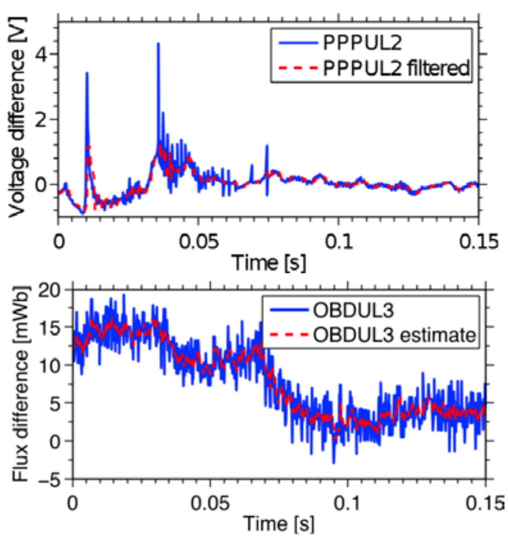

***Fig. R16-3-13:** (top) Voltage difference and (bottom) flux difference corrected via the signal processing techniques described in the text.*

A database of NSTX-U equilibria was formed with the ISOLVER code; these shapes are shown on the left of Fig. R16-3-12. These data are used to train an observer of the form $I_P Z_P = \sum \alpha_i (\psi_{U,i} - \psi_{L,i})$, where i is an index over flux loop pairs and the fluxes $\psi_{U,i}$can be compensated to subtract out any direct pickup from the PF coils. The results of this exercise are shown on the right side of Fig. R16-3-12. When using only the single pair of loops as in NSTX, a large variation is found between the actual value of $I_P Z_P$and the fit value (light blue points). On the other hand, when the full set of NSTX-U loops is used, an excellent fit is obtained (orange points). A similar fit function is then applied using the same fit parameters $\alpha_i$to compute $I_P dZ_P/dt = \sum \alpha_i (V_{U,i} - V_{L,i})$. With these two fit functions, the realtime values of Z_P and dZ_P/dt, as well as their produce, could be determined.

While these sensor-related improvements held great promise, it was found once operations started that additional filtering and/or processing of the measurements was required. For the analog voltage differences, it was found that noise from rectifier switching and spikes from fast MHD transients were contaminating the measurements. These were corrected by including causal low-pass and median filters in the processing of the sensor data (see Fig. R16-3-13 top frame). The flux differences, computed in software after analog integrator of the individual loops, were found to be corrupted by bit noise. This problem was remedied via a Kalman filter, which used both the numerically integrated voltage difference and the software flux difference to estimate the true flux difference (see Fig. R16-3-13 bottom frame).

The position indicators derived from this data were used to create a vertical control law. In particular, the voltage request for the PF-3 coils was determined as

$$V_{PF-3U} = V_{PF-3U,shape} + Dd(I_P Z_P)/dt \; + \; P\delta\psi_V + Ix_{int}$$
$$V_{PF-3L} = V_{PF-3L,shape} - Dd(I_P Z_P)/dt \; - P\delta\psi_V - Ix_{int}$$

where

$\delta\psi_V = I_P Z_{P,request} - I_P Z_P$ and x_{int} is the time integral of $\delta\psi_V$.

Note that when using the PCC shape control algorithm described in Section R16-3-1, all of the P,I, and D terms are used. However, under ISOFLUX shape and divertor control, the P & I values are set to zero and only the derivative term is used.

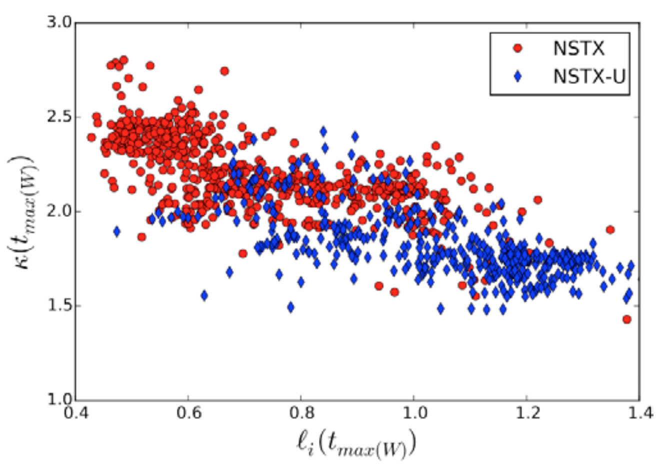

Fig. R16-3-14: Comparison of the elongation achieved in NSTX-U to that achieved in NSTX, as a function of external inductance.

This control law was used to control the vertical position of NSTX-U plasmas, with some empirical-tuning of the proportional (P), integral (I) and derivative (D) gains. Figure R16-3-14 shows a comparison between the NSTX-U and NSTX elongation at the time of maximum stored energy, as a function of internal inductance (l_i) [R16-3-6]. The majority of NSTX-U points are in the medium to higher range of l_i. However, within the l_i range of overlap, NSTX-U has achieved similar elongation values. Note that the natural elongation of the plasma decreases with aspect ratio, such that achieving the same elongation for a fixed l_i is more difficult in NSTX-U than in NSTX. Therefore, the results in Fig. R16-3-14 show that the vertical control measurements and algorithms are well poised to support future high-performance operations.

Section R16-3-5: Error Field Correction

Error fields in a machine like NSTX-U can be generated by a number of mechanical imperfections, for instance tilts of the poloidal or toroidal field coils or non-circularity in the PF coils. Error fields were observed in NSTX, where the dominant effect was a time-dependent tilt of the TF coil as it interacted with stray fields produced by the OH leads [R16-3-7]. Note that these leads and their associated stray fields were located at the top of the machine, while the TF and OH coils were mechanically fixed at the bottom.

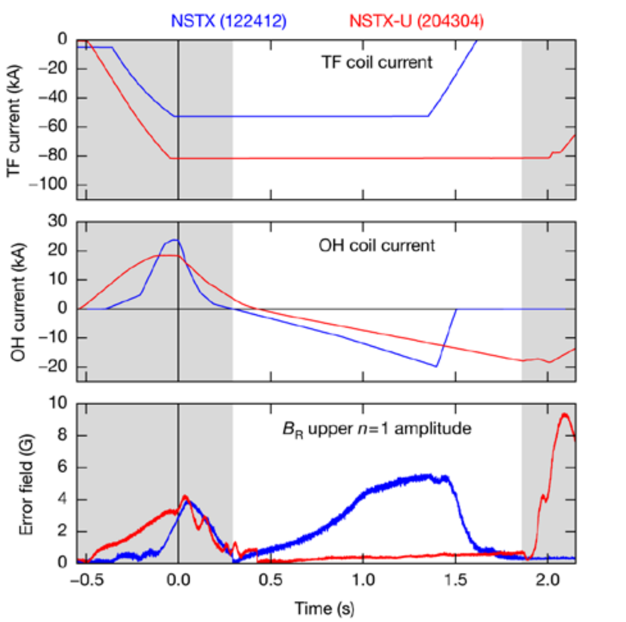

Fig. R16-3-15: Comparison of fields measured during a coils-only vacuum shot on NSTX (blue) and on NSTX-U (red). During the time period shaded in white, the TF current is constant and the OH current passes through zero and steadily ramps to more negative values. In the same time period, a measured n=1 error field (bottom plot) is clearly present in the NSTX shot and absent from the NSTX-U shot.

For NSTX-U, this error field source was eliminated by design [R16-3-8]. In particular, a coaxial lead assembly at the bottom of the machine is used to feed the OH coil, eliminating any effective loop area from the OH leads. Coils-only vacuum shots demonstrate that this coaxial OH lead assembly successfully eliminates the time-dependent n=1 error field due to the OH/TF interaction. This result is best illustrated in Fig. R16-3-15, which shows a comparison of the measured n=1 error field during coils-only vacuum shots in NSTX and NSTX-U. During the time period shaded in white, the OH current ramps steadily through zero to increasingly negative values while the TF remains constant. In the NSTX case (blue), the measured error field amplitude increases from zero to ~5 G over the course of the OH ramp. In the NSTX-U case (red), on the other hand, the measured error field remains below 1 G for the duration of the OH ramp. Note that the measured error field amplitudes are 're-zeroed' when the OH current passes through zero to isolate the time-dependent error fields generated by the OH current ramp. These results demonstrate that the OH/TF error field that was found to impact plasma performance in NSTX was successfully designed out of NSTX-U.

However, in spite of the elimination of the OH/TF time-dependent error field, additional error field studies proved to be important in improving the performance of the machine.

Improvements in performance were first demonstrated in a series of n=1 error field scans in late February. In this case, illustrated in Fig. R16-3-16, an n=1 field is applied, proportional to the PF-5 current magnitude; the phase of the n=1 field and the constant of proportionality are variables to be adjusted by the operator. This proportionality to PF-5 was chosen because the PF-5 coil is known to have out-of-round features whose error fields must be corrected. The reference plasma in this case is a 700 kA Ohmic scenario. In the example shown in Fig. R16-3-16, adjustments of the applied n=1 phase at fixed proportionality resulted in either shorter or longer discharges. This asymmetry implies the presence of an error field, with a best correction occurring with an applied field phase of 315 degrees (toroidal angle).

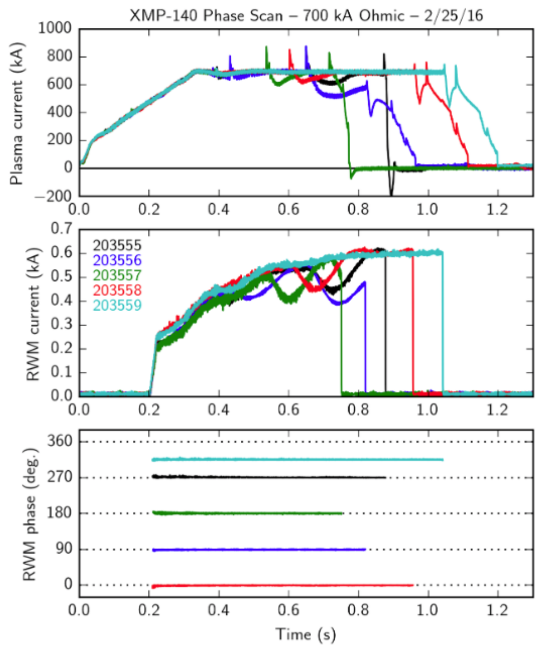

Fig R16-3-16: *Results of applying n=1 fields of various phases at fixed proportionality to the PF-5 coil current. The best performance as judged by plasma duration is a toroidal phase of 315°.*

In order to better resolve the best feed-forward error field correction, n=1 fields were applied in a 'compass scan' format to determine the optimum error field correction for locked mode avoidance over a sequence of shots. More specifically, the amplitude of the applied n=1 was ramped in each shot at fixed phase until the plasma disrupts. The waveforms from one such compass scan are shown in Fig. R16-3-17, where the plasma current in the top frame shows that different shots disrupt at different times.

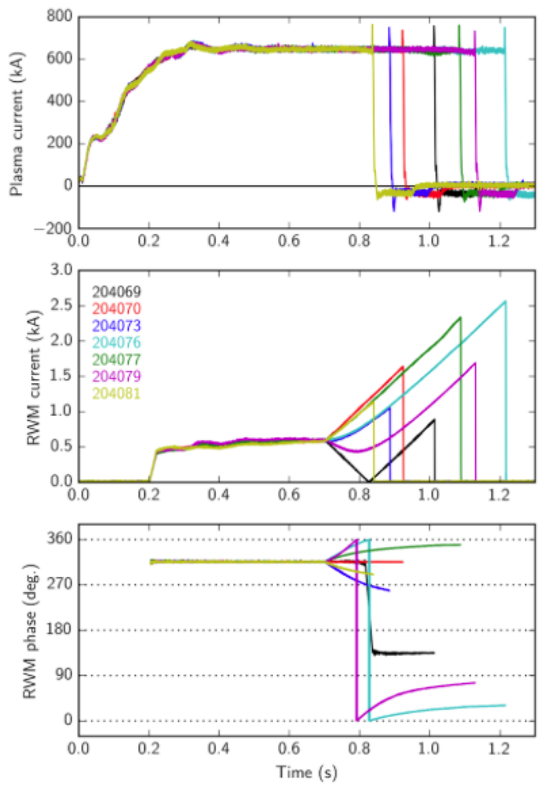

Fig. R16-3-17: *Seven discharges from a sample compass scan. The top frame shows the plasma current, the middle frame shows the RWM coil currents, and the bottom frame shows the phase of the applied field.*

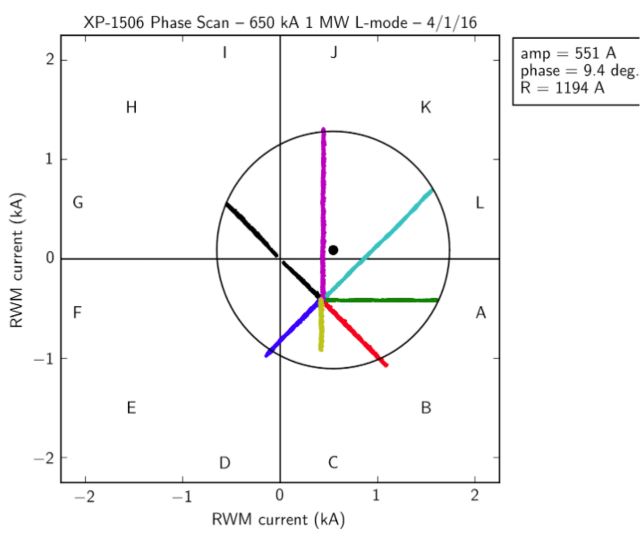

Fig. R16-3-18: *Phase space plot of the compass scan data in Fig. R16-3-17. The resulting circle is centered away from zero with at an amplitude that is comparable to the PF-5 proportional amplitude, but at a phase of 15° rather than 315°.*

These are 700 kA diverted L-mode plasmas formed with a 20 kA ohmic precharge, with a density of $1.3\text{x}10^{13}$ cm^{-3}, and heated by 1 MW of neutral beam power. The middle frame shows the RWM coil current. All shots have an initial evolution as per the optimal solution from the experiment described in Fig. R16-3-16 (and other similar experiments). At 0.7 seconds, however, the RWM coil currents diverge, with ramping amplitudes of various phases, as shown in the bottom frame. The fact that the different phases disrupt at different applied field amplitudes confirms that a nonzero error field must be corrected in these L-mode discharges in order to provide optimum locked mode avoidance.

The results from Fig. R16-3-17 can be reframed as a phase space plot of the applied RWM currents as a function of time, ending at the point of a disruption. As such, the waveforms from Fig. R16-3-17 are shown in phase space format in Fig. R16-3-18. This figure shows that the currents at time of disruption map to a circle whose center is shifted away from zero. The center of this circle is the optimum correction for locked mode avoidance, which is similar in magnitude but differs slightly in phase when compared to the initial PF-5 proportional results in Fig. R16-3-16 (15° versus 315°).

An error field compass scan was completed in three different configurations: (i) the case shown in Figs. R16-3-17 and R16-3-18, (ii) a similar case at twice the plasma density, and (iii) a comparable high density case with an 8 kA (rather than 20 kA) OH precharge. The second scan, which was conducted to assess the density scaling of the locking threshold in this 1 MW beam-heated L-mode scenario, found that the locking threshold was largely unaffected by the higher density; this implies that the rotation driven by the beam is the dominant effect, compared to the diamagnetic rotation that is thought to dominate in Ohmic plasmas. The third and final scan, which was conducted to assess if the error field measured in the compass scans is due to the OH coil, found no change in the required error field correction. The fact that the required correction did not change with a large change in the OH pre-charge implies that the OH is *not* the source of the error field measured by the compass scans.

The optimized error field correction determined from the three compass scans described above was used successfully in many of the best H-mode plasmas from this campaign (e.g., shots 204112 and 204118 discussed in detail in Section R16-3-9).

The figures above describe the optimization of the error field correction after the start of the plasma current flattop. However, experiments were also conducted to establish if there is an optimal correction strategy very early in the shot, during the breakdown and early ramp-up phases. An example of this type of experiment is shown in Fig. R16-3-19. The upper left frame shows the plasma current evolution, which is largely similar for each L-mode discharge in the set. The middle frame on the left shows that the RWM current amplitude is flat at approximately 600 A from t=0 for each of the cases, except for the blue case with no correction current. The bottom left frame shows that the phase of the applied field varies for different discharges, and it is the effect of these phase changes that is of interest. Note that the black case is the phase that was found to be optimal for the plasma current flattop.

The somewhat surprising results of the scan are shown in the right column of the figure. First, the density during this early phase of the shot is shown in the top right, where it can be seen that the green and magenta cases, corresponding to 285° and 240°, respectively, is elevated during the ramp up as compared to the other phases and the reference. Conversely, the density is depleted in the black case, which corresponds to 15° (the optimum plasma current flattop correction). The elevated (depleted) density could be indicative of better (worse) correction since small locked modes in the ramp-up can result in particle loss and therefore depleted density. Returning to the figure, the middle frame on the right shows the neutron emission, where the black case shows depleted neutron emission, which is another indication of poor correction in the applied field phase that later in the shot is optimum for error field correction. Finally, the core rotation speed, as measured by the rtV_{phi} diagnostic, shows highest early rotation for the corrections in the range of 195°–285° (red, magenta, and green). In the 15° case (black), on the other hand, the core of the plasma is nearly locked until around 350 ms when it spins up to match the other cases during the plasma current flattop. Since faster rotation for the same applied torque (from the beam) implies reduced drag from error fields, it is clear that the optimal flattop correction is different from optimal during the ramp-up phase.

These results show that the optimal correction likely varies during the shot, implying that there may be more than one error field source. One potential source, as noted above, is the out-of-round nature of the main vertical field coil (PF-5). Other candidate sources that may explain the time-dependent nature of the required error field correction are: (1) induced currents that flow in the vessel wall during ramp-up; and (2) a static tilt of the TF center rod with respect to the vertical axis of the PF-5 coil. First, the vessel currents are time-dependent in that they decay away after the ramp-up and therefore only have a large impact early in the discharge. The tilt of the center rod, on the other hand, could have a time-dependent effect in that the error field it produces has a dominant 1/1 component that only resonates with the plasma once q_0 drops below unity. In these 1 MW beam-heated L-mode plasmas, the q=1 surface enters the plasma around t=400 ms, which is consistent with the damping of the core rotation that is observed in the bottom right panel of Fig. R16-3-19. The various candidate error field sources are being investigated through additional physics analysis, including numerical calculations of the plasma response, as well as through *in situ* metrology of various coil shapes and alignments that is planned for the FY16/FY17 outage.

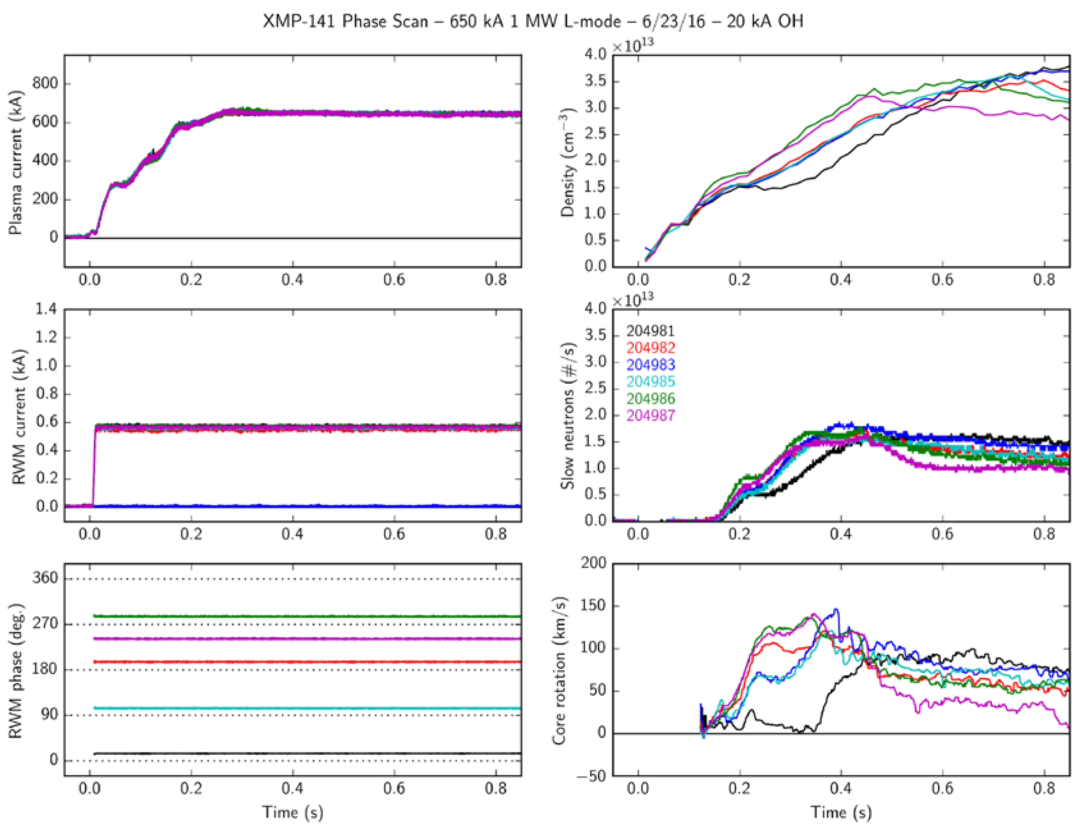

Fig. R16-3-19: *Results from an experiment to examine early error field correction. A constant amplitude of 600 A at different phases is applied from t=0, except in the blue reference case. Phases in the range of 195°–285° (red, magenta, green) show elevated density and core rotation, while the 15° case (black) shows depleted density and neutrons as well as minimal rotation.*

All of the error field correction efforts described to this point focus on n=1 error fields, which are the most damaging to the plasma. Higher order (n=2,3) fields can also elicit a plasma response, however, and are therefore of interest for achieving maximum performance. Such higher order corrections are anticipated in NSTX-U given that the main vertical field coil (PF-5) is known to have n=2,3 asymmetries, and a static feedforward n=3 correction was required to achieve maximum performance in NSTX.

One of the upgrades available to the NSTX-U device are three additional switching power amplifiers (SPAs), which in concert with the three existing SPAs are used to independently drive the six error field correction coils. This configuration facilitates the simultaneous generation of n=1,2,3 applied fields. In contrast, NSTX had only three SPA units such that only n=1,3 or n=2 fields could be generated. New measurements of the PF-5 coil indicate that the n=2 component of the error field could be larger than in NSTX due to changes in the mechanical supports of the coil during the upgrade project, so the ability to produce n=2 fields while maintaining the ability to correct odd-n fields is expected to be important.

To exercise the new six-SPA capability, simultaneous n=1,2 fields were generated to investigate the impact of various n=2 phases and amplitudes on the plasma. More specifically, the optimum PF5-proportional n=1 error field correction scheme is applied to produce long (~2 sec) 1 MW beam-heated L-mode discharges. Then, on top of the n=1 correction, a modulated n=2 field pattern with alternating phase and amplitude changes is applied. As shown in Fig. R16-3-20, the modulations in the n=2 fields (bottom left) produce changes in the observed core rotation (bottom right). In particular, the rotation rises slightly when fields are applied in the negative (180°) phasing, and it dips slightly with the opposite (0°) phasing. Furthermore, a strong deleterious response is observed in the core rotation, the plasma density, and even the plasma current at the highest amplitude 900 A in the 0° phasing. No such dramatic response is observed with 900 A in the 180° phasing. This asymmetric response will warrant further investigation of n=2 error field sources in NSTX-U.

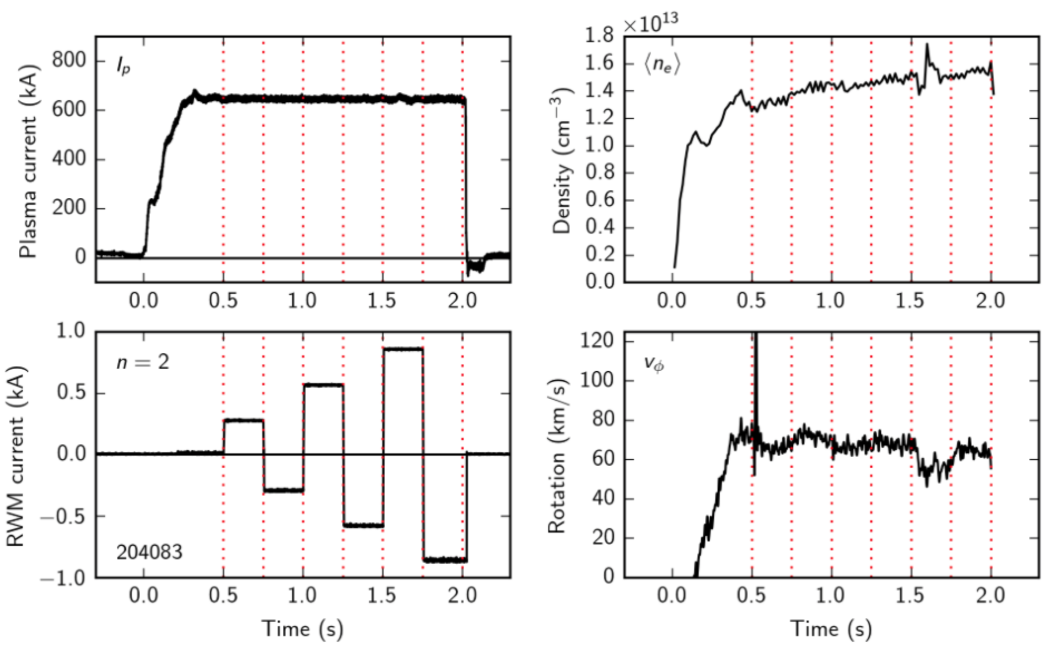

Fig. 16-3-20: *Results from an experiment with modulated n=2 applied fields. The core rotation (bottom right) increases slightly with negative (180°) phasing and dips with positive (0°) phasing. A strong deleterious response to the 900 A, 0° modulation is visible in the plasma density and even the plasma current in addition to the core rotation.*

Additional information on error field physics can be found in the macroscopic stability section of the NSTX-U FY-16 annual report.

Section R16-3-6: PFC Conditioning

Graphite is the main plasma facing component (PFC) material in NSTX-U with a mix of ATJ-grade and POCO graphite tiles. The discharges during the 2016 run campaign used three different plasma facing component conditioning techniques. The PFCs were initially prepared with a ~3 week long bake of the PFCs, accomplished during the period 9/12/16 through 10/20/16. Once plasma operations resumed, helium glow discharge cleaning (GDC) was used between shots to control deuterium recycling. Boronization of the plasma facing components during evening or weekends was used to control the oxygen levels.

A new boronization system, based on deuterated tri-methyl borane $B(CD_3)_3$, was installed in 2015 and 2016 [R16-3-9]. Compared to NSTX with a single dTMB inlet, the new system has dTMB inlets at each of the midplane, lower divertor, and upper divertor. The GDC electrodes, however, continue to be located near the midplane, as in NSTX. QMB measurements show that the dominant deposition of the boron thin films remains near the midplane, where the electrodes are located, though feeding gas into the divertors can make a modest (~20%) increase in the divertor deposition.

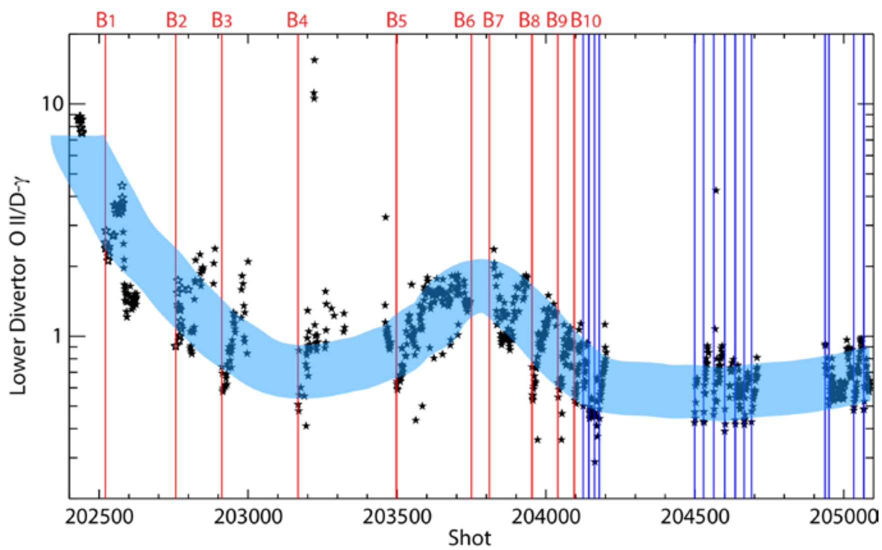

Fig. 16-3-21: *O-II/D-gamma ratio as a function of shot number.*

In order to monitor the condition of the PFCs, it was found that the O-II/D-gamma ratio provided a useful metric. The numerator in this quantity is proportional to the influx of singly ionized oxygen from the PFCs into the plasma, while the denominator provides a normalization against the incident ion flux. The ratio is therefore effectively indicative of the PFC surface oxygen concentration. These measurements were made with wide-angle filterscopes looking through the same window and at nearby wavelengths, so that variations in the window transmission are removed. Similar trends were also confirmed with spatially resolved and absolutely calibrated cameras.

This O-II/D-gamma ratio is shown in Fig. 16-3-21, as a function of shot number. A blue band is overlaid on the evolution of this ratio over the experimental campaign, simply to guide the eye to the underlying trends. The quantity is averaged over t=[0.05-0.2] s of each discharge, as the plasma programming tends not to vary considerably during this phase. Red vertical lines indicate when full-bottle boronizations (9 grams of dTMB per bottle) were applied, with the subscripts associated with each B indicating the count, while blue vertical bands indicate $1/5^{th}$- and $1/4^{th}$-bottle mini-boronizations. This spectroscopic ratio was initially quite high at the beginning of the run. However, repeated full-bottle boronization, as well as plasma operations, helped bring it down over time. Note the general trend of a drop in normalized O-II light (by 2-3x) following each boronization, followed by a subsequent rise. The only significant exception to this trend was following B_7. NSTX-U was filled with positive pressure of Argon and briefly vented to remove a fragment of a broken shutter, with the total time with ports open to New Jersey air of less than 5 minutes. However, there was some inevitable air ingress to the vessel, and thus a higher oxygen level even following the boronization. This oxygen was reduced by running NSTX-U, and the standard post-boronization trends were recovered soon after. Note also that the first H-mode discharge (202812) was observed after only the second boronization.

During the experimental campaign the frequency of boronization was increased as higher power discharges started challenging the PFCs. After the 10th full-bottle boronization, it was decided to try so called “mini-boronizations”, where 1/5th of a bottle was used the evening before each run day. This was motivated by the expectation that it would lead to more consistent conditions day-to-day, as opposed to having the conditions degrade over a series of days following a full-bottle boronization. In general, this strategy appears to have borne out. The level of oxygen emission immediately following mini boronization was comparable to those achieved with full bottles and the overall normalized oxygen emission was maintained within the range that had led to the most H-mode discharges. However, H-mode access was becoming more difficult in this later phase, and a full bottle boronization was being planned when operations were truncated in June.

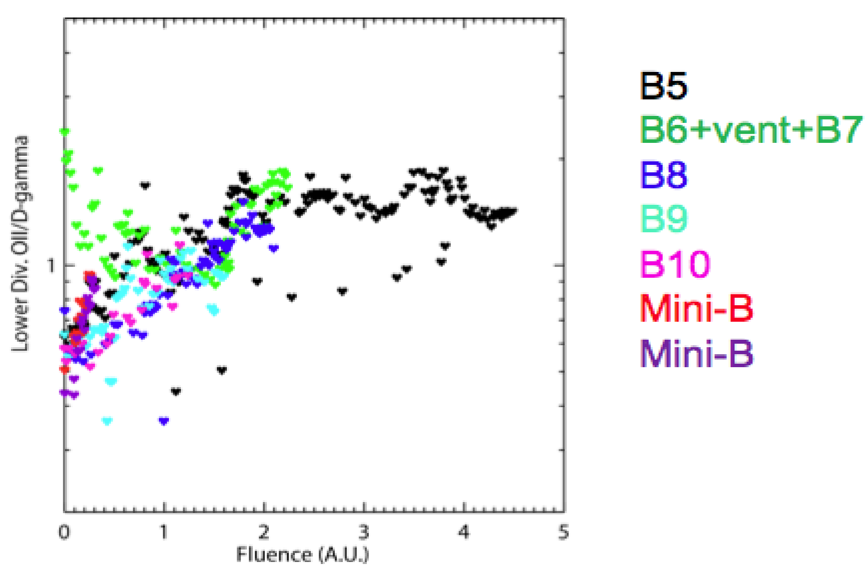

Fig. R16-3-22: *Normalized oxygen emission as a function of fluence since the last boronization, for various different boronization instances*

The normalized oxygen levels in Fig. R16-3-21 are plotted against shot numbers. Some of this data is replotted in Fig. R16-3-22 as a function of the integrated lower divertor incident ion fluence since the last performed boronization. Here the fluence is calculated as the time integral of the lower divertor D-α (which is proportional to the incident ion flux). Oxygen emission over the year is shown to range between two consistent extremes, the minimum representative of boron-coated graphite tiles and the maximum representative of deconditioned tiles. Replacing shot number with fluence normalizes the evolution of lower divertor oxygen emission following each boronization (with the exception of B_7 which followed the vessel vent), indicating the role of boron thin coating erosion in the evolution of the PFCs. The oxygen evolution following mini boronizations is also shown to happen on a faster time scale, consistent with the lower amount of deposited boron and the erosion argument.

Lithium evaporative coatings were not applied during the 10 week run campaign, however, the LITER probes were brought to an operational state. The four NSTX-U LITER assemblies are designed for use at Bay K and Bay F, with two assemblies available for each location. Activities during the FY16 run included reinstallation and recommissioning of the Thermionics stepper motor controllers, including the installation of new cabling. The LITER fill station was set up and used to outgas each of the LITER assemblies. Each of the four empty LITER assemblies was then installed in the machine for alignment checking, with good fits found for each assembly. All lithium handling procedures associated with LITER were updated, the LITER technical team was sent to lithium safety training, and the full LITER process was approved by the Activity Certification Committee (ACC). The LITERs themselves were on the threshold of being filled with lithium for evaporation when the run ended due to the failure of the PF-1aU coil.

The impurity granule injector (IGI) was also fully commissioned as a tool for future scenario development. The instrument was fully assembled, both from a mechanical view and a control perspective. This includes the plasma control system interface. The injector was installed on the machine and its preliminary test procedure (PTP) completed. The XMP defined to test the IGI on plasma for the first time was being run when the PF-1aU coil failed. Hence, this system will be ready for use when operations resume.

Section R16-3-7: Shutdown State Machine

It was decided before the FY16 NSTX-U run began to implement PCS code for automatically shutting down the discharge based on events. There were two motivations for this work. First, the largest forces on the coils and their support structures in NSTX often occurred during transients while trying to control an already-disrupting plasma. By accepting that the plasma is disrupting and attempting instead to control it rapidly to zero current, these transient loads can be reduced. Secondly, the development of plasma shutdown methods, both during normal operations and during off-normal events, is critical for the ultimate development of the ST and tokamak reactor lines, and it is therefore important that NSTX make contributions in this area.

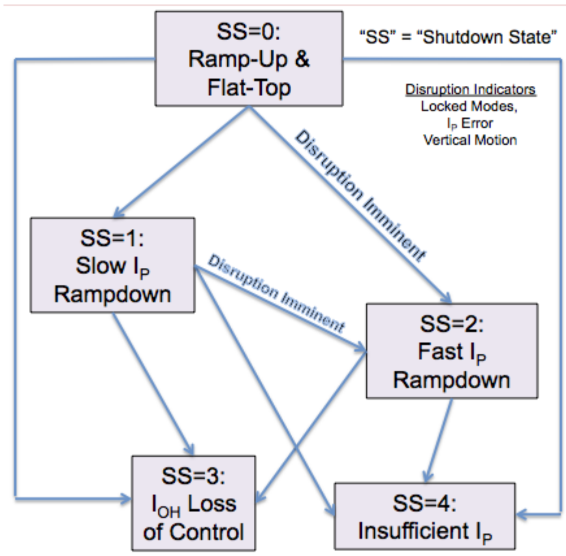

***Fig R16-3-23**: State machine architecture implemented in the NSTX-U PCS*

This code is based on a state machine formalism, described by Fig. R16-3-23. In this system, the plasma is initiated in the SS=0 state, for ramp-up and flat-top control; this will be referred to as "Flat-Top Control" below even though it is used for the ramp-up as well. There are two terminal states: SS=3 occurs when the OH current has exceeded a final threshold, which implies an imminent loss of OH current control and therefore plasma current control, while SS=4 corresponds to the case where the plasma current has vanished (either due to being ramped down or a disruption). In either of these terminal states, all gas injection is stopped, the neutral beams are turned off, and all coil currents are returned to zero.

In between the two terminal states and the initial SS=0 state reside the two plasma rampdown sequences. SS=1 contains a slow rampdown, which is intended to be entered when the plasma is in a normal state. Only i) an operator waveform, ii) the OH current dropping beneath an initial threshold, or iii) the OH coil approaching an I^2t limit could drive this transition.

The fast rampdown state, on the other hand, is intended to cover cases where the plasma has entered an unhealthy state, and needs to be quickly ramped down. The present code allows transitions to the fast rampdown state when any of the following occur:

- Large n=1 modes are detected by the Resistive Wall Mode (RWM) sensors. These modes could be either an RWM or n=1 locked mode, but would in either case be highly detrimental to plasma performance. Note that although the realtime processing of the RWM sensors was developed during the FY-16 run, various software switches in the state machine were not configured to permit them to trigger the shutdown.

- Excessive vertical motion was detected by the vertical position observer (see Section R16-3- 4 for more details on the vertical position and motion estimation).

- The fractional plasma current error current error, $|I_P-I_{P,request}|/I_{P,request}$, exceeded a threshold.

- The plasma current dropped beneath a threshold while under ISOFLUX control, determined as the lowest plasma current for rtEFIT to work correctly (typically around 300 kA).

From a software perspective, certain choices were made in order to expedite this coding process. The state machine itself resides in the “system category”. This is a location in the PCS code base that is defined to do various synchronization functions. Provision exists in that location for changing the condition of any or all NSTX-U actuators based on the state machine state. However, the various checks against thresholds are all done in the code location where quantities are first computed, with only flags sent to the system category state machine. This allows the state machine code to be unencumbered by numerical details, while allowing the diagnostic subject matter experts to optimize the disruption detection algorithms without disrupting the state machine code.

It is additionally worth noting that NSTX did not have any software system such as this. Some aspects were of course included (such as the Insufficient I_P check), but they were local in the code and did not have the ability to enforce changes to all actuators at once. An example use of this system is shown in Fig. R16-3-24. The top left frame shows the achieved plasma current (blue) as well as the I_P request. The discharge was initially programmed to run beyond one second; however, the rampdown is initiated at ~0.75 seconds by the shutdown handler. The reason for this is visible in the second frame on the left, where the vertical controllability metric $Z_P(dZ_P/dt)$ exceeds the threshold of 0.6 m^2/s. The evolution of the variable SS is shown in the third frame on the left. The discharge begins with SS=0, but transitions to SS=2 (Fast Rampdown) when the vertical motion threshold is exceeded. It stays in this state until approximately 0.9 seconds, when the plasma current is has dropped beneath the “Insufficient I_P” threshold of 60 kA.

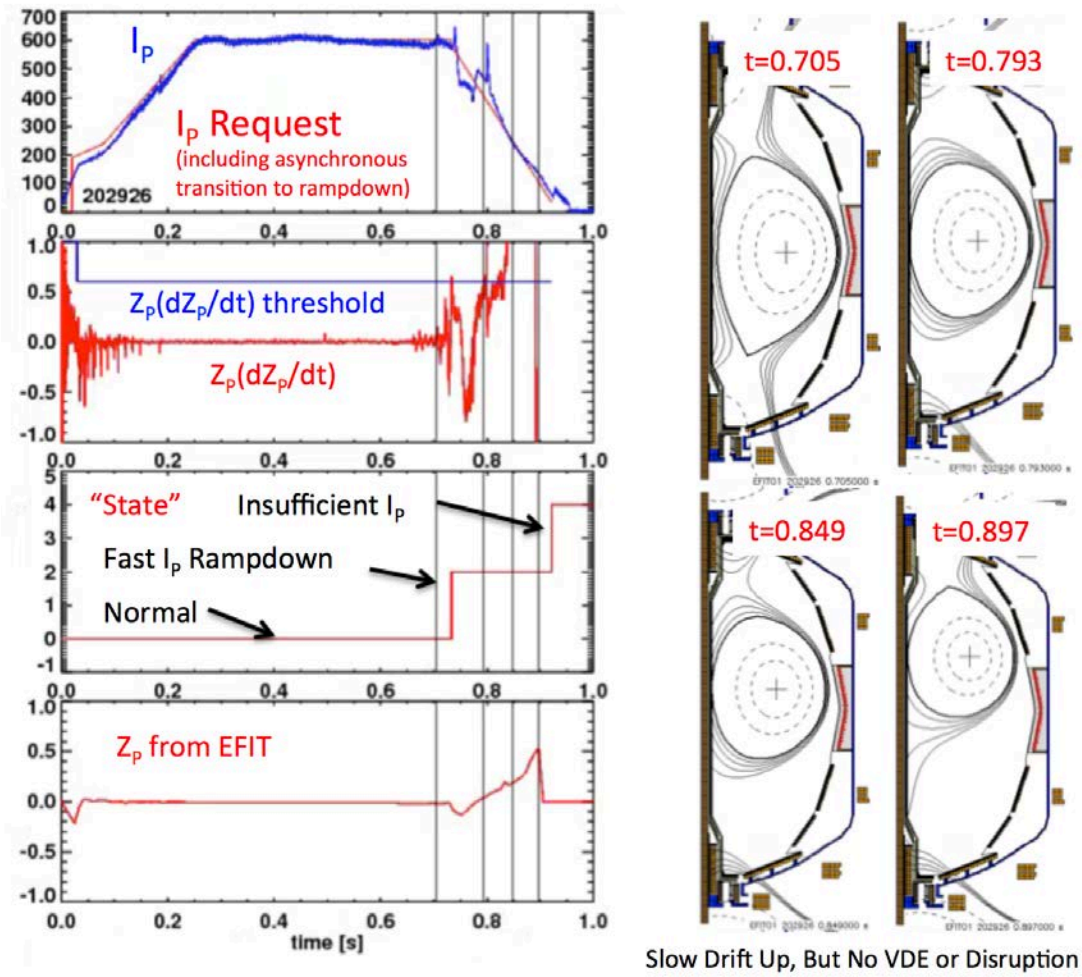

Fig. R16-3-24: *Example of a discharge asynchronously terminated by the shutdown handler. See text for details.*

The final plot on the left column shows the vertical position of the plasma. It can be seen that the plasma has an initial downward kick, and then only a slow evolution in Z_P. This evolution can be better understood by examining the plasma shape evolution on the right side of the figure; the times selected for the flux plot correspond to the black vertical lines in the time traces. It is clear that the plasma is pushed onto the center stack by the shutdown state machine, and the vertical position is reasonable well controlled. It is only when the plasma current has been reduced to very low levels that the vertical drift becomes large, and even then, the plasma does not impact the upper divertor. This example shows the utility of this control scheme for reducing disruption effects such as halo currents.

The shutdown handling mechanism has also been used for the controlled shutdown of healthy discharges, as shown in Fig. R16-3-25. These are 600 kA diverted L-mode discharges, heated with 1 MW of neutral beam power. At t=1.5 seconds, the shutdown is initiated by a pre-programmed switch to the slow rampdown state, and a long rampdown of the plasma current is initiated. The neutral beams hold steady, then begin a pre-programmed phase of modulation. The stored energy (W_{MHD}) decreases at the same time, on account of both the beam power and plasma current reduction. As for the shape, the plasma is limited on the center column during the early phase of the rampdown, as evidenced by the drop in elongation. The shape is held fairly constant from that point till the end of the discharge. The density drops throughout the rampdown, driven again by the loss of beam fuelling, lack of gas fueling, and reduction in plasma current, and this enables a roughly constant Greenwald fraction through the rampdown. These rampdowns were used on the majority of L-mode shots in the second part of the run campaign.

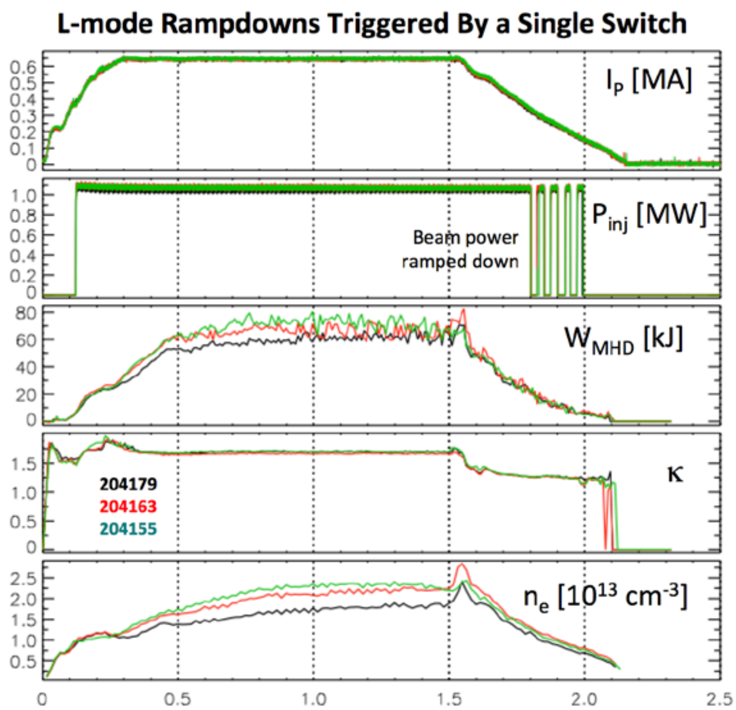

Fig R16-3-25: *Controlled rampdown of three morning fiducial discharges from consecutive days. See text for details.*

Two aspects of the shutdown handling mechanism were not fully implemented during the truncated campaign. First, the code flags were never configured to allow the B_P or B_R n=1 mode identification to trigger the shutdown. However, the raw and processed RWM sensor data was fully present in the realtime system, as described in Section R16-3-10. Note also that the vertical motion sensing system is somewhat sensitive to large n=1 perturbations due to imperfections in the sensors, and therefore has some functional overlap with the dedicated RWM sensors. Secondly, the transition path from Slow Rampdown (SS=1) to Fast Rampdown (SS=2) was not fully activated. After an initial attempt and subsequent code revision, PCS was poised to allow this transition when operations were halted for the year.

Despite these limitations, a study has been done on the route by which NSTX-U discharges were terminated during the 10 week run campaign. As shown in Fig. R16-3-26, the most common shutdown method was to pass from Flat Top Control [SS=0] to Fast Shutdown [SS=2] and then Insufficient Ip [SS=4]; these generally related to cases where some MHD related even initiated the discharge process, as in Fig. R16-3-24. The second most common case was from Flat Top Control [SS=0] to Show Shutdown [SS=2] and then to Insufficient Ip [SS=4]; these are generally L-modes cases with smooth plasma current rampdowns as in Fig. R16-3-25. The third most common case goes from Flat Top Control [0] to Insufficient Ip [4]; these are cases where the discharge fails to form properly and I_P and shape control are never established.

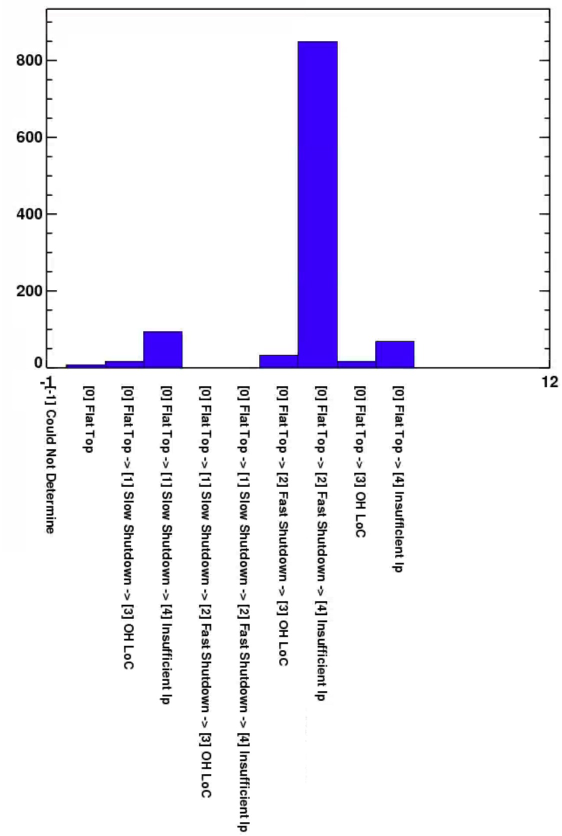

Fig. R16-3-26: *Histogram of the various possible trajectories of the state variable.*

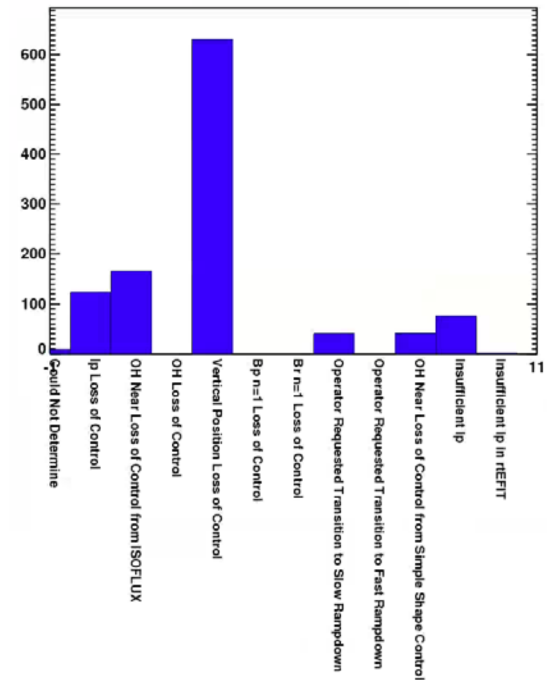

Fig. R16-3-27: *Histogram of the event which takes the plasma out of the SS=0 Flat Top and Ramp-Up state.*

We have also done a study of the first event that drives the plasma out of Flat Top Control [SS=0]. As shown in Fig. R16-3-27, the most common event is a loss of vertical control. It is worth emphasizing again that the vertical motion sensors also have sensitivity to large n=1 perturbations. Therefore, some of these events classified as vertical position loss of control may indeed be large RWMs or locked modes. The second most common cause was so called "OH Near Loss of Control" from ISOFLUX. This occurs when the OH coil current reaches a limit near, but still separated from, the ultimate limit. In this case, a slow rampdown is initiated. The third most common reason for leaving the SS=0 state is an I_P Loss of Control, which occurs when the plasma current deviates from the target current by more than a predefined fraction of the target. The final large cause of leaving SS=0 is Insufficient I_P, corresponding again to cases where the discharge fails to form properly. It is important to reiterate that the B_P and B_R realtime n=1 analysis was fully functional at the end of the run campaign, but the shutdown state machine was not configured to change states based on that data.

Section R16-3-8: Operation of the Digital Coil Protection System

The NSTX-U digital coil protection system is designed to prevent coil currents, or combinations of coil currents, that can damage the coils or their supporting hardware. This is done by i) measuring the currents in the coils in real-time, ii) using those currents to compute forces, stresses, torques, and coil heating, iii) comparing those quantities to limit values, and iv) shutting down the power supplies if those limit values are exceeded. This is accomplished by one instance of the coil protection software running on the plasma control computer, and one instance running on a dedicated stand-alone machine. Note that the limits are generally set by fatigue allowables, so that tripping DCPS does not by itself indicate a dangerous situation for the machine. Also, the DCPS force and stress allowables were derated to 80% of the ultimate fatigue allowables during this 10 week run campaign, providing an extra degree of conservatism.

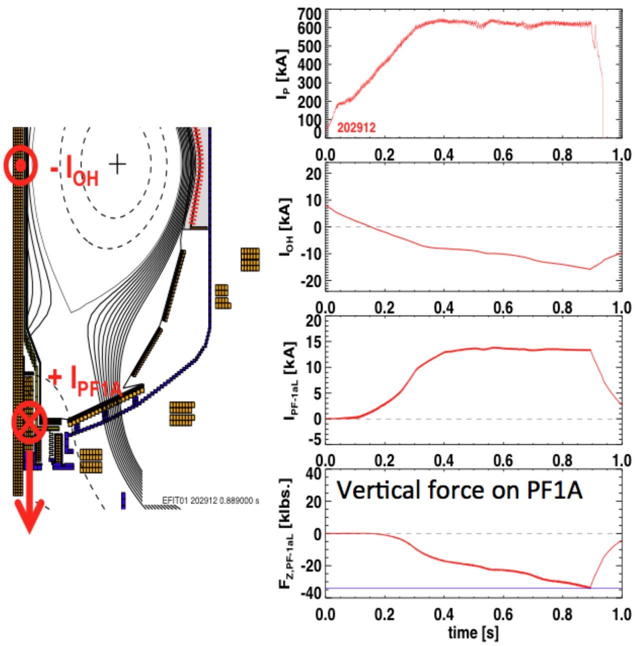

Fig. R16-3-28: *Example time traces from a shot with a trip due to the vertical force on the PF-1aL coil.*

An example calculation is show in Fig. R16-3-28. In this case, a 600 kA plasma current discharge is formed. The OH coil swings to apply loop voltage, approaching 17 kA of current. At the same

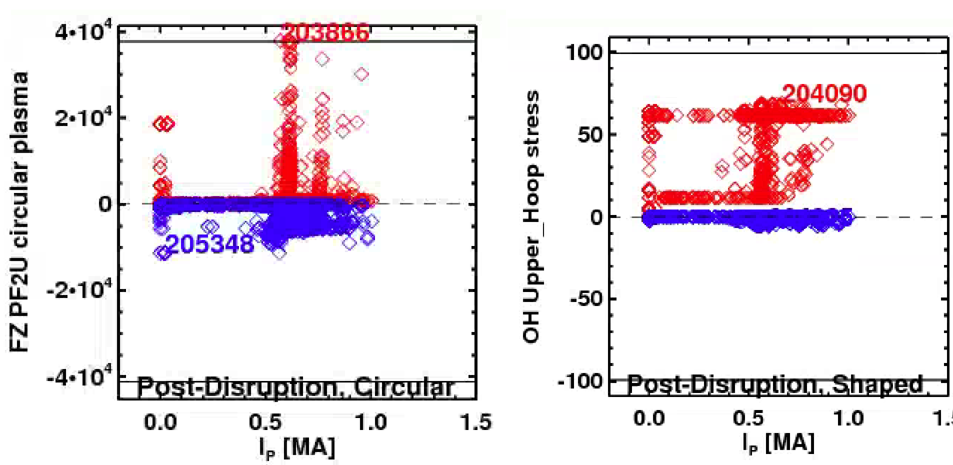

Fig. R16-3-29: *(left) Vertical force on the PF-2U coil (in lbsf) and (right) the OH Coil hoop stress (in MPa).*

time, the PF-1aL current flat-tops at approximately 14 kA of current. Given that the PF-1aL current is positive (parallel to I_P) while the OH current is negative, there is a downward force on the PF-1aL coil, which ultimately reaches the -34 klbs lower limit. When this limit is reached, a DCPS fault is issued, and all power supplies are suppressed and bypassed. While this leads to an abrupt termination of the plasma, the coils are well protected.

The DCPS has proven highly effective in the first year of NSTX-U operations. Fig. R16-3-29 shows the maximum and minimum vertical force on the PF-2U coil at any time in the shot, as a function of the plasma current; each point corresponds to a single discharge. There are many discharges in the 600-700 kA range which approach the limit, and some which cross this limit leading to trips. These are all L-mode scenarios which, given the high internal inductance, require large divertor coil currents to divert. H-mode scenarios at this plasma current do not come near to challenging this (or any other) force limit at these lower currents.

As a second example, the hoop stress at the upper part of the OH coil is shown on the right. This is often dominated by the stress due to the OH coil precharge, with the large number of 20 kA pre-charge shots yielding the repeated stresses of ~65 MPA. There are a few cases with larger

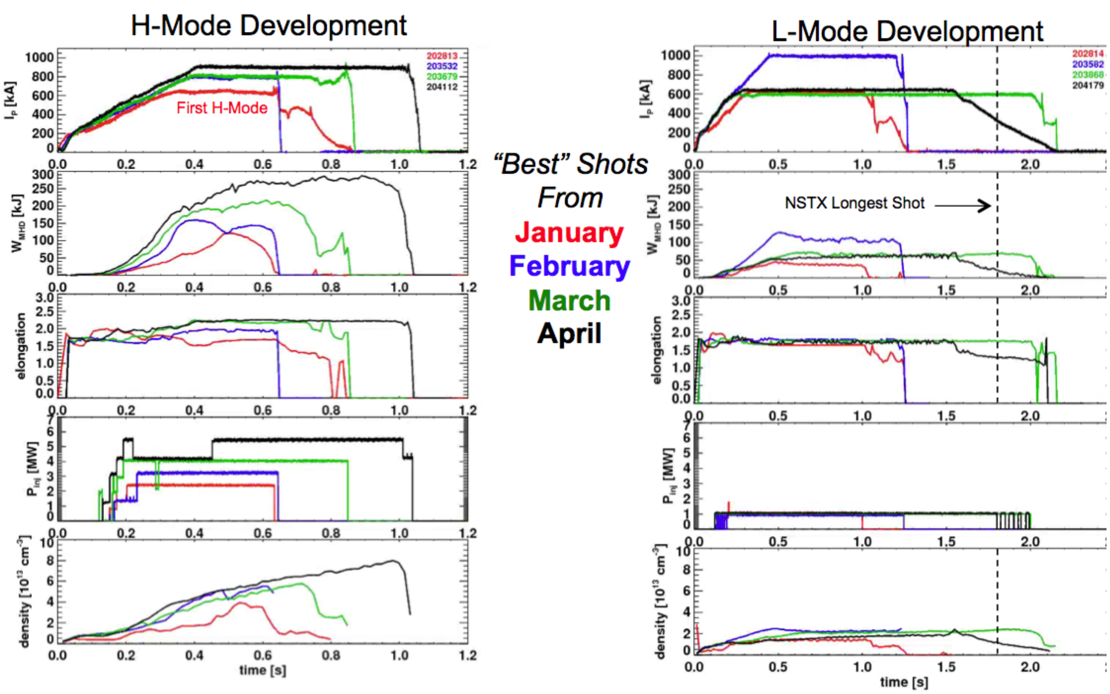

Fig. R16-3-30: *Progress in (left) H-mode scenarios, and (right) L-mode scenarios. See text for details.*

stress; these correspond to when the OH coil runs to larger negative current at the end of the discharge, while the local divertor coils are running positive currents. The interaction of these coils is then to provide a larger hoop force on the OH coil than due to the OH current alone. The limits in this case are based on derating the allowable OH stress of 125 MPA by the same 80% safety margin. DCPS computes ~400 of these types of forces, stresses, torques, and temperature rises. As such, the results presented in Fig. R16-3-28 and R16-3-29 are not more notable than many others that could have been selected. They show that DCPS is functioning properly, protecting the machine while allowing for scenario development.

Section R16-3-9: High Performance Scenario Development

Given the progress in developing the elements of scenarios, it is not surprising that NSTX-U made steady progress during the 10 week operations campaign. This progress is described in the sections below.

R16-3-9-1: Example Scenarios

This progress is shown clearly by the progressions in Fig. R16-3-30, which shows the "best" L- and H-mode discharges from each of January, February, March, and April (all 2016). Consider first the L-mode discharges in the right-hand column. The early discharge 202614 from January, at I_P=600 kA, lasts approximately 1 second, with 1 MW injected power. These were extended to I_P=1 MA in February, with stored energy of ~100 kJ. In March, the lower current case was pushed to longer duration, exceeding in duration any shot ever taken on NSTX. Finally, in April, the smooth rampdown of these scenarios was developed, as described in Section R16-3-7. Note that the elongation of these discharges was largely the same, as the high internal inductance of L-mode cases restricts the shaping flexibility. This high internal inductance leads to a requirement for large divertor currents as well, and so 1 MA was near the limit of the L-mode plasma current for the present coil protection system settings.

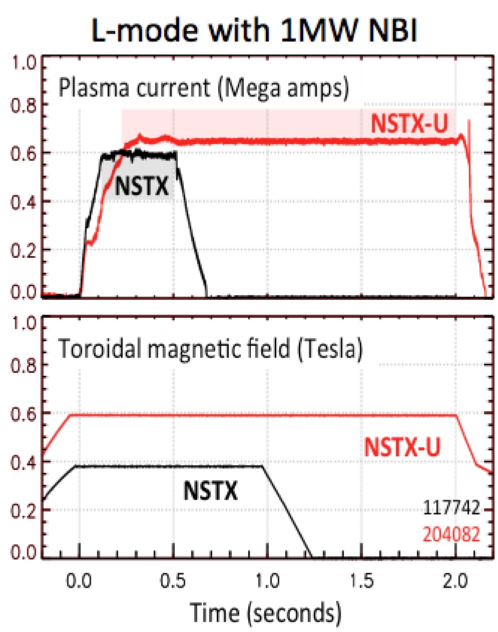

***Fig. R16-3-31**: Comparison of similar NSTX and NSTX-U L-mode discharges. See text for details.*

Some elements of the progress in H-mode scenarios are shown on the left of Fig. R16-3-30. The first H-mode shot from January, 202813, transitions later in the discharge, and achieves a peak energy of ~150 kJ with ~2.5 MW of beam heating. It has an elongation of approximately 1.5. By February (shot 203532) the H-mode plasma current was raised to 800 kA, the neutral beam power was higher at 3 MW, and the elongation was approaching 2. By March, the beam power was 4 MW, with elongations of 2.2-2.3 and stored energies exceeding 200 kJ. By April, neutral beam powers of 6 MW were being injected, with the stored energy approaching 300 kJ.

The contrast between NSTX and NSTX-U is easily seen in comparing L-mode scenarios in Fig. R16-3-31. The NSTX case in black shows a typical 600 kA plasma at B_T=0.4T; the maximum fields run in NSTX during the last 5-6 years of operations were 0.55 T, and these with special approval. The NSTX-U shot has a 1.7 s flat-top duration, at substantially higher field.

R16-3-9-2: High Pressure, High Beta, and Long Duration Plasmas

NSTX-U has made progress during the 10 week operational campaign towards the long term goals of the program. As evidence of this, Fig R16-3-32 shows the volume average plasma pressure, averaged over the flat-top duration, as a function of two different parameters. The averaging over the flat-top duration provides values that are less than the peak value for the discharge, but that are more representative of the performance. Red points correspond to legacy NSTX data with dTMB conditioning of the PFCs, blue points correspond to NSTX cases with lithium conditioning of the PFCs, and black points are NSTX-U cases with PFC conditioned by dTMB. The calculations are done with the EFIT02 instance of the EFIT code.

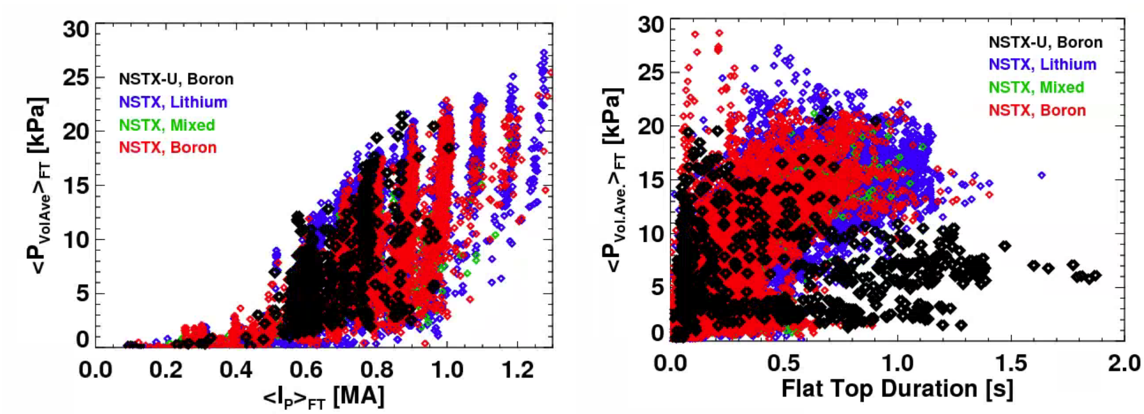

Fig. R16-3-32: Volume average pressure, averaged over the plasma current flat-top, as a function of (left) the plasma current, and (right) the flat top duration.

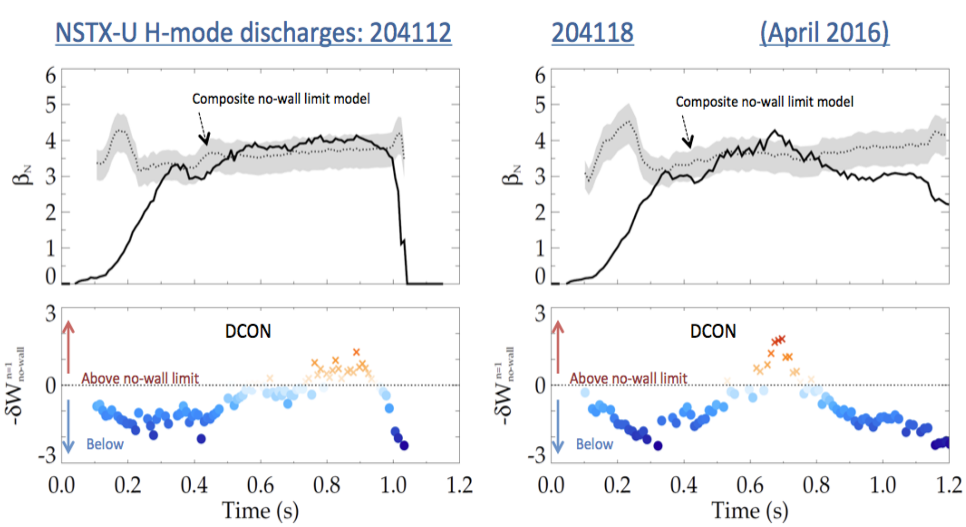

***Fig. R16-3-33**: Model (top) and DCON (bottom) calculations of ideal n=1 stability for two high-performance discharges in NSTX-U.*

The left side of Fig. R16-3-32 shows the average pressure as a function of the flat-top plasma current. NSTX discharges did go to higher current levels than in the initial 10 week campaign of NSTX-U. However, in the region of 800-900 kA, the NSTX-U cases are already exceeding the volume average pressure achieved in NSTX. The same data is plotted as a function of flat-top duration on the right of Fig. 16-3-32. The longest duration NSTX-U shots are in L-mode, and therefore have a reduced volume averaged pressure. However, there are some NSTX-U points exceeding 20 kPa for durations approaching a second; these are close to the NSTX performance boundary.

The MHD stability of some of these high performance discharges is shown in Fig. R16-3-33. Discharge 204112 (left) was shown in Fig. R16-3-30, while discharge 204118 (right) is a similar 1 MA case. The top frame shows the value of β_N computed by EFIT02, as well as a composite model for the n=1 no-wall limit [R16-3-10]. This is a simple formula for the no-wall limit based on equilibrium parameters such as aspect ratio, internal inductance, and pressure peaking, derived from a large database of NSTX DCON runs. From this comparison, it is apparent that the NSTX-U discharges are approaching or exceeding the no-wall limit. The bottom frame of each figure shows DCON calculations of the n=1 no-wall δW, where negative numbers indicate stability and positive numbers indicate instability. These calculations show that NSTX-U plasmas have indeed exceeded the n=1 no-wall limit, and are therefore in the wall stabilized regime (note that no n=1 feedback was used on these discharges)

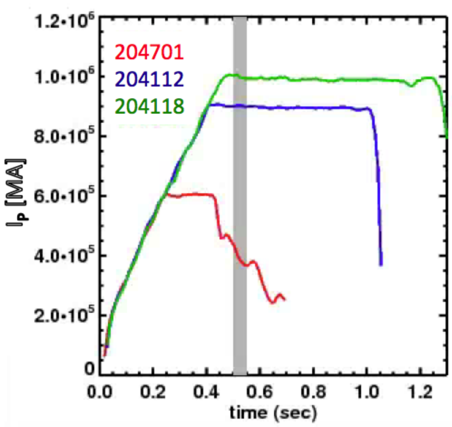

Fig. R16-3-34: *Plasma current evolution for the cases whose current drive components are studied in Fig. R16-3-35.*

R16-3-9-3: Non-Inductive Current Drive Fraction Calculations

Initial calculations of the NSTX-U non-inductive current fractions have been done with the TRANSP code, run in a special configuration. The BEtween and Amongst Shot TRANSP (BEAST) system uses data available immediately after the discharge to make TRANSP runs, with the goal of having each run complete before the next discharge is taken. Input data includes the neutron emission, the EFIT01 equilibrium, and the T_e & n_e profiles from multi-pulse Thomson scattering. A uniform Z_{eff} has been assumed, and T_i=1.2T_e is assumed if ion temperature data is not available. The fast ion diffusivity is adjusted via a feedback scheme to provide a reasonable match between measured and calculated neutron emission. The BEAST results provide input for session leaders, such as fraction of non-inductive current drive, thermal confinement, etc., that can be used for deciding on conditions for subsequent shots. However, given these limitations, it is clear that BEAST results are best taken as initial guidance, and not as final answers.

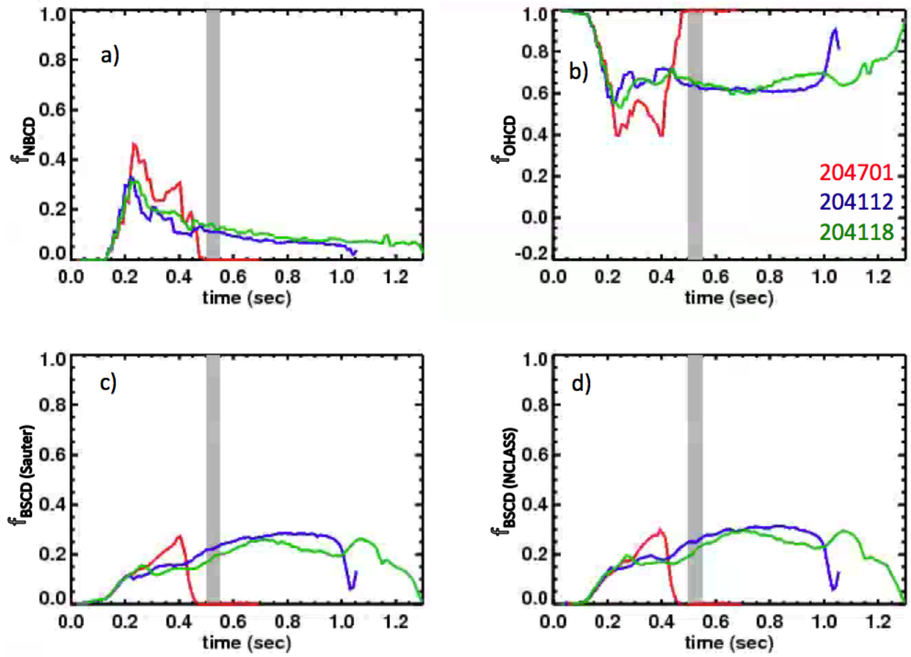

Fig. R16-3-35: *Current drive components for three NSTX-U H-mode plasmas*

Fig. R16-3-34 shows the plasma current waveforms for three discharges to be considered in this section. These are the 900 kA and 1000 kA discharges 204112 and 204118, discussed previously in Fig. R16-3-33, and the 600 kA discharge 204701. The non-inductive current components are shown in Fig. R16-3-35. The neutral beam current drive fraction is shown in frame a). It is as high as 30-40% early in the discharges, but drops to ~10% as the discharges evolve. The Ohmic current drive fractions are shown in frame b). For shot 204701, these are in the vicinity of 0.4-0.5, implying non-inductive current fractions in the range of 0.6 to 0.5. For the higher current discharges, the Ohmic current fractions are around 0.6, implying non-inductive fractions of 0.4. The bootstrap current fractions are shown in the final two frames, where c) shows the calculation from the Sauter model and d) shows the calculation from the NCLASS code. The bootstrap current fractions generally peak at ~30% for these discharge.

Section R16-3-10: Real-time RWM mode identification and feedback algorithms

NSTX had a set of 48 RWM sensors, used to detect non-axisymmetric magnetic perturbations growing on time scales of approximately 1-100 msec. These were digitized both in CAMAC transient digitizers, and with the realtime data stream. The data from these perturbations was processed following the shot using a sophisticated set of processing routines, while a subset of those routines was also coded into the realtime analysis.

For NSTX-U, this system was reconstituted and upgraded, with the new realtime mode identification algorithm incorporating virtually all of the offline analysis procedures. In particular, a series of equations were added to the sensor processing routines, to remove pickup due to vessel eddy currents; these have been present in the off-line analysis code for more than a decade, but were not in the realtime compensation code until this year. When combined with the AC compensation for the SPA currents added in 2010 and the original direct pickup compensations, all the major off-line compensations are now available in the realtime code. These upgrades to the realtime algorithm facilitate more accurate realtime mode identification and feedback. This is visible in Fig. R16-3-36, where the realtime and offline codes have virtually identical phase and amplitude response for B_P (left) a B_R (right) mode identification. Though the feedback algorithm was not turned on during the run, the mode identification algorithm ran routinely in the

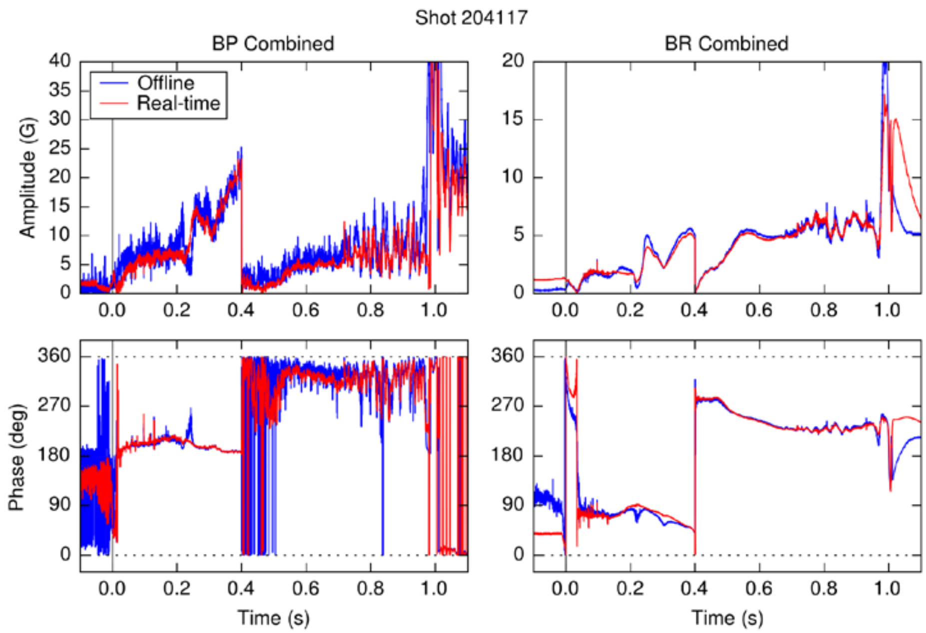

Fig. R16-3-36: *Comparison of offline and realtime n=1 field amplitudes and phases as measured by the B_P and B_R RWM sensor arrays. The realtime calculations shown here were computed in the background but in real time by PCS during Shot 204117. Though the compensation coefficients have been improved since this shot, these data demonstrate the strong matching between the offline and realtime mode identification algorithms.*

background on hundreds of plasma discharges.

The n=1 amplitude and phase are primarily used in the RWM feedback algorithms. These algorithms were upgraded and tested, but were not used before the early termination of the run after 10 weeks.

Section R16-3-11: Other Plasma Control System Improvements

In addition to the plasma control work noted above, some other work has been done, which aids the development of high performance scenarios and in general supports the research program. These activities include:

- The neutral beam powers were brought into the realtime system and properly calibrated, including the nonlinear dependence of the neutralization fraction on acceleration voltage.

- The neutral beam control algorithm from PCS was modified, separating it from the β_N control function. The provisions for grouping beams or controlling them individually was improved. PCS controlled the off-time of the neutral beams on the vast majority of discharges.

- A 4 channel realtime rotation diagnostic, based on charge exchange spectroscopy, was deployed. The data is connected to PCS and is available for future rotation control studies.

- NSTX operated with two high field side puff valves, connected to the plasma by 0.125" diameter tubes. NSTX-U has added two additional puff valves, connected to the plasma by 0.25" diameter tubes. These larger diameter valves have proven valuable for shortening the duration of the gas injection from these valves, which is important for particle control in H-mode scenarios. The 0.125" valve proved to be useful for fueling during long L-mode discharges, where a long, steady flow rate was preferred. The supersonic gas injector (SGI), however, was not installed on NSTX-U during the 10 week run campaign.

- The plasma control system was configured to provide permissives for the Impurity Granule Injector (IGI).

Appendix: XMPs

The machine commissioning activities described in this report were largely conducted as "eXperimental Maching Proposals" (XMPs). These are document written by a single author and reviewed by the Physics Operations branch head (D. Mueller) and the Research Operations division head (S. Gerhardt). Note that the single author in many case is representing a team of researchers all working towards a common goal.

The XMPs run in FY-16 to commission the machine are listed here.

XMP #	Author	Title	Status or Note
101	Battaglia	Breakdown Optimization	Complete
105	Boyer	Software Test for n=0 Control	Complete
106	Myers	Magnetics calibrations	Complete
110	Liu	ssNPA and FIDA Checkout	Partially Complete
114	Podesta	CHERS NB Modulation Study	Partially Complete
115	Boyer	ISOFLUX Commissioning	Complete
116	Battaglia	Initial H-Mode Development	Complete
120	Boyer	Strikepoint Control	Complete
126	Mueller	Ip and R Control	Complete
127	Boyer	Neutral Beam Commissioning	Complete
128	Battaglia	Increase L-Mode Elongation	Complete
130	Lunsford	LGI Commissioning	No
132	Gerhardt	Fast Rampdown Sequence Commissioning	Complete
134	Bell	Ne GDC for Spectroscopy	Complete
137	Battaglia	Increase Ip and Kappa in L- and H- Mode	Complete

138	Boyer	Vertical Control Checkout	Complete
140	Gerhardt	PF-5 Proportional EFC Test	Complete
141	Myers	More PF-5 Proportional EFC	Complete
142	Battaglia	Reduced MHD H-mode Development	Complete
143	Gerhardt	Assess Vessel Conditions	Continuing Activity
144	Gerhardt	NSTX-U Morning Fiducial	Continuing Activity
145	Gerhardt	Flat-Top H-mode Transition Scenarios	Complete
146	Myers	Higher Order Feed Forward EFC in L-Mode	Complete
147	Boyer	Improve L-Mode Fiducial	Complete
148	Kaye	BEAST Validation	Complete
149	Seachrest	MSE-LIF Diagnostic Neutral Beam Testing	Complete
150	Skinner	He Density Scan for Zeff Calibration	Complete
151	Guttenfelder	L-Mode Development in Support of Core and Boundary XPs.	Partially Complete
152	Boyer	Improved rtEFIT and drSEP	Complete
153	Battaglia	H-mode access and control development in boronized wall conditions	Partially Complete
154	Boyer	Inner Gap Control Checkout	Complete

References:

[R16-3-1] M. Boyer, et al, "Real-Time Equilibrium Reconstruction and Plasma Shape Control on NSTX-U", to be submitted to Nuclear Fusion.

[R16-3-2] D. Gates, et al, Nuclear Fusion **46**, 17 (2006).

[R16-3-3] S. A. Sabbagh, et al, Nuclear Fusion **41**, 1601 (2001).

[R16-3-4] S.A. Sabbagh, et al., Nuclear Fusion **46**, 635 (2006).

[R16-3-5] J.R. Ferron, et al., Nuclear Fusion **38**, 1055 (1998).

[R16-3-6] M. Boyer, et al., "Commissioning Upgrades to the NSTX-U Plasma Control System", 43rd EPS Conference on Plasma Physics", 2016.

[R16-3-7] J.E. Menard, et al., Nuclear Fusion **50**, 045008 (2010).

[R16-3-8] J.E. Menard, et al., Nuclear Fusion **52**, 083015 (2012).

[R16-3-9] C.H. Skinner, et al. "Advances in Boronization on NSTX-Upgrade", PSI-22, 2016.

[R16-3-10] J.W. Berkery, et al., Nuclear Fusion **55**, 123007 (2015).

I. Boundary Science Research Highlights

The Boundary Science group consists of three topical science groups (TSGs) including: pedestal physics and control, divertor and scrape-off layer physics, and materials and plasma facing components. Progress in each of these areas is described below.

A. Pedestal Structure and Control TSG Research Highlights

A central goal of the NSTX-U Pedestal Structure and Control TSG is to characterize H-mode access and L-H power threshold, characterize the pedestal structure, understand the turbulence in pedestal and identify common characteristics in phenomenology of different types of edge-localized modes (ELMs), and develop control approaches to improve the plasma performance. Below, we report on recent work undertaken by this group.

1. Energy exchange dynamics across the L-H transition

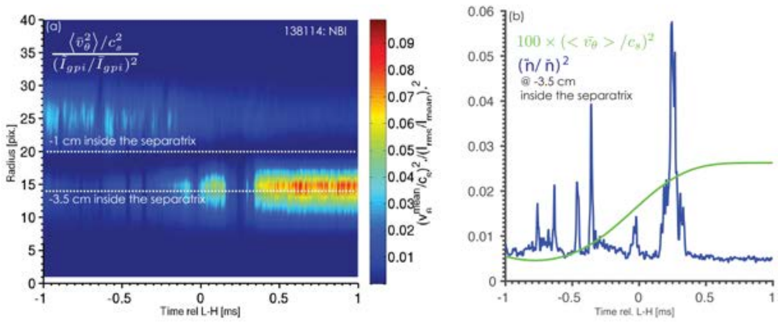

Figure BP-PED-1: *Energy ratio of the kinetic energy to the free thermal energy for the NBI case. (a) Radial profile as a function of the time relative to the L-H transition. (b) Time history at 3.5 cm inside the separatrix of the thermal free energy and 100 times the kinetic energy.*

The energy exchange dynamics across the low-to-high-confinement (L-H) was studied in NSTX discharges using the gas puff-imaging (GPI) diagnostic. The investigation focused on the energy exchange between flows and turbulence at the time of the L-H transition. We applied this study to three types of heating schemes, since L-H transitions exhibit a power threshold. Results show that on average across the database, the poloidal correlation (1 cm inside the separatrix) increases for □ 6.8 to □ 8 cm during the transition to H-mode. The radial correlation length, however, decreases during the H-mode transition. These correlation changes across the L-H transition are consistent with an increase of the edge velocity shear during the L-H transition [BPR-PED-1].

Using a velocimetry approach (orthogonal-programming decomposition), the velocity fields across a 24 × 30 cm GPI view during the L-H transition was obtained with good spatial and temporal resolutions. Analysis using these velocity fields shows that the production term, which is a proxy for the transfer of the energy from mean flows to turbulence or vice-versa, is systematically negative just prior to the L-H transition, which is inconsistent with the predator-prey paradigm [BPR-PED-1]. This is further reinforced when the energy ratio between the kinetic energy in the mean flow to the thermal free energy is observed to be less than 1 (Figure BP-PED-1), suggesting that turbulence depletion mechanism may not be playing an important role in the transition to the H-mode. Finally, an order-of-magnitude analysis showed that the contribution of

Reynolds stress to the mean poloidal flow cannot be excluded. These results span a large database of NSTX discharges to show Reynolds work is too small to directly deplete the free energy in the turbulence across the L-H transition [BPR-PED-1].

2. ELM evolution patterns and 2D imaging

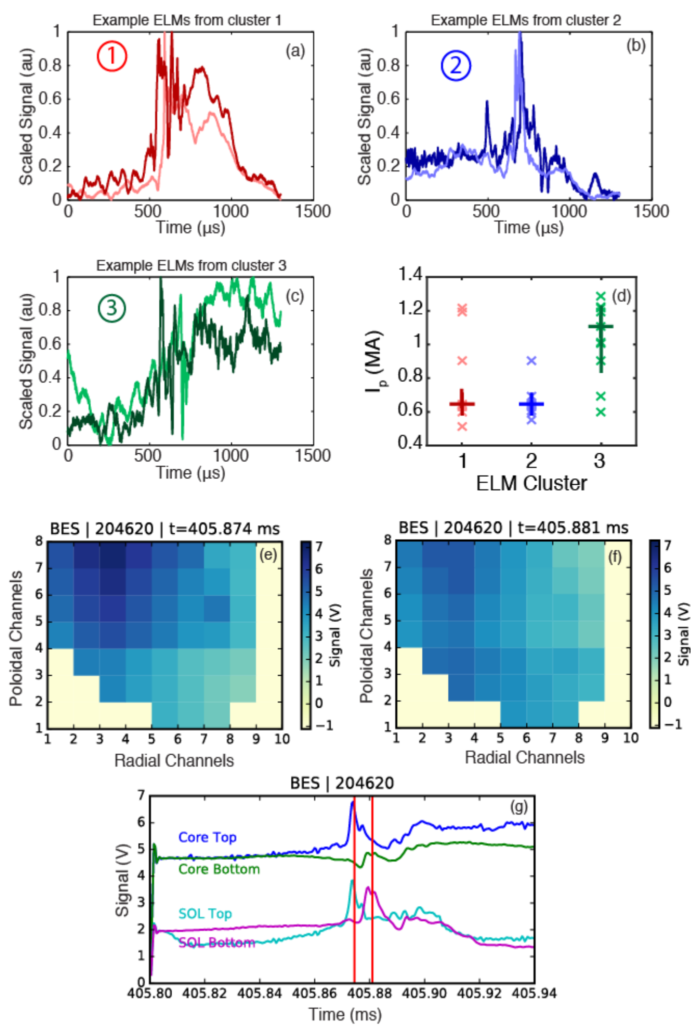

Figure BP-PED-1: *(a-c) Characteristic ELM evolution patterns; (d) plasma current values and ranges for the ELM clusters; (e, f) 2D BES images of an ELM event in NSTX-U; and (g) ELM evolution showing spatial variation*

Characteristic ELM evolution patterns on Alfvenic timescales were identified from beam emission spectroscopy (BES) measurements with unsupervised machine learning techniques, and the evolution patterns correspond to distinct regimes for ELM-relevant parameters [BPR-PED-2, BPR-PED-3]. Figure BP-PED-2, panels a-c show example ELMs for the identified evolution patterns. The variation in evolution patterns suggests that underlying physical mechanisms impact the nonlinear evolution of ELM events. Indeed, Panel BP-PED-2d shows that the identified evolution patterns segregate into low and high current regimes [BPR-PED-2]. The identified evolution patterns and corresponding parameter regimes can contribute to the formulation or validation of nonlinear ELM models, and nonlinear BOUT++ simulations for the observed evolution patterns have begun.

2D measurements of NSTX-U ELM events were obtained with the reconfigured and expanded BES system [BPR-PED-3]. Figure BP-PED-2, panels e-g show the 2D evolution of an ELM event on Alfvenic timescales. In an animated movie of the ELM event, a structure is observed moving down the field of view. The 2D measurements will provide new opportunities to investigate the pedestal dynamics during ELM events.

3. Edge fluctuation observations in ohmic discharges

A quasi-coherent edge mode with frequency ~40 kHz, likely a density fluctuation, is observed in Ohmic plasmas in NSTX using the GPI diagnostic. This mode is located predominantly just inside the separatrix, with a maximum fluctuation amplitude significantly higher than that of the broadband turbulence in the same frequency range. This is the first observation of a quasi-coherent edge mode in an Ohmic diverted tokamak, and so may be useful for validating tokamak edge turbulence codes [BPR-PED-4].

4. Transport analysis of highly-shaped discharges with lithium coating

Previous analysis showed that the discharge performance improved substantially in NSTX with increasing pre-discharge lithium evaporation, in both moderately shaped [BPR-PED-5, BPR-PED-6, BPR-PED-7] and strongly shaped [BPR-PED-8] plasmas. To quantify this effect, a sequence of H-mode discharges with increasing levels of pre-discharge lithium evaporation ('dose') with high triangularity and elongation boundary shape, and without inter-discharge helium glow discharge conditioning, was analyzed with the SOLPS edge transport code [BPR-PED-9]. Globally, energy confinement increased, and recycling decreased with increasing lithium dose, similar to the previous lithium dose scan in medium triangularity and elongation plasmas. Data-constrained interpretive modeling with SOLPS quantified the edge transport change: the electron particle diffusivity decreased by 10-30x (Figure BP-PED-3). The electron thermal diffusivity decreased by 4x just inside the top of the pedestal, but increased by up to 5x very near the separatrix. These results provide a baseline expectation for lithium benefits in NSTX-U, which is optimized for a boundary shape similar to the one used in this experiment.

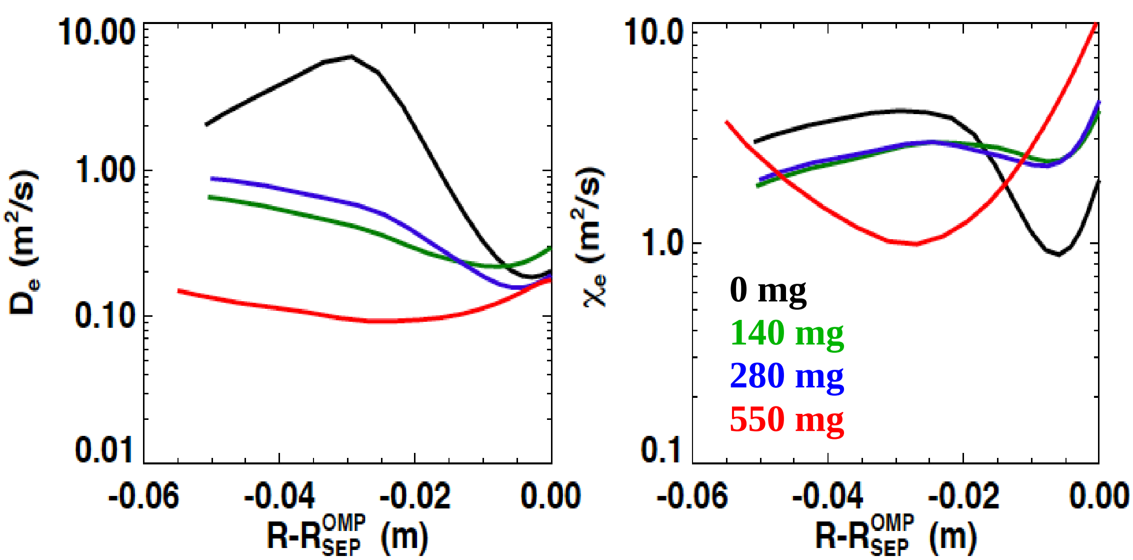

***Figure BP-PED-3**: (a) effective electron particle diffusivity D_e and (b) electron thermal conductivity χ_e vs. distance from the separatrix at the outer midplane. The lithium evaporation dose is indicated.*

5. Effect of NBI power on edge stability in highly-shaped NSTX discharges

Studying the effect of neutral beam injected power (P_{NBI}) on plasma edge profiles and magnetohydrodynamic (MHD) stability is central to the understanding of ELMs. An undergraduate student participating in the Science Undergraduate Laboratory Internships (SULI)

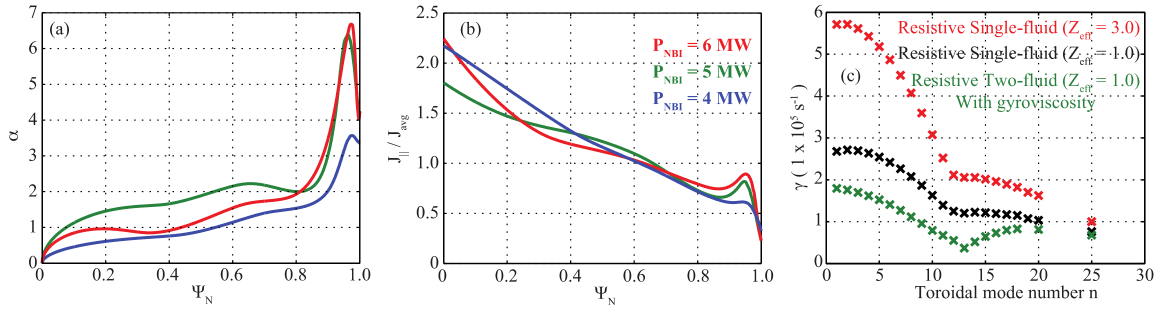

Figure BP-PED-4: *Effect of NBI power level (a) MHD α as a function of normalized poloidal flux; (b) normalized parallel current density as a function normalized poloidal flux; (c) growth rate vs toroidal mode number for different resistivity values.*

program studied the effect of P_{NBI} on the plasma kinetic profiles and edge stability, under the tutelage of NSTX-U scientists. The analysis was performed using the Pedestal Analysis toolkit developed by Dr. T.H. Osborne from GA, and was based on three NSTX H-mode discharges with I_P = 1.0 MA and P_{NBI} = 4 (#132549), 5 (#132547) and 6 MW (#132543), which were the reference boronized highly-shaped H-modes reported in the previous section [BPR-PED-9]. The plasma edge stability was calculated using the ideal MHD code ELITE and the two-fluid resistive MHD code M3D-C[1]. Preliminary analysis shows that the normalized edge pressure gradient, and parallel current density, $J_{||}$ / J_{avg}, for the 5 and 6 MW discharges are comparable, figure BP-PED-4 (a-b). For these two discharges, the ELITE calculations predict that all ideal modes are stable, which is confirmed by the M3D-C[1] calculations which predict that these ELMs are triggered by resistive modes of low toroidal mode number, as shown in figure BP-PED-4(c) for the discharge with P_{NBI} = 6 MW. ELITE also predicts that all ideal modes are stable for the 4 MW discharge and M3D-C[1] calculations for this discharge are still in progress.

6. First look at the H-mode pedestal structure from NSTX-U H-modes

Understanding the underlying physics that controls the H-mode pedestal in tokamak plasmas is an important issue due to its strong impact on the overall plasma performance. A key element for the plasma edge stability and pedestal structure analysis on NSTX is the python-based Pedestal Analysis toolkit, as described in the previous section.

This toolkit has been updated to allow analysis of NSTX-U plasmas, which is now being used to analyze the first NSTX-U H-mode plasmas. As an example, Figure BP-PED-5 (a) shows the equilibrium reconstruction of the NSTX-U H-mode discharge #204118 (I_P = 1.0 MA, P_{NBI} = 5.5

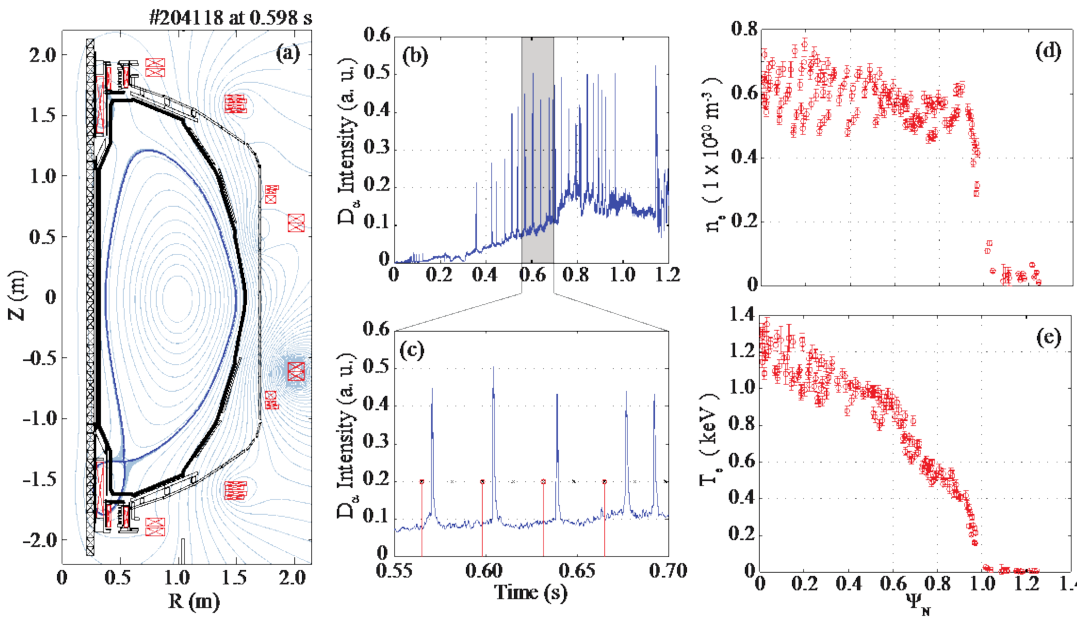

***Figure BP-PED-5**: (a) Example of equilibrium reconstruction of the NSTX-U H-mode discharge. (b) – (c) D_α emission from the lower divertor showing ELMs. (d) Example of ELM-synced density profile from Thomson scattering. (e) Example of ELM-synced temperature profile from Thomson scattering.*

MW, κ = 2.1 δ_L = 0.68 and δ_U = 0.35), with panels (b) and (c) showing ELMs in the D_α emission from the lower divertor. Panels (d) and (e) show the electron density and temperature profiles from Thomson scattering measurements corresponding to the times indicated panel (c). Providing support on the use of this toolkit is an important component of collaboration between GA and PPPL and, during the course of the last year, Dr. G.P. Canal has provided support on the use of the Pedestal Analysis Toolkit to many NSTX-U scientists.

7. Interpretive modeling of ELM stability

a. Pedestal gyrokinetic studies in lithiated discharges

Linear (local) gyrokinetic predictions of edge microinstabilities in highly shaped, lithiated and non-lithiated NSTX discharges [BPR-PED-7] have been performed using the gyrokinetic code GS2 [BPR-PED-10]. It is found that microtearing modes dominate the non-lithiated pedestal top.

The stabilization of these modes at the lithiated pedestal top is a consequence of the electron temperature pedestal extending further inwards, as observed experimentally. Kinetic ballooning modes are found to be unstable mainly at the mid-pedestal of both types of discharges, with unstable trapped electron modes nearer the separatrix region. At electron wavelengths, electron temperature gradient (ETG) modes are found to be unstable from mid-pedestal outwards for $\eta = 2.2$, with higher growth rates for the lithiated discharge. Near the separatrix, the critical temperature gradient for driving ETG modes is reduced in the presence of lithium, reflecting the reduction of the lithiated density gradients observed experimentally.

b. Stabilizing effect of resistivity

Additional analysis of NSTX discharges with lithium conditioning for ELM suppression were conducted with two-fluid resistive MHD [BPR-PED-11], building on the previous ideal MHD stability analysis [BPR-PED-6, BPR-PED-7]. The stabilizing effects of enhanced edge resistivity on ELMs in NSTX H-mode discharges with lithium conditioning were identified for the first time. This new linear stability analysis of the experimentally-constrained equilibrium with the NIMROD code suggests that the change in the equilibrium plasma density and pressure profiles alone due to lithium-conditioning may be insufficient for a complete suppression of low-n peeling-ballooning modes. The enhanced resistivity due to the increased effective electric charge number Z_{eff} after lithium conditioning, mainly from carbon impurity increase, provides additional edge stabilization of current and pressure driven modes. Notably, this stabilizing effect by enhanced edge resistivity became evident only in two-fluid NIMROD simulations.

c. ELM pacing modeling using M3D-C1

M3D-C1 simulations aimed at a better understanding of ELM-pacing by lithium granule injection (LGI) have been performed. A newly implemented ablation model valid for sub-mm Li granules provides a realistic density source, allowing to model granule injections of realistic size and speed in NSTX-U plasmas. We plan to validate the code against experimental data from NSTX-U discharges, specifically the measured granule ablation time, penetration depth and the increase of line integrated electron density. The maximum pressure gradient induced by the LGI scales with the granule size. The injection velocity and angle have to be carefully chosen to reach maximum ablation when the granule is at the top of the pedestal. 3D simulations of granule injections into a pedestal close to marginal stability are used to study ELM pacing efficiency, as a function of injection characteristics, i.e. granule size and speed.

8. Theoretical work on L-H transition physics

Recent work [BPR-PED-12] addresses a popular model for the L-H transition, in which the energy in turbulent fluctuations is directly depleted via Reynolds-stress-induced energy transfer to the zonal flows. Previous experimental attempts to validate this model have used energy balance between zonal flows and nonzonal (turbulent) ExB velocities, concluding that the mechanism was viable. However, the new article demonstrates that parallel electron force balance couples the nonzonal velocities with the free energy carried by the electron density fluctuations, replenishing the turbulent ExB energy until the sum of the two turbulent free energies is exhausted. Since that sum is typically two orders of magnitude larger than the energy in turbulent ExB flows alone, the Reynolds-stress-induced energy-transfer mechanism is likely to be much too weak to explain the rapid turbulence suppression at the L-H transition.

9. Progress on diagnostics enabling pedestal studies in NSTX-U

a. Gas Puff Imaging Diagnostic on NSTX-U

The GPI diagnostic was re-installed on NSTX-U with new zoom optics to search for edge turbulence structure below the ion gyro-radius scale, and with 10x improved sensitivity, due to a new fiber bundle and optical filter. Edge turbulence data was taken at 100,000 frames/sec using background D_α light without a GPI gas puff, which qualitatively showed the expected edge and SOL turbulence and L-H transitions. A gas puff will be needed in for quantitative analysis of further GPI results.

b. 2D Beam Emission Spectroscopy

The BES system, maintained and operated by U. Wisconsin, provides 2D imaging of density fluctuations in the outer plasma and pedestal regions. With Alfven-scale time resolution, the BES system can resolve the fast dynamics of turbulence and instabilities. As described in the Facility and Diagnostics section, an upgrade of the BES system was completed in FY2016. The expansion to 48 detection channels extends the spatial coverage available for experiments, and the 2D reconfiguration of BES sightlines enables 2D imaging and flow field analysis.

c. Development of the pulse burst laser system

Progress was made in the development of the pulse burst laser system, which is slated to provide measurements of the edge pedestal density and temperature evolution on a fast time scale,. The design of the laser system was completed, and a full characterization was performed. The laser is capable of providing 1 J/pulse energies at 30 Hz, 1 kHz over 50 ms, and 10 kHz over 5 ms. Beam profiling in the far field of the laser beam was performed to show that the beam quality is adequate for Thomson scattering for the various operation regimes. Figure BP-PED-6 displays an example of the measured beam profile at 30 Hz repetition rate.

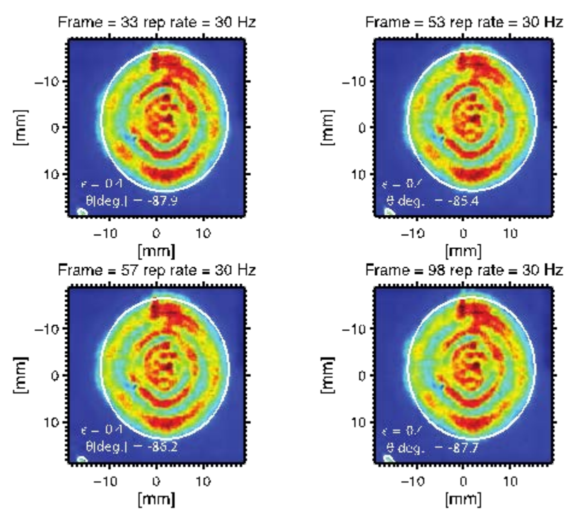

***Figure BP-PED-6**: Example of beam profiles at 30 Hz at four different time slices.*

References

[BPR-PED-1] A. Diallo et al., IAEA-FEC 2016, to be submitted.
[BPR-PED-2] D.R. Smith et al, Plasma Phys. Control. Fusion **58**, 045003 (2016).
[BPR-PED-3] D.R. Smith et al, Invited Talk, 21st Topical Conference on High-Temperature Plasma Diagnostics (2016).
[BPR-PED-4] S. Banerjee, A. Diallo, and S.J. Zweben, Phys. Plasmas **23,** 044502 (2016)
[BPR-PED-5] J.M. Canik et al., Phys. Plasmas **18,** (2011) 056118.
[BPR-PED-6] R. Maingi et al., Nucl. Fusion **52**, 083001 (2012).
[BPR-PED-7] D.P. Boyle et al., Plasma Phys. Control. Fusion **53**, 105011 (2011).
[BPR-PED-8] R. Maingi et al., J. Nucl. Mater. **463,** 1134 (2015).
[BPR-PED-9] R. Maingi et al., Fusion Eng. Des. at press, (2016).
[BPR-PED-10] M. Coury et al., Phys. Plasmas **23**, 062520 (2016)
[BPR-PED-11] D. Banerjee, P. Zhu, and R. Maingi, Phys. Rev. Letts. submitted (2016).
[BPR-PED-12] T. Stoltzfus-Dueck, Phys. Plasmas **23**, 054505 (2016).

B. Divertor and Scrape-off Layer TSG Research Highlights

The NSTX-U divertor and SOL TSG encompasses a range of topics, including e.g. plasma-materials interactions (PMI). This group connects the pedestal TSG and the materials and PFCs TSG, and has some overlap in the areas of research. We have attempted to separate these for the annual report, but overlap is still evident. For organizational purposes, this section is divided into SOL physics, PMI and wall conditioning (including core impurity spectroscopy which falls in the responsibility of this group), and power exhaust. The latter section includes both inter-ELM and ELM heat flux, active management via radiative divertors, and the impact of 3-D fields. The associated topic of innovative divertor design is considered in the final sub-section.

1. SOL Turbulence and Transport

(a) Modeling of turbulence and effect on SOL width

Motivated by recent experimental and theoretical papers [BPR-DSOL-1, BPR-DSOL-2, BPR-DSOL-3], Lodestar, in collaboration with S. Zweben, has undertaken a detailed analysis and modeling of the observed edge turbulence and its implications for the scrape-off layer width. Length and time scales and dimensionless parameters between operational modes including ohmic, low confinement (L), and high confinement (H) modes using the NSTX edge turbulence gas puff imaging (GPI) database [BPR-DSOL-1, BPR-DSOL-2] were compared with theoretical estimates for drift and interchange rates, profile modification saturation levels, and a resistive ballooning condition. Five dimensionless parameters characterizing drift-interchange turbulence in NSTX were obtained and employed to assess the importance of turbulence in setting the scrape-off layer heat flux width and its scaling. An explicit proportionality of the heat flux width to safety factor and major radius (qR) was obtained under these conditions. Quantitative estimates and reduced model numerical simulations suggest that the turbulence mechanism was not negligible in determining the heat flux width in NSTX, at least for discharges with high plasma current, where the heat flux width is smallest. This may have important, and potentially favorable, implications for future high current, large R devices including ITER and spherical tori [BPR-DSOL-4].

(b) SOL blobs in NSTX and NSTX-U

A detailed description of the structure and motion of discrete plasma blobs (a.k.a. filaments) in the edge and scrape-off layer of NSTX was published for representative Ohmic and H-mode discharges [BPR-DSOL-5]. Individual blobs were tracked in the 2D radial versus poloidal plane using data from the GPI diagnostic taken at 400,000 frames/sec. A database of blob amplitude, size, ellipticity, tilt, and velocity was obtained for ~45,000 individual blobs. Empirical relationships between various properties are described, e.g., blob speed versus amplitude and blob tilt versus ellipticity. The blob velocities are also compared with analytic models.

The GPI diagnostic was re-installed on NSTX-U with new zoom optics to search for edge turbulence structure below the ion gyroradius scale, and with x10 improved sensitivity due to a new fiber bundle and optical filter. Edge turbulence data was taken at 100,000 frames/sec using background Dα light without a GPI gas puff, which qualitatively showed the expected edge and

SOL turbulence and L-H transitions. A gas puff will be needed in for quantitative analysis of further GPI results.

(c) Intermittent divertor filaments in NSTX and NSTX-U L-mode discharges

Divertor filaments due to intermittent fluctuations were studied in L-mode discharges in NSTX to understand transport due to edge blobs and their contribution to the divertor particle fluxes. In diverted Ohmic L-mode NSTX discharges, intermittent filaments on the divertor target were imaged via neutral lithium emission with frame rates up to 200 kHz and <1 cm resolution [BPR-DSOL-6]. Broadband fluctuations (frequency spectrum decreasing for $f \geq 10$ kHz) up to 20-50% in standard deviation/mean were observed between $\psi_N \sim 1.02$ and 1.3 (which maps to the low field side limiter), as shown in Figure BP-DSOL-1. Spiral-shaped divertor correlation regions were observed up to $\psi_N \sim 1.02$ and extended for over a toroidal turn as shown in Figure BP-DSOL-2, where the cross correlation between a single pixel and the entire image of lower divertor neutral lithium emission is shown for pixels at two different radial locations. The spiral motion of the filaments at the target, inferred from the evolution of the time-delayed cross correlation, is consistent with a radial and poloidal downward motion upstream, as previously observed in NSTX H-mode discharges [BPR-DSOL-7].

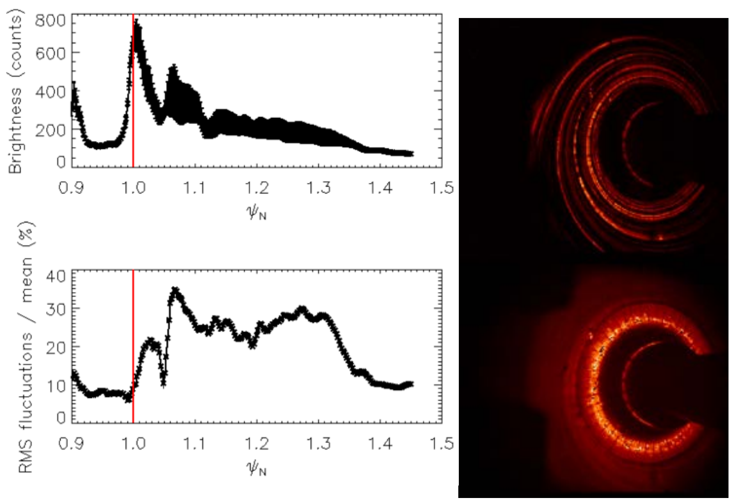

Figure BP-DSOL-1: *Neutral lithium brightness (top) and fluctuation levels(bottom) as a function of divertor radius (left); steady state (right-bottom) and fluctuating (right-top) component of lower divertor neutral lithium brightness.*

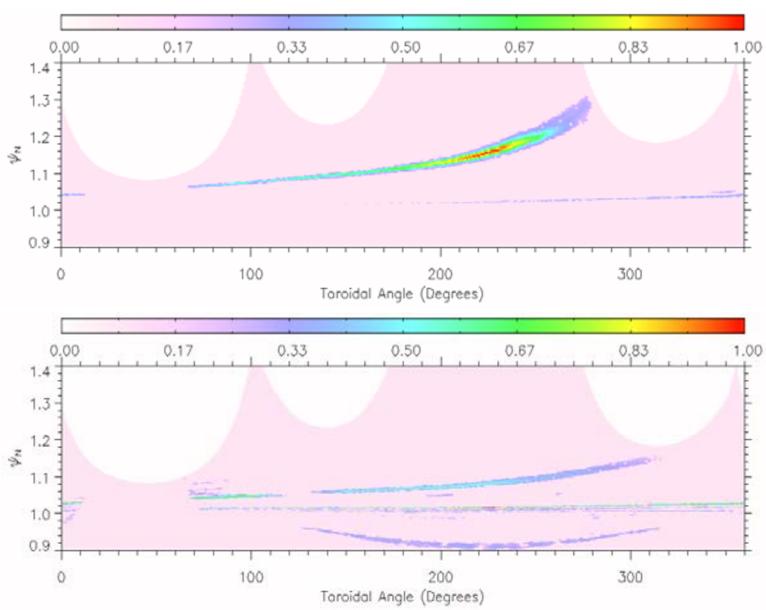

Figure BP-DSOL-2: *Cross correlation between single pixel and entire image of lower divertor neutral lithium emission as a function of toroidal angle and radius for a pixel in the far SOL (top) and a pixel in the proximity of the outer strike point (bottom).*

Fluctuations in neutral lithium emission have zero-delay cross correlation up to 0.8 in value with ion saturation current from divertor Langmuir probes at the same radial and toroidal location. Divertor filaments are correlated with midplane blobs measured by the GPI diagnostic. The cross-correlation with midplane blobs is observed to peak at zero delay at every radius in the region that magnetically connects to the GPI field of view. Cross correlation values between midplane blobs and divertor filaments reach values up to 0.7-0.8 in the far SOL ($\psi_N \sim 1.2$-1.3) and decrease to 0.4 at $\psi_N \sim 1.05$.

In NSTX-U, a more sensitive camera with optimized throughput allowed imaging of divertor turbulence for the first time using C III emission at frame rates up to 140 kHz in NBI-heated lower-divertor-biased double-null L-mode discharges.

Imaging with C III enabled the study of filament dynamics along the inner and outer divertor legs, as opposed to filament footprints on the divertor target typically measured via Li I or D_α. The fast camera field of view is shown in Figure BP-DSOL-4 together with the equilibrium reconstruction of an NSTX-U L-mode discharge. Broadband fluctuations with field-aligned filaments and up to 20% in standard deviation/mean were observed in both the outer and on the inner divertor legs, as shown in Figure BP-DSOL-4 (left). Cross correlation analysis, in Figure BP-DSOL-4 (center, right), shows the absence of correlation of intermittent filaments in the outer leg with filaments in the inner leg. Time-delayed cross correlation of filaments on both the inner and outer leg indicate apparent poloidal motion of the filaments towards the X-point. Toroidal motion is opposite for inner and outer leg filaments and inconsistent with rigid rotation of a flux tube, similarly to recent observations in Alcator C-Mod [BPR-DSOL-8].

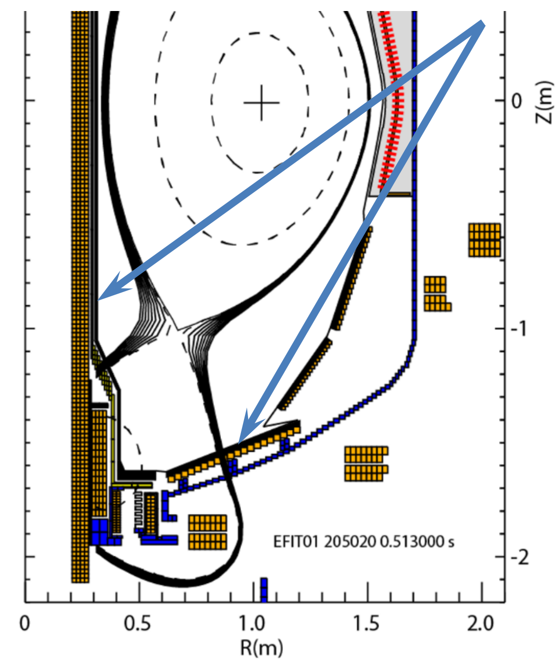

Figure BP-DSOL-3: *Fast camera field of view and equilibrium reconstruction of an NSTX-U L-mode discharge.*

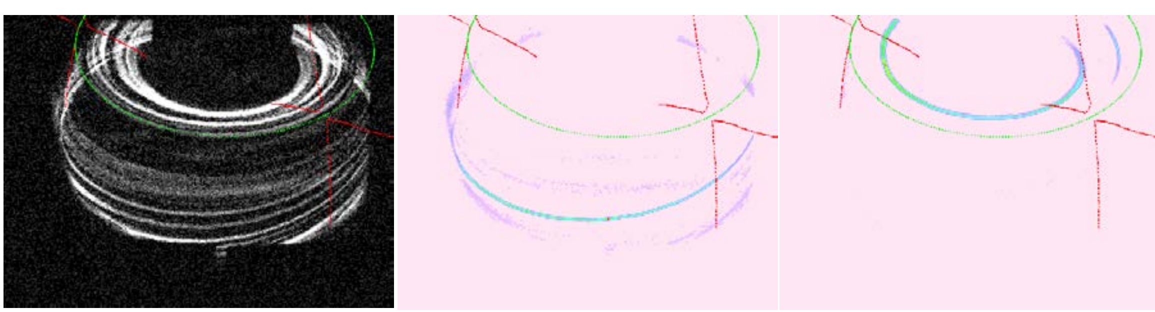

Figure BP-DSOL-4: *Divertor filaments on inner and outer diver imaged via C III emission (left), zero-delay cross correlation regions of pixels in the outer divertor leg (center) and in the inner leg (right). Overlaid in green is the location of the X-point and in red is the last closed flux surface at two different toroidal locations.*

2. PMI, wall conditioning, and core impurity spectroscopy

(a) Toroidal asymmetries in impurity influxes in NSTX

Toroidal asymmetries in divertor carbon and lithium influxes were observed in NSTX, arising from toroidal differences in surface composition, leading edges, externally-applied three-dimensional (3D) fields and toroidally-localized edge plasma modifications due to RF heating. Understanding toroidal asymmetries in impurity influxes is critical for the evaluation of total impurity sources, often inferred from measurements at a single toroidal location. The impact of toroidal asymmetries on the total divertor impurity sources estimates was assessed. The study of toroidal asymmetries was enabled by the full toroidal coverage of divertor impurity emission via two absolutely calibrated fast visible cameras [BPR-DSOL-6].

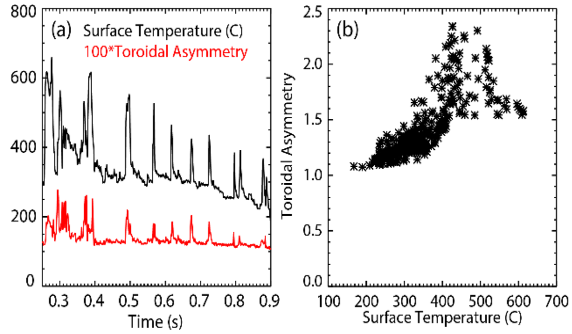

Figure BP-DSOL-5: Time histories of toroidal profile peaking and T_{surf} at the strike point (a); toroidal peaking of neutral emission as a function of T_{surf} at the strike point (b).

Higher divertor lithium influxes were measured in areas with thicker lithium coatings corresponding to regions where evaporation was not shadowed by the center stack. Toroidal asymmetries in lithium influxes only appeared transiently and were not related to the degradation of lithium coatings in regions with lower deposition. Transient asymmetries in lithium influxes were correlated with the radial peaking of lithium emission, large increases (up to 5x) in gross lithium influxes and the surface heating of lithium coatings. A degree of toroidal asymmetry was estimated as the ratio of lithium influxes at two different toroidal locations (with thick and thin coatings, ϕ=80°/ϕ=40°). As shown in Figure – BP-DSOL-5 (a,b), toroidal asymmetries larger than 1 were observed for surface temperatures T_{surf} above the lithium melting point (180°C) and no asymmetries are observed when lithium sputtering was consistent with physical sputtering. Differential heating or different sputtering response of coatings with different

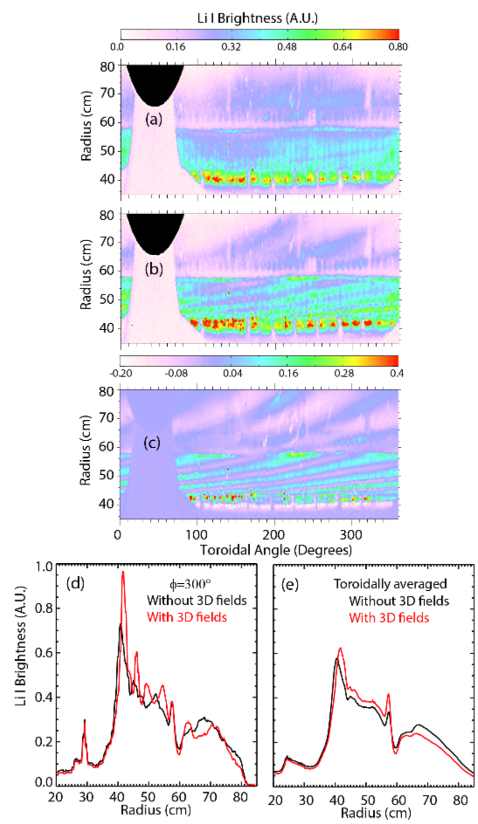

Figure BP-DSOL-6: Lower divertor neutral lithium emission before and during application of n=3 3D fields (a-b); difference between neutral lithium emission during and before application of 3D fields (c); radial profiles of neutral lithium emission at a single toroidal location (d); toroidally-averaged radial profiles of neutral lithium emission (e).

thickness can be the cause of the asymmetries which could lead to inaccuracies in the total source evaluation from measurements at a single toroidal location.

Externally-applied 3D fields led to strike point splitting and helical lobes observed in divertor impurity emission. Toroidal-averaging of helical divertor footprints showed that the impact of non-axisymmetric incident particle fluxes on total sources can be negligible. A lower single null discharge with P_{NBI}=3 MW, I_p=650 kA, q_{95}=8 had blips of $n=3$ fields applied from the midplane resistive wall mode coils (50 ms, 750 A). Footprints of neutral lithium emission at the strike point are shown in Figure BP-DSOl-6 (a-b) before and during application of 3D fields. Typical strike point splitting was observed in Li I emission. The difference in neutral lithium emission during and before the application of 3D fields (Figure BP-DSOL-6(c)) isolates more clearly the perturbation on the divertor fluxes due to the applied fields, showing its periodicity. Local enhancement in impurity influxes at a given toroidal angle (Figure BP-DSOL-6(d)) was on the order of 30-50% at the lobes location. Toroidal-averaging of the radial profiles over 240° (covering two periods of the non-axisymmetric perturbation) enabled the study of the impact of 3D fields on the total divertor particle sources and effectively simulated the rotation of the applied fields. Toroidally-averaged profiles are shown in Figure -(e) before and during application of 3D fields. A redistribution of far SOL fluxes to the near SOL is evident in Figure -(e) but the comparable toroidally-averaged profiles with and without applied fields indicate that while stationary 3D fields could challenge PFCs due to the enhanced local heat fluxes and T_{surf}, they do not seem to significantly affect the total divertor impurity influxes in NSTX.

(b) On the utility of helium wall conditioning before lithium evaporation

Operation in NSTX typically used either periodic boronization and inter-shot helium glow discharge cleaning (HeGDC), or inter-shot lithium evaporation without boronization. The initial deployment of Li evaporation followed inter-shot HeGDC. To assess the viability of operation without HeGDC, dedicated experiments were conducted in NSTX in which Li evaporation was used while systematically shrinking the HeGDC between shots from the standard 10 minutes to zero (in steps from 10min -> 6.5min -> 4min -> 0) [BPR-DSOL-9]. Good shot reproducibility without HeGDC was achieved with lithium evaporations of 100 mg or higher. Evaporations of 200-300 mg typically resulted in very low ELM frequency or ELM-free operation, reduced wall fueling, and improved energy confinement. The use of HeGDC before lithium evaporation modestly reduced divertor D_α by ~ 20% in the outer SOL, but not at the strike point. The main difference occurred between 0 and 4 min HeGDC, i.e. only modest HeGDC duration was needed to reduce the far SOL particle flux. Pedestal electron and ion temperature also improved modestly with increasing HeGDC, suggesting that HeGDC prior to Li evaporation is a useful tool for experiments that seek to maximize plasma performance.

(c) EUV spectroscopy of core impurities

Significant progress has been made to the three core high resolution extreme-ultraviolet (EUV) spectrometers which are dubbed the X-ray and Extreme Ultraviolet Spectrometer (XEUS, 8 – 70 Å), the Metal Monitor and Lithium Spectrometer Assembly (MonaLisa, 50 – 220 Å), and the

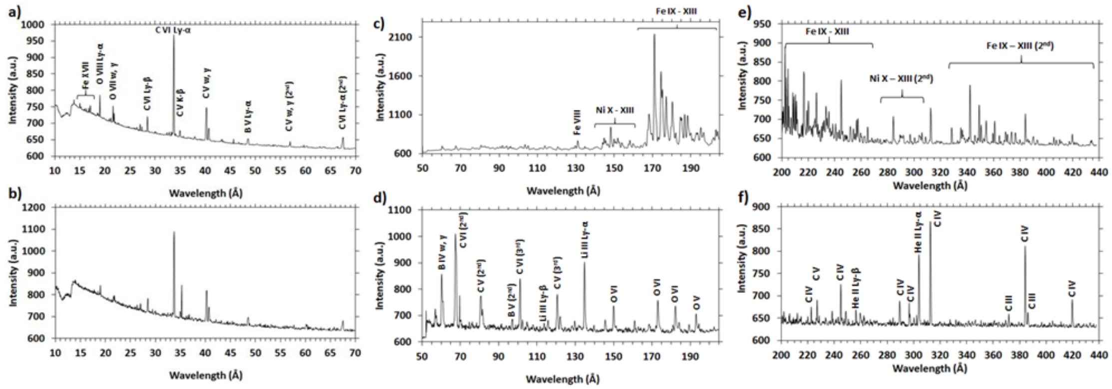

Figure BP-DSOL-7: *Example of spectra taken from NSTX-U shot 205079. XEUS spectra shown for times (a) 0.17 s and (b) 0.73 s. MonaLisa spectra shown for times (c) 0.03 s and (d) 0.73 s. LoWEUS spectra shown for times (e) 0.03 s and (f) 0.73 s. Figures adopted from Ref [BPR-DSOL-10].*

Long-Wavelength and Extreme Ultraviolet Spectrometer (LoWEUS, 190, 440 Å). All three are operational and have collected initial data, which have been presented in Ref [BPR-DSOL-10]. The results include impurity lines from He, Li, B, C, O, Fe, and Ni with temporal resolution below 10 ms and spectral coverage from 8 – 440 Å. The results show that a typical NSTX-U plasma has M-shell Fe and Ni (components of stainless steel) lines radiating in the early phase of the discharge from 10 ms and continuing until the neutral beam injectors turn on, usually after 100 ms (See Fig. BP-DSOL-7). After the Fe and Ni lines disappear the spectra is dominated by C emissions, followed by O, He, Li, and then B. These lines have been used for monitoring impurity levels, assessing wall conditioning techniques, and benchmarking atomic codes.

3. Power Exhaust

(a) Study of ELM heat flux profile evolution and comparison to MHD simulations in NSTX and DIII-D

The behavior of ELM heat flux profile has been experimentally investigated in NSTX and DIII-D and comparison to MHD simulations was made. NSTX ELMs are primarily on the peeling side (n=1-5) and show contraction in most cases, while ELMs in DIII-D demonstrate both broadening and contraction [BPR-DSOL-11]. A pedestal collisionality scan has been performed to look for the relation between heat flux behavior and pedestal stability regime in DIII-D. A linear MHD stability simulation using ELITE showed that heat flux profile in the low collisionality case (ν_e*=0.3) contracts during the ELM, compared to the inter-ELM value, and has the most unstable mode number (n=7-8), close to the kink-peeling boundary (Figure BP-DSOL-8). As the collisionality is increased to ν_e*=0.9, ELM heat flux profile begins to broaden and the operating point moves more toward the ballooning side with most unstable n-number of 12-14. At the highest collisionality of ν_e*=3.5, heat flux profile broadens significantly and the plasma was found completely against the ballooning boundary with most unstable n-number of ~50. A non-linear MHD simulation of ELM heat flux has been also performed using the JOREK code in

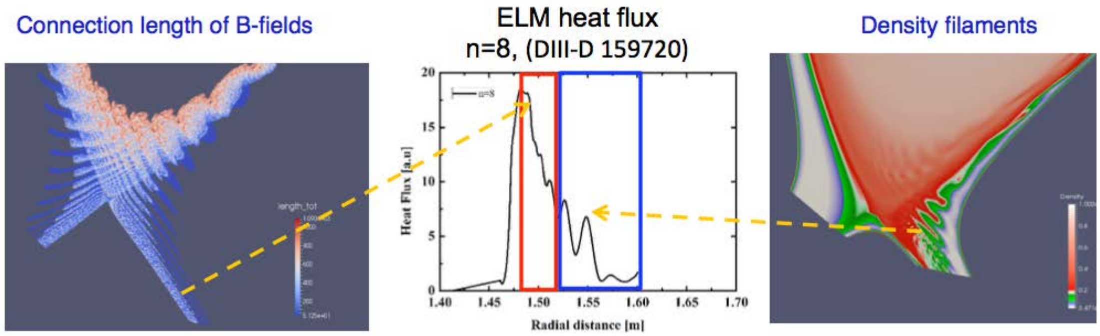

Figure BP-DSOL-8: *Contour plot of poloidal connection length of B-fields (left), density filaments (right), and radial heat flux profile (middle), induced by an ELM for low collisionality case (ν_e*=0.3) in DIII-D. Simulation was done with a non-linear MHD code JOREK.*

order to reproduce the experimentally observed trend in DIII-D. Single-mode run has been the main mode of simulation so far and it revealed that the size of perturbed energies by ELM burst decreases with the increase of n-number and that magnetic energy (W_{mag}) perturbation is closely related to the formation of homoclinic tangles through which heat transport occurs primarily by conduction. On the other hand, kinetic energy perturbation (W_{kin}) is the main contributor to the filament formation through which heat transport takes place mostly by convection. It is found that these two mechanisms also affect different part of heat flux profile; tangles largely on the near SOL region and filaments mainly on the far SOL region. Simulation of ELM heat flux using multi-harmonics of n-number is also in progress.

(b) Inter-ELM and ELM-free divertor heat flux broadening induced by EHO in NSTX

Recent study on multi-machine database of inter-ELM divertor heat flux indicates that the midplane SOL power fall-off length for ITER is expected to be very narrow, which will induce small divertor heat flux width. An Edge Harmonic Oscillation (EHO) is observed to significantly broaden the divertor heat flux and decrease the divertor peak heat flux during certain inter-ELM and ELM-free periods of H-mode operation in NSTX. Figure BP-DSOL-9 shows an example that EHO reduces the q_{peak} significantly by spreading the heat flux distribution. The EHO seems not change the deposited power on the divertor, which indicates the EHO do not enhance the heat transport in NSTX.

The amplitude of the EHO can significant affect the divertor heat flux. Figure BP-DSOL-10 shows an increasing A_{wet} with the n=1 amplitude of EHOs, the data was extracted from the inter-ELM data. An EHO-induced filament around separatrix rotating in the counter-current direction was also observed by gas puff imaging diagnostic. The increased divertor heat flux width might be caused by EHO-induced rotating current filaments.

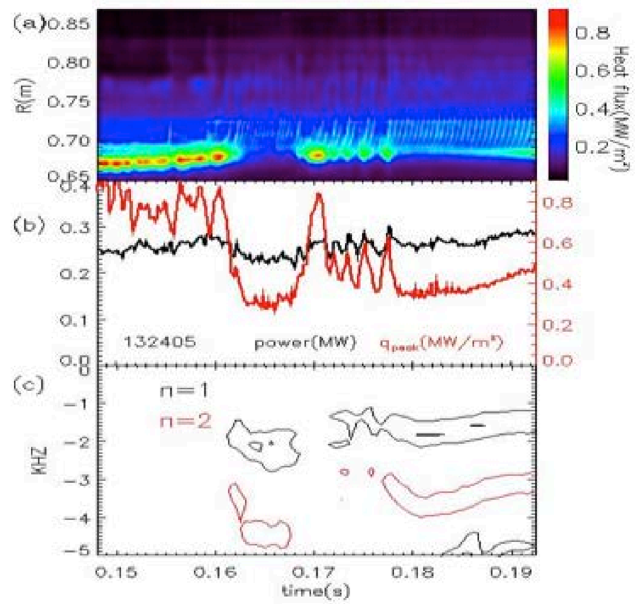

Figure BP-DSOL-9: *Divertor heat flux in (a) ELM-free H mode, (b) deposited power on divertor (black line) and peak heat flux (red line), and (c) magnetic oscillation detected by Mirnov coil.*

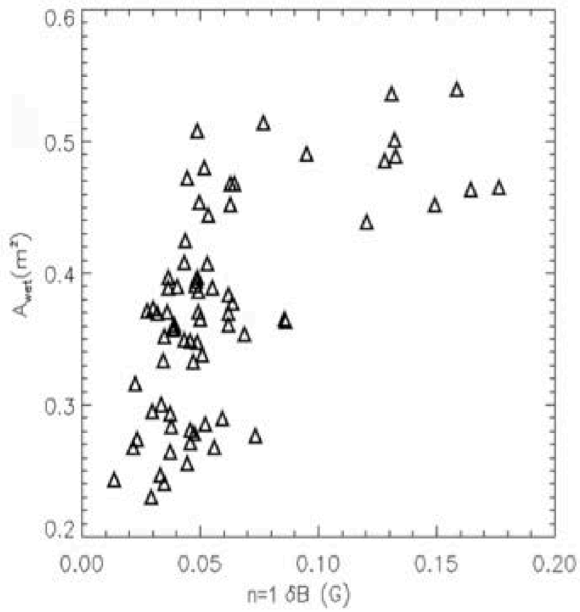

Figure BP-DSOL-10*: Relationship between A_{wet} and the n=1 EHO amplitude.*

(c) Shielding and amplification of non-axisymmetric divertor heat flux by plasma response to applied 3-D fields in NSTX and KSTAR

Recent work in NSTX showed [BPR-DSOL-12] that ideal plasma response from IPEC can significantly shield or amplify vacuum footprints from field line tracing. The spherical tokamak geometry of NSTX enables measurement of divertor footprints with almost full toroidal and radial coverage of lower divertor plates. Figure BP-DSOL-11 shows footprints with n=1 magnetic perturbations in NSTX. Experimentally observed footprint by a wide angle visible camera is illustrated in figure BP-DSOL-11(c). The connection length (L_c) profile for the case of vacuum approximation (blue, figure 1(d)) shows that L_c rapidly decreases only at the very plasma edge (Ψ_N~0.97). This corresponds to the very weak vacuum footprint splitting shown in Figure BP-DSOL-11 (b). However, ideal plasma response dramatically amplifies modeled splitting, see Figure BP-DSOL-11 (a), and this produces a better agreement with the camera image demonstrated in Figure BP-DSOL-11(c). Accordingly, the L_c profile begins to decrease (Figure BP-DSOL-11(d)), in a significantly deeper region, Ψ_N~0.75, which is a consequence of strong amplification of applied n=1 fields. However, for the case of n=3 in NSTX, applied 3-D fields are primarily shielded by ideal plasma response; the shielding effect of resonant fields is greater than the amplification effect of non-resonant fields.

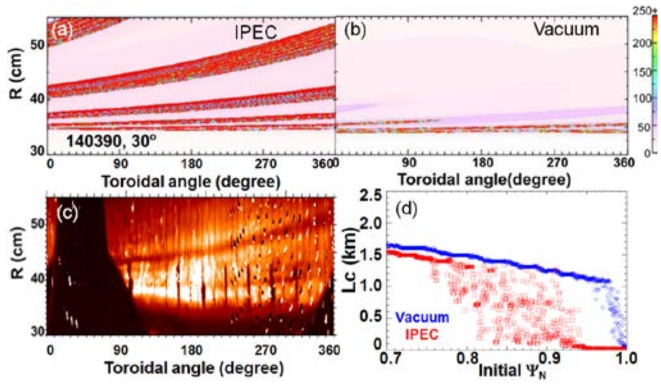

Figure BP-DSOL-11: *Divertor footprints in the presence of applied n=1 magnetic perturbations in NSTX. (a) and (b) are contour plots of connection lengths from field line tracing with and without ideal plasma response, respectively. Plot (c) is the experimentally observed footprint from a wide angle visible camera. Panel (d) shows the profile of connection length for the vacuum (blue) and ideal plasma response (red) case.*

Shielding and amplification of applied 3-D fields has been also observed in KSTAR by ideal (IPEC) plasma response modeling [BPR-DSOL-13]. AC waveforms were used to produce time varying spectrum of 3-D fields that continuously changed alignment with equilibrium pitch. For n=2 perturbations, two distinctive phases were closely examined; resonant (90^o phase) and non-resonant (0^o phase) configurations. It was revealed that deep penetration of applied n=2 fields is inhibited by the shielding effect of resonant components even with kink excitation of non-resonant components in both phases. As in NSTX, non-resonant components of the applied n=2 fields are amplified due to kink excitation, while resonant components are strongly shielded. This shielding effect dominates over the amplification effect of non-resonant fields, producing the end result that the applied n=2 fields are significantly screened. Radial location of lobes in the measured heat flux profile shows better agreement with that from field line tracing when plasma response is taken into account in the calculation. Observed heat flux splitting for 0^o phase is stronger than 90^o. This is consistent with that shielding effect should have been stronger for 90^o due to higher toroidal rotation speed (V_t) as has been observed by CES measurement.

(d) Radiative divertor preparation for NSTX-U

A radiative divertor technique is planned for the NSTX-U tokamak to prevent excessive erosion and thermal damage of divertor plasma-facing components in H-mode plasma discharges with auxiliary heating up to 12 MW. In the radiative (partially detached) divertor, extrinsically seeded deuterium or impurity gases are used to increase plasma volumetric power and momentum losses. A real-time feedback control of the gas seeding rate is planned for discharges of up to 5 s duration. The outer divertor leg plasma electron temperature T_e estimated spectroscopically in real time will be used as a control parameter. A vacuum ultraviolet spectrometer McPherson Model 251 with a fast charged-coupled device detector has been developed for temperature monitoring between 5 and 30 eV, based on the $\Delta n = 0, 1$ line intensity ratios of carbon, nitrogen, or neon ion lines in the spectral range 300–1600Å. A collisional-radiative model-based line intensity ratio will be used for relative calibration, as shown in Figure BP-DSOL-12. Atomic data from ADAS was used in these calculations. A real-time T_e-dependent signal within a characteristic divertor detachment equilibration time of ~10–15 ms is expected.

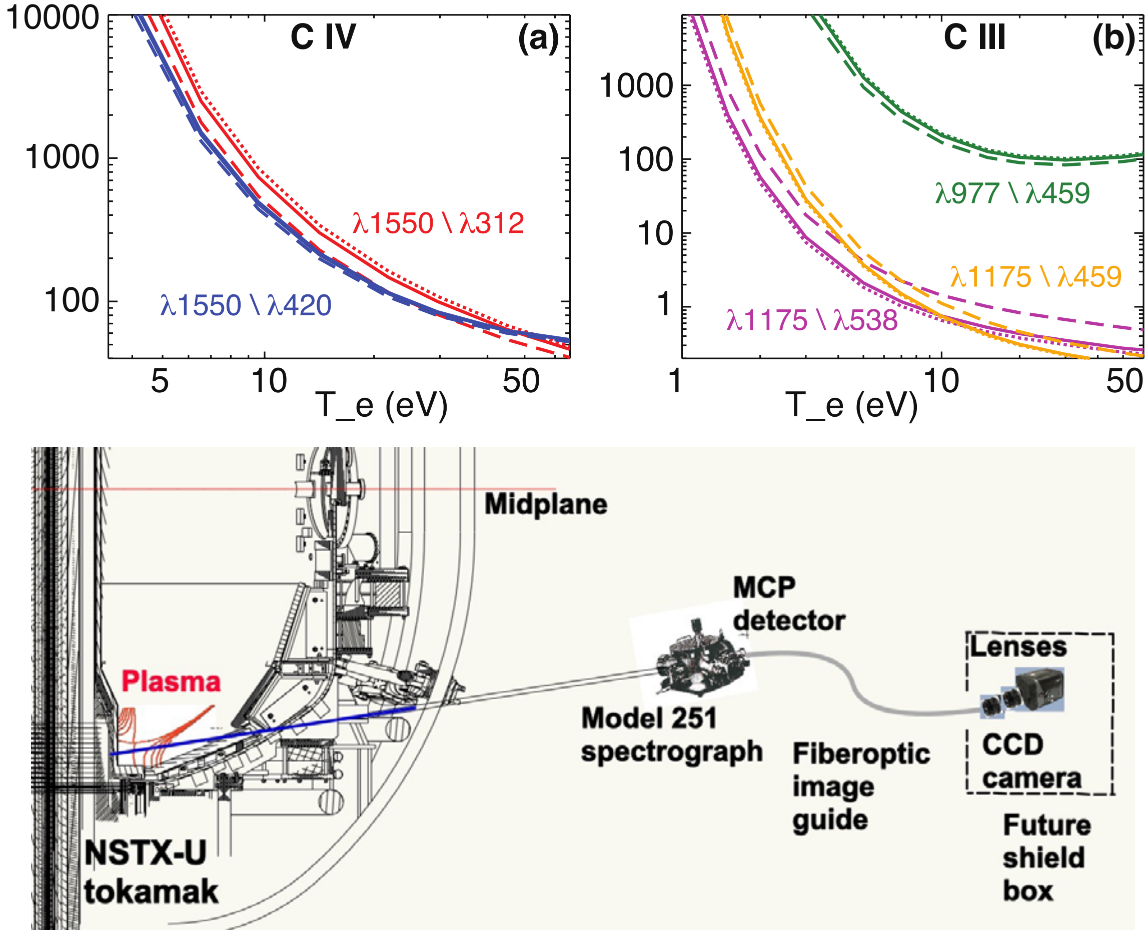

Figure BP-DSOL-12: (a) and (b): sample calculations from a collisional-radiative model for line ratio technique; (c) schematic of layout of detectors to be used in feedback.

(e) Radiative divertor feedback control with visible imaging

Initial measurements towards the implementation of divertor plasma temperature feedback for radiative divertor real-time control were obtained with the new LLNL Vision Research Phantom v1211. Imaging via C III is envisioned for the development of a radiative divertor feedback signal derived from the C III radiation shell position along the divertor leg. The C III emission shell typically sits at electron temperatures on the order of 5-10 eV and its detachment from the divertor target floor has been used as a proxy for divertor detachment in other fusion devices, e.g. DIII-D.

The new fast camera images the lower divertor via a re-entrant horizontal port which provides a radial view of the inner and outer strike points. A schematic of the field of view is shown in Figure BP-DSOL-13, together with the equilibium reconstruction of an NSTX-U H-mode discharge (204117). A 10Gb/s point-to-point connection (copper 10GBase-T) was established with an achieved transfer speed of 3.6 Gbs (over 10 times faster than other fast cameras at PPPL). The achieved transfer speed will allow the transfer of the 256x192 12 bit pixels at a maximum of 4.5 kHz. Initial measurements were performed to establish the imaging of the C III radiation front and the C III emissivity under typical high-triangularity H-mode conditions with an attached outer strike point. An image of the in-vessel PFCs as illuminated by the vessel filaments and an image

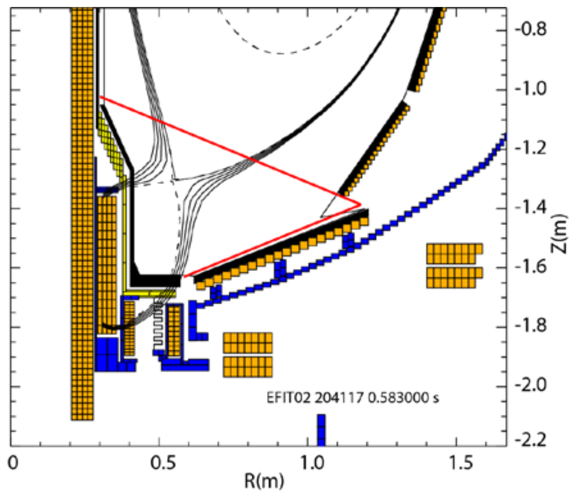

Figure BP-DSOL-13: *Schematic of the divertor control camera field of view and equilibrium reconstruction of a high triangularity NTSX-U discharge (204117).*

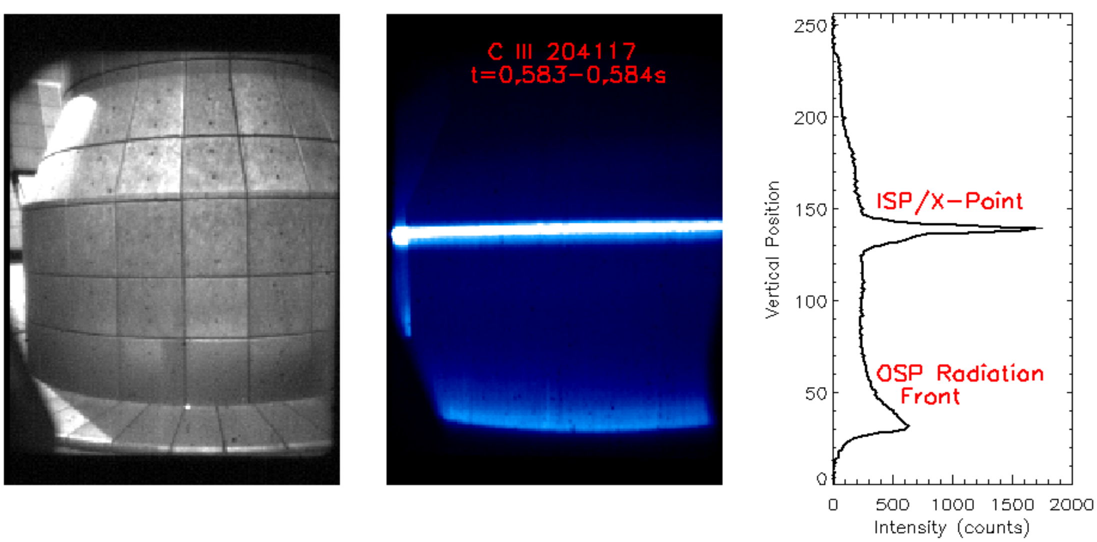

Figure BP-DSOL-14: *NSTX-U divertor as imaged by the divertor control camera and illuminated by the in-vessel filament (left), C III radiation profile averaged over 1 ms in a high triangularity NSTX-U discharge (center), 1D vertical profile of C III emission showing inner and outer strike point C III radiation front.*

of the C III emission (averaged over 1 ms) are shown in Figure BP-DSOL-14 (left and center, respectively). A vertical cut of the C III emission is shown in Figure BP-DSOL-14 (right). Radiation shells at the inner and outer divertor legs can be identified. The optimized throughput allowed imaging with as low as 10-20 μs exposure providing 10 times more light than what needed for the 4.5 kHz acquisition. Behavior of the emission shell during the transition to detachment still needs to be experimentally verified in NSTX-U. Development of the real-time acquisition is envisioned for the next experimental campaign with local analysis of the vertical position of the emission shell which is to be returned to the Plasma Control System.

(f) Kinetic Neoclassical Calculations of Impurity Radiation Profiles

Maintaining tolerable divertor heat loads in ITER and subsequent burning plasma devices will require radiating 80% or more of the total input power. An understanding of the spatial distribution of that radiation in tokamak edge and scrape-off-layer plasmas is needed to ensure the accuracy of such predictions. Existing diagnostic techniques can determine the total radiated power, but only with poor spatial accuracy. The modeling of tokamak impurity transport and radiation carried out to date has been with fluid plasma codes that inherently miss kinetic and non-local neoclassical effects that can be dominant in the steep pedestal region of H-mode plasmas.

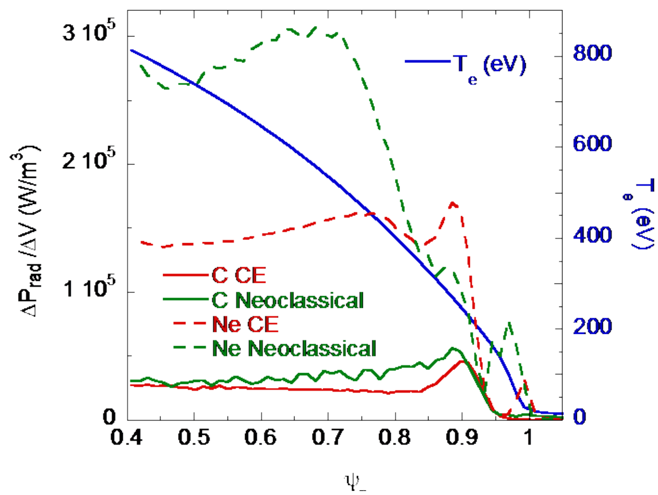

Figure BP-DSOL-15: XGC0 radial profiles of the integrated radiation density as a function of the normalized poloidal flux for the equilibrium (red) and neoclassical cases in runs with carbon (solid) and neon (dashed) impurity. These profiles represent the contribution to the total power made by each radial cell in the mesh (DP) divided by its volume (DV). The electron temperature profile is included for reference.

To fill this need, the drift-kinetic, particle-in-cell transport code XGC0 has been extended to resolve the individual charge states of two impurity species and to compute the associated radiation and electron cooling [BP-DSOL-14]. Generalized collisional radiative ionization and recombination rates from the ADAS [BP-DSOL-15] database are used to evolve the impurity charge state distributions in time. To verify the algorithm, the approach to coronal equilibrium starting from singly charged carbon ions was demonstrated using plasma profiles from NSTX H-mode shot 139047 at 580 ms [BP-DSOL-16]. For this test, the electron profiles were held fixed and all other physical processes were disabled. The radiated power profile evolved in time in the expected manner and approached the analytic value determined directly from the ADAS rates.

Neoclassical effects were then individually activated in a series of subsequent simulations so that their impact on the radiated power could be quantified. For finite orbit width, orbit squeezing, X- and orbit-loss, and neutral recycling the consequences were modest and transitory. Only turning on Fokker-Planck collisions had a long-term effect. First, the collisions moved ions from confined to loss orbits, resulting in a steady source of recycled neutrals. Second, the collision driven inward pinch pushed non-stripped ions further into the core, leading to an increase in the radiated power there relative to coronal equilibrium, as shown in Figure BP-DSOL-15 for carbon and neon.

(g) Non-Maxwellian kinetic corrections

A method to compute kinetic corrections to analytic non-Maxwellian distribution functions has been documented [BPR-DSOL-17]. A simple analytic formula (called the interpreted non-Maxwellian distribution function, INMDF) has been introduced for the description of localized super-thermal tails. From this INMDF, velocity phase space integrals are computed and evaluations of the effects of super-thermal tails are shown for the secondary electron emission, the characteristic curve of the Langmuir probe and the entropy. Many results are shown but the most important one relevant to NSTX-U is the following. There is a direct application on the interpretation of NSTX-U Langmuir probes data in presence of kinetic effects. Indeed, instead of using the ad-hoc diffusion parameter in the Langmuir probe formula, we can fit the best INMDF which recovers experimental data. A future application of the INMDF is the observation of non-Maxwellian electrons from Thomson scattering system, which will be upgraded in FY2017.

Physical interpretation of the simplest INMDF

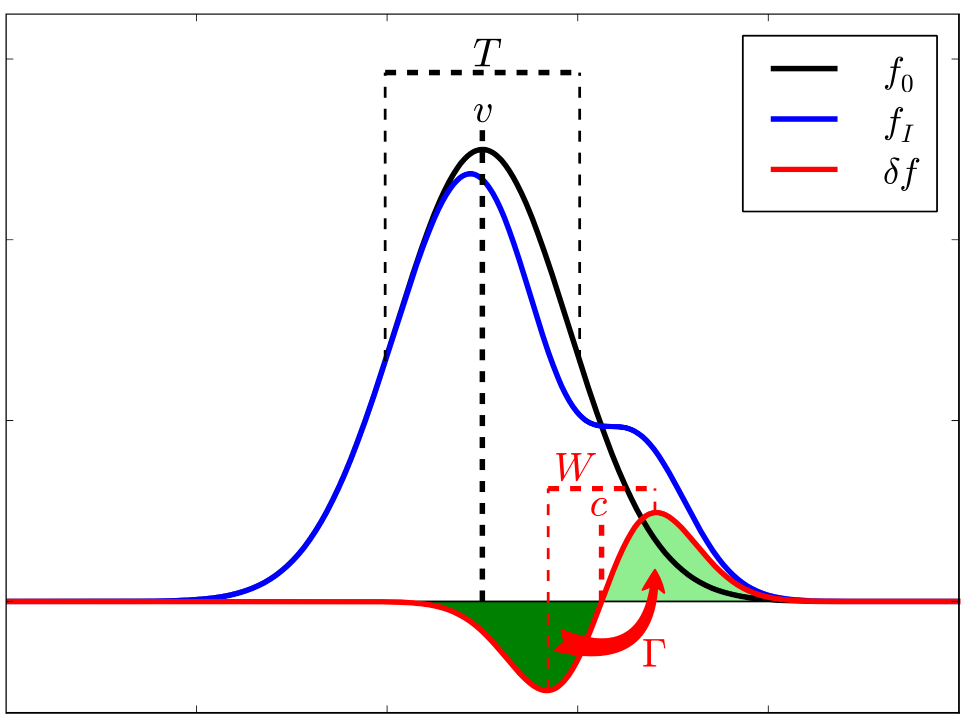

Figure BP-DSOL-16: *Schematic representation of how to interpret non-Maxwellian kinetic corrections.*

4. Advanced divertor projections

(a) NSTX-U snowflake divertor simulations with UEDGE:

Understanding of power exhaust and divertor geometry is required for finding operational regimes of NSTX-U with lower heat flux on divertor plates. The state-of-the-art fluid code UEDGE, which simulates edge plasmas with neutrals and impurities, has been extended to include different magnetic geometries. A robust grid generator Gingred for various snowflake and double-null geometries has been built externally to UEDGE, but allowing UEDGE simulations on these advanced grids. The main advantage of Gingred is to simplify and standardize the grid generation independently of the UEDGE convergence which can be challenging enough by itself. The capability to constraint the divertor legs of the grid by complex plates geometries has been added as shown in Fig. 1 by the snowflake-minus and snowflake-plus grids for NSTX-U simulated magnetic equilibriums. Artificial plates or NSTX-U walls can be used to study different divertor geometries.

UEDGE converged solutions with a fixed fraction carbon impurity model have been obtained on different snowflake and double-null grids as well as with the full impurity model. The physics interpretation of UEDGE simulations and the scan of some parameters are under progress and will be presented at the 2016 APS conference.

Snowflake-minus grid	Snowflake-plus grid

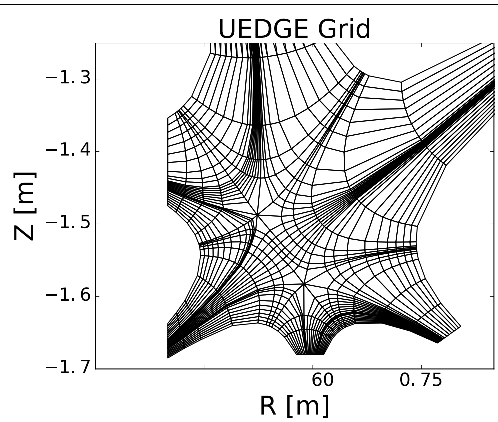

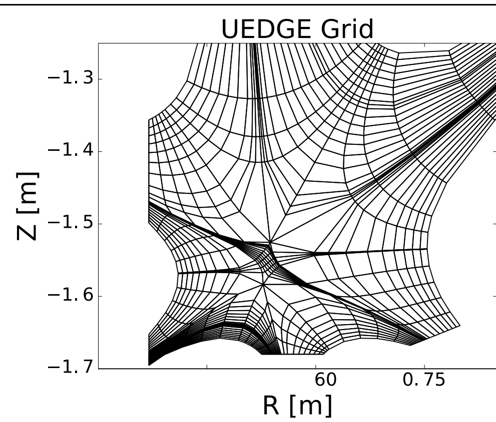

Figure BP-DSOL-17: *Grids used for snowflake divertor calculations with the UEDGE code.*

b) Study of the effect of n = 3 magnetic perturbations on the NSTX-U snowflake divertor configuration

The ELM control coils and the snowflake (SF) divertor configuration are two potential solutions proposed to solve two separate outstanding issues on the path towards self-sustained burning plasma operations. These two solutions have been tested separately in several machines worldwide but, in a reactor, they would have to operate simultaneously. It is, therefore, important to investigate the compatibility between these two solutions and to identify possible conflicts that could prevent them from operating simultaneously.

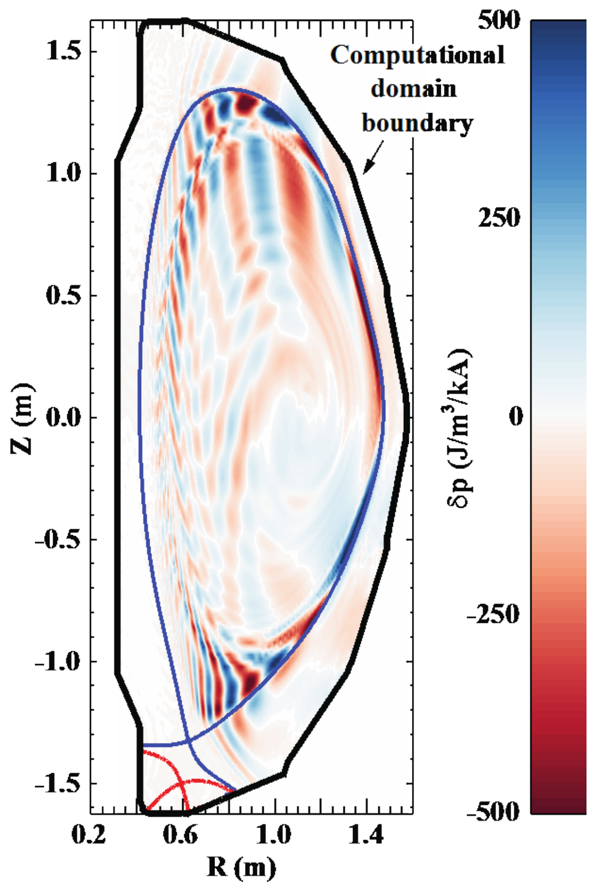

Figure BP-DSOL-18: Perturbation of the plasma pressure due to n = 3 magnetic perturbations from the M3D-C[1] two-fluid plasma response model.

To investigate the impact of applied n = 3 magnetic perturbations on the SF divertor configuration, the two-fluid resistive magnetohydrodynamic code M3D-C[1] was used to estimate the single- and two-fluid plasma responses to these perturbations, Figure BP-DSOL-18. The single-fluid calculations show a significant reduction of the resonant tearing components with respect to the vacuum approach calculations for both SN and SF configurations. In the two-fluid calculations, the tearing components are significantly reduced in the plasma edge and significantly amplified in the region of low electron rotation perpendicular to the magnetic field. The differences between the single- and two-fluid plasma responses are mainly caused by the different screening mechanism of these two plasma models. While the screening of resonant magnetic perturbations (RMPs) in the single-fluid model is caused by the **E x B** rotation, the screening of RMPs in the two-fluid model is caused by the local electron fluid velocity perpendicular to the magnetic field. The perpendicular electron velocity is found to depend linearly on the magnitude of the poloidal magnetic field. Therefore, the main plasma mechanism for screening in the two-fluid model is weakened in the null-point region. This indicates that perturbations applied by coils closer to the null-point region could have a stronger effect on the ergodization of the edge of SF plasmas and thus cause an enhanced transport in the pedestal region. This suggests that lower values of current in ELM control coils closer to the null-point region would be required to suppress ELMs. This effect is expected to be stronger in the SF configuration due to its lower poloidal field in the null-point region.

In this work, the NSTX-U midplane resistive wall mode, error field correction coils were used to apply the n = 3 perturbations to the plasmas and no significant differences between the SN and SF plasma responses is found. The results show that, independent of the plasma response model used, the SF has more and longer magnetic lobes than those in the SN configuration. The intersection of these longer and additional magnetic lobes with the divertor plates are expected to cause more striations in the particle and heat flux target profiles leading to a larger wetted area and smaller peak heat fluxes onto the PFCs [BPR-DSOL-18].

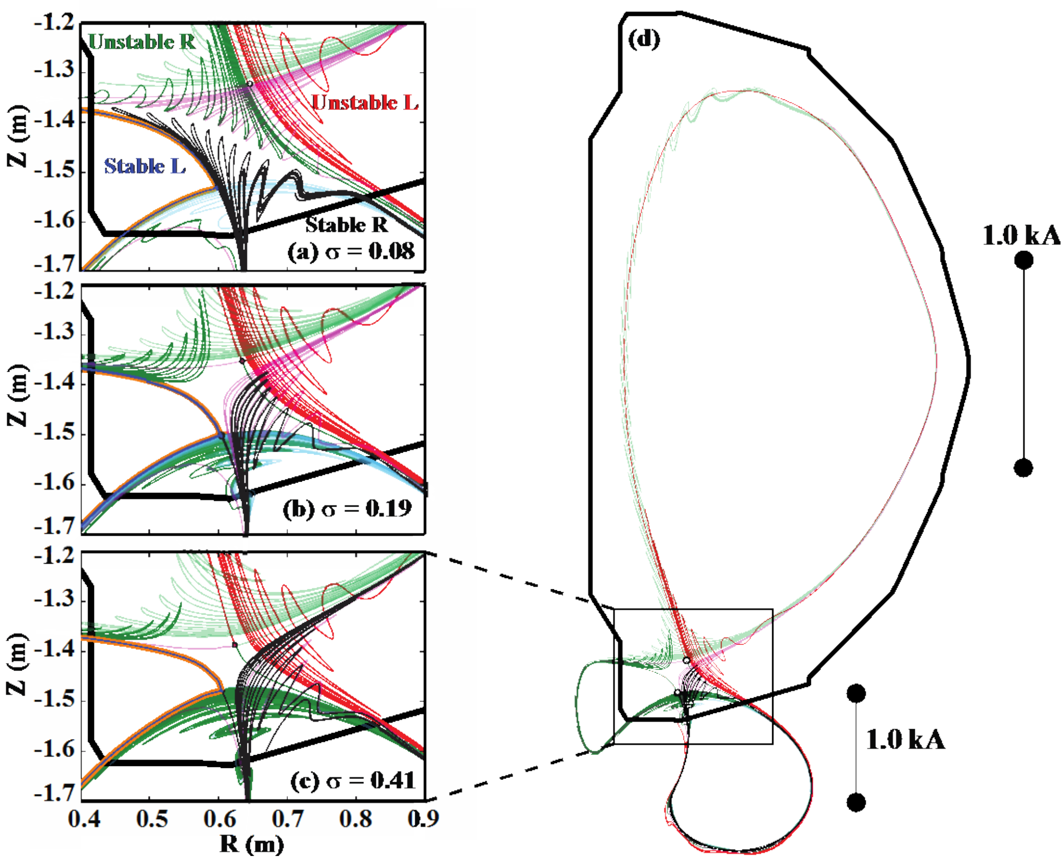

Figure BP-DSOL-19: (a)-(c) stable and unstable manifolds of 3D perturbation to a snowflake configuration; (d) perturbed separatrix – poloidal cut. See text for description.

Another important aspect of this study is the impact of RMPs on the transport in the null-point of the snowflake configuration. As shown in BP-DSOL-19 (a-c), the manifolds associated to the primary (Unstable Left) and secondary (Stable Right) null-points of simulated NSTX-U snowflake plasmas can intersect each other, for sufficiently short distance between null-points, normalized to the plasma minor radius, σ, and enhance the particle and heat transport into the private flux region and additional divertor legs. For this study, the computational domain of the simulated NSTX-U plasma equilibrium had to be extended well beyond the vacuum vessel to include the manifolds entirely, Figure BP-DSOL-19(d). Particle, momentum and energy transport simulations using the code EMC3-Eirene are in progress to investigate this effect of RMPs on the transport in the null-point of the snowflake configuration.

(c) Advanced divertor configuration simulations with the EMC3-EIRENE code

A set of advanced divertor configurations in NSTX-U have been explored numerically with the EMC3-EIRENE code and compared to a standard divertor configuration. A generalization to the classical snowflake configuration (which is based on the magnetic topology without addressing the position of the divertor plates) results in a set of significantly different divertor geometries. The implementation of the magnetic configuration is very flexible in EMC3-EIRENE, which makes this an ideal tool to benchmark different advanced divertor configurations.

Simulation results for the edge plasma density are presented in the Figure BP-DSOL-20, for (a) a standard poloidal divertor configuration (SD), (b) a near exact snowflake divertor configuration (neSF+) and (c) an X-divertor like configuration (XD, which is generated by an asymmetric snowflake minus configuration). All simulations are based on the same input parameters for fuelling rate, heating power and anomalous cross-field diffusion. The simulated peak heat flux is correlated to the flux expansion on the target: we find that the near exact snowflake configuration has a reduced flux expansion with respect to the SD configurations, which results in heat flux peaking by a factor of 3. The XD configuration on the other hand, has an increased flux expansion that allows a mitigation of peak heat load by 40-45 %.

Magnetic perturbations result in the splitting of the separatrix into two distinct branches of helical lobes that guide field lines from the bulk plasma to the divertor targets. The EMC3-EIRENE code allows to address these non-axisymmetric configurations (see Figure BP-DSOL-20, panels d-f below), and it has been found that strong localized flux expansion can mitigate the non-axisymmetric peaking of divertor heat loads [BPR-DSOL-19].

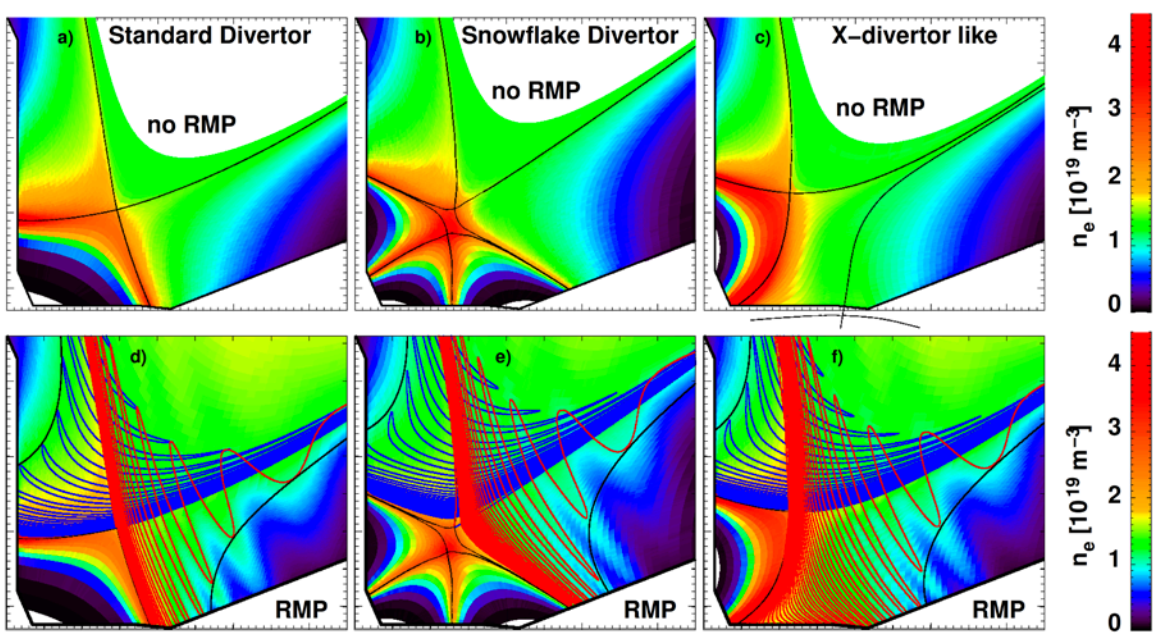

Figure BP-DSOL-20: *Comparison of EMC3-EIRENE simulations of the standard, snowflake, and X-divertor for NSTX-U. Panels (a) – (c) show the equilibria, while panels (d) – (f) show the impact of applied magnetic perturbations.*

References

[BPR-DSOL-1] S.J. Zweben et al., Nucl. Fusion **55**, 093035 (2015).
[BPR-DSOL-2] S. J. Zweben et al., Plasma Phys. Control. Fusion **58**, 044007 (2016).
[BPR-DSOL-3] J. R. Myra, D. A. D'Ippolito, and D.A. Russell, Phys. Plasmas **22**, 042516 (2015).
[BPR-DSOL-4] J. R. Myra, D. A. Russell and S. J. Zweben, submitted to Phys. Plasmas (2016).
[BPR-DSOL-5] S. J. Zweben et al., Plasma Phys. Control. Fusion **58**, 044007 (2016).
[BPR-DSOL-6] F. Scotti, A. L. Roquemore, and V. A. Soukhanovskii, Rev. Sci. Instrum. **83**, 10E532 (2012).
[BPR-DSOL-7] R.J. Maqueda and D.P. Stotler, Nucl. Fusion **50**, 075002 (2010).
[BPR-DSOL-8] J. Terry et al., submitted to Nucl. Mater. Energy (2016).
[BPR-DSOL-9] R. Maingi et al., submitted to Nucl. Mater. Energy (2016).
[BPR-DSOL-10] M.E. Weller et al., Rev. Sci. Instrum. **87**, *at press* (2016).
[BPR-DSOL-11] J-W. Ahn et al., submitted to Nucl. Mater. Energy (2016).
[BPR-DSOL-12] K. Kim et al., Plasma Phys. Control. Fusion **57** 104002 (2015).
[BPR-DSOL-13] J-W Ahn et al., KSTAR Conference 2016, Daejeon, Korea, February 24 – 26, 2016.
[BPR-DSOL-14] D.P. Stotler et al., submitted to Nucl. Mater. Energy (2016).
[BPR-DSOL-15] H. P. Summers, "The ADAS User Manual, Version 2.6", http://www.adas.ac.uk.
[BPR-DSOL-16] A. Diallo et al., Nucl. Fusion **53**, 093026 (2013).
[BPR-DSOL-17] O. Izacard et al., Phys. Plasmas **23**, 082504 (2016).
[BPR-DSOL-18] G.P. Canal et al., "Study of the plasma response to $n = 3$ magnetic perturbations in the NSTX-U snowake divertor", Nucl. Fusion 2016, submitted.
[BPR-DSOL-19] H. Frerichs et al., *Phys. Plasmas* **23**, 062517 (2016).

C. Materials and Plasma-Facing Components TSG Research Highlights

The Materials and PFC (M&P) research program on the NSTX-U exists to perform the critical research needed to address the fundamental question of what materials are suitable to a fusion plasma experiment and, eventually, a fusion power plant. In the context of the NSTX-U program, this practically means gaining an understanding of the existing materials and wall-conditioning techniques (carbon plasma-facing components (PFCs) + boronization and lithiumization) in use in the machine so that incremental upgrades to reactor-relevant systems (e.g. high-Z tungsten/molybdenum and flowing liquid lithium) will provide the greatest knowledge gain and minimize the operational learning curves.

The research program in M&P has been divided into three main thrust areas: surface science to support long-pulse operation, tokamak induced material migration, and vapor-shielding physics. Each of these thrusts addresses needs of both solid and liquid PFCs with-respect to future power-producing reactors.

Numerous research updates are described below, related to the M&P TSG. The FY 2016 run campaign has featured measurements and new results from the MAPP diagnostic, as well as spectroscopic analyses of PFC evolution. These diagnostic systems have enabled new studies of boronization and will enable similar examinations of lithium wall conditioning in future run campaigns. Significant progress has been made in the theory and modelling of these complex surfaces and chemical environments and this is also detailed below in contributions describing fundamental molecular-dynamics simulations and whole-machine modelling.

Looking beyond the current run year, the M&P TSG is preparing for future upgrades with the development of new diagnostics, new actuators and new PFCs. The spectroscopic coverage of the machine will be supplemented in the upper divertor and campaign-integrated erosion measurements will be made possible with novel implanted-depth markers. The Granule Injection system has been tested and installed and is ready to examine the effect of in-situ impurity injection on the material surfaces in the machine. Much of this effort is conducted to support the future upgrades to a high-Z machine. The first phase of this multi-step upgrade process is to replace a single, continuous row of tiles in the outboard divertor of NSTX-U. The PFCs for this upgrade have been designed and fabricated in this past year and will eventually enable more reactor-relevant studies to progress in the NSTX-U. Technical highlights are now discussed.

1. First Material Analysis and Particle Probe (MAPP) measurements on NSTX-U

a. Pre-run and early run work summary

The Materials Analysis and Particle Probe (MAPP) was installed on NSTX-U on June 2015. The MAPP was set up for X-ray Photoelectron Spectroscopy (XPS) measurements in October 2015, with data from the first boronization in NSTX-U obtained later that month.

During the campaign, MAPP carried two ATJ, one TZM and one Au samples, the latter used for energy calibration. One of the ATJ samples remained on the samples holder through the whole campaign, and it will be used for post-mortem studies at the University of Illinois. The remaining samples were replaced several times in the campaign for offline laboratory studies and the evaluation of reproducibility in separate sample exposures throughout the run.

b. Methodology

When new samples were installed, baseline XPS data were collected. The samples were then exposed to boronization in NSTX-U, and an additional XPS data set was collected. The samples were then inserted for exposure to one day worth of plasma fluence. A set of XPS data was collected at the end of each plasma operations day. This methodology of data collection improved the time resolution by two orders of magnitude compared with earlier PFC diagnostic methods, i.e., one day instead of months between the start and end of an experimental campaign.

c. General chemical behavior description ATJ graphite

Figure BP-MP-1 shows a summary of the evolution of the surfaces of one of the ATJ samples from its baseline to after several days of plasma exposure. The untreated ATJ sample, labeled "-2" in Fig. BP-MP-1, shows a dominant C1s peak where the C-C interactions are the majority. The sample at this point was almost 90% carbon, the remaining percentage being oxygen. After boronization ("0" in Fig. BP-MP-1), the oxygen concentration dropped below 5%, as did the carbon, decreasing to 57%. The boron concentration was over 30% for all the boronizations.

With exposure to the plasma, the oxygen concentration increased as the days progressed as shown by Fig. BP-MP-1 (a). This oxidation can also be seen in Fig. BP-BP-MP-1 (c), where the B-O component increased its area while the B-B and B-C components decreased. Additionally, the B-C interaction in the C1s panel decreased, which could be evidence of sputtering and material migration.

In the final day before a new boronization, i.e., corresponding to the traces labeled "12" in Fig. BP-1, the oxygen total peak is the largest, while almost all the area of the B1s envelope belongs to the B-O bonds. That day, the oxygen concentration was close to 20%, while the boron dropped to 21% and the carbon was 59%. A similar behavior was observed for all of the boronizations in which a full d-TMB bottle was used.

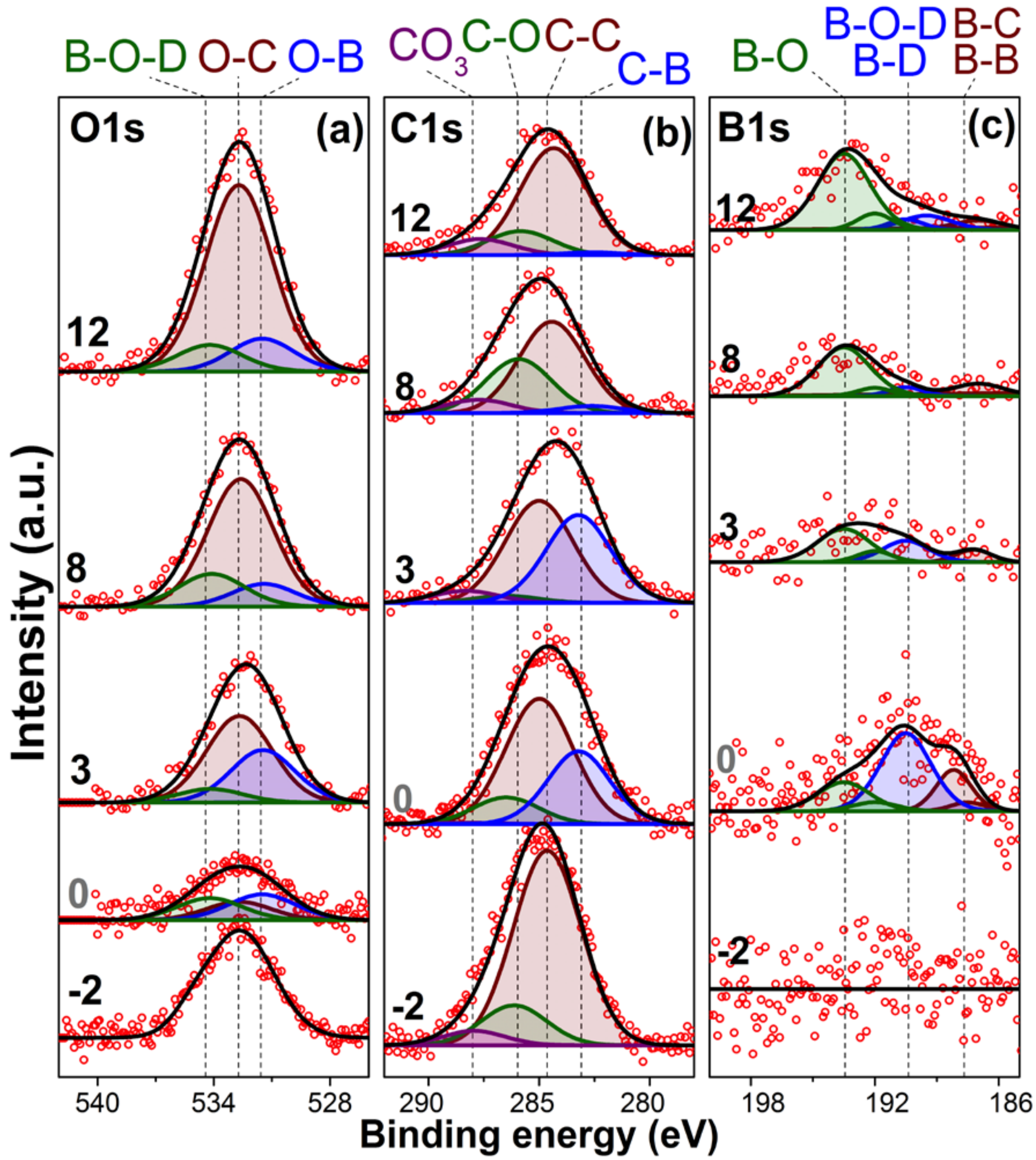

Figure BP-MP-1: *XPS peaks deconvolution for three region scans of boronized graphite exposed to NSTX-U plasmas over 12 days. The labels represent days after boronization. The traces with the label "-2" are the ATJ graphite baselines.*

d. Plasma performance investigation

The correlation of PFC conditioning with plasma performance was investigated during boronization. The overall variation on plasma behavior observed through a campaign can be attributed to many different reasons; this is particularly true in the FY16 campaign, since it encompassed the start-up of NSTX-U. It was clear, however, that the machine performed better shortly after boronization.

The boronization applied on March 26 provided a great opportunity to investigate this correlation. Figure BP-MP-2 shows a summary of the plasma performance and the PFC modification during the same dates.

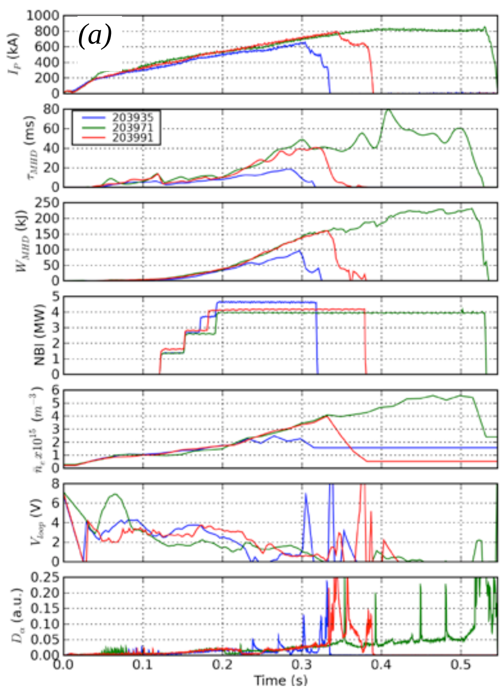

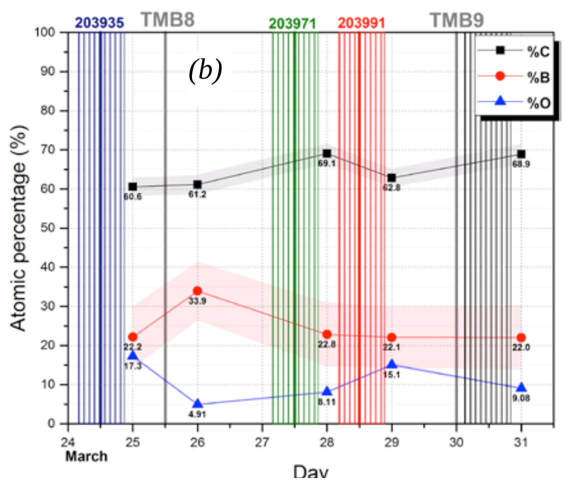

***Figure BP-MP-2**: a) Plasma performance for three different discharges on three different days 203935 pre-boronization, 203971 shortly after boronization and 203991 after boronization and plasma exposure, b) Shows the concentration measured with XPS following those discharges and following boronization on March 26.*

The plasma shot 203935 was chosen to represent the discharges before boronization; the last boronization had been performed five days prior to that day. It can be seen in Fig. BP-MP-2b) how the oxygen concentration on the ATJ sample was relatively high compared with freshly boronized samples (>5% as mentioned above). Relatively poor performance was observed under these conditions, with the lowest plasma current, stored energy, electron average and electrons average density.

A full bottle boronization was performed on March 26, the oxygen concentration after the conditioned dropped to 4.91% as customary after the procedure. Plasma operations resumed on March 27; shot 203971 occurred on that date. As Fig BP-MP-2a) shows, the performance of this discharge is the best out of the three shots on the figure. The pulse duration almost double that of 203935, while the confined energy and density almost tripled. At the end of this day, XPS shown an increase in the oxygen concentration, yielding a value of ~8.1%.

Further observations on the effect of the oxygen concentration on the plasma were done on March 29. Shot 203991 was selected as a representative shot. As shown in Fig BP-MP-2a, the pulse duration, confined energy and density were lower than that of 203935. These values, however, did not dropped as low as the those registered in 203971. Consistent with the trend of lower oxygen percentage leading to better performance, the concentration registered at the end of the day on March 29 was between the values measured on March 25 and 26, yielding ~15%.

The injected beam power was almost the same for the discharges described. Although this parameter usually greatly influences plasma performance, the fact that it stayed almost constant over the dates in discussion allowed a more controlled investigation of the effect of PFC conditioning on the plasma. It is also worth mentioning that the target requests for plasma shape and control were similar.

e. Analysis of high Z samples

XPS studies were also conducted on the TZM allow sample (Ti 0.5%, Zr 0.08%, Mo 99%), to evaluate the effects of boronization and plasma operations on this high Z substrate.

The initial analysis of the data collected with MAPP, displayed in Figure BP-MP-3 shows that immediately after boronization, there is a sharp increase in the intensity of the boron peak. This indicates that a layer of boron is in fact deposited on the TZM surface. Another difference in the spectra after boronization is the appearance in the C1s region of the B-C bonds, and the drastic reduction of the intensity of the oxygen peak. The data also shows that after several days of plasma operations, the top layer (mostly carbon and boron) is sputtered away, thus reducing the intensity of the B and C peaks, and increasing the intensity of the Mo peak. Other changes after plasma operations include higher levels of boron oxide, and an increase in oxygen concentration.

To study these kinds of high Z materials is of great importance to the program, as the next upgrade to the divertor will feature a row of TZM tiles, followed by lithium conditioning of TZM.

The analysis of these data sets up the baseline to analyze how the chemistry of such substrates will evolve as plasma exposure and condition progress through the campaign. In addition, these results will be used as reference for several controlled laboratory experiments that will be performed at the University of Illinois.

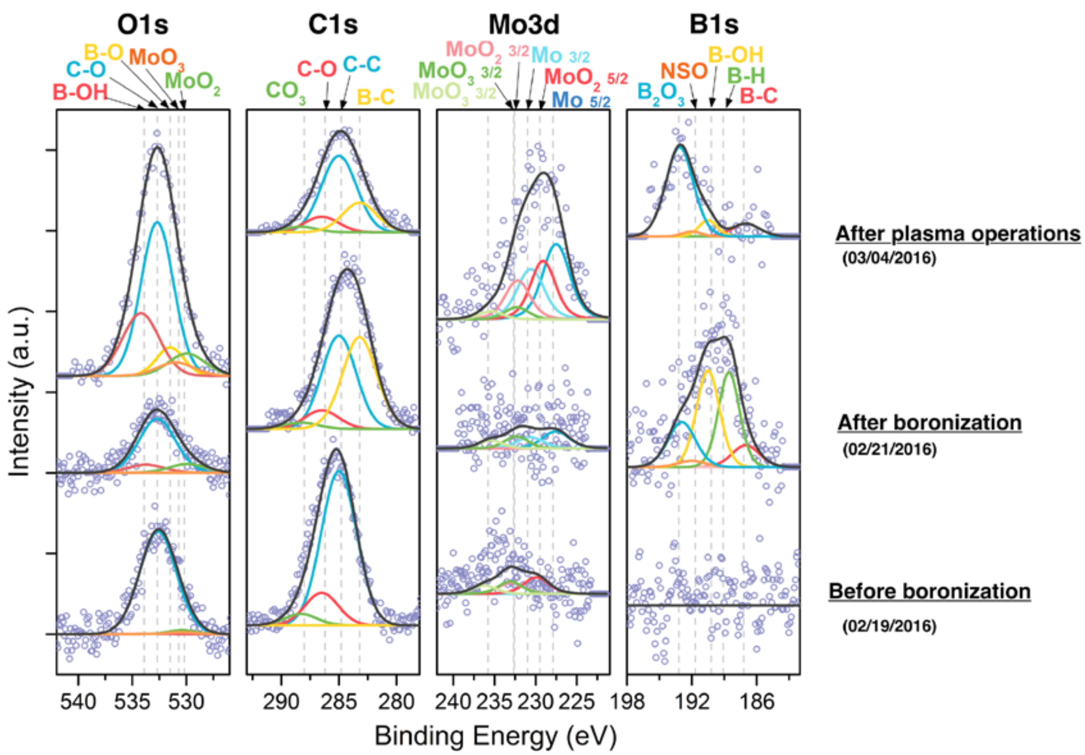

Figure BP-MP-3*: XPS peaks deconvolution for three region scans of boronized TZM alloy exposed to NSTX-U plasmas. The samples were treated as indicated by the legends.*

f. Improved capabilities for FY2016

The full motion control capabilities for MAPP were achieved in FY2016 with the ability to perform measurements between plasma discharges. The sequence for remote operation is shown in Figure BP-MP-4.

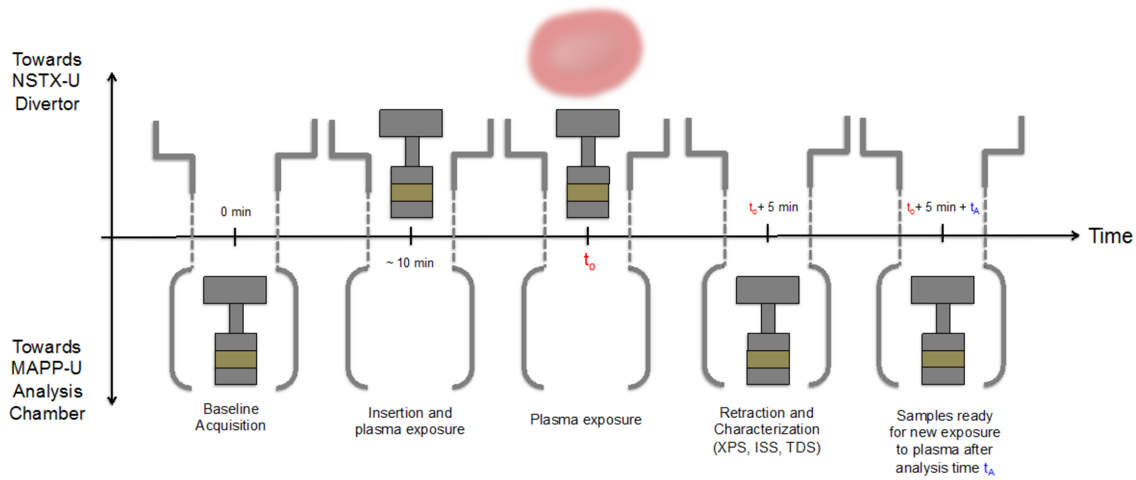

Figure BP-MP-4: *Sequence of between shots operation of MAPP in NSTX-U.*

MAPP will be a key diagnostic in the upcoming campaign to understand multiple aspects of PFC conditioning. In particular, the effects of Li conditioning on plasma performance can be investigated as a function of time, and the longevity of its effectiveness can be correlated with the evolution of PFC surface chemistry.

2. Advances in understanding boronization in NSTX-U

Boronization has been effective in reducing plasma impurities and enabling access to higher density, higher confinement plasmas in many magnetic fusion devices. We have characterized the deposition from new deuterated tri-methyl boron (dTMB) boronization system in NSTX-U. Reducing the glow discharge pressure from 4 mtorr to 2 mtorr helped the deposition uniformity. With the same input quantity of dTMB, the deposition at Bay H bottom increased by a factor x2-3 and at E top by x5 -7, consistent with an increased ion mean free path at the lower pressure. Subsequent boronizations used 1.7 mtorr (0.23 Pa), the lowest pressure GDC could be reliably sustained however the deposition was still an order-of-magnitude higher in the region of the GDC electrodes in the midplane than at the top and bottom divertor. The new boronization system has three gas injection ports that could be used to tailor the deposition pattern. Using D top injector enhanced the E top deposition by 30% and the C lower injector enhances the F bottom injector by 21%. Since the lower divertor interaction is usually dominant in plasma discharges, subsequent boronizations used solely the C lower gas injector.

A novel surface analysis probe, MAPP [BPR-MP-1] was used to measure changes in surface composition of samples exposed to the boronization and to subsequent plasmas. MAPP is the first *in-vacuo* surface analysis diagnostic directly integrated into a tokamak and can perform chemical surface analysis of plasma facing samples exposed in the vessel without sample retrieval from the tokamak vacuum. On NSTX-U the MAPP is inserted into a gap at the outer perimeter of the lower divertor, the samples moved to be flush with the divertor tiles and exposed to plasma. XPS measurements of the surface oxygen concentration showed that the surface oxygen concentration measured the day after a full boronization was 4% - 9% and rose up to 26% after 142 s of plasma exposure. During a 2-week maintenance break, the surface O concentration rose from 4% after boronization #6, to 11% following venting the vessel to argon and several He-GDC tile conditioning procedures. The effect of the changing surface conditions on plasma impurities was monitored by filterscopes that viewed the lower divertor and observed O II 441 n.m., D- γ and D-α emission lines. The O II emission normalized to D-γ was typically lower by a factor x5 after boronization but subsequently rose back to its original value. Similar behavior was observed in the surface oxygen concentration as measured by MAPP XPS O 1s line. The fast and slow O II emission rise after mini (1.5 g-TMB) and full bottle (9 g-TMB) boronizations was correlated with the fast and slow respectively rise in plasma facing surface atomic oxygen concentration as measured by MAPP XPS (Figure BP-MP-5). While this behavior is not unexpected, the result is of interest as it is one of the first direct correlations of plasma parameters with measurements of the plasma facing surface composition.

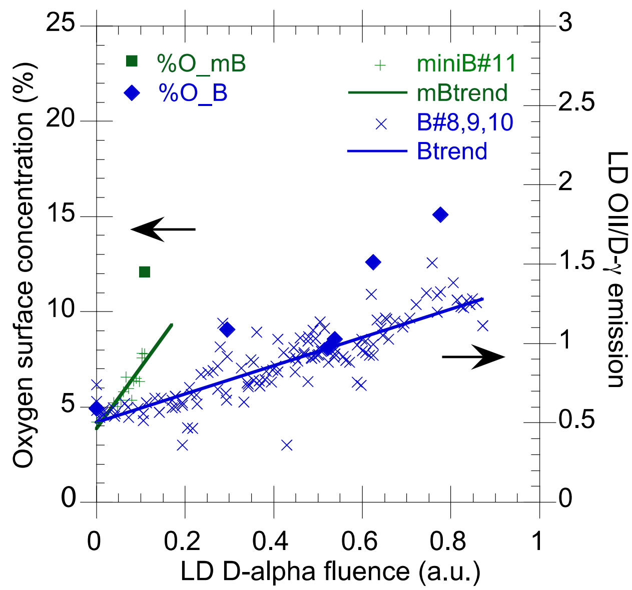

***Figure BP-MP-5**: Fast rise in O II emission after mini-boronization using 1.5 dTMB (shown as +, miniB#11), compared to the slower rise after 'full-bottle' boronizations (shown as x, B#8,9,10). The fast and slow O II emission rise is consistent with the respective rise in surface atomic oxygen concentration as measured by MAPP XPS shown as ■ and ◆ respectively, all plotted against the cumulative lower divertor D-α fluence. The mBtrend and Btrend lines are linear fits to O II emission data.*

3. Evolution of NSTX-U boronized plasma facing components during the FY16 experimental campaign

The main PFC material in NSTX-U is graphite, with a mix of POCO and ATJ-grade tiles. Boronization with deuterated tri-methyl borane (dTMB, $B(CD_3)_3$) was regularly performed at a rate of ~ one bottle of dTMB (9 g) per week for the duration of the experimental campaign with dTMB injected during helium glow discharge (GDC). Regular helium GDC was also performed between discharges. The conditions of the PFCs were monitored during the experimental campaign using filterscopes with views of the upper divertor, lower divertor and center stack PFCs, a high-resolution spectrometer, and filtered visible cameras [BPR-MP-2, BPR-MP-3]

Impurity emission and the hydrogen-to-deuterium ratio (H/D) were used to infer PFCs conditions during the experimental campaign. Singly-ionized oxygen brightness (O II, 441 nm) measured using the filterscopes was observed to drop following each boronization. In order to account for the variability of discharge conditions, oxygen brightness (proportional to the oxygen influx from the PFCs) was normalized to D-γ brightness (proportional to incident ion fluxes) and sampled in the early part of the discharge (between 0.05 and 0.2 s, where the shot-to-shot variability was minimized). The O II to D-γ ratio can therefore be indicative of PFCs surface oxygen concentration. This ratio is plotted in Figure BP-MP-6-(top) as a function of shot number for the entire experimental campaign. Vertical red lines are used to indicate full bottle boronizations. One can notice a drop in oxygen emission by a factor of 3-5 following each boronization and a fast recovery within a few 10s of discharges. A blue band is overlaid to guide the eye towards the overall trend of oxygen evolution. After the initial improvement in wall conditions, higher power discharges started challenging PFCs and the frequency of full bottle boronizations was increased to support H-mode discharge development. "Mini -boronizations" (1/4-1/5th of a dTMB bottle every night, indicated with blue vertical lines in Figure BP-MP-6) were therefore attempted to achieve constant daily wall conditions. Following mini-boronizations, the oxygen level dropped to the same level as after full boronizations with, however, a faster recovery of the high oxygen levels. Plotting the evolution of the O II / D-γ ratio as a function of

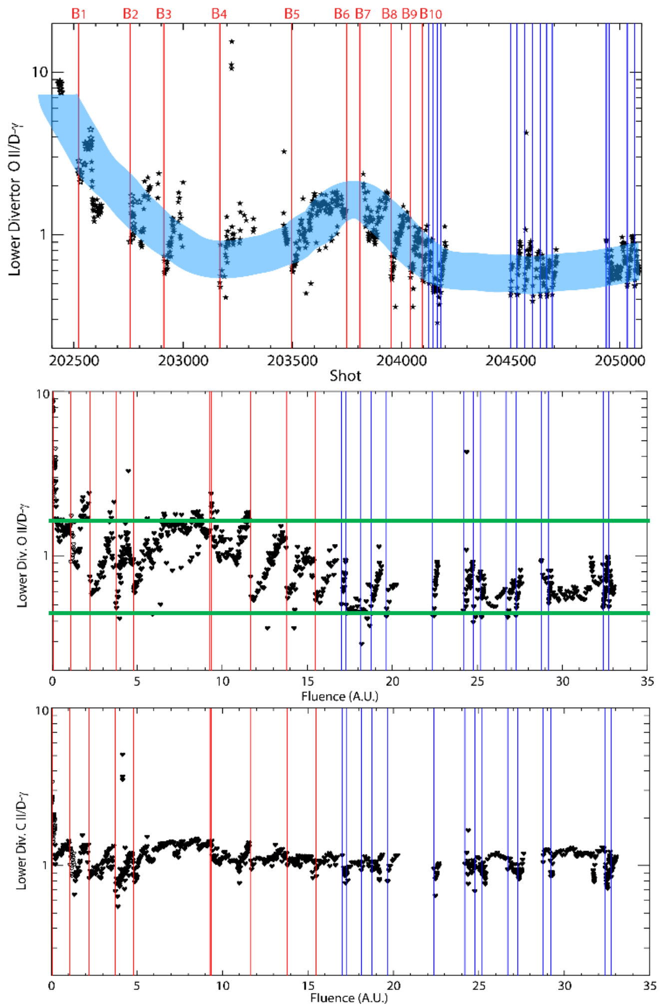

Figure BP-MP-6: *Lower divertor O II/D-γ ratio as a function of shot number (top) and as a function of divertor fluence (center). Lower divertor C II/D-γ ratio as a function of divertor fluence (bottom).*

lower divertor incident particle fluence (evaluated from the time integral of the divertor D-α emission, Figure 6-(center)), normalized the recovery of oxygen emission following boronizations (i.e., the oxygen recovery after each full-bottle boronization happened on a similar fluence scale). Mini-boronizations showed reduced fluence scales (consistently with the 1/5th of the deposited coating) but the increased frequency was successful in maintaining the oxygen levels in the range that more reliably led to H-mode access. The constant deconditioning rate can be observed more clearly plotting the O II / D-γ ratio as a function of ion fluence since the last performed boronization as in Figure BP-MP-7. Oxygen emission ranged between two extremes, a minimum (consistent for both mini and full-bottles) which was representative of boron-coated tiles and a maximum which was representative of deconditioned tiles. The consistent fluence scale for all the full bottles boronizations and the faster degradation observed with mini-boronizations are indicative of the role of thin coatings erosion in the evolution of the PFCs. Marginal changes were observed in the emission from other impurities (e.g., carbon), as shown in Figure BP-MP-6 (bottom panel).

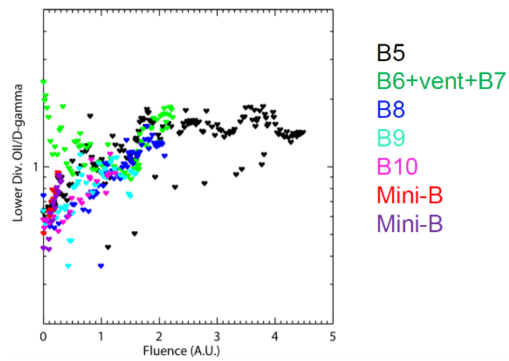

***Figure BP-MP-7**: Lower divertor O II/D-γ ratio as a function of divertor fluence since the last boronization.*

The results obtained with the filterscopes were confirmed from spatially resolved visible cameras filtered with narrow-bandpass interference filters. As an example, radial profiles of lower divertor O II (441 nm), B II (703 nm), CD (430 nm), and D-γ brightness as measured by the TWICE-I and II systems [BPR-MP-3] are plotted in Figure BP-MP-8 as a function of normalized flux coordinate at the divertor for two L-mode fiducial discharges performed at the beginning (black) and at the end (red) of a run day. Over the course of a day, O II emission increased by a factor of 2.5 with a marginal reduction in B II emission and unchanged emission due to chemically sputtered carbon.

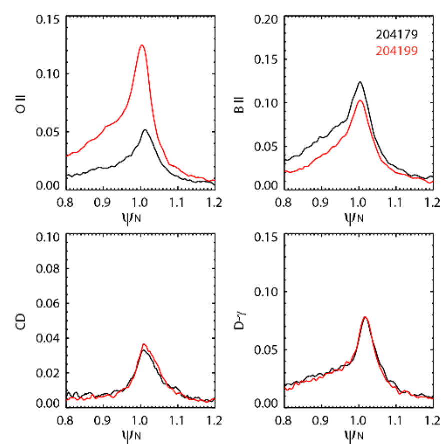

***Figure BP-MP-8:** Radial profiles of lower divertor O II, B II, CD, and D-γ brightness (normalized by lower divertor Dα) for two L-mode fiducial discharges.*

The evolution of the H/D ratio from the PFCs closely followed the evolution of O II emission, indicating the role of residual water in the graphite tiles. The H/(H+D) ratio was observed to consistently drop to 2-3% following each boronization, recovering to ~5% after a few days. This is shown in Figure BP-MP-9, where the H/(H+D) ratio from lower divertor (black) and upper divertor (red) is shown as a function of fluence. The H/(H+D) ratio was typically steady during discharges but was often observed to jump during disruptions, which is indicative of flash heating of wall components. The level of H/D ratios achieved with the implemented conditioning strategy was consistent with past experience with boronization in NSTX.

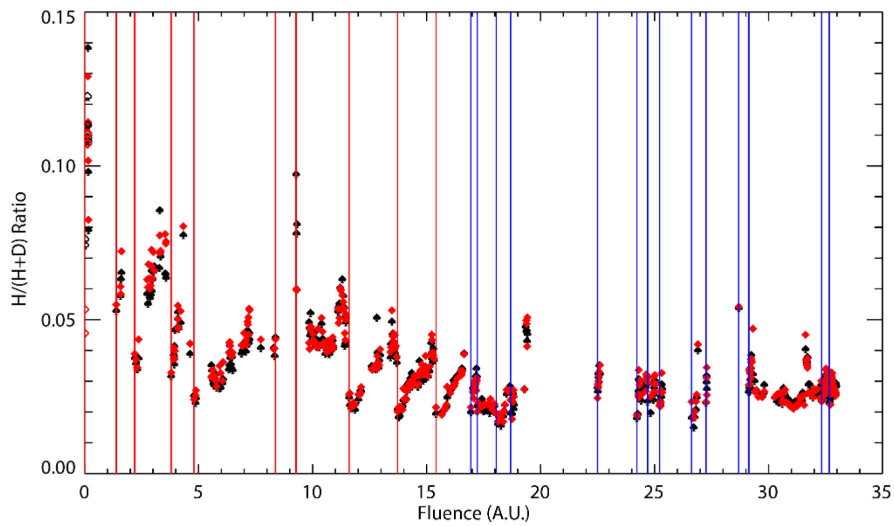

Figure BP-MP-9*: Evolution of H/(H+D) ratio from the lower (black) and upper (red) divertor for the FY16 experimental campaign.*

4. Contributions to Fundamental Surface Science Studies

In order to establish an understanding of the effects of boronization of NSTX-U PFCs and fusion wall materials surface chemistry in general, we perform a study of deuterium uptake, with particular attention to the role of boron, oxygen, carbon and deuterium. We compare atomistic simulations to XPS measured data obtained using the MAPP (see sections 1&2 above). Decomposition into the constituent XPS peaks was guided also by our atomistic simulations. The qualitative and quantitative chemical evolution of the surface caused by deuterium bombardment is observed by the concurrent changes in the O1s, B1s and C1s spectra.

This subtle interplay of boron, carbon, oxygen and deuterium chemistry is explained by reactive molecular dynamics simulations, verified by quantum-classical molecular dynamics and successfully compared to the measured data. The high degree of qualitative and quantitative agreement between the theoretically anticipated and measured chemistry in the complex BCOD surface allows us to decipher the deuterium retention chemistry and yield per D. The initially negligible role of oxygen in bonding D in the BCO (<5% of D is bonded to O) is changed significantly with D uptake, reaching almost 20% of D, in strong contrast to the role of oxygen in the D retention of LiCO surfaces. However, uptake of D into a boronized carbon surface is close but larger in value to previously predicted for a lithiated and oxidized carbon surface. Thus, for surfaces saturated with D, the D retention reaches 89.6% for BCOD and 86% for LiCOD. The similarity of the retention curves for various matrices containing Li and B, in spite of different chemistry, is unexpected, having in mind the different chemistry of D-retention in the Li and B matrices and the reduction in divertor D-alpha emission with lithium consistent with a drop in recycling coefficient from R ~ 0.98 to R ~ 0.9. The B matrices hold a few percent more D than the Li matrices, a consequence of the B atoms having strong chemical reactivity and variability in their coordination number.

Boron in general is more reactive than carbon because of the so-called octet rule, i.e. a coordination number of four is preferred for B atoms, and in our simulations we sometimes even find coordination numbers of five and six. Also electron withdrawing ligands on B such as O further increase D uptake on B. Thus, the role of B in the retention of D does not change with increasing D accumulation. However, the role of carbon in D retention decreases with D accumulation, since C, somewhat surprisingly, is less flexible in its coordination number than B. Considering the unchanged role of B in D binding, more of the impacting D is available to bond to O. Besides, the accumulated D bonds to the O binding partners B and C, creating BCD and destroying their bond to O and making room for O-D. This situation contrasts to the case of LiCO where Li does not play a significant role in D bonding. It is rather oxygen that plays the major role, as it is retained in high concentration in the surface due to the long range interactions of Li and O.

5. Advances in Material Migration Modeling in NSTX-U

Significant progress has been made in developing a mixed material evolution model for NSTX-U, using the WallDYN code framework. WallDYN allows for the calculation of time- and poloidally-resolved surface concentrations and impurity erosion fluxes for a fully mixed C/Li/O/Mo environment. Unlike other modeling approaches that attempt to iteratively couple plasma transport and surface effects and run into computational hurdles due to the disparate time and length scales, WallDYN operates by parameterizing the outputs of plasma transport and surface sputtering codes into rate equations, which can be solved simultaneously without strenuous computing requirements. Development so far has focused on the Li/C/O system, using plasma data from the FY2010 NSTX campaign. Significant parameter scans have been carried out to understand the impact that poorly constrained aspects of the WallDYN surface model may have on the calculation of observable quantities. It has been determined that the Li-C mixed material interaction, specifically how the Li surface binding energy (SBE) changes with C content, has the strongest effect on calculations of PFC composition evolution. Figure BP-MP-10a shows Li concentration profiles near the outer strike point after 1 second of plasma exposure, calculated using a variety of interaction models between the associated elements, and a clear and significant distinction can be made between profiles with different Li-C interaction terms. The 10-50% uncertainty introduced by this mixed material coupling factor also persists at higher plasma exposure times. The uncertainty in Li-C mixed material sputtering also leads to large uncertainties in Li erosion flux from the outer strike point, as seen in Figure BP-MP-10b. Preliminary analysis suggests that a weaker Li-C mixed material sputtering interaction may agree better with the scale of typical Li erosion fluxes measured in NSTX, though this will be tested more thoroughly in NSTX-U. Controlled surface science experiments are also planned to more tightly constrain Li mixed material sputtering rates.

Features currently implemented in the NSTX-U WallDYN model include composition-dependent physical sputtering, chemical sputtering, realistic deuterium ion and neutral fluxes, and impurity ionization/recombination in the main SOL. Progress is ongoing on impurity ionization in the far SOL, Li diffusion into graphite, and oxide sputtering and migration. In parallel with the computational effort, experiments are planned on NSTX-U to test and improve the WallDYN material migration model. Measurable composition changes are expected in the vicinity of the

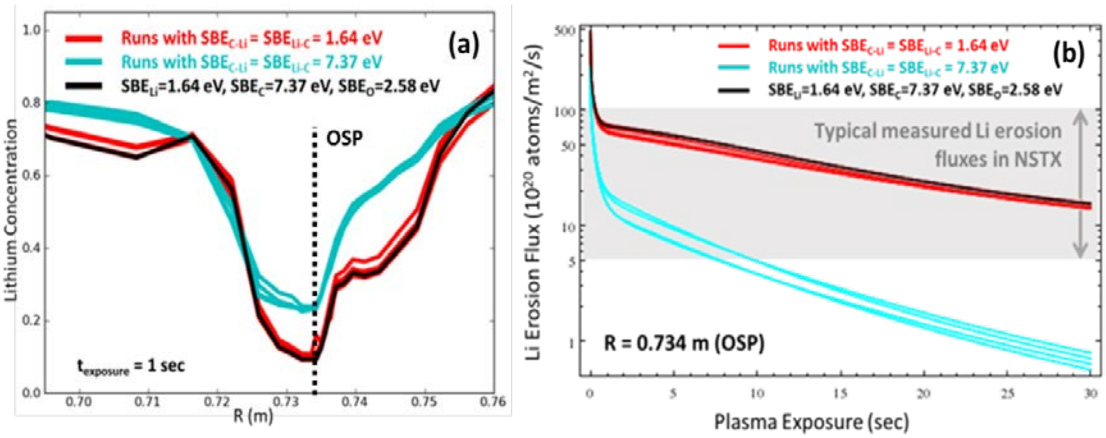

Figure BP-MP-10: *WallDYN calculation of (a) Li concentration near OSP after 1 second of plasma exposure, and (b) Li erosion flux from OSP vs. exposure time, for an NSTX low-δ H-mode discharge. By both metrics, the most significant unknown aspect of the surface model is the Li-C SBE coupling term.*

MAPP diagnostic (described elsewhere) during lithiated operations. MAPP will thus provide novel, shot-to-shot in situ analysis of surface composition during migration experiments, to complement spectroscopic measurements of gross erosion and campaign-integrated measurements of deposition on witness plates. These experiments will allow for the fine-tuning of the material migration model and the eventual development of predictive capability.

6. Implanted Depth Marker Diagnostic Development

To get first estimates on net erosion of high-Z components, low-Z depth marker species will be implanted into the lower divertor high-Z tiles in NSTX-U. Using implanted depth markers on tiles allows for measurements to be made on bulk material rather than using multiple deposited layers as depth markers, which can significantly modify properties such as hydrogenic diffusion and thermal conductivity. The depth markers provide campaign-integrated net erosion (or deposition) measurements to be made with ex-situ analysis. Due to a number of low-Z species already being present in NSTX-U operations (i.e. Li, B, C, O), fluorine (F) was identified as the optimum species for depth marker implantation. Due to a number of strong resonances in the $^{19}F(p,\alpha\gamma)^{16}O$ nuclear reaction [BPR-MP-4], nuclear resonance profiling [BPR-MP-5] can be used with a proton beam to determine the depth of the F implantation peak to high accuracy.

Preliminary work at MIT has demonstrated the proof-of-principle for this technique. F depth markers have been successfully implanted into TZM alloy uniformly over a 10 mm x 10 mm area. Implantation of F at an energy of 4.8 MeV into TZM results in an implantation peak location of 1.58 μm according to predictions from SRIM. Measurement of the depth of the implantation peak using the nuclear resonance profiling with the 1370 keV cross-section resonance was measured to be 1.60 μm. This good agreement strongly supports the high accuracy of this technique even at depths of microns.

The robustness and reliability of the technique continues to be improved as impacts of depth straggle and energy straggle have been investigated and the cross-section of the $^{19}F(p,\alpha\gamma)^{16}O$ nuclear reaction has been measured explicitly for the MIT experimental set-up, which has slightly different geometries than the measurements made in literature. Currently, investigations into the impact of F diffusion at transient high temperatures and extended moderate temperatures (i.e. bake-outs) are underway.

7. Improved spectroscopic diagnostic coverage of the upper divertor and central stack of NSTX-U

In order to diagnose the in-situ behavior of lithium coatings and the impact of lithium on poloidal and toroidal asymmetries in lithium coatings, and correspondingly, on plasma conditions and stability; new high-resolution UV-VIS-NIR spectroscopic diagnostics have been installed in NSTX-U to monitor the previously uncovered upper divertor and central stack region and ready to get the data for the next NSTX-U campaign. The diagnostics consist of a high-speed ProEM-HS 512 camera, an IsoPlane SCT320 spectrometer and 32 sightlines: 16 sightlines on the upper divertor and 16 sightlines on the central stack.

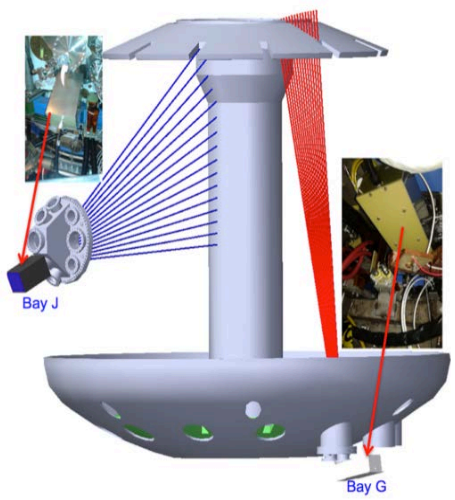

***Figure BP-MP-11**: Layout of upper divertor and central stack spectroscopy.*

These spectroscopic views of the central stack is obtained from one port at the Bay J equatorial plane for spectroscopy. A port at the Bay G bottom has been allocated to this project to provide views of the upper divertor, as shown in Figure BP-MP-11. This spectrometer is the same as the recently upgraded LLNL DIMS system. This spectrometer can work with up to 3 different gratings: one low resolution grating (600 G/mm) to monitor wide regions of the spectrum, up to 900nm; one high resolution grating (3600 G/mm optimized for UV) to measure fine spectral features of selected spectral lines (i.e. to measure temperature), Figure BP-MP-12 shows the spectral resolution is ~ 0.03nm with 20μm slit width; one

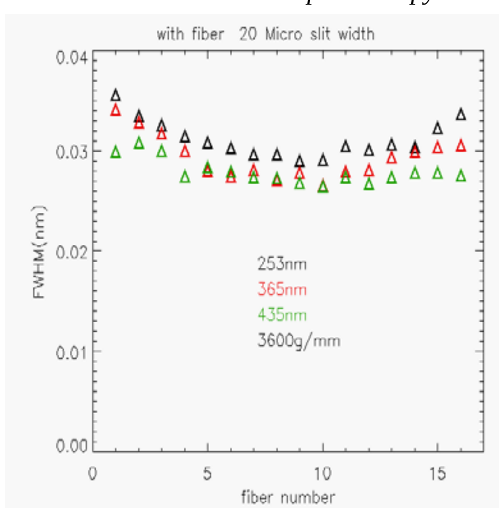

***Figure BP-MP-12:** The tested spectral resolution for 3600G/mm grating.*

intermediate resolution (2400 G/mm optimized for visible light) to monitor the intensity of multiple impurity lines at once. The frame rate can be higher than 500Hz since the high-speed ProEM-HS 512 camera.

8. Granule Injector

The NSTX-U granule injector was installed and tested, and is ready for use in experiments when plasma operations resume. The Granule Injector can radially drive solid microgranules of varying impurity species into the edge of the NSTX-U discharge at frequencies up to 300 Hz. Gravitationally accelerated granules are horizontally redirected by a dual bladed rotary turbine [BPR-MP-6] at speeds ranging from 50 - 150 m/sec. Upon entry into the discharge the granules ablate and generate a high density flux tube. This can result in the generation of an ELM. Experiments are planned to assess the triggering efficiencies of Lithium, Carbon and Boron Carbide granules. The installed system is shown in Figure BP-MP-13.

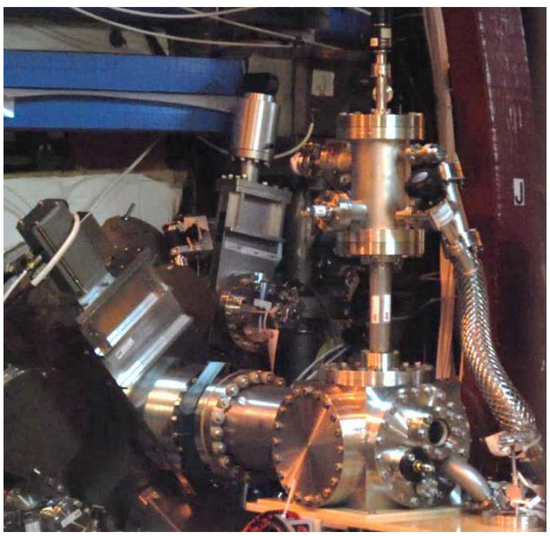

Figure BP-MP-13: *Installed NSTX-U Granule Injector*

The effectiveness of granule injection as an ELM triggering actuator depends upon the granule penetration depth and mass deposition location within the steep gradient region of the plasma pedestal. To project these quantities, a neutral gas shielding (NGS) model[BPR-MP-7] was utilized. In this model, as the ablating granule enters the discharge, a dense neutral cloud is formed which screens the granule from further incident heat flux. Based on a series of granule injection experiments performed at DIII-D by PPPL personnel[BPR-MP-8], we were able to benchmark the NGS model for alternate injection species[BPR-MP-9] and consequently use this calculation to project granule injection behavior in NSTX-U discharges. Coupling this information into the 3D MHD code M3D-C1 provided initial simulations of pedestal control by lithium granule injection [BPR-MP-10].

9. High-Z Divertor Tiles for NSTX-U High-Heat Flux Experiments

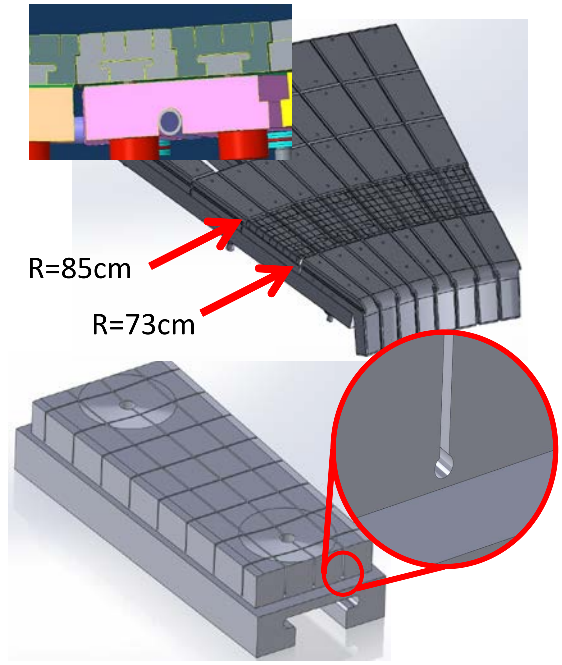

Figure BP-MP-14*: Elements of the NSTX-U High-Z Divertor Upgrade (Phase 1). Top inset shows a cross-section of the two PFC designs interfacing with the existing NSTX-U "T-bar" mounting system. Right top figure shows the intended installation replacing Row 2 in the outboard divertors. Bottom left figure shows an individual tile geometry which features dish-pan geometry at front-access bolt-holes and edge chamfers to mitigate leading edge effects. The bottom inset highlights the castellation-base stress-relief feature.*

The NSTX-U long-range plan calls for a gradual change in PFC material from the existing graphite tiles to high-Z surfaces. This change is motivated by surface-science and linear-device studies indicating that the lithium behavior on metallic substrates is significantly different from behavior on graphitic surfaces. There is little expectation that a power reactor will feature graphite surfaces leading to the need for complex and subtle interpretations of current experiments with respect to plans for future reactors. A gradual upgrade to high-Z PFCs will provide the NSTX-U program with two major benefits: first high-Z PFC performance and impact on core scenarios can be assessed in their own right and studies of lithium-coated and flowing-Li systems can be assessed with an integrated core scenario.

The NSTX-U completed a design and has nearly completed fabrication of a complete set of high-Z tiles for the outboard divertor. Elements of this design are shown in Figure BP-MP-14. The design was intended to replace, nearly one-for-one, divertor tiles in the outboard divertor of NSTX-U so as to minimize in-vessel modifications and changes to mounting hardware. In order to increase the allowable heat-flux to the front-surface, a castellated design was utilized. This design separates the location of peak temperature and peak stress which is advantageous as TZM rapidly weakens at elevated temperatures.

The design is rated for heat-flux impact factors of 10 $MJm^{-2}s^{-1/2}$, or nominally $10MWm^{-2}$ for a full second. This will minimize the impact on operations and provide a reference point for future designs in other high-heat flux regions of the machine.

The High-Z tile project included the development of several experimental and diagnostic tiles to support future research milestones. These included the development of in-tile calorimeter probes and a modified Langmuir probe system for the outboard divertor. Several material exposure samples are planned including the MIT implanted depth-markers to provide campaign-integrated measurements. The tile fabrication job is nearing completion and the full set of divertor tiles are expected at PPPL by September 2016.

References

[BPR-MP-1] B. Heim et al., IEEE Trans. on Plasma Science **40**, 735 (2012).

[BPR-MP-2] F. Scotti, A. L. Roquemore, and V. A. Soukhanovskii, Rev. Sci. Instrum. **83**, 10E532 (2012).

[BPR-MP-3] F. Scotti and V.A. Soukhanovskii, Rev. Sci. Instrum, **86**, 123103 (2015).

[BPR-MP-4] S.O.F. Dabaneh, K. Toukan, and I. Khubeis, Nucl. Instrum. Meth. Phys. Res. B **83,** 319 (1993).

[BPR-MP-5] F. Bodart and G. Deconninck, Nucl. Instrum. Meth. B **197,** 59 (1982).

[BPR-MP-6] D.K. Mansfield et al., Nucl. Fusion **53**, 113023 (2013)

[BPR-MP-7] P.B. Parks, et al., Nucl. Fusion **28**, 477 (1988).

[BPR-MP-8] A. Bortolon et al., Nucl. Fusion **56**, 056008 (2016).

[BPR-MP-9] R. Lunsford et al., Fusion Eng. & Design, at press (2016).

[BPR-MP-10] A. Fil et al., submitted to Nuclear Materials and Energy (2016)

II. Core Science Research Highlights

The Core Science group consists of three topical science groups (TSGs) including: (a) macroscopic stability, (b) transport and turbulence, and (c) energetic particles. Each of these TSG areas is covered as a sub-section in the core science report below.

A. Macroscopic Stability TSG Research Highlights

Macroscopic stability research at NSTX-U in FY2016 was aimed at enabling long-pulse high performance in both the short and long-terms. Equilibrium reconstructions of NSTX-U discharges with EFIT were quickly established. Compass scan experiments confirmed optimum error field correction phase and amplitude. Long pulse H-mode discharges above the no-wall ideal stability limit were achieved. NSTX-U discharges with MHD activity were analyzed, tearing instability studies with MARS and resistive DCON were performed, and halo current data has been successfully collected in NSTX-U along with the development of international multi-machine database for halo currents.

Capabilities for future stable high performance operation also advanced in FY2016. This included significant advancement of the DECAF code, including a reduced kinetic model for resistive wall mode stability as well as a module for tearing mode analysis, and full non-linear simulation with M3D-C1 code to predict vertical displacement event and halo current dynamics. Hardware capabilities also progressed, including testing of massive gas injection valves and design work for future enhanced 3D magnetics, advanced MHD spectroscopy based on Nyquist diagram, and systematic optimization of NCC configuration for 3D neoclassical transport.

EFIT reconstructions of NSTX-U equilibria

A common description of the plasma is given by the solution to the Grad-Shafranov equation, a second order PDE describing a toroidally symmetric MHD equilibrium. The code EFIT solves this equation, finding the solution most consistent with available diagnostic data. Two versions of this code [MS-1] are automatically run after each NSTX-U discharge, with different constraint sets. These are labeled EFIT01, relying only on magnetic measurements, and the “partial kinetic” EFIT02, which augments the magnetic data with a diamagnetic flux constraint and a pressure profile constraint. During the NSTX-U FY16 run campaign, the EFIT code was run on 1906 discharges. EFIT01 reconstructions have been available from the very first shots of the campaign.

Observation and Analysis of MHD Activity

A variety of low-n MHD activity has been observed in NSTX-U, including sawteeth, 1/1 helical core modes, 2/1 modes, and 3/2 modes. The behavior of these modes was found to be affected strongly by differences in beam injection and density despite nominally similar current density profiles, suggesting the influence of non-ideal effects. In particular, whether the plasma begins sawtoothing or forms a non-sawtoothing helical core mode upon the formation of the q=1 surface appears to depend sensitively on the plasma parameters. These observations provide fertile ground for testing linear and nonlinear models of mode growth, saturation, and interaction.

Two examples of the observed MHD activity are show in Fig. MS-1. In NSTX-U discharge

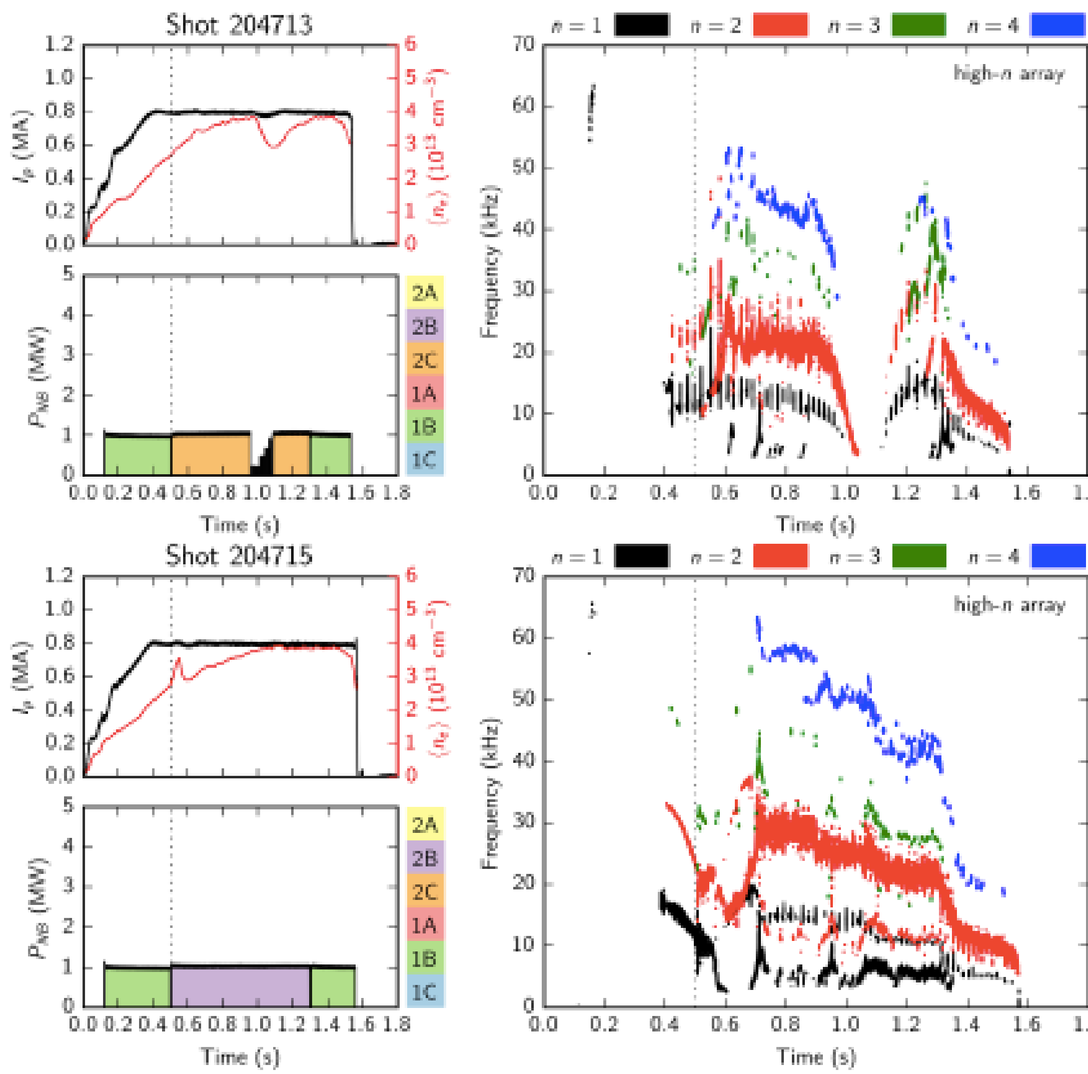

Figure MS-1*: Left (from top to bottom): the plasma current (black line) and density (red line) of NSTX-U discharge 204713; the injected neutral beam power of 204713; the plasma current and density of 204715; and the injected neutral beam power of 204715. Right: The magnetic spectrogram of 204713 (top) and 204715 (bottom).*

204713, neutral beam source 2C was used during flattop. Discharge 204713 begins sawtoothing (hashed black lines at ~10 kHz in top right panel) at 400 ms, which coincides with the formation of the q=1 surface. A 3/2 mode (solid red line at ~20 kHz in top right panel) is found to arise at around 450—500 ms. Different behavior is seen in discharge 204715 despite a nominally identical ramp-up. Rather than sawtoothing, a 1/1 helical core (solid black line starting at ~18 kHz in bottom right panel) is found to arise at 400 ms. This mode spins down, and is replaced by a sawtoothing core at ~650 ms. Unlike 204713, neutral beam source 2B, which is more tangential than 2A, is used during flattop. This apparently has the effect of unlocking the 2/1 mode (solid black line at ~5 kHz in bottom right panel) at ~650 ms. Like 204713, this discharge also exhibits a strong 3/2 mode.

Finally, a significant observation in NSTX-U is that the plasma tends to be locked from the q=2 surface outward in most L-mode discharges. Similar behavior had been observed on NSTX; this was eventually overcome in NSTX through the use of high-density startup scenarios and error field correction with the NSTX RWM coils. Understanding and mitigating these error fields will be necessary to optimize the performance of NSTX-U.

A series of compass-scan experiments run on NSTX-U (see Error Field Correction section) have shown that the existing RWM coils are not able to prevent or reverse the plasma locking in the L-mode scenarios that have been developed so far. It is observed that the plasma unlocks soon after entering H-mode, most likely due to the significant rise in edge density at that time. It is also observed that the 2/1 mode can be unlocked through the use of the new, more tangential neutral beam. This suggests that density control and neutral beam injection may be promising strategies for unlocking the L-mode edge in upcoming campaigns.

Linear analysis of tearing mode instability observed in NSTX-U

NSTX-U L-mode discharges with low-power NBIs (1-3MW) often showed unstable n=1 tearing modes during operation. An example is shown in Figure MS-2, where one can see the n=1 mode first appearing at 380ms and then followed by unstable n=2 and 3 modes. After 500ms, the frequency of n=1,2 and 3 modes started to synchronize each other, but the initial time delay suggests that the n=1 mode is what's subjected to tearing mode instability and the higher n>1 tearing modes might be seeded by the n=1 islands.

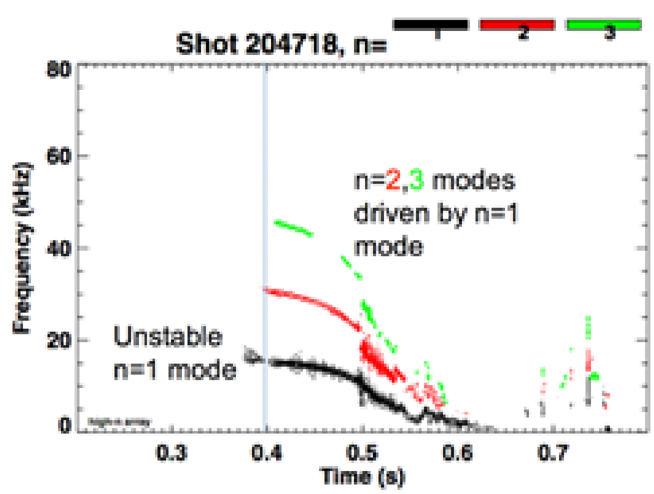

Figure MS-2: *Time dependence of mode frequency measured by Mirnov coils in NSTX-U. The n=1,2 and 3 modes are presented by black, red and green curve respectively.*

To understand whether or not the n=1 mode is naturally unstable, the MARS-F code and the newly developed resistive DCON code were applied to investigate n=1 tearing instability based on the reconstructed equilibrium using LRDFIT, from #204718 with $q_0 = 1.34$, $q_{edge} = 6.33$ and β_N=2.33. MARS-F finds an unstable tearing mode with the growth rate $\gamma = 1.7 \times 10^{-3} \omega_A$, where ω_A is the Alfvén frequency at the center of plasma. The eigenfunction of radial plasma displacement ξ_r is plotted in Figure MS-3. It shows m=2 harmonic of ξ_r at q=2 resonant surface, has even parity, but m=3 and m=4 harmonics have the clear odd parity of tearing structure at q=3 and 4 resonant surfaces respectively. This means the tearing instability is driven by m>2, n=1 modes, instead of the typically expected m=2, n=1 mode.

To confirm the MARS-F results, resistive DCON was also applied to estimate the stability index, Δ' matrix from the outer region. In the identical case, the diagonal terms corresponding to q=2, 3 and 4 surfaces in Δ' matrix were shown to be Δ'(q=2)=-4.29<0, Δ'(q=3)=10.0>0 and Δ'(q=4)=3.18>0, respectively. This indicates that m>2, n=1 modes are possibly unstable but m=2, n=1 mode is stable, consistent with MARS-F's finding.

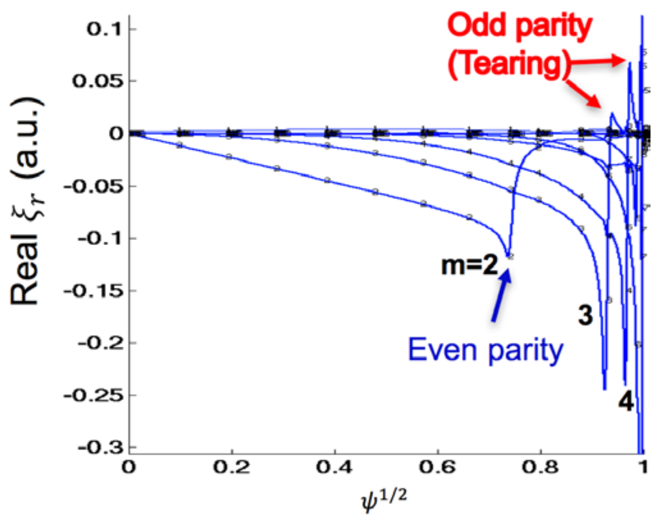

***Figure MS-3**: Poloidal Fourier harmonics of dominant real part of ξ_r is plotted as the function of $\psi^{1/2}$, where ψ is the poloidal flux. The PEST coordinates are adopted in the MARS-F simulation.*

The MARS-F and resistive DCON analysis both shows that the n=1 tearing mode can be naturally unstable in NSTX-U L-mode discharges depending on the operational conditions, and also interestingly, the tearing instability can be driven by q>2 surfaces. Extended analysis with other target plasmas and profile variations is in progress, to predict or avoid tearing mode instability in NSTX-U L-mode operations.

Error Field Correction

Error fields in a machine like NSTX-U can be generated by a number of mechanical imperfections, for instance tilts of the poloidal or toroidal field coils or non-circularity in the PF coils. Error fields were observed in NSTX, where the dominant effect was a time-dependent tilt of the TF coil as it interacted with stray fields produced by the OH leads. Note that these leads and their associated stray fields were located at the top of the machine, while the coil was mechanically fixed at the bottom.

For NSTX-U, this error field source was eliminated by design. In particular, a coaxial lead assembly at the bottom of the machine is used to feed the OH coil, eliminating any effective loop area from the OH leads. Coils-only vacuum shots demonstrate that this coaxial OH lead assembly successfully eliminates the time-dependent n=1 error field due to the OH/TF interaction. This result is best illustrated in Fig. MS-4, which shows a comparison of the measured n=1 error field during coils-only vacuum shots in NSTX and NSTX-U. During the time period shaded in white, the OH current ramps steadily through zero to increasingly negative values while the TF remains constant. In the NSTX case (blue), the measured error field amplitude increases from zero to ~5 G over the course of the OH ramp. In the NSTX-U case (red), on the other hand, the measured error field remains below 1 G for the duration of the OH ramp. Note that the measured error field amplitudes are 're-zeroed' when the OH current passes through zero to isolate the time-dependent error fields generated by the OH current ramp. These results demonstrate that the OH/TF error field that was found to impact plasma performance in NSTX was successfully designed out of NSTX-U.

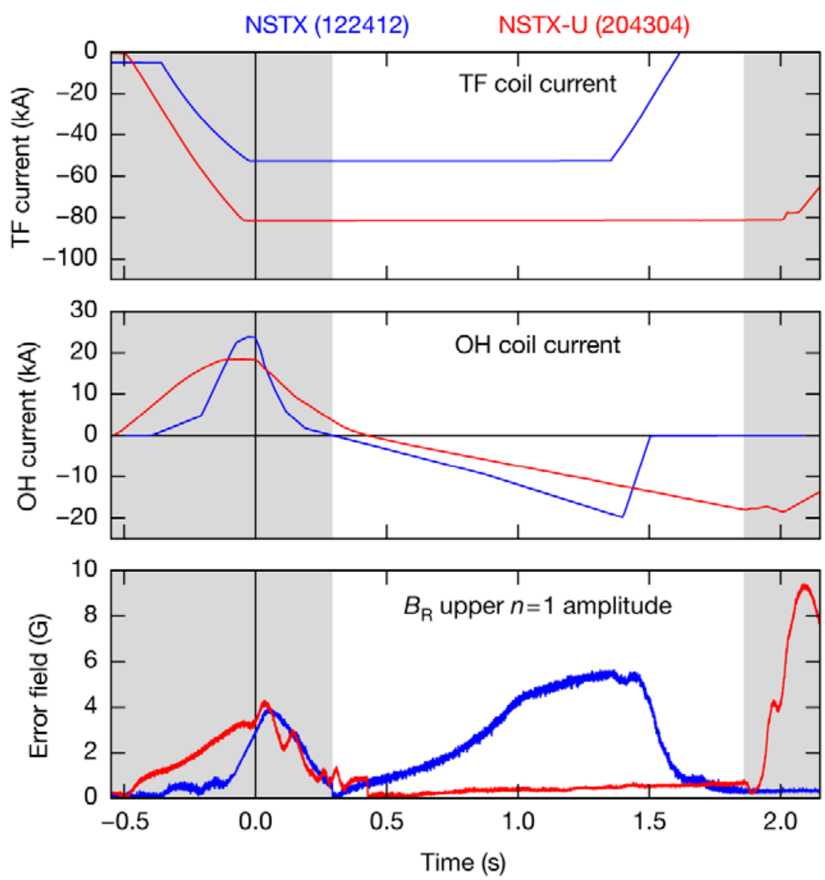

Figure MS-4*: Comparison of fields measured during a coils-only vacuum shot on NSTX (blue) and on NSTX-U (red). During the time period shaded in white, the TF current is constant and the OH current passes through zero and steadily ramps to more negative values. In the same time period, a measured n=1 error field (bottom plot) is clearly present in the NSTX shot and absent from the NSTX-U shot. This demonstrates that the coaxial OH lead assembly in NSTX-U eliminated the OH/TF-generated error field.*

However, in spite of the elimination of the OH/TF time-dependent error field, additional error field studies proved to be important in improving the performance of the machine.

Improvements in performance were first demonstrated in a series of n=1 error field scans on 2/25/2016. In this case, an n=1 field is applied, proportional to the PF-5 current magnitude; the phase of the n=1 field and the constant of proportionality are variables to be adjusted in the algorithm. This proportionality to PF-5 was chosen because the PF-5 coil is known to have out-of-round features whose error fields must be corrected. The reference plasma in this case is a 700 kA Ohmic scenario. In the example shown in Fig. MS-5, adjustments of the applied n=1 phase at fixed proportionality resulted in either shorter or longer discharges. This asymmetry implies the presence of an error field, a best correction occurring with an applied field phase of 315 degrees (toroidal angle).

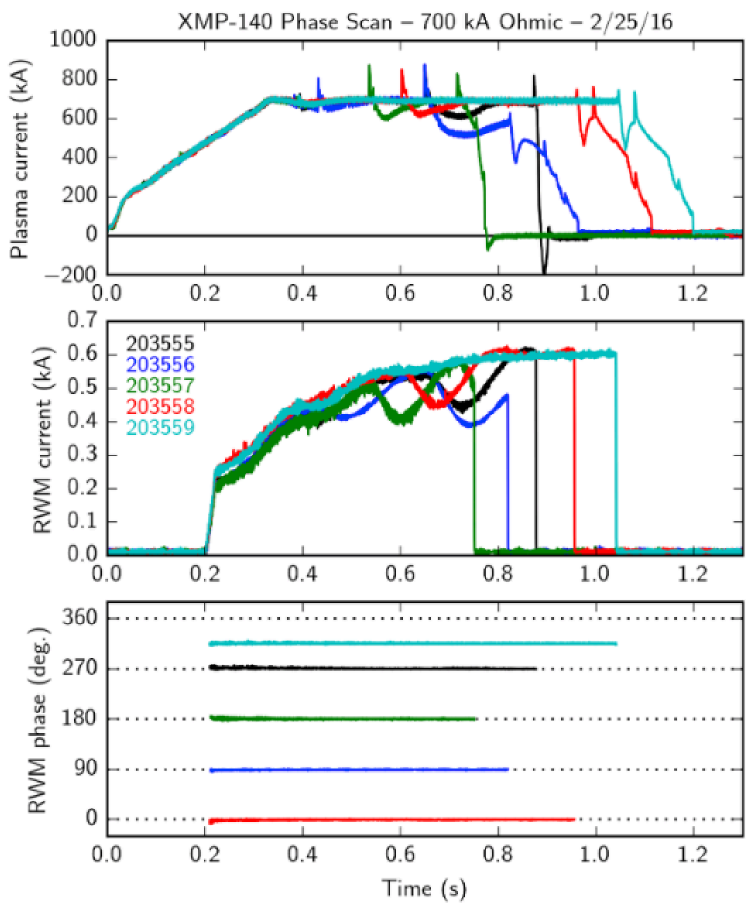

***Figure MS-5**: Results of applying n=1 fields of various phases at fixed proportionality to the PF-5 coil current. The best performance as judged by plasma duration is a toroidal phase of 315°.*

In order to better resolve the best feed-forward error field correction, n=1 fields were applied in a 'compass scan' format to determine the optimum error field correction for locked mode avoidance over sequence of shots. More specifically, the amplitude of the applied n=1 was ramped in each shot at fixed phase until the plasma disrupts. The waveforms from one such compass scan are shown in Fig. MS-6, where the plasma current in the top frame shows that different shots disrupt at different times. These are 700 kA diverted L-mode plasmas formed with a 20 kA Ohmic precharge, with a density of 1.3×10^{13} cm^{-3}, heated by 1 MW of neutral beam power. The middle frame shows the RWM coil current. All shots have an initial evolution as per the optimal solution from the experiment described in Fig. MS-5 (and other similar experiments). At 0.7 seconds, however, the RWM coil currents diverge, with ramping amplitudes of various phases, which are shown in the bottom frame. The fact that the different phases disrupt at different applied field amplitudes confirms that a nonzero error field must be corrected in these L-mode discharges in order to provide optimum locked mode avoidance.

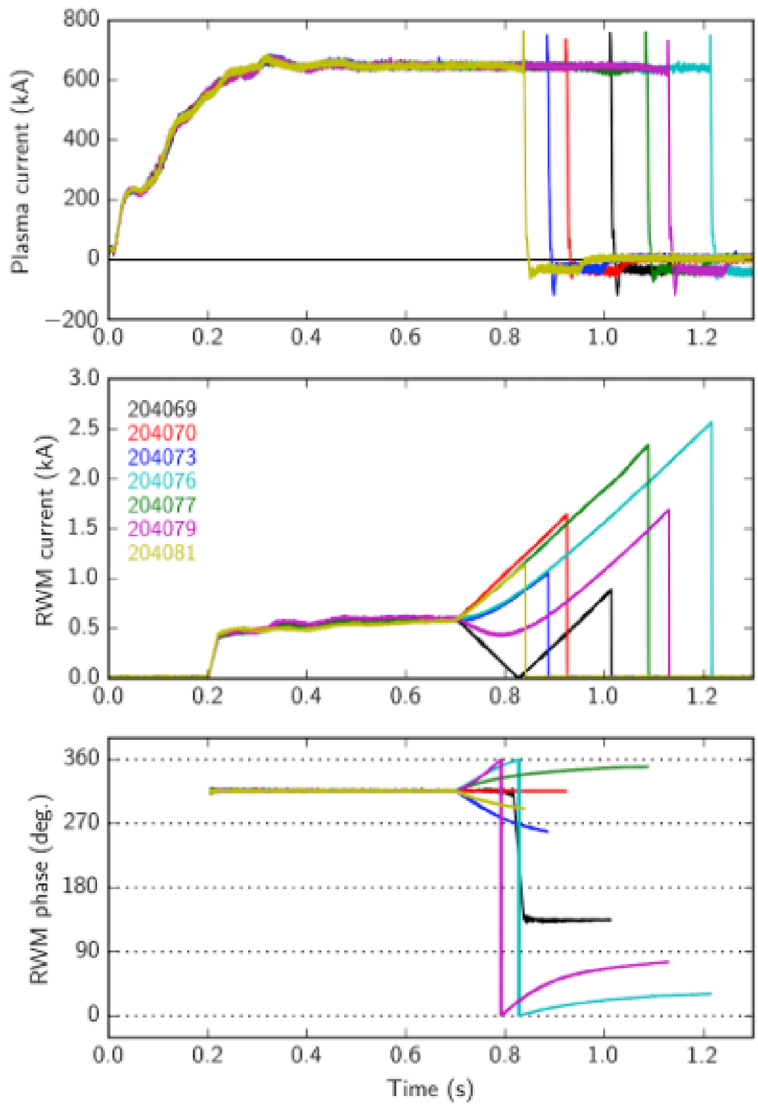

Figure MS-6*: Seven discharges from a sample compass scan. The top frame shows the plasma current, the middle frame shows the RWM coil currents, and the bottom frame shows the phase of the applied field. See text for additional details.*

The results from Fig. MS-6 can be reframed as a phase space plot of the applied RWM currents as a function of time, ending at the point of a disruption. As such, the waveforms from Fig. MS-6 are shown in phase space format in Fig. MS-7. This figure shows that the currents at time of disruption map to a circle whose center is shifted away from zero. The center of this circle is the optimum correction for locked mode avoidance, which is similar in magnitude but differs slightly in phase when compared to the initial PF-5 proportional results in Fig. MS-5 (15° versus 315°).

An error field compass scan was completed in three different configurations: (i) the case shown in Figs. MS-6 and MS-7, (ii) a similar case at twice the plasma density, and (iii) a comparable high density case with an 8 kA (rather than 20 kA) OH precharge. The second scan, which was conducted to assess the density scaling of the locking threshold in this 1 MW beam-heated L-mode scenario, found that the locking threshold was largely unaffected by the higher density; this implies that the rotation driven by the beam is the dominant effect, compared to the diamagnetic rotation that is thought to dominate in Ohmic plasmas. The third and final scan, which was conducted to assess if the error field measured in the compass scans is due to the OH coil, found no change in the required error field correction. The fact that the required correction did not change with a large change in the OH pre-charge implies that the OH is *not* the source of the error field measured by the compass scans. The optimized error field correction determined from the three compass scans described above was used successfully in many of the best H-mode plasmas from this campaign.

These figures describe the optimization of the error field correction after the start of the plasma current flattop. However, experiments were also conducted to establish if there is an optimal correction strategy very early in the shot, during the breakdown and early ramp-up phases. An example of this type of experiment is shown in Fig. MS-8. The upper left frame shows the plasma current evolution, which is largely similar for each L-mode discharge in the set. The middle frame on the left shows that the RWM current amplitude is flat at approximately 600 A from t=0 for each of the cases, except for the blue case with no correction current. The bottom left frame shows that the phase of the applied field varies for different discharges, and it is the effect of these phase changes that is of interest. Note that the black case is the phase that was found to be optimal for the plasma current flattop.

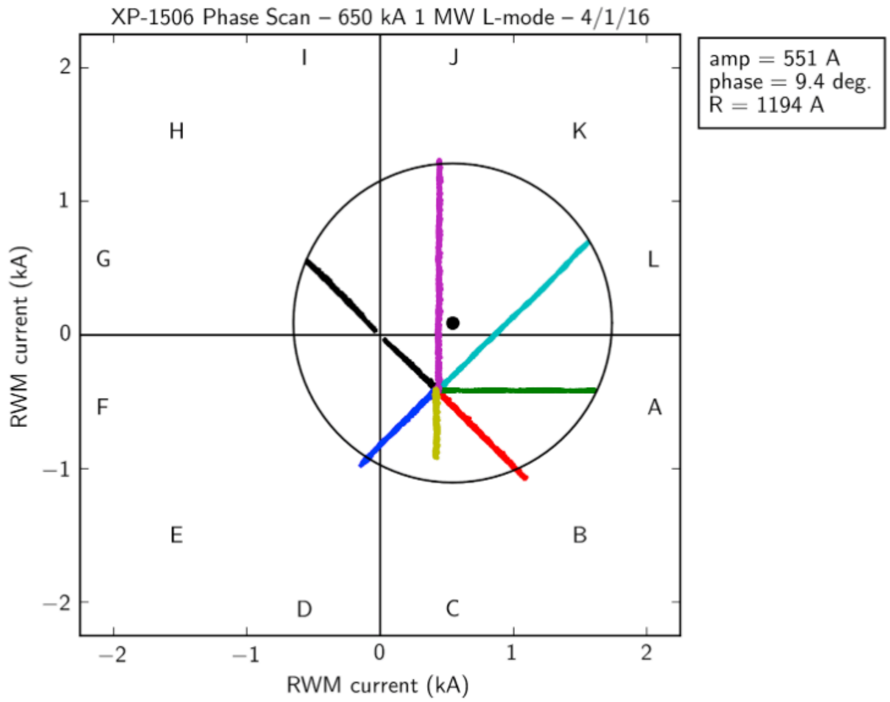

Figure MS-7*: Phase space plot of the compass scan data in Fig. 7.3. The resulting circle is centered away from zero with at an amplitude that is comparable to the PF-5 proportional amplitude, but at a phase of 15° rather than 315°.*

The somewhat surprising results of the scan are shown in the right column of the figure. First, the density during this early phase of the shot is shown in the top right, where it can be seen that the green and magenta cases, corresponding to 285° and 240°, respectively, is elevated compared during the ramp up as compared to the other phases and the reference. Conversely, the density is depleted in the black case, which corresponds to 15° (the optimum plasma current flattop correction. The elevated (depleted) density could be indicative of better (worse) correction since small locked modes in the ramp-up can result in particle loss and therefore depleted density. Returning to the figure, the middle frame on the right shows the neutron emission, where the black case shows depleted neutron emission, which is another indication of poor correction in the phase that later in the shot is the optimum error field correction. Finally, the core rotation speed, as measured by the rtV_{phi} diagnostic, shows highest early rotation for the corrections in the range of 195°–285° (red, magenta, and green). In the 15° case (black), on the other hand, the core of the plasma is nearly locked until around 350 ms when it spins up to match the other cases during the plasma current flattop. Since faster rotation for the same applied torque (from the beam) implies reduced drag from error fields, it is clear that the optimal flattop correction is far from optimal during the ramp-up phase.

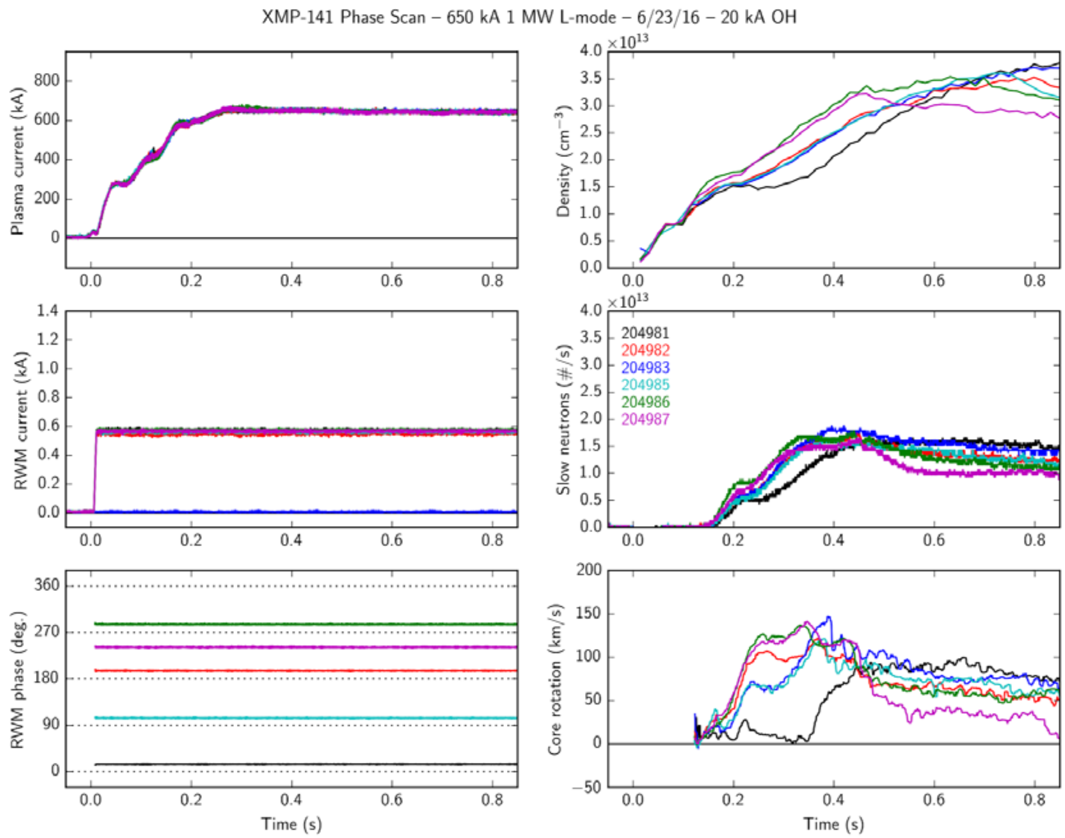

Figure MS-8: *Results from an experiment to examine early error field correction. A constant amplitude of 600 A at different phases is applied from t=0, except in the blue reference case. Phases in the range of 195°–285° (red, magenta, green) show elevated density and core rotation, while the 15° case (black) shows depleted density and neutrons as well as minimal rotation. These asymmetries suggest that the optimum flattop phase of 15° is actually detrimental during the ramp-up phase, and that the dominant error field source may be changing as a function of time.*

These results show that the optimal correction likely varies during the shot, implying that there may be more than one error field source. As mentioned, experiments in which the OH pre-charge was varied have eliminated misalignment of the OH coil as a dominant source of error field. One potential source, as noted above, is the out-of-round nature of the main vertical field coil (PF-5). Indeed, the relative distance measured between PF-5 coil and vessel indicates dR up to ~2cm, generating n=1-3 error field components. It is also shown, however, that the empirically optimized corrections described earlier are largely inconsistent with the one predicted by the PF-5 error field model, in either flattop or early ramp-up. Figure (Fig. MS-9) shows the estimation of the kink-dominant part [MS-2] of the remnant field (Gauss) with PF-5 error as a function of the applied RMP currents (radius, kA) and toroidal phase (round circle), based on the reconstructed #204077. One can see that the predicted optimal correction points to ~90° with only about 150A, but the optimal correction found at the flattop and at the early ramp-up required much larger currents up to 600A and with very different toroidal phases. This preliminary analysis indicates the possibility of (1) much larger error field sources (2) time-varying nature of error field sources or at least in coupling, (3) onset of locked modes by other physics mechanisms than the conventional Kink-coupling.

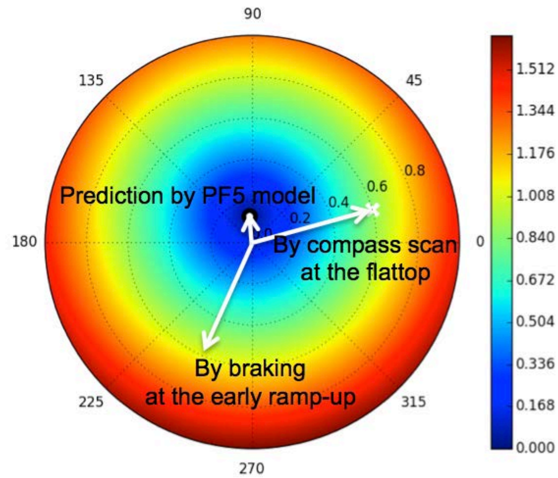

Figure MS-9*: Predicted RWM coil current and phase to compensate error field from PF-5 coil model vs. empirically optimized corrections.*

Therefore, *in-situ* metrology of various coil shapes and alignments is planned again for the FY16/FY17 outage, but also another candidate source will be investigated to explain the time-dependent nature of the required error field correction, possibly with the induced currents that flow in the vessel wall during ramp-up. These vessel currents are time-dependent in that they decay away after the ramp-up and therefore only have a large impact early in the discharge. The eddy fields that would be expected during a typical NSTX-U current ramp have been calculated using a simple model of the NSTX-U vessel and passive plate structures using VALEN (Fig. MS-10). While significant, these fields do not appear to be large enough to explain the observed behavior.

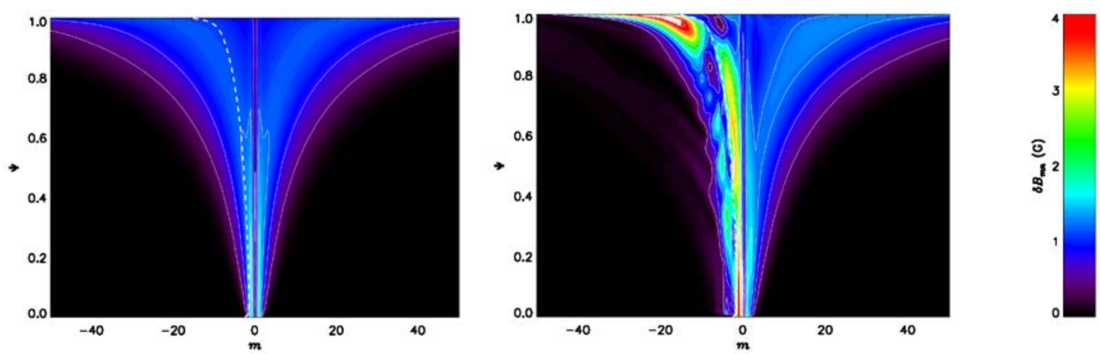

Figure MS-10*: Left: the spectrum of the eddy-current fields during NSTX-U current ramp-up as calculated by VALEN. Right: The total fields including the plasma response in a model H-mode equilibrium as calculated by M3D-C1. The calculated response shows both kinking in the core and in the edge of the plasma.*

The potential effect of error fields from both coil misalignments and eddy currents is being calculated using IPEC and M3D-C1. Once the dominant sources of error fields are understood, the efficacy of the proposed non-axisymmetric control coil (NCC) design [MS-3] to correct these fields will be evaluated.

Finally, another error field source to be considered is a static tilt of the TF center rod with respect to the vertical axis of the PF-5 coil. The error field produced by this source has a dominant 1/1 component that only resonates with the plasma once q_0 drops below unity. In the 1 MW beam-heated L-mode plasmas, the q=1 surface enters the plasma around t=400 ms, which is consistent with the damping of the core rotation that is observed in the bottom right panel of Fig. MS-8.

All of the error field correction efforts described to this point focus on n=1 error fields, which are the most damaging to the plasma. Higher order (n=2,3) fields can also elicit a plasma response, however, and are therefore of interest for achieving maximum performance. Such higher order corrections are anticipated in NSTX-U given that the main vertical field coil (PF-5) is known to have n=2,3 asymmetries, and a static feedforward n=3 correction was required to achieve maximum performance in NSTX.

NSTX-U plasmas have exceeded the no-wall ideal stability limit

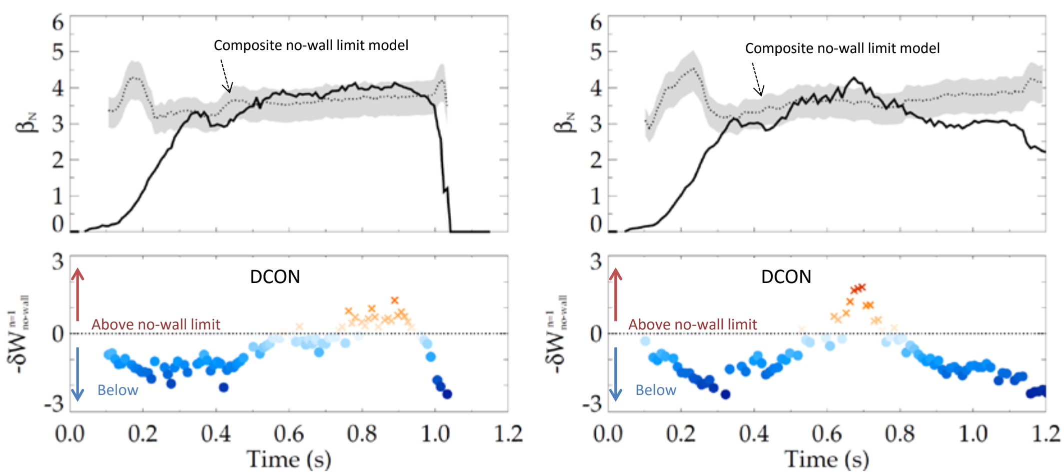

Figure MS-11: *(top) β_N and the composite no-wall limit model calculated in DECAF, and (bottom) the negative of the n=1no-wall δW calculated by DCON for NSTX-U H-mode discharges (left) 204112 and (right) 204118. The DCON results confirm that NSTX-U has gone above the no-wall limit, and the composite model does a good job predicting the DCON result.*

Long-pulse H-mode discharges in NSTX-U were analyzed with the DCON stability code [MS-4], which confirmed that NSTX-U achieved operation above the ideal stability no-wall limit. Figure MS-11 shows normalized beta (a measure of the ratio of plasma to magnetic pressure) vs. time for NSTX-U discharges 204112 and 204118. In the bottom panels the negative of the change in potential energy term, -δW, calculated with DCON for toroidal mode number n=1 and without a wall in the calculation is plotted so as the indicate when the stability crosses from below (blue) to above (red) the n=1 no-wall limit. Also included on the top panels is the composite no-wall limit model that was developed for NSTX, which includes internal inductance, pressure peaking, and aspect ratio [MS-5]. The estimate does a good job at predicting the NSTX-U no-wall limit despite being developed for NSTX discharges in different ranges of those parameters.

The disruption event characterization and forecasting (DECAF) code

The disruption event characterization and forecasting (DECAF) code was written at NSTX-U in order to facilitate a comprehensive framework for disruption prevention through forecasting and avoidance, or prediction and mitigation of the detrimental consequences. The ultimate goal of such an approach is to provide forecasts, which integrate with a disruption avoidance system and are utilized in real-time during a device's operation. Previously reported DECAF work focused on the first step: quantitative statistical characterization of the chains of events which most often lead to disruption of plasmas. Here we will specifically outline progress on the development of DECAF in three areas: identification of rotating MHD modes, characterization of a set of resistive wall mode (RWM) disruptions, and the development of a reduced kinetic model for RWM stability.

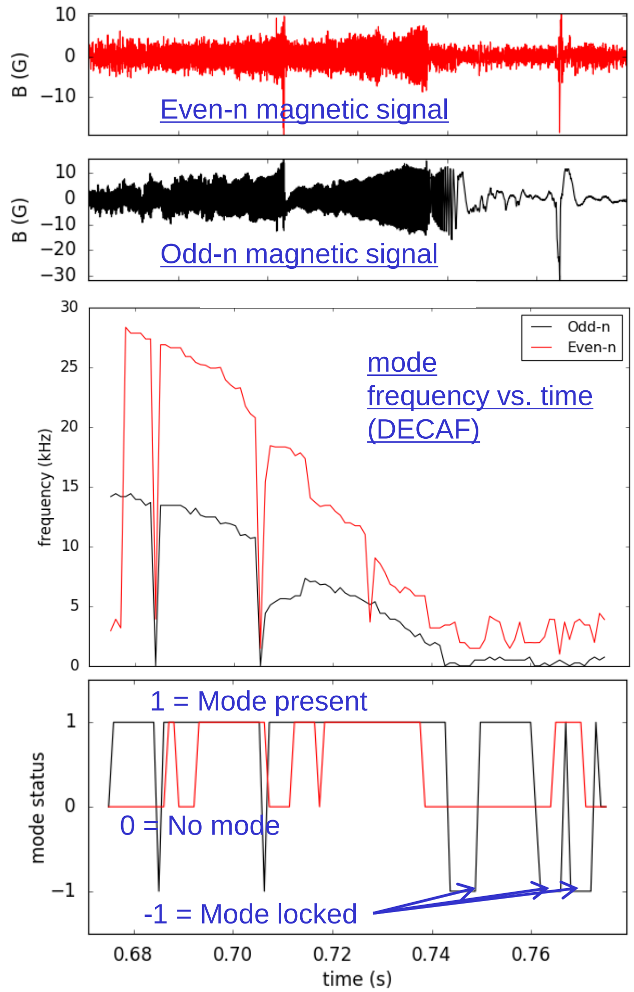

Figure MS-12: *Identification of rotating MHD in DECAF for NSTX-U discharge 204202.*

Identification of rotating MHD modes in DECAF

An essential step for DECAF analysis of tokamak data is identification of rotating MHD activity, such as neoclassical tearing modes. The initial goals were for the code to identify existence of rotating MHD modes and to track characteristics that lead to disruption, such as rotation bifurcation and mode locking. The approach taken was to apply a fast Fourier transform (FFT) analysis to determine the mode frequency and bandwidth evolution. Figure MS-12 shows the even-n and odd-n magnetic signals for NSTX-U discharge 204202, the mode frequencies determined by DECAF and the mode status, showing odd-n locking late in the discharge.

Characterization of a set of RWM disruptions in NSTX

In order to test the DECAF code's robustness and gain physics insight, analysis was performed on a database of 44 NSTX discharges that were pre-determined to have unstable RWMs, which lead to disruptions.

The RWM is identified in NSTX by a variety of observations [MS-6,MS-7] including an exponential growth in that magnetic signal on low frequency poloidal magnetic sensors located between the plasma and the vacuum vessel.

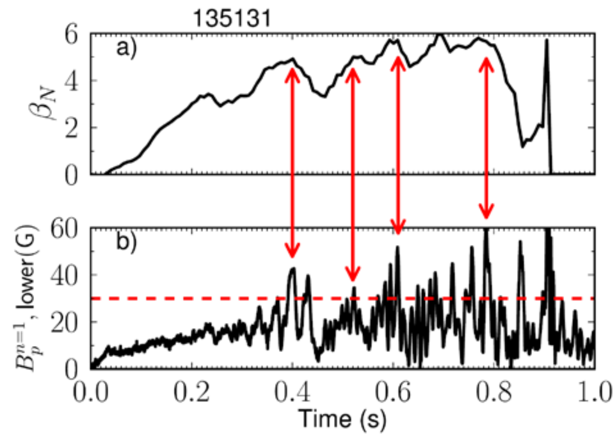

Figure MS-13: *β_N and n=1 signal on lower poloidal magnetic sensors from NSTX discharge 135131, showing that RWM warnings are sometimes associated with minor disruptions that cause decreases in β_N, with subsequent recovery.*

Because the RWM was independently identified in these discharges, the relatively simple test of setting a threshold in these magnetic signals will suffice to determine its timing. In the future, however, more sophisticated warnings for RWM marginal stability such as a reduced kinetic model (next subsection) or use of the mismatch between the observer of the RWM state-space controller and measured signals will be used.

The present version of the DECAF code, with eight event tests, was run on the 44 selected discharges to gain insight into common event chains that result during RWM disruptions in NSTX. Naturally, the RWM event was detected in all of the discharges, as were plasma current not meeting request (IPR) and the disruption warning itself (DIS), by definition. However, additionally, loss of wall proximity control (WPC) and low edge safety factor (LOQ) warnings also resulted in each of the 44 discharges. The pressure peaking warning (PRP) occurred on a majority of the discharges analyzed (34 of 44), and typically occurred with or after the RWM, not before. Loss of vertical stability control (VSC) was present in most of the discharges as well (31 out of 44) and some of the cases where it did not occur in DECAF were due to lack of good equilibrium reconstruction during the vertically drifting phase. Low density (LON) warnings occurred less often in this database (11 out of 44) and there were no

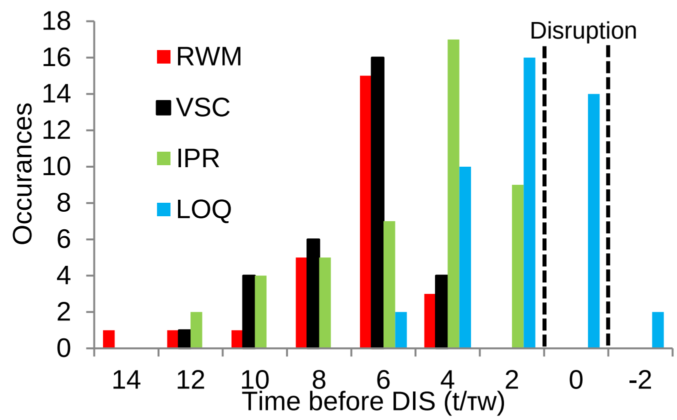

***Figure MS-14**: Histogram of the timing of various disruption chain events in the 44 discharge NSTX database before the time of disruption, within 70 ms.*

instances where the density reached the Greenwald limit (GWL). Note that tearing modes were stable during these discharges and therefore no tests for tearing modes (such as previously described) will be included in the analysis of the database presented here.

With the RWM $B_p^{n=1}$ lower sensor amplitude threshold of 30G ($\delta B/B_0$ ~ 0.67%) used here the RWM warning was typically found near the disruption limit. In 59% of the cases, the RWM event occurred within 20 τ_w of the time of disruption (DIS) (where τ_w is the time scale of penetration of magnetic flux through the conducting structure, taken here to be 5 ms). Additionally, many of the earlier RWM warnings could not be considered false positives; they cause decreases in β_N, with subsequent recovery (as illustrated in Fig. MS-14).

Examining the common chain of events more closely can provide insight into how to cue avoidance systems to return to normal plasma operations. For example, if the RWM can be detected in real-time by a growing exponential signal on an external magnetic sensor, as demonstrated here, it is useful to know what the typical routes of plasma behavior directly follow the RWM so that plasma control systems may be employed to avoid them. Even in the work presented here, with a limited dataset and the limited amount of tests currently in DECAF, we can find interesting trends. Of the 44 RWMs, they were followed immediately by WPC and VSC (the two events related to bulk plasma motion) each 13 times, PRP 11 times, IPR 6 times, and LOQ once. The RWM event never proceeded immediately to LON or DIS without another event happening first. Looking at the two-event chains that happened directly after RWMs, we find that even though there are theoretically 42 two-event combinations that could occur from the seven currently tested for (in addition to RWM), six two-event chains accounted for 70% of the cases in this database. A histogram of the timing of some of the disruption chain events is shown in Fig. MS-14.

A reduced kinetic model for RWM stability

Generally the approach for unstable RWM avoidance is that real-time physics-based models will be employed for early warning of approaching marginal RWM stability. Unstable RWM detection based on an experimentally measured exponentially growing magnetic signal is useful for characterizing the timing of the RWM and its place in the chain of events leading to disruption of the plasma current (as shown in the previous subsection), but it can potentially come too late to take corrective action. One example of possible early warning is to examine when the plasma toroidal rotation profile falls into a weaker RWM stability region based upon kinetic stability theory [MS-8]. The recent success of kinetic modification

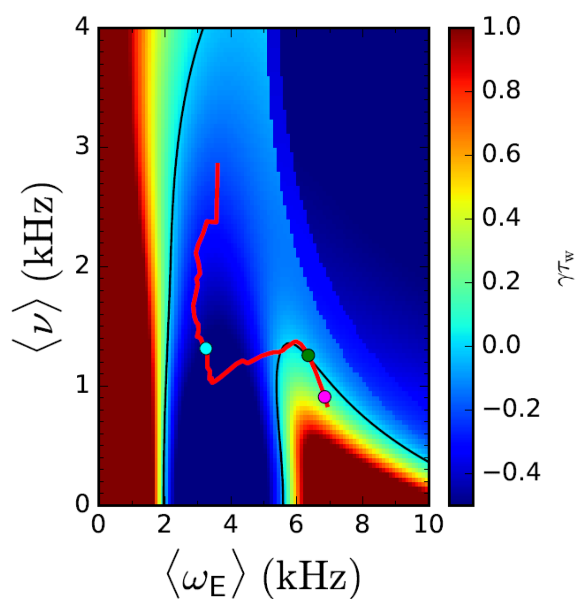

Figure MS-15: *Trajectory of NSTX discharge 139514 through <ω_E> vs. <ν> space. The colored contours represent the predicted growth rate at the C_β at the end time.*

to ideal theory, which contains stabilizing resonances via mode-particle interaction, in describing experimental RWM stability limits [MS-5] gives confidence in this approach. This approach will enable, for the first time, for an unstable growing RWM to be *anticipated*, rather than reacted to. One might then use a plasma rotation control system [MS-9] to avoid these unfavorable profiles, or use active control of the RWM [MS-10].

Models for ideal fluid stability δW terms have been previously developed for NSTX [MS-5], and have now been implemented in DECAF and tested for NSTX-U discharges (see, for example, Fig. MS-11). For resistive wall mode stability, once the kinetic term δW_K is defined, the normalized growth rate $\gamma\tau_w$ can be calculated from the RWM dispersion relation. For the kinetic δW_K term, full calculations with codes such as MISK cannot be performed in real time. Therefore there is a desire to simplify kinetic theory to facilitate real-time calculation.

Any such model must capture the essential physics learned from the successful application of kinetic theory to experimental results in recent years. Namely:

- Resonance between ω_E and ω_D of trapped thermal ions at lower plasma rotation, and with ω_b at higher plasma rotation provides a stabilizing component to δW_K, but in between these the kinetic effects are weaker, allowing for instability [MS-11,MS-12].
- Increased collisionality tends to damp the rotational resonance stabilization (see Fig. 3 of Ref. [MS-13]) and shift it to slightly lower rotation (see Fig. 6 of Ref. [MS-11]).
- The imaginary term of δW_K from trapped thermal ions tends to peak at lower plasma rotation than the real part (see Fig. 8 of Ref. [MS-7]) so that plasmas move in kinetic stability space as rotation changes in looping paths (see Fig. 5 of Ref. [MS-11]).

To that end, Gaussian functions were used to represent kinetic resonances. The positions of the peaks in $\langle\omega_E\rangle$ are determined by typical experimental ranges of ω_D and ω_b and the height, width, and position all dependent on collisionality. Coefficients for the functions were selected to reflect NSTX experience.

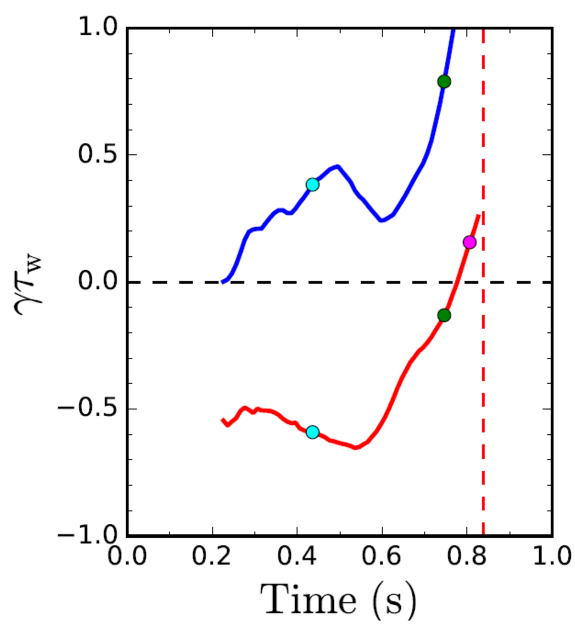

Figure MS-16: *Calculated ideal (blue) and kinetic (red) normalized growth rates for NSTX discharge 139514.*

Calculated $\langle\omega_E\rangle$ and $\langle\nu\rangle$ are used in the reduced kinetic model to calculate δW_K and finally, δW_K is used in the kinetic RWM dispersion relation to find $\gamma\tau_w$. Then, one can produce a stability diagram in the $\langle\omega_E\rangle$ vs. $\langle\nu\rangle$ space at a given level of C_β by plotting contours of $\gamma\tau_w$ (similar to Fig. 6 in Ref. [MS-11]). Here we show the trajectory of an NSTX discharge in this space as time increases and $\langle\omega_E\rangle$ increases while $\langle\nu\rangle$

decreases (Fig. MS-15). In this type of diagram the unstable region changes with time as C_β changes; the contours shown in the figure are for the C_β level at the discharge end time.

Finally and most importantly, it is natural to simply plot the growth rate as a function of time. In Fig. MS-16 we do this for the same discharge for both the fluid and kinetic growth rate, where it is easy to see the transition into the unstable range at a time of around 0.8s.

It is worth noting that the above analysis and plotting has been performed post-discharge on NSTX data. Naturally in the future the goal is to implement this model in real time, in which case the crossing (or even the approach) to the unstable region would be used in a disruption avoidance system to trigger a response to maintain stability. Disruption avoidance via plasma rotation profile control [MS-9] is close to becoming reality with the recent implementation of real-time velocity diagnostics [MS-14].

Halo current research

ITPA analysis of non-axisymmetric and rotating halo currents (ITPA MDC WG-6)

Large halo currents are often driven in the metal components of a tokamak vessel when a disrupting plasma comes into contact with the first wall. Halo currents are known to exhibit non-axisymmetric and rotating features in several devices including JET, Alcator C-Mod, DIII-D, ASDEX Upgrade, and NSTX. Such non-axisymmetries are of great interest to ITER because they can increase mechanical stresses during a disruption, especially if the rotation resonates with the natural frequencies of the vessel. As such, the ITPA MHD, Disruption, and Control Topical Group formed a working group to conduct a multi-machine analysis of these phenomena. This working group (ITPA MDC WG-6) is led by researchers on the NSTX-U team. The ITPA non-axisymmetric halo current database presently includes data from C-Mod, DIII-D, AUG, and NSTX. This fiscal year, a collaborative visit to ASDEX Upgrade resulted in the addition of hundreds of AUG shots to the database. Measurements from JET will be added as they become available. The various contributions to the database are processed within a common analytical framework to facilitate direct comparisons between devices.

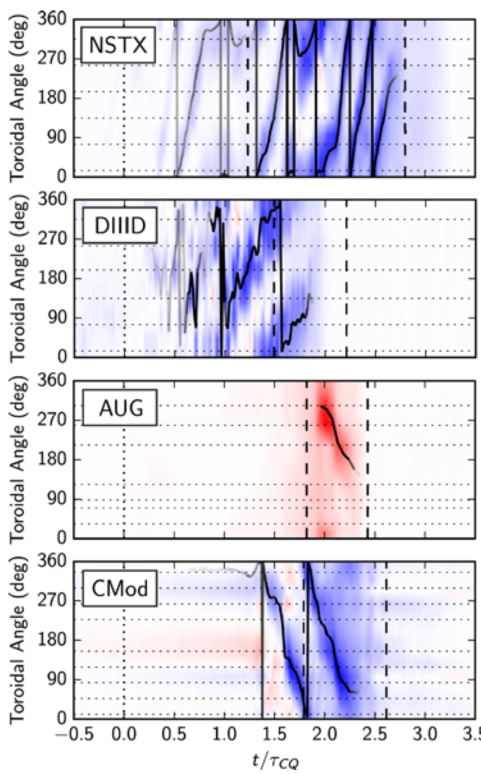

Figure MS-17: *Toroidally resolved measurements of non-axisymmetric and rotating halo currents in four different devices. Color represents the halo current magnitude, while the black lines track the toroidal phase of the rotating halo current lobe. Time is normalized to the characteristic fast quench time for each device,* τ_{CQ}.

Figure MS-17 shows representative halo current measurements from each of the four devices in the database. These data are obtained from toroidally resolved arrays of halo current sensors that are comprised of either shunt tiles or segmented rogowski coils. In each panel of the figure, the halo current amplitude, I_h, is plotted in color as a function of time and toroidal angle. The timebase is normalized to the characteristic 'fast' quench timescale for each device, τ_{CQ}. The black lines represent the toroidal phase of the rotating halo current lobe. It is clear that significant non-axisymmetries and rotation are observed in each device. Furthermore, similar rotation frequencies are observed across devices. In light of the current-quench-normalized timebase, this indicates that the physics driving the rotation may be linked to the current quench.

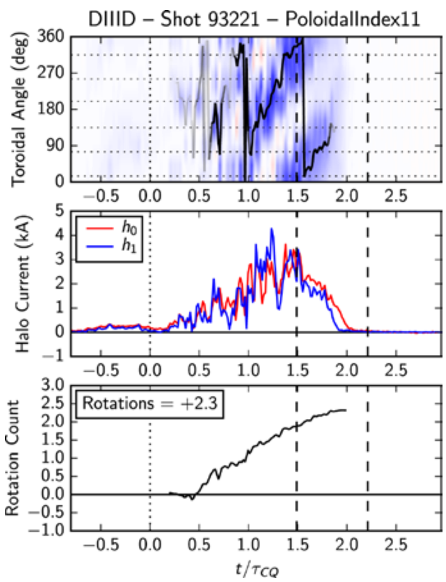

Figure MS-18: *Sample analysis of DIII-D halo currents. The* n=0 *and* n=1 *mode amplitudes*, h_0 *and* h_1, *are comparable until the halo currents symmetrize late in time. More than two complete rotations are observed.*

The details of the analysis presented in Fig. MS-17 are shown in Fig. MS-18. In order to quantify the non-axisymmetry and rotation, the data are toroidally decomposed at each time point using a simplified model function of the form $I_h(\phi) = h_0 + h_1\sin(\phi - h_2)$, where ϕ is the toroidal angle, h_0 is the n=0 amplitude, h_1 is the n=1 amplitude, and h_2 is the n=1 phase. In Fig. MS-18, h_0 and h_1 have comparable amplitudes until late in the disruption when h_1 decays away and the halo currents symmetrize. This late symmetrization, which is frequently observed, is likely due to the loss of closed magnetic surfaces in the plasma. Finally, in order to quantify the total amount of rotation during a given halo current pulse, $h_2/2\pi$ is integrated in time. More than two complete rotations are observed during the sample DIII-D disruption shown in Fig. MS-18.

The results from the halo current analysis in Fig. MS-18 facilitate the correlation of various quantities of interest. In Fig. 3a, total rotation is plotted against measured non-axisymmetry. Here, non-axisymmetry is quantified in terms of the toroidal peaking factor, TPF = $\max[I_h(\phi)]/\mathrm{mean}[I_h(\phi)]$, while rotation is quantified using the rotation count metric from Fig. MS-18. Fig. MS-19a shows that C-Mod has low-to-modest peaking and modest rotation, AUG has high peaking but little rotation, NSTX has high peaking and high rotation, and DIII-D spans the parameter space, except at high rotation. Thus, the collective IPTA non-axisymmetric halo current database covers a broader parameter space than is spanned by any single machine.

Finally, in Fig. MS-19b, the measured non-axisymmetry (TPF) is plotted against the 'halo current magnitude.' Here, the halo current magnitude is defined as the peak halo current measured in each shot normalized to both the pre-disruption plasma current and the median of all halo current magnitudes for a given device. As Fig. MS-19b shows, the halo current magnitude and the toroidal peaking factor are positively correlated. Additionally, both DIII-D and C-Mod have outlier populations at large halo current magnitude. The outlier populations are not the same, however, in that those from DIII-D are highly peaked while those from C-Mod are quasi-symmetric. Regardless, the overarching positive correlation between TPF and halo current magnitude warrants further investigation. This positive correlation runs counter to the published inverse correlation between the TPF and the 'halo current fraction,' which is instead defined as the total inferred halo current normalized to the pre-disruption plasma current. This result highlights the importance of determining the relationship between the halo current magnitude and the halo current fraction. If it is in fact the case that larger halo currents produce larger non-axisymmetries, then it is even more imperative for the success of ITER to understand the physical processes that drive halo current non-axisymmetries and rotation.

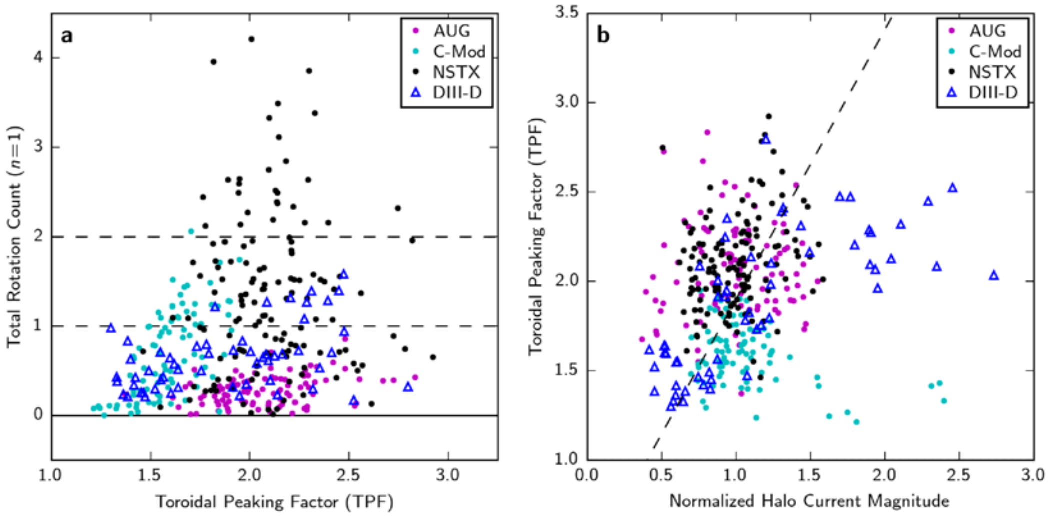

Figure MS-19: *Scatterplots of non-axisymmetry (toroidal peaking factor), rotation, and halo current magnitude from the ITPA non-axisymmetric halo current database. The halo current magnitude is normalized to both the pre-disruption plasma current and the median of all halo current magnitudes from a given device.*

The results of this multi-machine analysis of non-axisymmetric and rotating halo currents will be presented at the 26th IAEA Fusion Energy Conference in Kyoto, Japan in October 2016.

Halo current measurements in NSTX-U

NSTX-U is equipped with several arrays of halo current sensors. First, two rows of toroidally resolved shunt tile measurements (10 shunt tiles in total) are installed in the lower outboard divertor in a configuration similar to that used to acquire the NSTX data in the ITPA database described above. Additionally, 18 shunt tiles are installed on the new NSTX-U center column at various toroidal locations and vertical positions. Finally, an array of 'rotated mirnovs' at the midplane of center column acts as a segmented rogowski coil to measure currents flowing vertically in the center stack casing. Each of these halo current sensor arrays was instrument for the FY16 campaign, and halo current data from both the shunt tiles and the rotated mirnovs was successfully acquired. Pending post-run calibrations of the shunt tiles, the NSTX-U halo current data will be analyzed and compared to previous results.

The measurements from the center stack shunt tile array will be the first shunt tile measurements form the center column of a spherical torus. These data are of particular interest given the success of the NSTX-U shutdown handler in PCS, which drives plasmas into the center column in a controlled manner in order to prevent vertical displacement events that can stress the vessel and the coils. The halo currents which were recorded on the center column late in these controlled shutdown events will be studied in detail.

Disruption Modeling

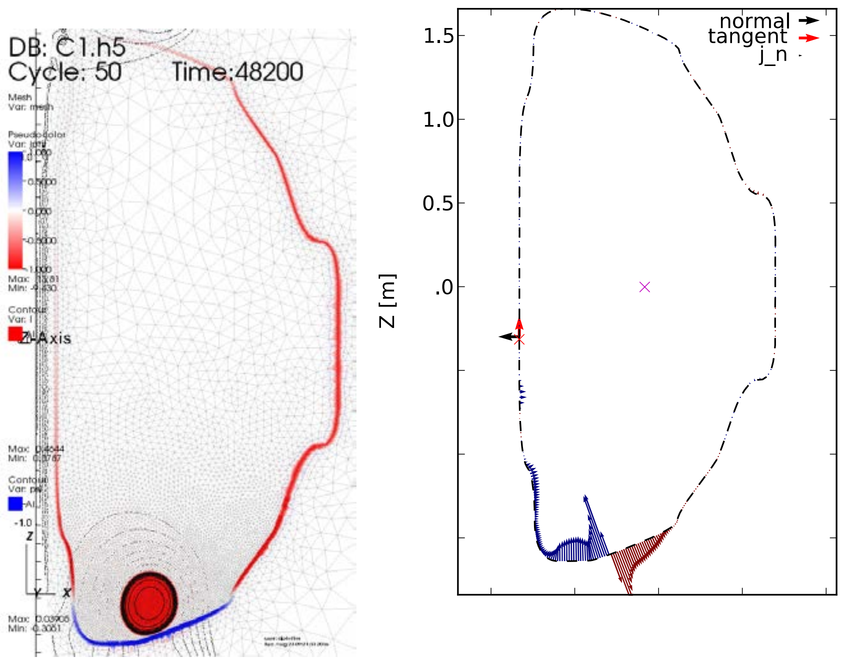

Figure MS-20*: (left) The toroidal current density roughly 30 ms into a M3D-C1 simulation of a VDE in NSTX, during the current quench. Note the significant induced currents in the wall. (Right) The normal current density at the wall (*i.e. *Halo currents) in the simulation at the same time. Figures courtesy D. Pfefferlé.*

Initial calculations of vertical displacement events in NSTX plasmas have been performed with the extended-MHD code M3D-C1. These calculations seek to quantify the electromagnetic forces produced in the wall by both induced eddy currents and Halo currents during disruptions, and to guide the development of future Halo current diagnostics on NSTX-U. In these calculations, M3D-C1 is initialized with a vertically unstable reconstructed Grad-Shafranov equilibrium, and the plasma is then evolved according to the extended-MHD equations in the presence of a resistive wall [MS-17]. As the plasma displaces toward the wall, significant induced currents and Halo currents are observed in the simulations (*c.f.* ***Figure MS-20***). Once the plasma becomes limited by the divertor, the edge safety factor drops due to the scraping-off of the edge, and the plasma eventually becomes unstable to non-axisymmetric modes.   Initial calculations show that the non-axisymmetric wall forces induced in this type of event are highly localized to the conducting structures in the divertor, and are small relative to the axisymmetric forces. Work is ongoing to improve the modeling of the temperature of the Halo region in these simulations, which is found to affect the growth rate of non-axisymmetric modes considerably. These calculations represent a significant advance over previous calculations because of the physically realistic timescales (~30 ms) that can be modeled with M3D-C1 at realistic levels of resistivity while considering fully 3D evolution.

Massive gas injection and electromagnetic particle injector research

MGI System

Predicting and controlling disruptions is an important and urgent issue for ITER. Methods to rapidly quench the discharge after an impending disruption is detected are also essential to protect the vessel and internal components of an ST-FNSF. In support of this activity, NSTX-U will employ three Massive Gas Injection (MGI) valves that are very similar to the double flyer plate design being considered for ITER. NSTX-U will be the first device to operate this valve design in

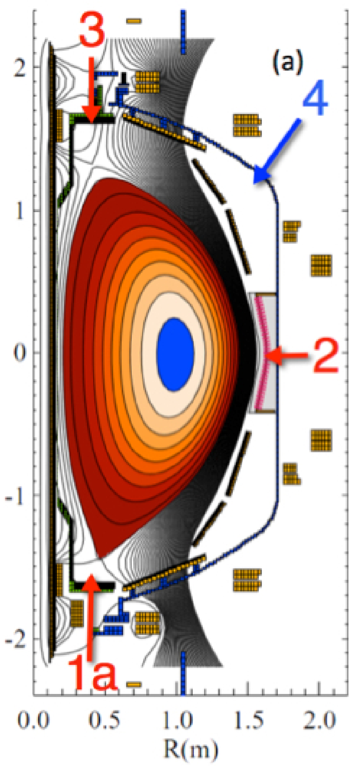

Figure MS-21: *Existing (Red) and Planned (Blue) MGI valve locations on NSTX-U.*

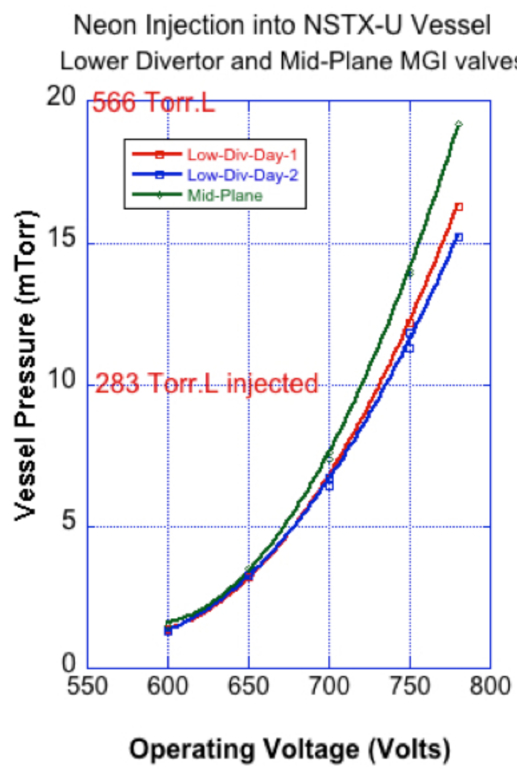

Figure MS-22: *Vessel pressure increase as a function of operation voltage for the valves located at positions 1a and 2.*

plasma discharges. These valves have been tested off-line and deliver the required amount of gas (~ 200 – 400 Torr.L) to support NSTX-U experiments, which will offer new insight to the MGI data base by studying gas assimilation efficiencies for MGI gas injection from different poloidal locations, with emphasis on injection into the private flux region. The valve has also been successfully operated in external magnetic fields of 1 T. A recently published journal paper [MS-15] describes the results obtained from these off-line tests.

Three of these valves have been installed on NSTX-U. These correspond to locations 1a, 2 and 3 in Fig. MS-21. In preparation for FY16 MGI experiments, the goal of which was to conduct a comparison of the mid-plane to lower divertor injection locations, the lower-divertor and mid-plane valves were commissioned and prepared for full operational capability. The capacitor based power supplies needed to operate these valves were operated at 1kV, which is more than the ~800V needed for injecting 400 Torr.L of neon into NSTX-U. Both these valves were then tested for full operation in nitrogen, helium, and neon at the full operating pressure of 10,000 Torr. Figure MS-22 is a plot of the amount of neon injected as the operating voltage is increased. These valves are now ready to support plasma operation. During the FY16 NSTX-U outage the upper MGI valve will be commissioned and prepared for full operational capability.

EPI System

While the MGI system may be adequate for most disruptions, the warning time for the onset of some disruptions could be much less than the MGI system response time. To address this important issue, a novel system based on the rail-gun concept was designed, components fabricated and the system fully assembled. The system consists of a 1m long rail gun powered by a 20mF, 2kVcapacitor bank. The capacitor bank parameters are essentially the same as that used for the transient CHI experiments on NSTX. A photo of the system is shown in Fig. MS-23.

The device referred to as an Electromagnetic Particle Injector (EPI) is fully electromagnetic, with no mechanical moving parts, which ensures high reliability after a period of long standby, and is described in a recent journal publication [MS-16]. In addition to responding on the required fast time scale, its performance substantially improves when operated in the presence of high magnetic fields [MS-16]. The system is also suitable for installation in close proximity to the reactor vessel. Experimental results from the operation of this system will be presented at the 2016 IAEA Fusion Energy Conference.

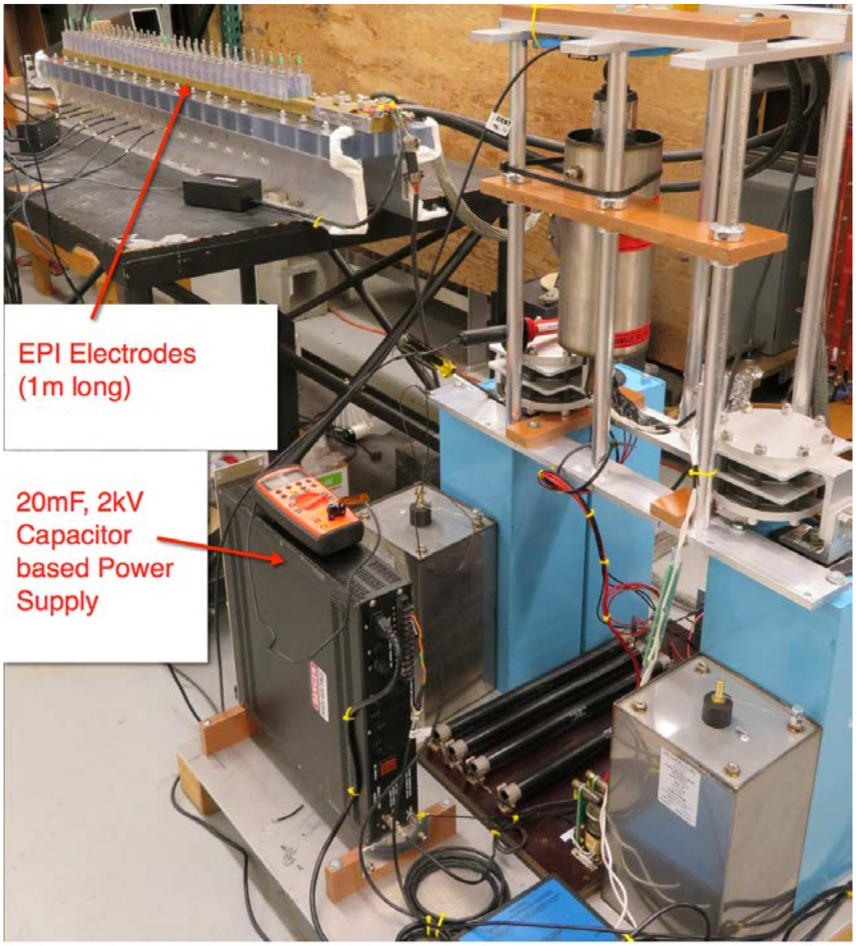

Figure MS-23*: The EPI system, at the University of Washington, showing the main acceleration electrodes and the power supply.*

Advanced 3D MHD Spectroscopy in NSTX-U

3D Magnetic Diagnostics Upgrades on NSTX-U

Progress has been made on a conceptual design for possible upgrades to the 3D magnetic field diagnostics on NSTX-U. Past experience on greatly extending and verifying the 3D magnetic diagnostics on DIII-D has been leveraged to study proposed magnetic sensor designs as part of collaborative research between General Atomics and the NSTX-U team. The existing 12-sensor arrays on NSTX-U are found to have sufficient coverage of the torus to simultaneously measure toroidal mode numbers less than n=6 on both the low and high field side of the torus; however, the poloidal coverage is insufficient to resolve the local poloidal structure. Note that signals from the new array of poloidal field sensors installed on the centerstack ("HBP" in Fig. MS-24) were not acquired in 2016 so the data quality from that location has not yet been verified; however, data in the 2017 campaign with the HBP poloidal field sensor array is anticipated.

Recent analysis has focused on improving the capability to measure stationary or near-stationary 3D fields that may result from the plasma response to external sources of non-axisymmetric fields such as intrinsic field errors or non-axisymmetric control coils. Ongoing study of the expected plasma response structure in NSTX-U at high plasma pressure as predicted by the MARS-Q code has identified the top and bottom of the machine as favorable locations where relatively large radial and poloidal field perturbations are especially expected when applied fields couple strongly to the plasma. An example is shown in Fig. MS-24 where the n=1 current in the lower NCC coil array is shifted toroidally by 150° with respect to the upper NCC coil. This coil configuration couples strongly to the damped resistive wall mode (RWM) leading to significant 3D field perturbations at the top and bottom of the device and much smaller fields along the centerstack. Previous studies of active RWM feedback performance have also identified the top and bottom of the device as preferred locations for additional probes. This study corroborates those results and further confirms that kinetic effects are not expected to diminish the plasma response. Future work is aimed at investigating the plasma response across a wide range of plasma equilibria in order to identify any benefit from an extensive set of field probes on the centerstack, and to optimize the sensor locations and dimensions.

Extended MHD Spectroscopy and Multi-mode Response Detection

In NSTX-U, NCC coils will be very important actuator to study 3D plasma response, ELM control, MHD instability control etc. Based on the Nyquist study of plasma response in DIII-D and NSTX-U plasma [MS-18, MS-19], a new method of extending NCC capability to measure the MHD spectroscopy and to reveal the detail information of plasma response is developed here. Associating with the frequency scan in Nyquist analysis, the new modified Nyquist method further includes the information of coil phasing. It requires to scan the coil phase at each given coil frequency. Considering the Padé approximation, the modified plasma transfer function depending on the coil phase and frequency is developed by assuming the linear plasma response. The transfer function with respect to different sensor in the machine is

$$P_j(\Delta\phi, f) = \sum_{i=1}^{N} \frac{a_i^j + b_i^j e^{-i\Delta\phi}}{f+\gamma_i}, \qquad (1)$$

where P_j is the plasma transfer function of jth sensors. f is the coil frequency of rotating the fields. γ_i is the eigenvalue of ith eigenmode and must be the same on different sensor due to the assumption of linear response. a_i^j and b_i^j are the coefficients of each eigenmode on different sensor. The phase difference between the upper and lower coils $\Delta\phi=\phi_{up} - \phi_{low}$, where ϕ_{up} and ϕ_{low} are the phases of upper and lower coils respectively. By fitting Eq.(1) to the measured plasma response, each major eigenmode responding to the external fields can be separated. The damping rate, real part of γ_i, of each eigenmode can be inferred by the extracted transfer function. This new method is not only applicable to NSTX-U with NCC coils but also any machine having two sets of coils which can rotate the coil current and the relative phase e.g. DIII-D or EAST devices. The experiments based on this new method has been proposed and accepted by DIII-D group. Here, we use the existing DIII-D experimental data and one MARS-F simulation to verify the modified Nyquist method and shows its power of analyzing the plasma response.

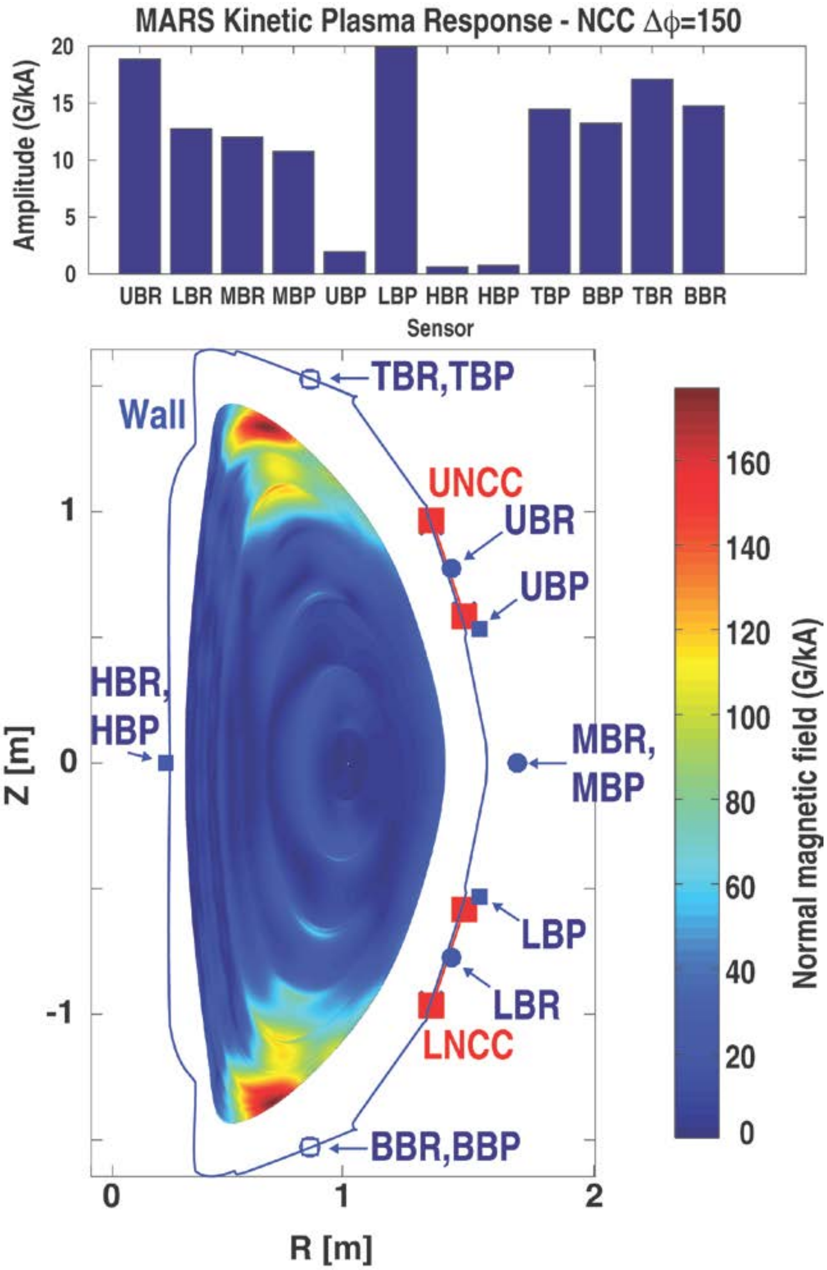

Figure MS-24*: (top) Synthetic magnetic sensor signals calculated based on the computed n=1 plasma response (bottom) as predicted by the MARS-Q code for an NSTX-U equilibrium at normalized beta of 5.5 and q95=6.9. The candidate sensor locations considered in this study include HBR, T/BBR, T/BBP, and MBR/P. The remaining sensor arrays are already installed. Additional sensor locations are under consideration.*

In DIII-D experiments, the n=2 plasma response experiment has shown the evidence of multi-mode response and ELM suppression thorough the coil phasing scan [MS-20]. However, many open questions related to [MS-20], need to be resolved e.g. how many and which major eigenmodes contribute to the multi-mode response, how to optimize the coil configuration to achieve more reliable ELM suppression. In this DIII-D experiments, the coil phase is scanned from 0 to 360 degree with zero coil frequency. Therefore, in this special case, f=0 in Eq.(1). In the fitting procedure, three poloidal sensors, MPID66M at low field side, MPID1A and MPID1B at high field side, are considered. The measurements of each sensor are fit by the corresponding $P_j(\Delta\phi)$ simultaneously. Here, a one pole model (N=1) and a three pole model (N=3) are applied to fit to the experimental data. The comparison of signal amplitude between the fitted plasma transfer functions and the experimental data, is reported in Fig. MS-25. It clearly shows the one pole case has a poor agreement with the experiments particularly at MPID1B sensor. On the other hand, the three pole case agrees well with both amplitude and phase of measured response at each sensor. The two pole model is also tested and can be better than one pole model but still cannot make a good fitting as the three pole transfer function. Besides indicating the multi-mode response, these results also provide the detailed information that three eigenmodes play major role to respond to the coil perturbation. Furthermore, the results also confirm that the plasma response observed in the experiments is linear. However, due to the zero coil frequency, the value of γ_i is meaningless, where the dimension of γ_i can be determined only when f is finite.

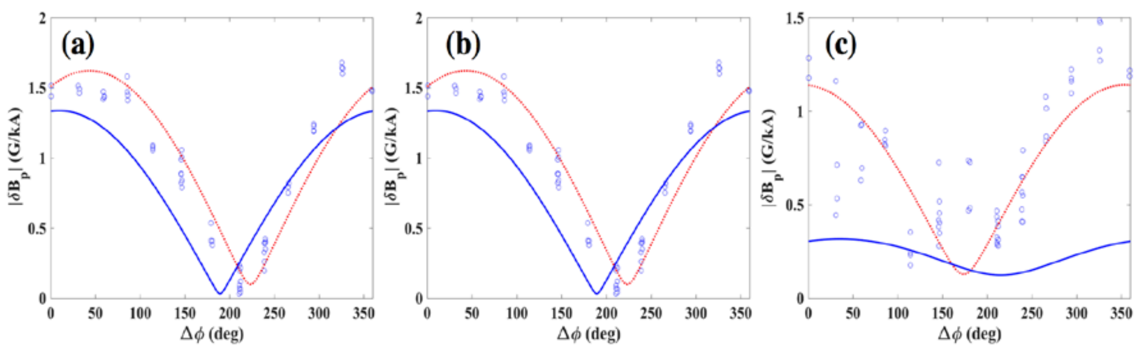

***Figure MS-25**: Phase scan of plasma response measured by the magnetic sensors (a) MPID66M at the low field side, (b) MPID1A and (MPID1B) at the high field side. The amplitude of poloidal magnetic perturbation $|\delta B_p|$ is compared among the experimental measurements('o'), the extracted one pole (solid line) and three pole (dotted line) transfer function.*

The fitting of transfer function in Eq.(1) is further verified with the n=1 fluid response simulated by MARS-F code, where one D-shape numerical equilibrium with β_N=0.97, aspect ratio A=0.24, is adopted. A radial sensor at the middle plane of LFS is assumed to measure the fluid response. In the MARS-F simulation, the coil phasing scan is performed at f=10 Hz, 30 Hz and 60 Hz respectively. Then Eq.(1) is applied to fit these simulated sensor measurements where the fitted Eq.(1) agrees well with the MARS-F simulation. In this numerical equilibrium, we find the plasma response is contributed by the two major eigenmodes, where the transfer function measured at the simulated sensor is

$$P = \frac{0.9+0.17i+(0.92-0.66i)e^{-i\Delta\phi}}{if-(-30.71-2.22i)} + \frac{2.27-0.094i+(16.9+0.027i)e^{-i\Delta\phi}}{if-(-458.7+0.299)i}. \quad (2)$$

On the right hand side of Eq.(2), the first term and the second term represent the least stable mode λ_1 and the secondary mode λ_2. To verify the reliability of extracted transfer function, the Nyquist contour simulated by MARS-F is compared with the one given by Eq.(2), where the phase difference of up-lower coils is Δϕ=240 deg in Fig. MS-26. It shows the transfer function can well repeat the response in whole frequency region, though Eq.(2) is obtained from the phase scan of the three low frequencies.

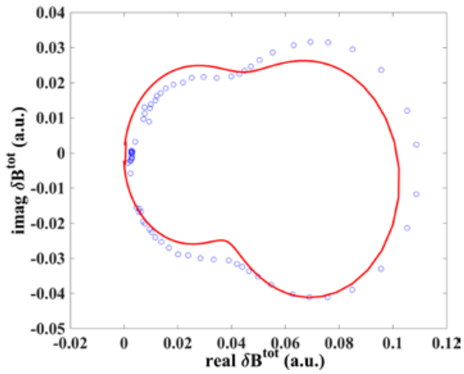

Figure MS-26: Comparison of Nyquist contour between the MARS-F direct simulation ('o') and the extracted transfer functions (solid line).

The DIII-D example and the numerical simulation indicate the new method can be valid in both experiments and the simulation. The new method greatly reduces the requirement of extracting the plasma transfer function, where the conventional Nyquist analysis requires scan the coil frequency in a wide range. The plasma response in the high frequency can be too weak and hard to be measured with small signal noise. It can also be polluted by other high frequency mode e.g. ELM. The new method can avoid the high frequency scan and stay with the low coil frequency by introducing the phase information. The other advantage of this method is to optimize the coil phase and frequency to amplify the preferred eigenmode for ELM suppression, which can be important to NSTX-U and other devices. For instance, we can choose the coil phase and frequency through the transfer function to amplify the secondary mode which may have more peeling structures leading to the small island open and stochastic of field lines. Fig. MS-27 illustrates this idea by calculating $|\lambda_1/\lambda_2|$ and $|\lambda_2/\lambda_1|$ respectively. It clearly shows the best phase to amplify least stable eigenmode is zero degree. The amplification of secondary mode is at 240 degrees. In particular, increasing the coil frequency can further amply the the secondary mode. This finite coil frequency may also be important to avoid the core mode locking.

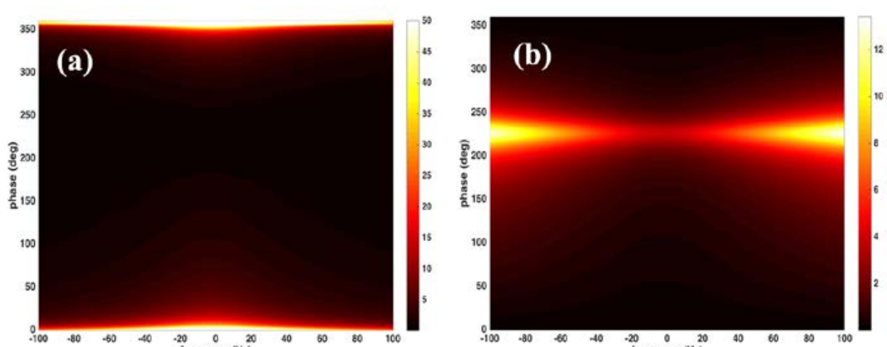

***Figure MS-27**: The phase and frequency scan of two extracted transfer functions' (a) $|\lambda_1/\lambda_2|$ and (b) $|\lambda_2/\lambda_1|$.*

After the installation of NCC coils in NSTX-U, the modified Nyquist analysis can be greatly helpful to the detection of MHD spectroscopy and very useful to design the MHD control system and to better predict plasma behavior with extracted transfer function. The method can also be a good candidate as a real-time monitor of the plasma stability in future long-pulse fusion reactor.

Study of 3D Physics Capabilities with NCC

Systematic NCC Optimization for NTV with Self-consistent Perturbed Equilibrium

The design studies of new non-axisymmetric control coil (NCC) have been continued to assess 3D physics capabilities and optimize NCC configurations. The optimization of coil configurations for NTV is particularly a complicated task, due to the non-linearity in the transport process with respect to the applied field and spectrum. A brute-force search has been greatly improved by coupling stellarator optimizer to IPEC, called IPEC-OPT [MS-2], as reported in the past. In addition, the newly developed method, general perturbed equilibrium code (GPEC) [MS-21], has also been applied to this problem of NCC optimization for NTV. GPEC provides two fundamental improvements; (1) GPEC solves 3D equilibrium and neoclassical transport together, giving self-consistent NTV calculations, and (2) more importantly, it reveals the NTV torque matrix, which entirely redefines the optimizing process.

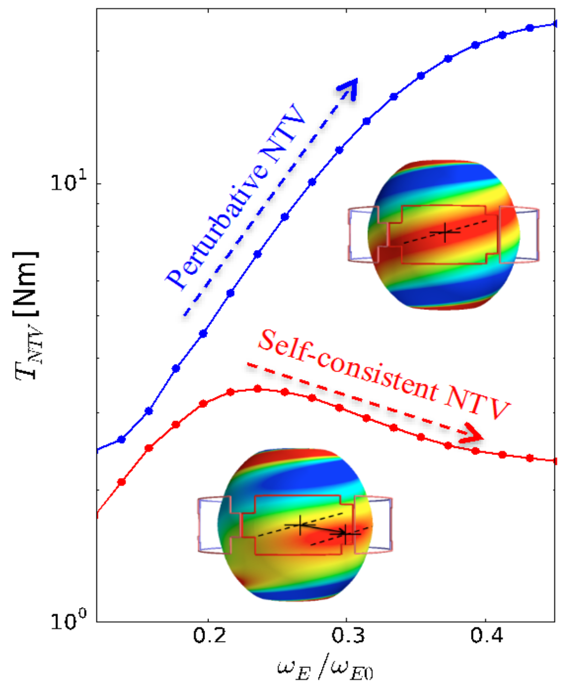

***Figure MS-28** :Perturbative NTV with IPEC vs. self-consistent NTV with GPEC for an NSTX-U target, as a function of E×B. Subfigures show plasma response to the applied 3D field for each.*

NTV torque profiles obtained by GPEC are kinetically consistent with both equilibrium and transport in 3D, which can be very important whenever local or global torque is substantial, due to the strong toroidal phase shift in response and consequent inefficiency in coupling between plasma and external field. This is called the self-shieling process as illustrated in Fig. MS-28, which can significantly change NTV predictions. In fact, the importance of self-consistent calculations with kinetic tensor pressure in 3D response has been highlighted by recent MARS-K applications to DIII-D [MS-19] and NSTX, as previously reported.

The self-consistent NTV torque matrix in GPEC is obtained by integrating energy and torque, $2\delta W + \frac{i\tau_\varphi}{n} = -\int \xi \cdot F[\xi] = \Xi_\psi^+ \cdot W_P \cdot \Xi_\psi$, where Ξ_ψ is a radial displacement vector in Fourier space, in which only the surface term remains since the volumetric term vanishes by the force balance. The anti-Hermitian part of the plasma response matrix function $W_P(\psi)$ is the torque response matrix function $\mathrm{T}(\psi)$, which provides NTV torque in any point of radius by the quadratic form involving the external field Φ on the control surface, i.e. $\Phi^+ \cdot \mathrm{T} \cdot \Phi$. Given $\mathrm{T}(\psi)$, one can immediately answer various questions for optimization. An important example is the maximum (or minimum) torque possible for any arbitrary interval (ψ_1, ψ_2), and corresponding 3D field distribution, with the integrated total torque up to the boundary ψ_b fixed. The answer is the maximum (or minimum) eigenvalue and eigenvector of the composite matrix $\mathrm{T}^{-1}(\psi_b)[\mathrm{T}(\psi_2) - \mathrm{T}(\psi_1)]$, giving NTV profile optimization by a single code run with much better efficiency and accuracy than the previously successful method with IPECOPT, as illustrated in Fig. MS-29.

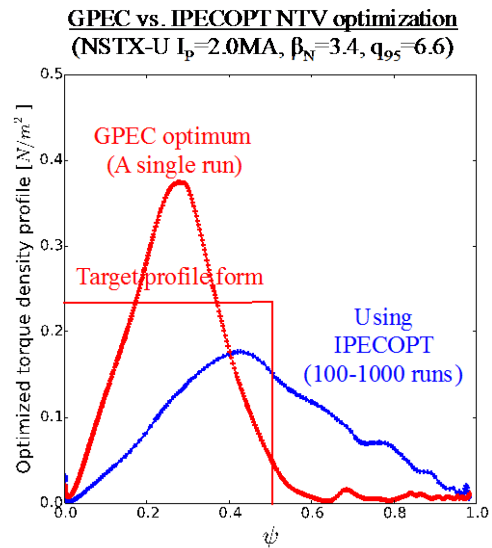

Figure MS-29*: Optimized torque profile to maximize torque in ψ<0.5 while minimizing torque in ψ>0.5 for an NSTX-U target, using GPEC vs. stellarator optimizers coupled with IPEC.*

Furthermore, the eigenvectors provide a way to properly order and decompose 3D fields with respect to local torque. In many cases, it has been shown that negative poloidal modes (backward helicity modes) play an important role in balancing the positive poloidal modes for local torque optimization. The access to the optimized field distribution is of course limited in practice by available coils, but it is also straightforward to couple the coils to the torque matrix function and optimize the current distributions in the coils, as has been actively studied in KSTAR with existing internal coils, and also in NSTX-U with non-axisymmetric control coils (NCC) and in ITER with error field and ELM control coils under design.

Comparisons of Resistive 3D Plasma Response in DIII-D and NSTX-U with NCC

Understanding the plasma response to applied and intrinsic non-axisymmetric resonant magnetic perturbation (RMP) and non-resonant MP (NRMP) fields is important for improving and controlling the confinement and stability of H-mode discharges. Currently, research being done by General Atomics in this area is focused on comparing differences between the plasma response predicted by the M3D-C[1] linear resistive MHD code in NSTX-U and DIII-D. The goal is to support a proposal for the installation of an in-vessel Non-axisymmetric Control Coil (NCC) in NSTX-U that will be capable of extending our understanding of RMP and NRMP physics to lower aspect ratio (A) and higher normalized beta (β_N) over a broad range of q_{95}.

An integral part of this research relies on constructing kinetic plasma equilibria for NSTX-U and DIII-D discharges and carrying out accurate field line integrations studies. These studies involve characterizing changes in the vacuum magnetic topology due to RMP fields compared to the magnetic topology predicted by M3D-C[1] simulations due to the RMP and NRMP fields. Field line integrations studies are carried out with the TRIP3DGPU code [MS-22], a parallelized version of the TRIP3D field line integration code [MS-23]. TRIP3DGPU integrates a set of nonlinear magnetic field line differential equations, with the accuracy of its solution primarily dependent upon the poloidal position (r, θ) of the magnetic field line, the toroidal angle step size ($\Delta\phi$), and the fidelity of the equilibrium magnetic field representation. Quantifying the accuracy of the field line integration studies, obtained from the TRIP3DGPU vacuum and plasma response simulations, is essential for interpreting the impact of the RMP and NRMP fields on the plasma in NSTX-U and DIII-D. Results from a set of detailed accuracy tests, described in the next section, provide limits on the integration step size and the lengths of the field lines that can be compared between the vacuum and plasma response results while maintaining the same level of accuracy.

(1) TRIP3DGPU field line integration accuracy test

The approximate nature of numerical integration methods and machine precision introduces errors in magnetic field line tracing. To characterize the field line integration accuracy, we define the difference between the normalized magnetic flux of the i^{th} step, Ψ_i, and its predecessor, Ψ_{i-1}, as the relative error, $RE_i = |\Psi_i - \Psi_{i-1}|$. Ideally, RE_i should remain zero when tracing in the equilibrium-only magnetic field.

The accuracy when tracing an axisymmetric equilibrium using a standard DIII-D equilibrium reconstruction compared to that with the same equilibrium recalculated using the Grad-Shafranov solver in M3D-C[1] is shown in Fig. MS-30. Here, the DIII-D equilibrium is reconstructed from shot 147170 at time slice 3745 ms with I_p = 1.60 MA, B_T = 2.0 T, q_{95} = 3.4, A = 3.0 and β_N = 1.8 [MS-24]. The NSTX-U case is based on a model equilibrium, i.e., not an actual plasma discharge, with I_p = 1.45 MA, B_T = 1.0 T, q_{95} = 8.7, A = 1.9 and β_N = 4.0.

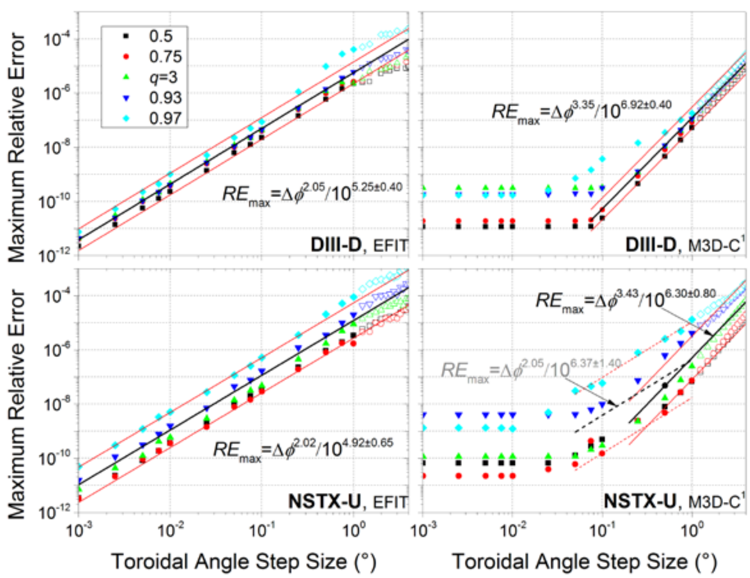

***Figure MS-30:** Maximum relative error as a function of the toroidal step size used to trace magnetic field lines in five different magnetic flux surfaces: 0.5, 0.75, q=3, 0.93, and 0.97 where the vacuum equilibria on the left are referenced as generic 'EFIT' reconstructions.*

Magnetic field lines from five magnetic flux surfaces, namely at Ψ = 0.5, 0.75, 0.93, 0.97, and q = 3, were traced with toroidal angle step sizes $\Delta\phi$ ranging from 0.001° to 4.0° in TRIP3DGPU for this accuracy test. Each field line traverses more than one poloidal turn with RE_{max} = max(RE_i) recorded. In reality, $\Delta\phi$ is rarely chosen to be greater than 1.0° due to the concern of numerical accuracy. In fact, we typically limit $\Delta\phi$ to between 0.001° and 1.0° as a compromise between accuracy and computational time. Therefore, in Fig. MS-30, data points with $\Delta\phi$ > 1.0° are marked with hollow symbols for information only. For each $\Delta\phi$, RE_{max}

typically becomes larger when tracing magnetic field lines closer to the plasma edge due to the curvature of local magnetic field.

In all four cases in this log-log plot, RE_{max} can be fitted and bounded by a band expressed as $\Delta\phi^{a}/10^{b\pm c}$. Since M3D-C[1] utilizes a finer 400 x 400 computational mesh than the standard 129 x 129 DIII-D and 121 x 121 NSTX-U equilibria and a high-order finite-element representation of the magnetic field, the M3D-C[1] field generally produces more accurate tracing results than EFIT from large $\Delta\phi$ down until RE_{max} saturates to a level at $\Delta\phi$ ~ 0.5°. The standard equilibria, however, utilizes a bicubic interpolation, whose RE_{max} in principle decreases monotonically with $\Delta\phi$ but it is not particularly useful in reality due to the potential excessively long computation time for $\Delta\phi < 0.001°$. In the expression of $\Delta\phi^{a}/10^{b\pm c}$, *a* is a parameter of particular interest and likely dependent on the computational mesh configuration and data interpolation method, as it controls the accuracy of approximating curves with straight lines. *a* is found to be approximately equal to 2 for the DIII-D and NSTX-U equilibria and 3.3 for M3D-C[1].

The local mesh quality especially at the boundary can impact magnetic field line tracing accuracy, as seen by RE_{max} at $\Psi = 0.97$, which resides outside the band for vacuum equilibria at $0.25° \leq \Delta\phi \leq 1.0°$ for both machines, and for the M3D-C[1] field at $0.05° \leq \Delta\phi \leq 0.75°$ in DIII-D. The M3D-C[1] mesh for NSTX-U seems to be a special case since all field lines, including $\Psi = 0.97$, show the same deviation. In the typical working range with $0.1° \leq \Delta\phi \leq 1.0°$, *a* is found to be 2.05 with a fairly large band width *c*, which suggests that this NSTX-U solution may be further improved by applying a better-quality M3D-C[1] mesh. Nevertheless, for all the different cases, RE_{max} remains below 10^{-4}, which corresponds to approximately 0.1 mm spatial difference. Therefore, it can be seen that by setting $\Delta\phi < 1.0°$ the accuracy of TRIP3DGPU field line integration is sufficient for interpreting the impact of plasma response on the 3D field line structures. In some cases when higher fidelity is necessary to resolve small islands, smaller $\Delta\phi$ can be chosen to reflect the spatial resolution requirements.

(2) Comparisons of DIII-D and NSTX-U vacuum and plasma response

As see in Fig. MS-31, the Poincare plots of the 9/3 islands for DIII-D with 4 kA RMP I-coil fields, undergo a significant change when the plasma response is included in the magnetic field line simulations. Here, the top and bottom subfigures show the M3D-C[1] vacuum field topology and single-fluid M3D-C[1] plasma response, respectively. This indicates that the plasma screening effect not only significantly reduces the island size but also modifies the poloidal location of the magnetic islands. Alternatively, Fig. MS-32 shows the Poincare plots of the 9/3 island for NSTX-U, with the top and bottom subfigures being the M3D-C[1] vacuum filed and M3D-C[1] plasma response, respectively. Here again, the plasma screening modifies the structure of magnetic islands and reduces the island size. Furthermore, in the center of 9/3 perturbations we see a splitting that results in 18/6 islands that are not observed in the DIII-D case.

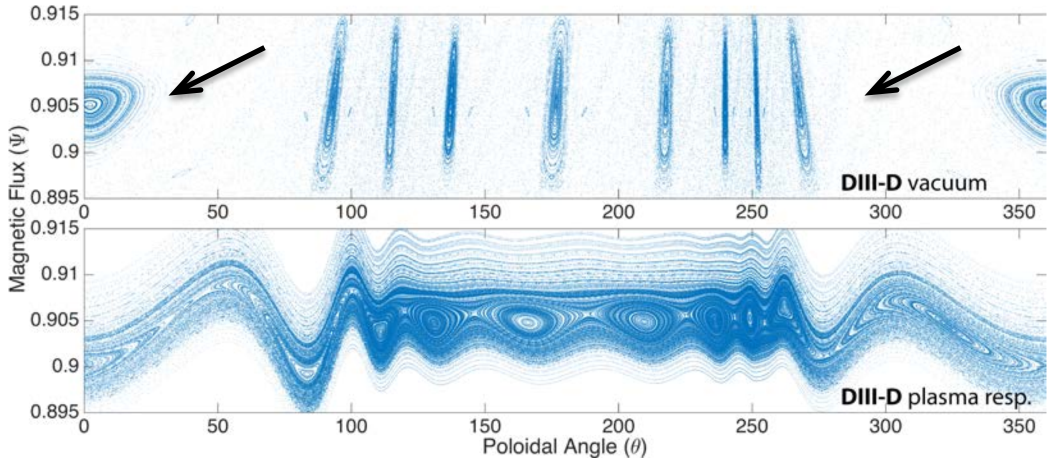

Figure MS-31: *Poincare plot for m/n = 9/3 islands in DIII-D discharge 147170 at 3745 ms; top: M3D-C¹ vacuum field, bottom: single-fluid M3D-C¹ plasma response*

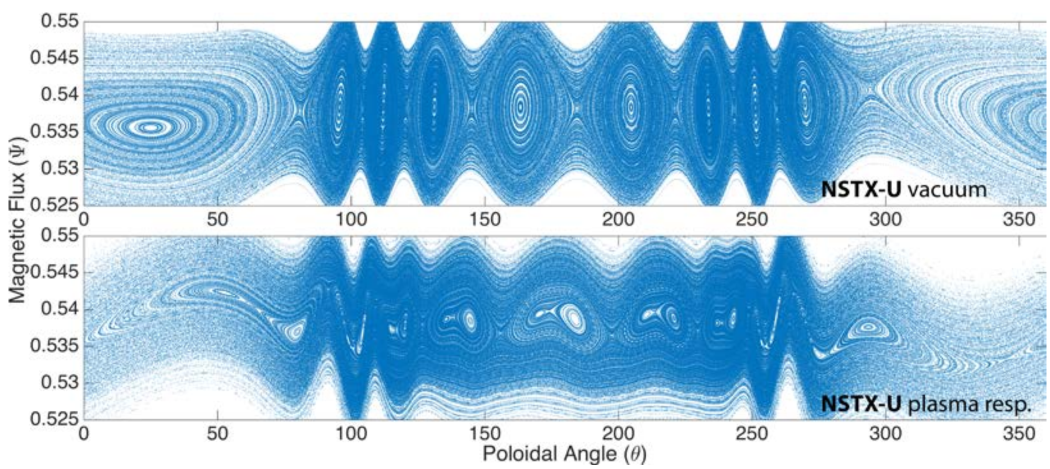

Figure MS-32: *Poincare plot for NSTX-U; top: M3D-C¹ vacuum field, bottom: single-fluid M3D-C¹ plasma response*

Comparing the vacuum versus plasma response in DIII-D and NSTX-U, we observe two competing effects. These are the screening of the RMP islands and a kinking of the flux surfaces due to the NRMP fields. By taking $\Delta\Psi_{\mathrm{vac}}/\Delta\Psi_{\mathrm{p.res}}$ for the largest island for both machines, where $\Delta\Psi$ is the difference between the maximum and minimum Ψ of the islands, the screening factors are found to be 3.83 and 2.20 for DIII-D and NSTX-U, respectively. In comparison to the 9/3 islands in DIII-D, the kink effect for NSTX-U is observed to be less significant, as can be seen by the DIII-D islands at 2.23° and 268.08°, which show large distortion and displacements in Ψ. This is likely due to the fact that the kink response is typically found to be stronger near the edge of the plasma and NSTX-U is operating at higher edge safety factor so the q = 3 surface is deeper inside the plasma.

As noted above, the M3D-C¹ code generates its own axisymmetric equilibrium starting from a kinetic equilibrium reconstruction. Ideally, these two Grad-Shafranov vacuum field solutions should be nearly identical, but in reality there are some differences. The difference between the two equilibria is used to assess how well the M3D-C[1] approximates the original kinetic equilibrium by comparing the location of O-points of both cases. In comparing the two equilibria for the cases shown above it is observed that the O-point locations are close to each other for DIII-D, but have a larger difference for NSTX-U. As an example, for the O-point near the outer equatorial plane, the poloidal angles for DIII-D are 2.23° vs 2.41°, with a difference less than one degree, while for NSTX-U, the poloidal angles becomes 74.77° vs 25.00°, showing a large discrepancy. This difference also exists in the location of other O-points, and its cause is under investigation. A potential cause is that the M3D-C[1] solution produces a better match to the equilibrium solution for DIII-D than NSTX-U. This may be due to the fact that vessel currents were not included in these M3D-C[1] calculations, which could have a more significant impact on the NTSX-U reconstructions than those in DIII-D. Future M3D-C[1] simulations will include a detailed model of the vessel currents and comparisons will be made to see if this resolved the differences.

References

[MS-1] S. A. Sabbagh et al., Nuclear Fusion **41**, 1601 (2001)
[MS-2] J.-K. Park et al., Nuclear Fusion **52**, 089501 (2012)
[MS-3] S. A. Lazerson et al., Physics of Plasmas **57**, 104001 (2015)
[MS-4] A. Glasser, Physics of Plasmas **23**, 072505 (2016)
[MS-5] J. W. Berkery, et al., Nuclear Fusion **55**, 123007 (2015)
[MS-6] S. A. Sabbagh et al., Nuclear Fusion **46**, 635 (2006)
[MS-7] J. W. Berkery et al., Physics of Plasmas **17**, 082504 (2010)
[MS-8] B. Hu and R. Betti, Physical Review Letters **93**, 105002 (2004)
[MS-9] I. R. Goumiri, et al., Nuclear Fusion **56**, 036023 (2016)
[MS-10] S. A. Sabbagh et al., Physical Review Letters **97**, 045004 (2006)
[MS-11] J. W. Berkery et al., Physical Review Letters **104**, 035003 (2010)
[MS-12] J. W. Berkery et al., Physics of Plasmas **21**, 056112 (2014)
[MS-13] J. W. Berkery et al., Physical Review Letters **106**, 075004 (2011)
[MS-14] M. Podesta and R. E. Bell, Review of Scientific Instruments (2016)
[MS-15] R. Raman et al., IEEE Transactions on Plasma Science (2016)
[MS-16] R. Raman et al, Fusion Science and Technology **68**, 797 (2015)
[MS-17] N.M. Ferraro et al., Physics of Plasmas **23**, 056114 (2016)
[MS-18] Z.R. Wang et al, 56th Annual Meeting of APS Division of Plasma Physics, **TI1.3** (2014)
[MS-19] Z.R. Wang et al, Physical Review Letters **114**, 145005(2015)
[MS-20] C. Paz-Soldan et al, Physical Review Letters **114**, 105001(2015)
[MS-21] J.-K. Park et al, 57th Annual Meeting of APS Division of Plasma Physics, **PI3.3** (2015)
[MS-22] R.C. Kalling, et al., Fus. Eng. Design 86 (2011) 399-406
[MS-23] T. E. Evans, et. al., Phys. Plasmas 9 (2002) 4957
[MS-24] T. E. Evans, Plasma Phys. Contr. F. 57 (2015) 123001
[MS-25] W. Wu, et al., 43rd European Physical Society Conference on Plasma Physics, July 4-8, 2016, Leuven, Belgium

B. Transport and Turbulence TSG Research Highlights

The completion of the first NSTX-U run campaign in 2016 has allowed for initial investigations of core transport and turbulence characteristics for both L-mode and H-mode discharges, as well as during L-H transitions. Work has also continued on analyzing previous results from NSTX and MAST, including validation of theory and simulation predictions.

1. First NSTX-U experiments

NSTX-U L-mode development

During commissioning, run time was allocated to develop diverted L-mode discharges over a range of plasma current (0.65-1.0 MA), line-averaged density ($1\text{-}4\times10^{19}$ m^{-3}), NBI heating powers (1-3+ MW) and tangency radii using the new 2nd NBI sources. While these discharges will be used for a variety of future core and boundary experiments, there is a priority to specifically develop quiescent L-modes suitable for validating simulations and models with transport and turbulence measurements. In particular, there is a multi-institutional effort to use NSTX-U L-modes at lower beta to validate electrostatic global gyrokinetic simulations at low aspect ratio and relatively large $\rho_*=\rho_i/a$ using multiple codes. This is an important step to be undertaken before benchmarking the electromagnetic versions of the codes, still under development in many cases.

Fig. TT-1 shows time traces from three example NSTX-U L-mode discharges with plasma currents of 0.65 and 0.8 MA, illustrating that relatively stationary discharges lasting 1.5 seconds were routinely obtained (with lower density plasmas extending to 2 seconds). Avoiding transitions to H-mode at higher power was accomplished via increased density using high field side gas fueling around 0.25-0.3 sec, visible in the inner-wall D_α emission. The higher density ($\sim4\times10^{19}$ m^{-3}), higher power (2.6 MW) discharges achieved normalized betas just over $\beta_N>2$ at $q_{95}\sim5$. Higher power >4 MW was injected into a few L-modes, but this resulted in L-H transitions and significant MHD that either disrupted the plasmas or resulted in H-L back transitions.

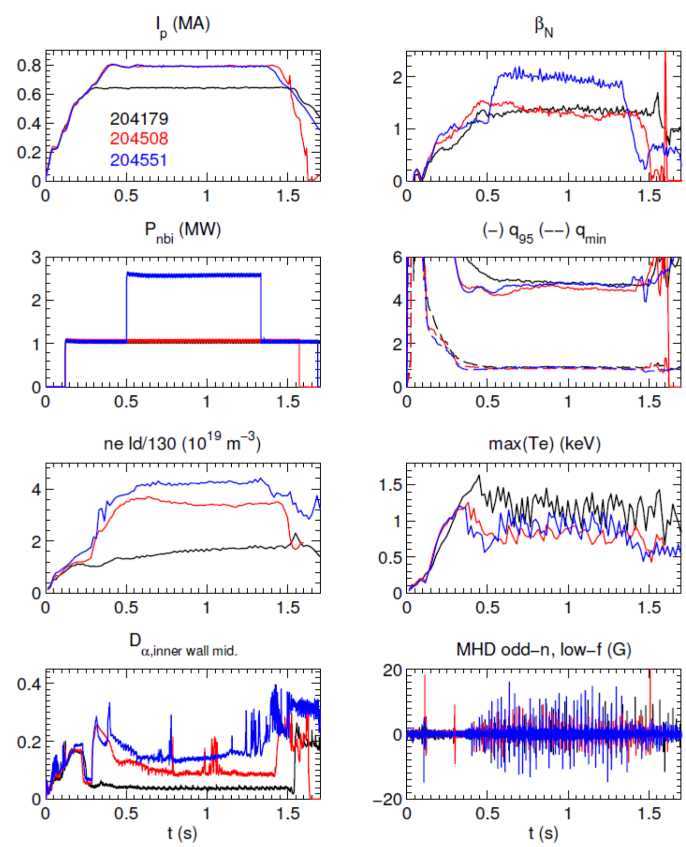

Fig. TT-1: Plasma time traces from three NSTX-U L-modes with varying plasma current, heating power and line-averaged density.

All the L-modes develop sawteeth after 0.4-0.5 s once q_{min} evolves below 1, as seen in the Mirnov coils, core electron temperature T_e, as well as neutron rate and hard x-rays (not shown). They have a period of Δt_{ST}~25-35 ms with an inversion radius around 125 cm, consistent with both T_e profiles and the q=1 surface from EFIT reconstructions (Fig. TT-2).

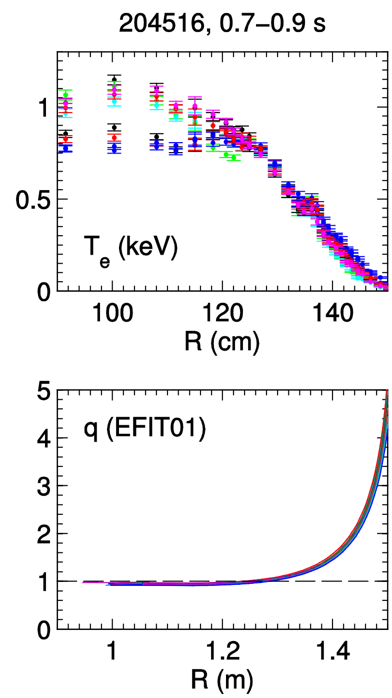

Fig. TT-2: T_e profiles (Thomson scattering) and q-profiles (EFIT01) during a 200 ms time window (0.7-0.9 s) illustrating the sawteeth inversion radius near the q=1 surface.

In many of the L-modes a strong ~8 kHz, n=2 mode also develops (apparent in Mirnov spectrograms, Fig. TT-3) that lowers the core density, temperature and rotation inside 135 cm, e.g. seen after t>1.3 secs in shot 204551 in Fig. TT-1. This mode is thought to be a 3/2 tearing mode, consistent with the location of the q=1.5 surface (Fig. TT-2) and the rotation frequency at this surface as measured by CHERs. A weak yet coherent ~8 kHz density fluctuation is also seen at the same radius in BES measurements (but not in adjacent channels), as well as in many chords of the soft x-ray diagnostic.

Additional L-mode discharges were successfully run at higher plasma currents up to 0.9 MA (q_{95}~4.5) and 1.0 MA (q_{95}~3.7), extending to the limit of available ohmic flux (~1.0 s at 1.0 MA). However these discharges all exhibit strong 3/2 tearing mode activity. The new 2nd NBI sources were also all tested in 0.8 MA L-modes. While CHERs measurements were unavailable for these shots, there are noteworthy changes observed in the Mirnov signals likely associated with changes in rotation and MHD stability (see Macrostability Research Highlights for more discussion of these features).

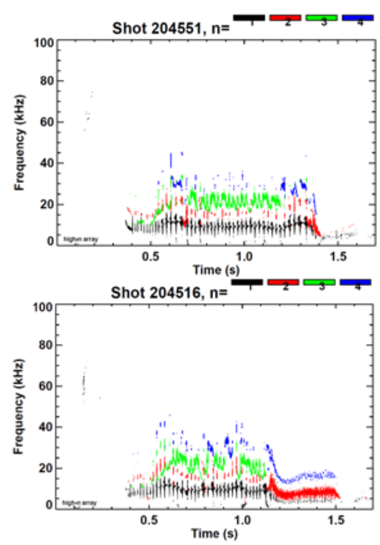

Fig. TT-3: Mirnov spectrograms for two "identical" 0.8 MA NSTX-U L-modes showing the eventual onset of an ~8 kHz, n=2 (3/2 tearing mode) at different times.

Transport analysis

Initial transport analysis of the NSTX-U L-modes has begun using the TRANSP code, focusing on discharges and time periods absent of the strong 3/2 tearing mode. Example density, temperature and toroidal velocity profiles are shown in Fig. TT-4 for the same shots in Fig. TT-1. The peak density varies by a factor of ~3, but the profiles are all very similar in shape. Ion temperature and toroidal velocity measurements are only shown for the discharge with higher heating powers, as the uncertainties in the lower power discharges are substantial for the carbon density. In the high power case it appears that the ion temperature is larger than the electron temperature near the magnetic axis, and the core rotation profile is relatively flat. It should be noted that the profiles shown represent time slices after recovery from a sawtooth crash.

The inferred Z_{eff} from the CHERS measured carbon density is quite low in these discharges (Z_{eff}~1.2), however there is evidence from FIDA and visible Brehmsstrahlung measurements that suggests Z_{eff} is larger. In the following TRANSP analysis Z_{eff}=2 has been assumed. TRANSP also requires an assumption on edge neutral density, however this does not influence the thermal transport analysis presented below.

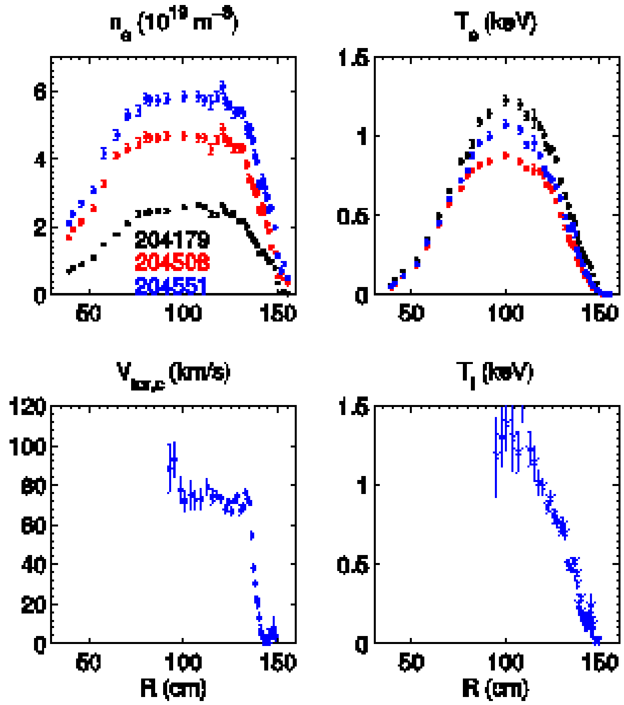

Fig. TT-4: Density, temperature and toroidal velocity measurements from Thomson Scattering and CHERS for the three shots in Fig. TT-1

In addition to measured electron and ion kinetic profile data, TRANSP analysis incorporates magnetic equilibria as computed by kinetic EFIT, and functions of time such as plasma current, neutron production rate, toroidal magnetic field, etc. The fast ion contribution is modeled using the NUBEAM module in TRANSP. New in this calculation is the use of a feedback algorithm that adjusts the Anomalous Fast Ion Diffusivity (AFID) during the calculation in order to bring the calculated and measured neutron rates into agreement. This AFID feedback algorithm is essential for the rapid completion of BEtween and Among Shots TRANSP (BEAST) runs during experimental operations, results of which can feed into preparation for subsequent discharges. It was found, especially for lower density discharges and discharges with obvious MHD activity, that up to 50% of the fast ion density/power could be lost through shine-thru, orbits leaving the main plasma and intersecting material surfaces or charge-exchange with thermal neutrals. A more rigorous validation of the NUBEAM calculation against FIDA and ssNPA measurements is a necessary future task.

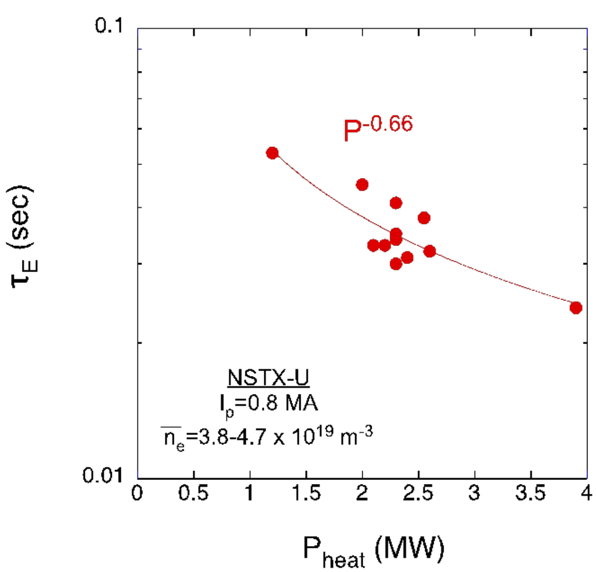

Fig. TT-5: Power degradation of the thermal energy confinement for L-mode discharges at Ip=0.8 MA.

The L-mode discharges described above formed the basis for attempted studies of the dependence of thermal energy confinement on plasma current and beam power. For this study, only discharges using NB1, where CHERS profiles could be obtained, were used. Times of interest were selected so that the discharge was in quasi-steady-state in terms of stored energy, as well as when the CHERS ion temperature measurements were good quality.

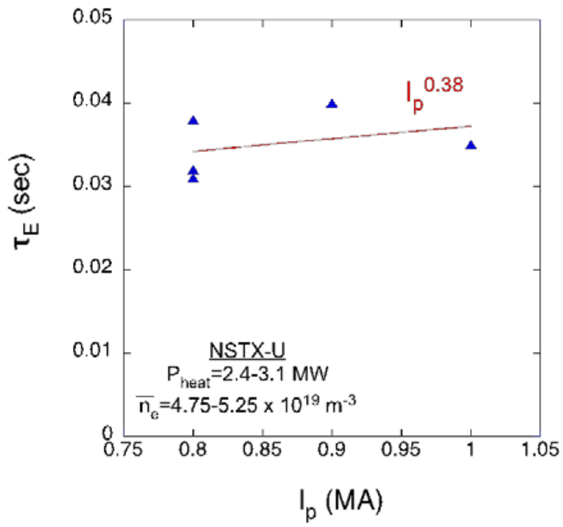

Fig. TT-6: Plasma current dependence of the thermal energy confinement for L-mode discharges.

The power dependence of the L-mode thermal confinement time is shown in Fig. TT-5. Discharges used for this study had I-p=0.8 MA, B_T=0.65 T and line averaged densities within the range of 3.8 – 4.7 x 10^{19} m^{-3}. The range of injected neutral beam power was 1 to 4.35 MW, but when fast ion losses are subtracted out, the range of neutral beam plus ohmic heating power is approximately 1.1 to 3.9 MW. There is a clear clustering of discharges in the 2 to 2.5 MW range, and the fit through the points is highly leveraged by the single minimum and maximum power points. With these caveats, this small collection shows a power degradation of $P^{-2/3}$, consistent with previous non-ST L-mode results [TT-1].

Assessing the plasma current dependence is more problematic due to the sparsity of discharges at constant power and line-averaged density that were part of a “controlled” current scan. Figure TT-6 shows the results for discharges contained within P_{heat}=2.4 – 3.1 MW and line averaged densities from 4.75 to 5.25 × 10^{19} m^{-3}, which had a current variation from 0.8 to 1.0 MA. Clearly, no strong current dependence emerges from this limited set of points. There does seem to be a slightly positive dependence of thermal confinement time on current ($I_p^{0.38}$), which is weaker than is found in conventional aspect ratio L-mode studies, but which also has a high statistical uncertainty.

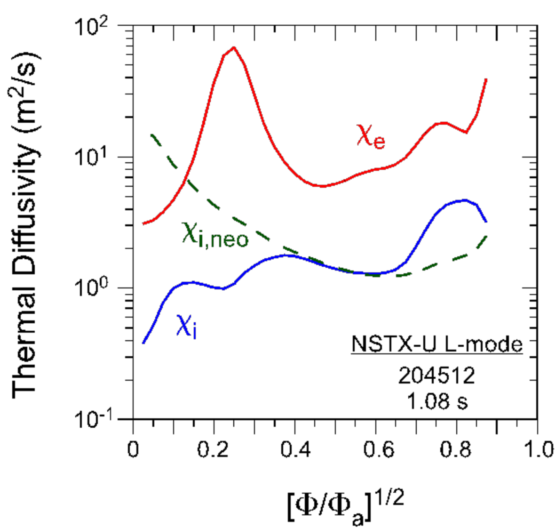

Fig. TT-7: Electron (red), ion (blue) and ion neoclassical (green) thermal diffusivities for an NSTX-U L-mode plasma.

The local transport in selected L-mode discharges has been assessed through local power balance calculations in TRANSP, and the result from one such discharge is shown in Fig. TT-7. Plotted are the profiles of the ion and electron thermal diffusivities, as well as the ion neoclassical values. The electron thermal

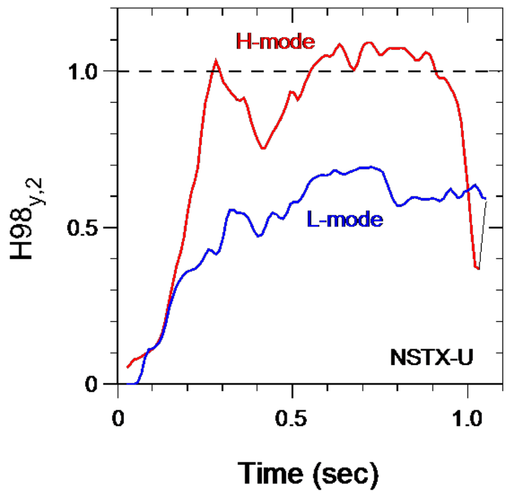

Fig. TT-8: Confinement enhancement factors as a function of time NSTX-U L and H-mode discharges.

diffusivity is very high and anomalous, ~7 – 20 m^2/s in the outer half of the plasma, consistent with previous NSTX results and indicating that the electron channel dominates the energy loss. Ion transport is lower, with χ_i ~ 1- 5 m^2/s in the outer portion of the plasma, and at or above the neoclassical level there.

H-mode plasmas were also produced in NSTX-U, and the thermal confinement times were seen to be at the $H98_{y,2}$ level or greater, as compared to L-mode plasmas, where this confinement enhancement factor was <1 (Fig. TT-8). In these H-mode plasmas, the electron thermal diffusivity was about a factor of two to three lower than that in L-mode discharges.

Microstability and transport modeling predictions

Local, linear gyrokinetic simulations using the GYRO code have been run for L-mode plasma 204551 shown in Figs. TT-1 & 4 to investigate predicted microinstability characteristics. Fig. TT-9(a) shows that at low $k_\theta\rho_s$<1 a strong ITG mode is predicted outside ρ>0.6 where the normalized gradient R/L_{Ti} is large. Somewhat surprising is that inside r<0.6 the electromagnetic microtearing mode is the dominant instability. This occurs because beta is increasing moving inwards which (i) stabilizes ITG, (ii) contributes to MTM instability as long as the electron temperature gradient is sufficient. The MTM is also enhanced due to the relatively large collisionality of these discharges. Also shown is the perpendicular E×B shearing rate (γ_E~$dv_\perp/dr$) that is larger than the ion scale linear growth rates between r=0.5-0.7. The strong E×B shear results almost entirely from the strong shear in toroidal rotation shown in Fig. TT-4. There is corresponding shear in the parallel velocity ($dv_\parallel/dr$) that can potentially drive Kelvin-Helmholtz instabilities. However, additional simulations including this drive term make little difference to the ITG growth rates (u′>0 in Fig. TT-9a) such that they still remain less the γ_E over a wide region. The ETG instability

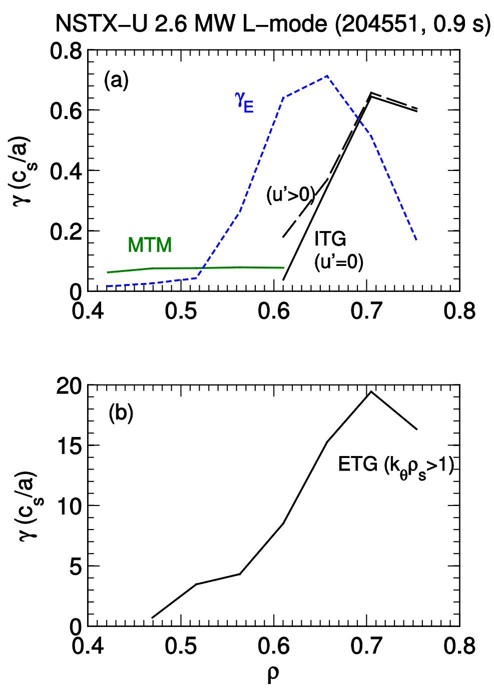

Fig TT-9: Profiles of maximum linear growth rates at (a) ion scales, (b) electron scales for L-mode 204551. The E×B shearing rate is also shown in (a).

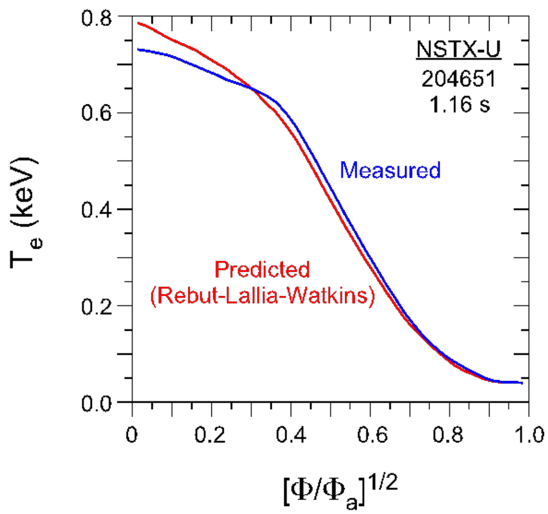

Fig. TT-10: The measured electron temperature profile (red) vs that predicted by the Rebut-Lallia-Watkins microtearing-induced electron transport model in an NSTX-U L-mode discharge.

at high $k_\theta\rho_s>1$ is also predicted to be unstable outside $\rho>0.5$ (Fig. TT-9b) with growth rates much larger than γ_E, so it is also a possible candidate for explaining the anomalous electron thermal transport. Nonlinear simulations will be pursued in the future to investigate the predicted importance of these instabilities.

Predictive calculations showed that the Rebut-Lallia-Watkins (RLW) model for microtearing-induced transport [TT-2] does an excellent job in predicting electron temperature profiles that agree with measured ones in at least one of these L-mode discharges. The result is seen in Fig. TT-10. The RLW was shown to predict T_e profiles accurately in high collisionality NSTX H-mode discharges [TT-3], consistent with gyrokinetic result showing the dominance of this low-k mode. For the NSTX-U L-mode, gyrokinetic simulations show that microtearing is present but is limited in space as the dominant mode. However, additional and more in depth gyrokinetic studies are needed to assess better the role of microtearing in these discharges.

Turbulence measurements

The U-Wisconsin beam emission spectroscopy (BES) system has been used to measure ion scale turbulence fluctuations in a n umber of NSTX-U L-mode plasma. Fig. TT-11(a) shows the power spectra of the normalized density fluctuations (assumed to be proportional to the BES intensity, $\delta n/n \sim \delta I/I$) in the 2.6 MW L-mode from above (204551). The spectra are measured at five adjacent radial positions between ~138-148 cm (corresponding to normalized radii r/a~0.7-0.95) and illustrate broadband frequency fluctuations up to ~200 kHz.

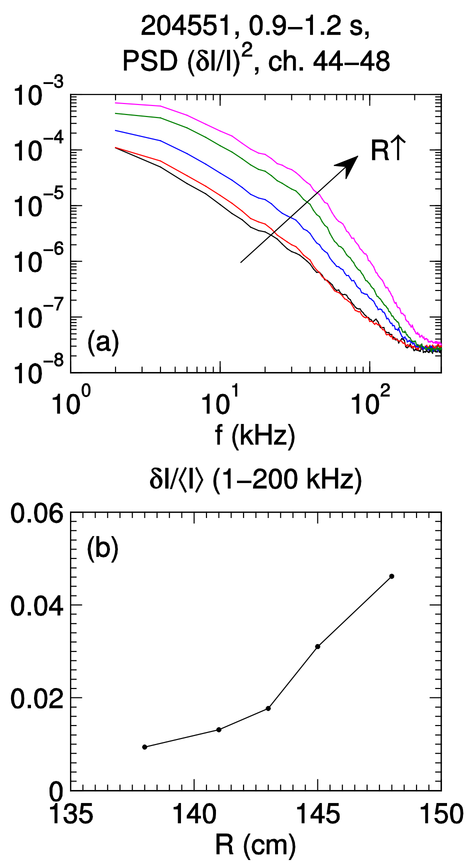

Fig. TT-11: (a) Power spectra of normalized density fluctuations from BES at different radii. (b) Radial profile of fluctuation amplitude (f=2-200 kHz).

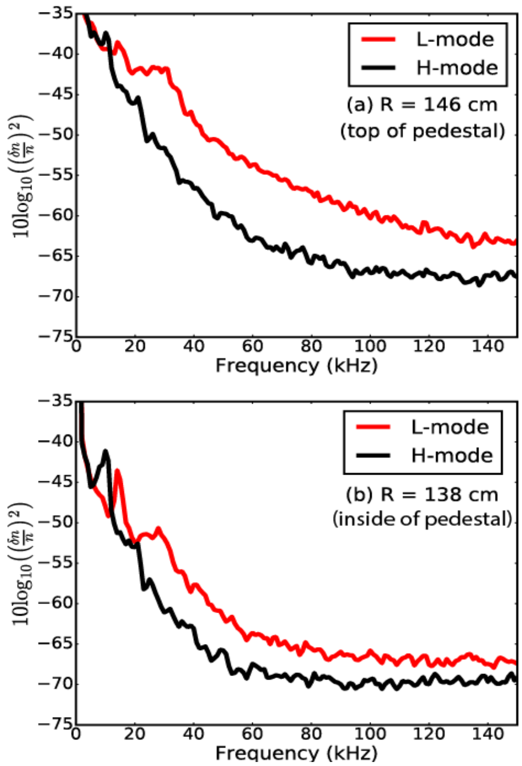

Figure TT-12: Autopower spectra of normalized density fluctuations across the L-H transition at (a) top of the pedestal, and (b) ~7 cm inward of the pedestal. Peaks in the spectrum below 15 kHz are MHD modes. Shot 204990, Ip = 0.65 MA, PNB = 1 MW.

The strength, frequency-integrated over 2-200 kHz, is quite substantial increasing from ~1% at the inner channel to >4% at the outer channel, suggesting the presence of strong ion scale turbulence. The 2D BES measurements will be used for future validation of gyrokinetic turbulence predictions.

Initial measurements of the turbulence in L-mode and H-mode NSTX-U plasmas have been conducted using the upgraded 2D BES system [TT-4]. Fig. TT-12 compares the density fluctuation spectra before and after an L-H transition at two locations. Broadband turbulence is observed up to 150 kHz in the pedestal region and up to 100 kHz several cm inside of the pedestal. Across the L-H transition, fluctuation levels drop by a factor of six in the pedestal region and a factor of three inward of the pedestal top. These results pave the way for future detailed studies of the turbulence across L-H transitions.

2. NSTX thermal transport analysis

Understanding thermal transport in spherical tokamaks, especially electron loss, is a key priority in the T&T topical science group. Analysis of NSTX thermal transport data has continued throughout FY16 including validation of gyrokinetic simulations, investigating the correlation between GAE/CAE activity and core electron temperature, and using neural net analysis in an attempt to parameterize core transport.

Global gyrokinetic simulations of ion scale turbulence

Good agreement in the ion thermal transport between ion-scale GTS simulations and

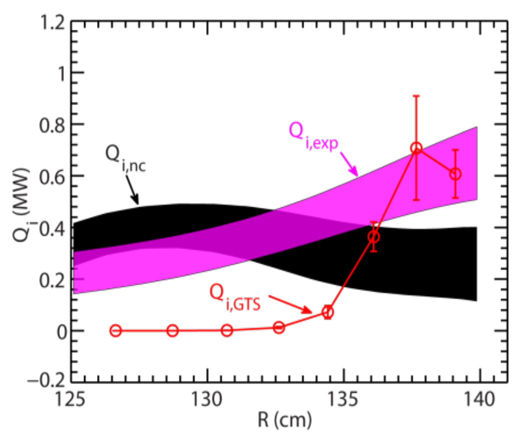

Fig. TT-13: Red circles: ion energy flux, $Q_{i,GTS}$, as a function of major radius from a nonlinear GTS simulation of an NSTX H-mode plasma (141767); magenta band: radial profile of experimental ion heat flux, $Q_{i,exp}$, from power balance analysis; black band: radial profile of neoclassical ion heat flux, $Q_{i,nc}$. The vertical widths of the magenta and black bands denote the experimental uncertainties. $Q_{i,GTS}$ is averaged over a quasi-steady saturation period, and the errorbars of $Q_{i,GTS}$ are the standard deviation of $Q_{i,GTS}$ in the averaging time period.

experiment has been found in an NSTX NBI-heated H-mode plasma (shot 141767), where electron-scale turbulence was observed to be reduced/stabilized by large electron density gradient [TT-5]. Fig. TT-13 compares the ion energy flux, $Q_{i,GTS}$, radial profiles at t=332 ms from the GTS simulation with those inferred from the experiment along with neoclassical ion heat flux, $Q_{i,nc}$, from NCLASS [TT-6]. It can be seen that $Q_{i,exp}$ is comparable to $Q_{i,nc}$ at $R \lesssim 132$ cm, which is consistent with the very small $Q_{i,GTS}$. At larger radius, i.e. $R \gtrsim 136$ cm, $Q_{i,GTS}$ is significantly larger than at smaller radius, consistent with $Q_{i,exp}$ being significantly larger than $Q_{i,nc}$. In fact, considering the error bars and uncertainties in $Q_{i,GTS}$, $Q_{i,exp}$ and $Q_{i,nc}$, $Q_{i,GTS}+Q_{i,nc}$ is approximately equal to $Q_{i,exp}$, indicating that the ion-scale turbulence is responsible for observed anomalous ion thermal transport. We note that $Q_{e,GTS}$ is significantly smaller than $Q_{e,exp}$ (not shown), which may be due to the possible contribution from some residual ETG turbulence that is not captured by this ion-scale GTS simulation or by electromagnetic effects, which are not yet taken into account by the GTS code.

Thermal transport due to Alfven eigenmodes

High frequency Alfvén activity was found to correlate with enhanced electron heat transport in the core, exhibited by the flattening of the electron temperature profile [TT-7]. This motivates a need for better understanding of the instability of these modes and their role in electron thermal transport. A parametric investigation of the dependence of electron heat transport on mode characteristics is undertaken to address this need.

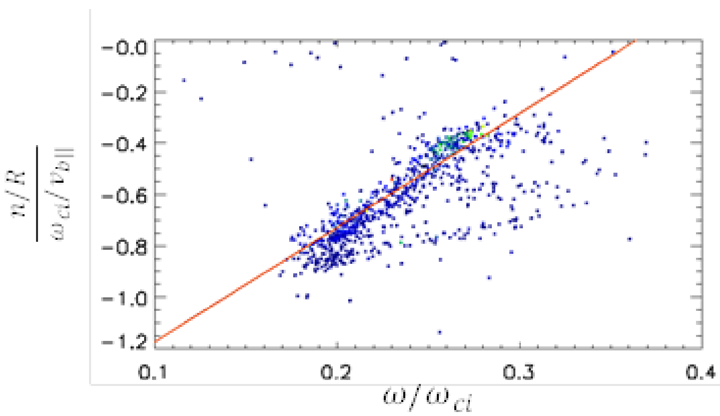

Fig. TT-14: Normalized toroidal mode number vs. normalized frequency for GAE and CAE modes in NSTX H-modes.

An existing database [TT-8] has been extended to include measurements of high-frequency Alfvén eigenmode activity. The toroidal mode number and frequency of these modes is found to be highly correlated across a wide range of shots and plasma parameters. This might be expected because the instability is thought to be governed by a parallel

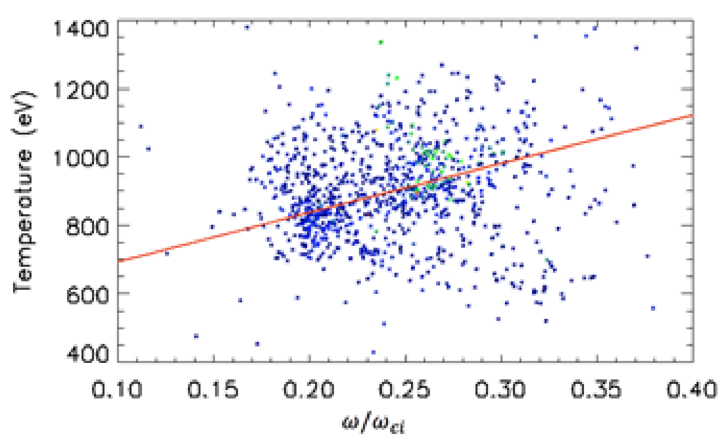

Fig. TT-15: Central temperature vs. normalized GAE/CAE frequency.

resonance condition, $\omega_{ci} = \omega - k_{||}v_{b||}$. This assumption is tested by investigating whether normalizations of frequency and mode number, motivated by the parallel resonance condition, lead to an improved the correlation.

The normalization for frequency is straightforward: $\omega \rightarrow \omega/\omega_{ci}$. While there is no measurement of $k_{||}$, the wave number normalization $k \rightarrow \frac{k}{\omega_{ci}/v_{b||}}$ is used to normalize $k_{tor} = n/R$. The maximum $v_{b||}$ on axis is chosen for the most energetic beam because the fast ion energy density peaks on axis, and intuitively it is expected that the most energetic beam is the most destabilizing to the modes. The correlation between frequency and mode number (Fig. TT-14) is found to improve significantly with this normalization, with correlation coefficient ρ increasing from $\rho = 0.18 \pm 0.03$ to $\rho = 0.85 \pm 0.05$. These coefficients use a weighting for each time corresponding to the total mode fluctuation power (δb^2). The improvement of correlation coefficient suggests that the parallel resonance condition does play a role in establishing the correlation between frequency and mode number.

One of the leading hypotheses for the mechanism of the anomalous electron thermal transport is the stochastization of electron orbits by resonant interaction with the modes. It might be expected that the frequency and mode number of these high frequency modes play roles in the effectiveness of this mechanism. This motivates an examination of the relationship between frequency and mode number and the transport. Although it would be natural to look at electron thermal diffusivity, this proves to be a noisy statistic, so other indicators of the anomalous transport are considered. Motivated by the anomalous flattening of the electron temperature profile associated with the transport, the correlation of central temperature with frequency and mode number is evaluated (Fig. TT-15). Central temperature is found to substantially correlate (calculated using δb^2 weighting) with both frequency and mode number, with $\rho = 0.34 \pm 0.05$ and $\rho = 0.46 \pm 0.05$ respectively. Of course, these correlations coefficients are substantially lower than one, indicating that there are other factors significantly influencing central temperature.

Nonlinear GYRO simulations of NSTX electron thermal transport

Electron scale turbulence has previously been studied on NSTX with a combination of experimental measurements from a high-k scattering system and gyrokinetic simulations. Recent work has shown that electron scale turbulence can be stabilized by the equilibrium electron density gradient after a controlled current ramp down experiment in an NSTX H-mode [TT-5]. Nonlinear electron scale gyrokinetic simulation has been shown to under-predict the experimental level of electron heat flux, both before and after the current ramp down. These results suggest ion scale turbulence might not be completely suppressed by ExB shear. Nonlinear gyrokinetic simulations of ion-scale turbulence and its contributions to electron thermal transport for this NSTX plasma have been initiated. In addition, a novel synthetic diagnostic for the high-k scattering system is under development to provide quantitative comparisons and constraints between experiments and simulations of electron-scale turbulence. A new mapping of GYRO coordinates to the real-space coordinates reveals an instrument response function that can be used to guide the choices of k-resolution for very-high-resolution nonlinear ETG simulations.

Neural net analysis of NSTX core

Understanding of plasma transport in tokamak plasmas is one of the most important issues to predict fusion performance of future devices including DEMO. In Spherical Torus (ST) devices, the ion transport is thought to be close to the neoclassical level. However, the electron transport is much more complicated which is thought to be governed by multiple microinstabilities such as trapped electron mode (TEM), electron temperature gradient (ETG) mode, microtearing (MT) mode, etc. Moreover, various fast particle instabilities also affect the anomalous electron transport. Because of this non-linearity and complexity of the mechanism determining the electron transport, statistical approaches have been taken to understand the phenomena using experimental database of NSTX. Here, we employ multiple linear regression (MLR) and neural network (NN) for the statistical study. A database was constructed at three radial points (ρ = 0.35, 0.50, 0.65) at interesting time points averaged over radius ($\rho = \pm 0.05$) and time (±15 ms) in NSTX shots. In total 680 shots are selected for building the database where 50%, 30%, and 20% are used for training, validation, and for test, respectively in NN. In this work, Levenberg-Marquardt algorithm is employed for training of NN. All the experimental data is taken from interpretive TRANSP runs. The selected input parameters are as following: R/L_{ne}, R/L_{ni}, R/L_{Te}, R/L_{Ti}, $R/L_{p,fast}$, n_i/n_e, T_i/T_e, P_{fast}/P_{tot}, q, s, $R\nabla V_{tor}/v_{th,i}$, $V_{tor}/v_{th,i}$, V_{ExB}/c_s, κ, δ_{lower}, δ_{upper}, Z_{eff}, ρ_*, α_{MHD}, β_t, $\nu_{ei}/(c_s/a)$. An example of the input parameter ranges for ρ = 0.50 in the database are presented in Fig. TT-16. The output parameters are chosen to be the gyro-Bohm normalized electron and ion heat fluxes, $Q_{e,i}/Q_{GB}$, where $Q_{GB}=\rho_*^2 c_s n_e T_e$.

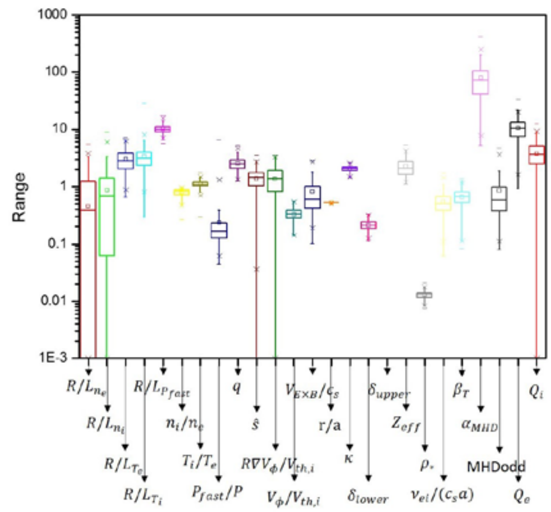

Fig. TT-16: Input parameter ranges at rho=0.5 for the NSTX database for neural net training and testing.

We establish the NN and optimize its structure by scanning the number of layers and neurons for each output parameter. After building an optimized NN, a sensitivity scan is done to determine the impact of input parameters to the output parameters to extract the most dominant input parameters for each output parameters. We hold the other input parameters to the mean values while monitoring an input parameter from -2σ to $+2\,\sigma$ where σ is standard deviation for the sensitivity scan. The dominant parameters for normalized Q_e and normalized Q_i are summarized in the table below, respectively at the three radial positions.

ρ	0.35	0.5	0.65
Q_e sensitive to:	P_{fast}/P_{tot}, Z_{eff}	R/L_{ne}, $\nu_{ei}/(c_s/a)$, β_t	s, $\nu_{ei}/(c_s/a)$, β_t
Q_i sensitive to:	P_{fast}/P_{tot}, Z_{eff}	T_i/T_e, κ, α_{MHD}	R/L_{Te}, $R/L_{p,fast}$, T_i/T_e, q, κ

The other statistical method, MLR exhibits similar results. The physical meaning of the dominant parameters in connection with turbulence theory is on-going where the regimes with various collisionality and beta are investigated separately with the statistical methods.

3. NSTX and MAST momentum transport

A recent publication [TT-9] summarized quasi-linear gyrokinetic simulations of momentum pinch based on NSTX H-modes. Predictions indicate the H-modes are most unstable to microtearing modes (due to high beta, β_T=12-16%, β_N=3.5-4.6), which do not contribute to momentum transport. Furthermore, the weaker ballooning modes that are predicted to be unstable (ITG, KBM and compressional ballooning modes, CBM) give negligible or outward momentum pinch, RV_φ/χ_φ~0, which is at odds with the experimental results RV_φ/χ_φ=-1 to -7 [TT-10]. The weak predicted pinch was shown to be a consequence of how both electromagnetic effects (at relatively large beta) and low aspect ratio influence symmetry-breaking of the instabilities.

To provide an additional experimental test of momentum pinch theory at low aspect ratio while minimizing electromagnetic effects, experiments were performed in MAST L-mode plasmas at lower beta values (β_T=4%, β_N=2). These experiments used applied n=3 fields to perturb the plasma rotation via neoclassical toroidal viscosity (NTV), similar to the NSTX approach. The initial results indicated momentum pinch parameters RV_φ/χ_φ = -(1 to 10) that are comparable to the NSTX H-modes, as shown by the solid black line in Fig. TT-17(b). However, initial quasi-linear gyrokinetic simulations predict very small momentum pinch (based on unstable ITG modes at $k_\theta\rho_s$=0.4), again at odds with the experimental observations.

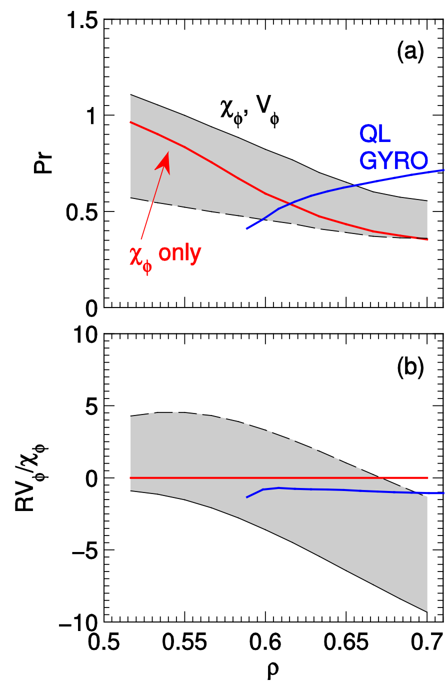

Fig. TT-17: (a) Inferred Prandtl number χ_φ/χ_i from the experiment fits assuming constant (in time) χ_φ (V_φ=0) (red line), constant χ_φ, V_φ (solid black line) or $\chi_\varphi(t)$,$V_\varphi(t)$~$\chi_i(t)$ (dashed black line). The quasi-linear gyrokinetic prediction is also shown (blue line). (b) Corresponding pinch parameter RV_φ/χ_φ from the different fits and quasi-linear gyrokinetic prediction.

Unlike the NSTX experiments, the application of brief 3D fields in these MAST L-modes caused a ~15% reduction in energy confinement, and corresponding increase in local thermal transport coefficients (χ_e, χ_i). If the momentum transport coefficients are assumed to follow this trend, [$\chi_\varphi(t)$,$V_\varphi(t)$~$\chi_i(t)$], the resulting fit gives both a smaller Prandtl number ($Pr=\chi_\varphi/\chi_i$) and momentum pinch parameter, shown by the dashed black lines in Fig. TT-17. Given the broad range of inferred Pr and RV_φ/χ_φ values due to uncertainty in the time-dependence of the transport coefficients (the shaded region), it is unclear if these results can be used to clarify the presence and strength of a momentum pinch. NSTX-U experiments have already been planned to investigate this further in low beta L-modes using both 3D field perturbations and NBI modulation.

References

[TT-1] Kaye, S.M., et al. Nucl. Fusion **37** 1303 (1997).
[TT-2] Rebut, P.H. and M. Brusati, Plasma Phys. Cont. Fusion **28** 113 (1986), Rebut, P.H., et al., in Proc. Of the 12th IAEA Conference on Plasma Physics and Controlled Nuclear Fusion Research, Nice, France, paper IAEA-CN-50/D-4-1 (a988).
[TT-3] Kaye, S.M., et al., Phys. Plasmas **21** 082510 (2014).
[TT-4] Smith, D.R. et al., Rev. Sci. Instrum **83**, 10D502 (2012).
[TT-5] Ruiz Ruiz, J., et al., Phys. Plasmas 22, 122501 (2015).
[TT-6] Houlberg, W.A., et al., Phys. Plasmas 4, 3230 (1997).
[TT-7] Stutman, D. et al., Phys. Rev. Lett. **102** 11502 (2009).
[TT-8] Fredrickson, E., et al., N.F. **54** 093007 (2014).
[TT-9] Guttenfelder, W., et al., Phys. Plasmas **23**, 052508 (2016).
[TT-10] Kaye, S.M., et al., Nucl. Fusion, **49**, 045010 (2009).

C. Energetic Particles TSG Research Highlights

One of the main challenges in Energetic Particle (EP) research is the accurate and quantitative prediction of stability and saturation level of EP-driven instabilities. Tools are available to compute EP transport for a given instability spectrum with a good level of confidence. The key issue is to obtain reliable predictions of the unstable spectrum for a given plasma scenario.
To address these issues, EP research on NSTX-U in FY-16 has focused on three main thrusts:

1) Characterize the fast ion distribution function resulting from NB injection on NSTX-U as a function of injection geometry
2) Assess the relation between properties of the fast ion distribution function and stability of EP-driven modes
3) Develop theoretical and numerical tools for improved simulations of EP interaction with instabilities

All three thrusts contribute to the NSTX-U Milestone R(16-2) on "Assessment of the effects of neutral beam injection parameters on the fast ion distribution function and neutral beam driven current profile" as described in a dedicated Section of this Report.
Results obtained during FY16 for each thrust are discussed in the following section. The last section summarizes EP-related work performed in collaboration with other facilities (e.g. DIII-D).

1. Characterize the fast ion distribution function resulting from NB injection as a function of injection geometry

One of the main elements of the NSTX Upgrade is the installation of a second, more tangential Neutral Beam (NB) line, see Fig. EP-1. Similar to the original NB line, the new line comprises three NB sources that can be operated independently with typical injection voltage 60-90kV. Sources from the new NB line has larger tangengy radii than NB line 1, spanning from R=110cm (near the magnetic axis) out to R=130cm. This provides much enhanced flexibility in NB injection parameters, from more perpendicular (through NB line 1) to more tangential and off-axis (through NB line 2).

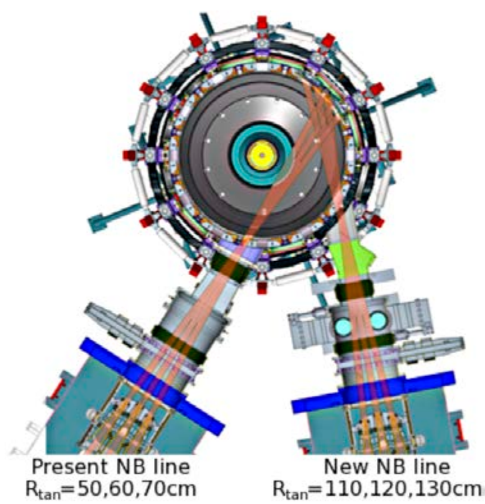

Figure EP-1: *Elevation of NSTX-U showing the original NBI lines (with smaller tangency radius and more perpendicular injection) and the new line with more tangential and off-axis NBI capabilities.*

One of the priorities during the first NSTX-U experimental campaign was an initial assessment of the fast ion distribution resulting from different NB injection parameters. Most of the experimental results are presented in the "Milestone R16-2" Section of this Report. A short summary is given below.
A dedicated experiment has focused on the characterization of the fast ion distribution vs NB injection from the available sources in quiescent L-mode plasmas. Short pulses (or "blips") of

each source were used to populate the fast ion distribution. Measurements were performed with the newly commissioned solid-state neutral particle analyzer (ssNPA) arrays and with vertical/tangential Fast Ion D-Alpha (FIDA) systems. Initial analysis of the available data confirm the main expectation that injection with NB line 2 results in the build up of a distribution with larger population of strongly co-passing fast ions than injection from NB line 1. More quantitative analysis is under way to assess the neutron rate response to each source and compare experimental values with predictions from TRANSP/NUBEAM. At present, discrepancies are observed at low injection voltage, V_{inj}~65kV, with the measured neutron rate being consistently lower than the predicted one. The discrepancy is partly resolved at higher voltages, V_{inj}=85kV. Possible causes of the discrepancies, such as uncertainties in the measured impurity content and/or in the effective NB species composition, are currently under investigation.

2. Assess the correlation between properties of the fast ion distribution function and stability of EP-driven modes

The following paragraphs describe the main new results obtained during FY-16 on energetic particle physics and EP-driven instabilities. Observations span from the effects of static or low-frequency perturbations, such as externally-imposed 3D fields and kink-like modes, up to the effects of instabilities near the ion-cyclotron frequency range, such as CAE/GAE and Ion Cyclotron Emission.

EP interaction with static and low-frequency perturbations

The capability of mitigating or suppressing EP-driven instabilities in a predictable way depends on knowing the relation between mode properties (notably its driving term) and the properties of the fast ion distribution function. The main goal is to be able to affect the mode stability by means of external (or controllable) "actuators" such as NBI with different injection parameters or 3D perturbations from external magnetic coils.

A notable example of the effects of external magnetic perturbations (MPs), excited through the NSTX set of external Error Field Correction coils, was reported in [EP-1]. It was found that amplitude and frequency bursts of high-frequency Global Alfvén eigenmodes strongly decreased during n=3 MP pulses. Those initial results have been extended to the MP effects on lower frequency TAEs in FY-16 through a detailed analysis performed via the full-orbit code SPIRAL [EP-2].

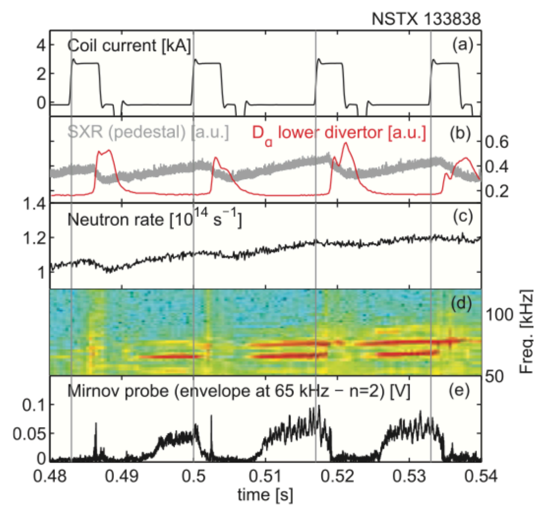

Figure EP-2: *NSTX scenario for TAE mitigation by externally applied n=3 magnetic perturbations. (a) MP coil current. (b) D_α emission from the divertor and soft x-ray emission from a chord traversing the pedestal. (c) The neutron production rate. (d) The effect of n = 3 MP on TAEs is visible on the Mirnov coil spectrogram. (e) The Mirnov signal at the TAE frequency reduces strongly after the coil current is ramped up and before the ELM crash.*

The reference H-mode scenario is shown in Fig. EP-2. Mitigation of TAE activity was observed for TAEs when pulsed n = 3 fields were applied to pace ELMs. The study of the role of fast ion transport in the perturbed equilibrium requires accounting for the plasma response to the applied 3D fields. The plasma response as obtained from the ideal MHD code IPEC was used to address the role of fast ion transport due to MP fields in NSTX. During FY-16 we further extend the investigation of the fast ion drive in these scenarios with the inclusion of the resistive MHD plasma response to the applied 3D magnetic perturbation. This allows for a more accurate modeling of the fast ion transport and a more quantitative comparison can be made with the experimental results. From SPIRAL simulations with the one- and two-fluid resistive MHD plasma response to the magnetic perturbation included, it was found that in response to MP pulses the fast ion losses increased. Based on results from other devices, it was initially assumed that a reduction of the fast ion drive for the instabilities could be responsible for the mitigation observed in these scenarios. However, simulations indicated that MPs did not affect the fast ion drive for the TAEs significantly but the Alfvén continuum at the plasma edge was found to be altered due to the toroidal symmetry breaking which leads to coupling of different toroidal harmonics. Specifically, the TAE gap was reduced at the edge creating enhanced continuum damping of the global TAEs, which is consistent with the observations. The results suggest that optimized non-axisymmetric MPs might be exploited to control and mitigate Alfvén instabilities by tailoring the fast ion distribution function and/or continuum structure.

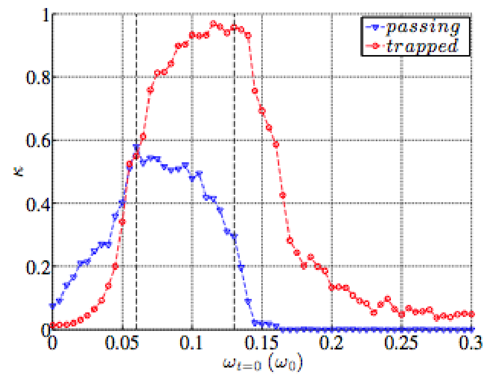

Figure EP-3: *Number κ of particles locked in phase with the mode at frequency ω, normalized to the total number of particles as the mode reaches saturation. Note the higher κ values for trapped particles, which mainly contribute to the mode drive in this phase.*

Significant fast ion losses are also observed when other low-frequency perturbations affect the fast ion population. So-called fishbone modes are a noticeable example. Linear and non-linear numerical simulations of NSTX scenarios have investigated the conditions for destabilization of fishbones [EP-3], with the goal of identifying stable regimes with reduced fast ion transport. The results show that the fishbone is driven unstable by both trapped and passing particles. In the initial, linear regime the contribution of passing and trapped particles is comparable (Fig. EP-3). In the nonlinear regime, the mode saturates due to flattening of beam ion distribution. The mode persists while its frequency sweeps down in such a way that the resonant trapped particles move out radially and keep in resonance with the mode. Correspondingly the flattening region of beam ion distribution expands radially outward. A substantial fraction of initially non-resonant trapped particles become resonant around the time of mode saturation and keep in resonance with the mode as frequency chirps down. On the other hand, the fraction of resonant passing particles is significantly smaller than that of trapped particles. Contrary to the linear regime, simulations show that trapped particles provide the main drive to the mode in the nonlinear regime (Fig. EP-3).

An important observation from this study is that plasma rotation is a destabilizing factor for these plasmas, see Fig. EP-4. In the linear phase, a new unstable region appears and extends to values of minimum safety factor, q_{min}, well above 1. This is important information for designing discharges that maintain an elevated q_{min} to improve performance and avoid or mitigate instabilities.

An additional reason to develop scenarios with elevated q_{min} is to avoid other instabilities such as sawteeth. During the initial NSTX-U operation, long sawtoothing L-mode scenarios have been achieved, that were previously un-accessible on NSTX. This provided the opportunity to investigate conditions for sawtooth appearance and to study their effects on fast ion confinement.

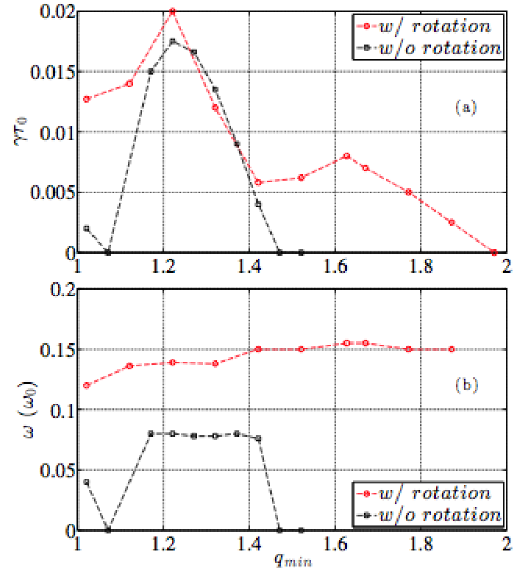

Figure EP-4: *Linear growth rate (a) and mode frequency (b) of fishbones in NSTX versus q_{min}. Results from simulations with and without rotation are shown.*

Because of the setup geometry, the t-FIDA and t-SSNPA are mainly sensitive to passing particles while v-FIDA and r-SSNPA are most sensitive to trapped particles. The combination of t-FIDA, v-FIDA, t-SSNPA and r-SSNPA can be used to separate the response of passing vs trapped fast

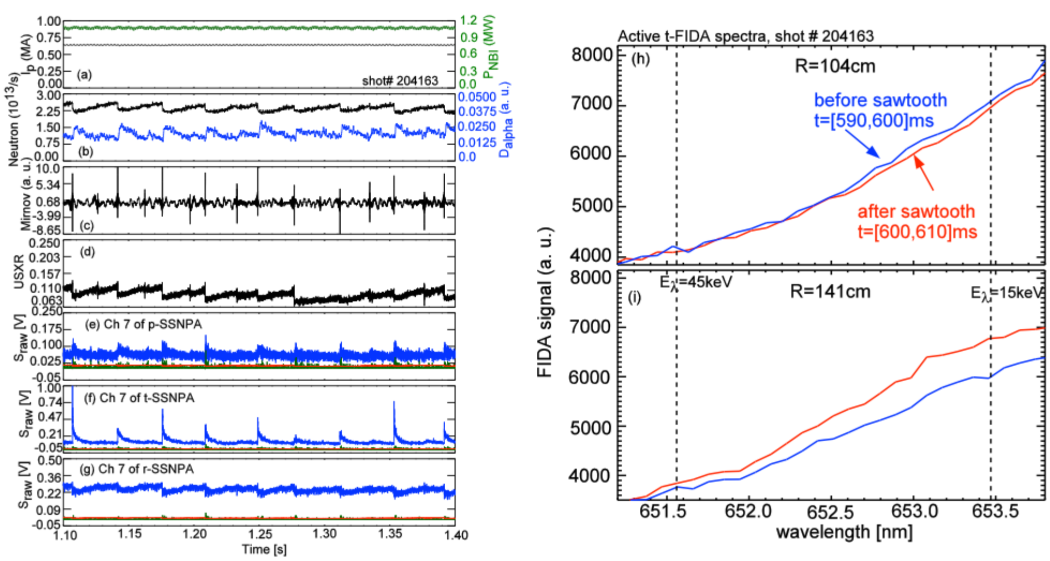

Figure EP-5: *Temporal evolution of (a) plasma current and injected NB power (b) neutron rate and midplane D_{alpha}, (c) low frequency (<50kHz) Mirnov signal, (d) Soft x-ray, (e) channel 7 of p-SSNPA, (f) channel 7 of t-SSNPA and (g) channel 7 of r-SSNPA. The "blind" detector signal and estimation of x-ray induced noise are also shown in (e-g) with green and red curves respectively. Comparison of the spectra of t-FIDA before and after one sawtooth event in (h) core channel R=104cm and (i) edge channel R=141cm.*

ions. Figure EP-5(e-g) shows the signals of three SSNPA subsystems in a time window with sawteeth, as seen from repetitive cycles in electron density data from Thomson scattering, neutron rate, Mirnov coil signal, and edge D_{alpha} emission. It has been observed that the signals of t-SSNPA significantly increase at sawtooth. The bursts on the t-SSNPA are the combined results of fast ions moving to the edge and increase in edge neutral density. The r-SSNPA, which is mainly sensitive to trapped fast ions, shows only slight drops at each sawtooth. Panels (h-i) show the active t-FIDA spectra before and after a sawtooth event at t=0.6s. It shows small reduction in core channels and relatively large increase in edge channels. However, there is almost no change for v-FIDA signals that are mainly sensitive to particles with small pitch (trapped or barely trapped). The SSNPA and FIDA data suggest that during sawteeth there is significant transport of passing fast ions from the core to the edge, while trapped particles are weakly affected.

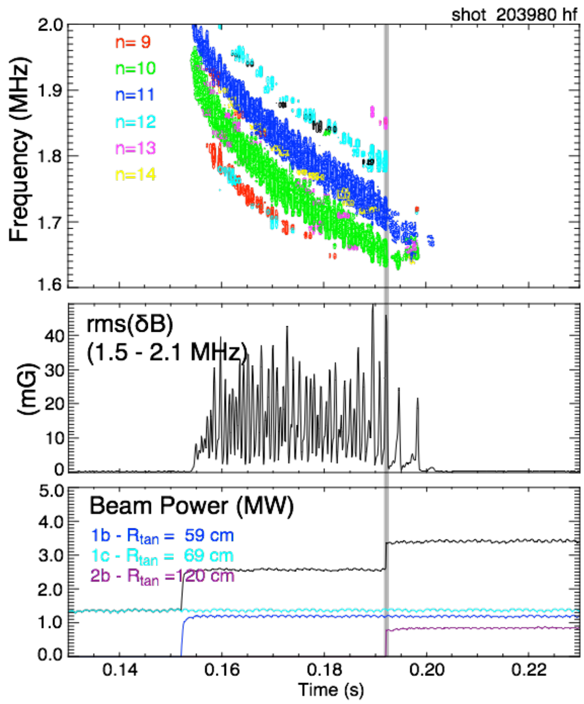

***Figure EP-6**: (a) spectrogram showing GAE modes. (b) Root-mean-square fluctuation level of GAE. (c) Injected NB power: black-total, colors represent the power injected from each individual source.*

Experimental observations of EP-driven Compressional and Global Alfvén eigenmodes

Experimentally, there were two significant new discoveries made during the FY-16 NSTX-U campaign on high-frequency Alfvénic modes. The observations are relatively new and much more theoretical and experimental work is required to fully understand their significance in the context of existing knowledge of energetic particle driven instabilities. The discoveries are (i) the observation that the new beam sources, with tangency radius outside the magnetic axis, very efficiently suppress the counter-propagating Global Alfvén Eigenmodes, and (ii) what appears to be Ion Cyclotron Emission (ICE) has been observed on NSTX-U.

It was found early that the original NSTX beam sources, with tangency radii inside the magnetic axis, would excite a similar spectrum of instabilities to those commonly seen on NSTX. Nearly all operation of NSTX-U has been at a nominal toroidal field of 6.5 kG, higher than NSTX could reach, and the plasma densities tended to be lower than was seen on NSTX. Thus, the spectrum of modes was typically shifted to higher frequencies. Nevertheless, counter-propagating, moderately high n-number modes were commonly seen in the frequency range from 1 MHz up to 2 MHz. Estimates of the minimum possible frequency for Compressional Alfvén Eigenmodes (CAE) with these n's were significantly higher, and the modes are assumed to be GAE. As the new NB line 2 sources came on line, it was quickly noted that use of these sources was anti-correlated with the presence of GAE. And soon experiments were performed where a NB line 2 source was added to a plasma with one or more NB line 1 sources and it was seen that the addition of more beam power could completely suppress the counter-propagating GAE (Fig. EP-6). This observation is qualitatively consistent with a theory of GAE instability developed by Gorelenkov [EP-4] where the drive/damping of resonant fast ions was dependent on the Larmor radius. The more tangential NB line 2 sources would have smaller Larmor radii (for the same energy). Estimates of the sign of the drive/damping based on a simple dispersion relation find that the observations are qualitatively consistent with this model. More detailed investigations are underway, using the unique HYM code to study the GAE stability in this regime.

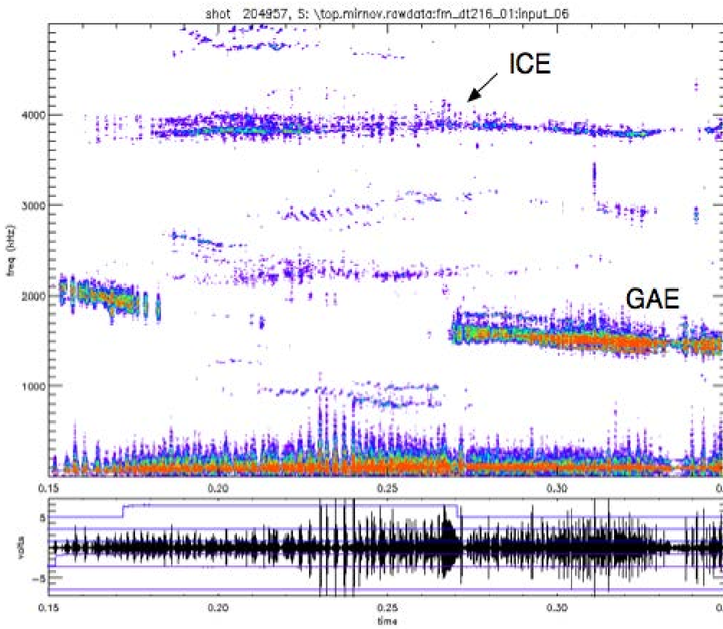

Figure EP-7*: Spectrogram of Mirnov coil showing Ion Cyclotron Emission from plasma edge.*

The capability to suppress the GAE with the substitution of sources at the same neutral beam power, or by adding more NB power, will prove to be a useful tool for understanding the role of GAE in electron heat transport.

Under some conditions in NSTX-U, a weak mode, or modes is seen at frequencies between ≈3.8MHz and 4.1MHz (Fig. EP-7). This frequency corresponds to the deuterium ion cyclotron frequency just inside the plasma edge. In lower field operation on NSTX and MAST, CAE were seen with frequencies near the edge deuterium ion cyclotron frequency and there is theoretical work suggesting that ICE in conventional tokamaks comes from CAE. However, these new modes appear to be qualitatively different than the CAE seen at lower field. The toroidal mode number appears low, either n=0 or n=1, whereas the CAE on NSTX near the cyclotron frequency tended to have toroidal mode numbers closer to 10. There is some anecdotal evidence suggesting a weak correlation with NB line 2 sources (or an anti-correlation with GAE activity). That such modes were not found on NSTX suggests that possibly the higher field is important. As of yet, there isn't much understanding of what controls their presence.

Validation and verification of CAE eigenmode codes

Two eigenmode codes—CAE [EP-5] and CAE3B [EP-6]—were developed in past years to predict compressional Alfvén eigenmode (CAE) structure and frequency. CAE3B solves the equations of Hall MHD for realistic plasma geometry inside the last closed flux surface, using the simplifying assumption $k_\parallel^2 \ll \frac{\omega^2}{v_A^2}$ to eliminate coupling with shear waves. CAE solves a simplified eigenmode equation $\nabla^2 E + \frac{\omega^2}{v_A^2} E = 0$ in a domain including not only the plasma, but the vacuum region bounded by the conducting wall surrounding the plasma. Recently, the code authors have undertaken to compare the predictions of the codes both with each other and with measurements from NSTX. These comparisons serve two purposes. First, comparison of the codes with each other can potentially verify that the codes accurately solve the equations representing their underlying physics models. Second, differences in the predictions of the two codes be used to evaluate the significance of differences in their physics models.

For the purposes of verification, both codes were adapted to use the same physics model so that any differences in their results, which should be negligible, would depend only on differences in their underlying numerical implementations. Specifically, the CAE3B model was further simplified, while extra physics was added to CAE, permitting direct comparison of the solutions from both codes using a simulation domain bounded by a closed surface just inside the separatrix. The results from the two codes are in good agreement for these simulations. For instance, the lowest frequency n = -3 eigenmode in discharge 130335, at t = 480 ms was found to have $f \approx 773$ kHz using the simplified CAE3B and the frequency found by the adapted CAE code differed by <<1%.

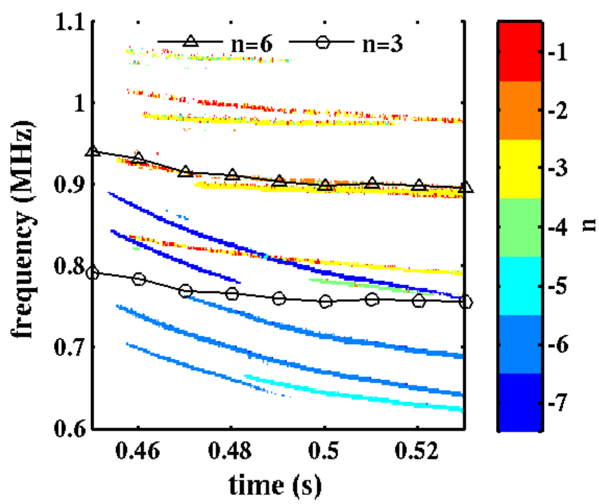

Figure EP-8*: Color contour plot shows high frequency modes from HF edge magnetic array colored by toroidal mode number (n). Overlaid lines show lowest eigenmode frequency from CAE3B vs. time for n = 3 ( ) and n = 6 ( ).*

Furthermore, in order to investigate the physics differences of the two codes, results from the full CAE3B code were compared with results from CAE using the same boundary and from CAE using the conducting wall as the boundary. It was found that the frequency differences for each these cases were small for the lowest frequency eigenmodes (e.g. <2% for the n=-3 eigenmodes) but of increasing significance as poloidal and radial quantum number increased.

The observed modes in 130335 were also compared to simulation results from the full CAE3B simulations at a sequence of times in the range t~440–520 msec in order to compare the predicted and observed frequency evolution (Fig. EP-8). It was found that modes in the experiment with $|n|$ >= 5 have frequencies substantially lower than the lowest from CAE3B for the same n, and a much higher frequency rate of change with time. In contrast, the observed modes with $|n|$ <= 4 tend to have a much lower rate of frequency change with time, comparable to that from CAE3B, as well as frequencies comparable to, or higher than the lowest eigenmode for each n. Figure EP-

8 shows the observed modes colored by mode number and, as examples, the time dependent frequencies of the lowest frequency CAE3B eigenmodes for *n*=-3 and *n*=-6. It should be noted that these simulation results do not include the plasma toroidal rotation (f_{ROT}~25 kHz on-axis), which is in the direction opposite to the mode propagation. Inclusion of rotation might Doppler shift the frequencies of the |*n*|>=5 eigenmodes so they are comparable to the experimental frequencies. Both codes are currently under development to include rotation, so the frequency shift will be included future simulations. Even so, it is unlikely that inclusion of rotation will lead to good agreement between the simulated and observed frequencies of the |*n*|>=5 modes over the whole time period shown in Fig. EP-8, given the strong experimental frequency variation, since the rotation speed changes relatively little. Consequently, even without rotation in the simulation, the results of the comparison are enough to suggest that the modes with |*n*|>=5 are not actually CAEs, but global Alfvén eigenmodes instead. This comparison demonstrates that the use of an eigenmode code can complement and substantially improve upon the identification analysis based on local dispersion relations developed in Ref. [EP-7].

The effort to compare CAE3B with observation in 130335 also served an educational objective. The simulations and analysis were performed by a student from Fordham University, Nicholas Geiser, a participant in the NSF Research Experience for Undergraduates program at UCLA.

Non-linear simulations of high-frequency AEs

A set of nonlinear simulations of CAEs, including coupling to KAW has been completed using the HYM code [EP-8]. Numerical results support an energy channeling mechanism for T_e flattening [EP-9], in which beam-driven CAE dissipates its energy at the resonance location close to the edge of the beam, therefore significantly modifying the energy deposition profile. Simulations show multiple unstable CAEs for a range of toroidal mode numbers n=4-9, coupled with KAW on the high field side. Resonance with KAW is located at the edge of CAE well, and just inside beam ion density profile, and the radial width of KAW is determined by the beam ion Larmor radius and $V_A(R)$ scale length as $(L\rho^2)^{1/3}$, where ρ is the effective Larmor radius, $\rho = \sqrt{3/4\,(n_b/n_e)}\,\rho_b$. It is shown that localization of KAW on HFS is related to the shape of the CAE effective potential well. Analysis of the particle phase-space for unstable CAEs shows that the resonant particles have wide range of pitch-angle

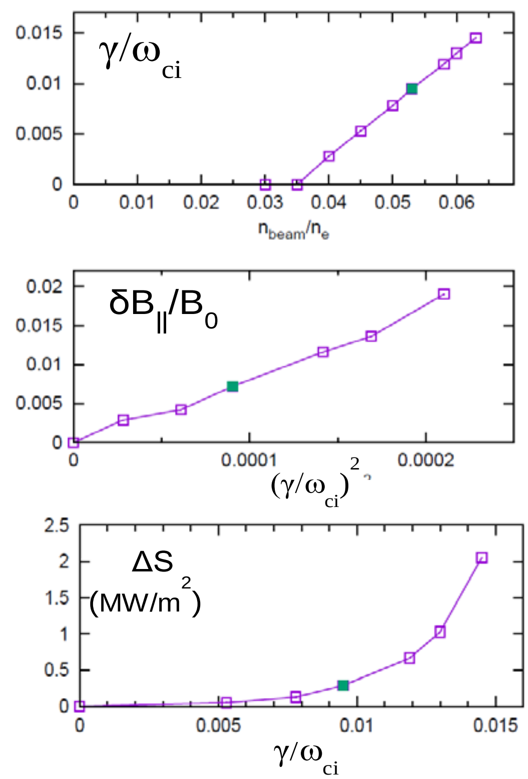

Figure EP-9: *(a) Growth rate of the n=4 CAE vs beam ion density; (b) Saturation amplitude vs γ^2; (c) Calculated change of the energy flux at the resonance location vs γ. (From Ref. [EP-10]).*

parameter λ= 0.1 – 1.2 and energies 10 – 60keV, but a relatively narrow range of resonant $v_{\parallel}$. While this group includes both passing and trapped particles, the co-CAE instability is shown to be driven by the trapped fast ions [EB-3].

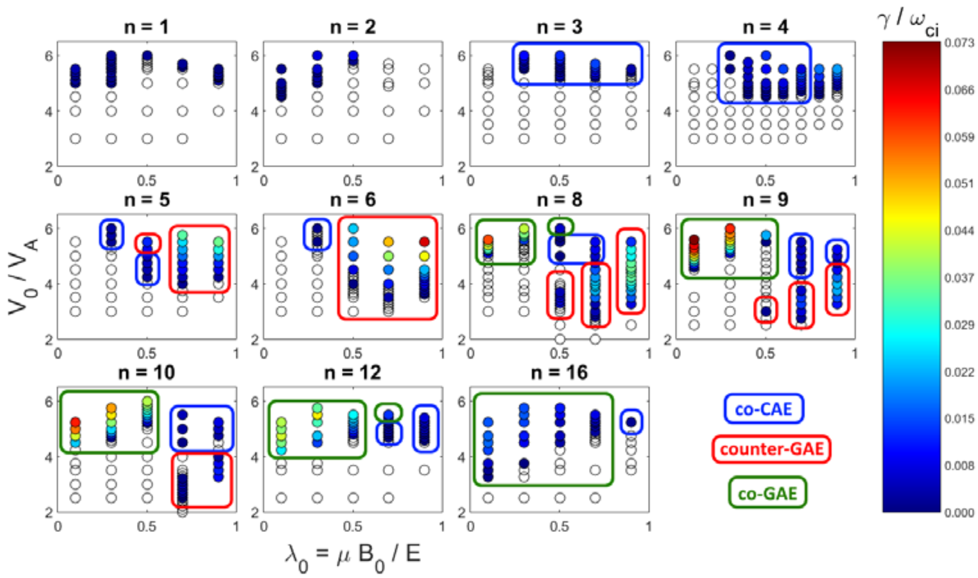

Figure EP-10: Normalized growth rates (γ/ω_{ci}) of the most unstable modes for each toroidal mode number (|n| = 1 – 16) and beam distribution parameters (λ_0 , V_b/V_A). White circles indicate distributions with no excited modes, while the color of a circle indicates the most unstable mode's growth rate.

An additional set of simulations have been performed for the n=4 CAE instability for varying the beam ion density. The results of these simulations, namely the scaling of the instability growth rate, saturation amplitude and mode-converted power are summarized in Figure EP-9. Beam ion power scan allows estimating a damping rate of CAE due to its linear coupling to KAW, and shows that this is the main damping mechanism, with the damping rate γ_{damp}= 0.66 γ_{drive} for the n=4 CAE. This sets up a threshold value of the beam power needed for the excitation of this mode for a given set of NSTX parameters at P~4MW. Nonlinear simulations demonstrate that the CAE instability saturates due to nonlinear particle trapping, which has been confirmed by scaling of the saturation amplitude with the growth rate $\delta B_{\parallel} \sim \gamma^2$ (Fig. EP-9b). Absorption rate, calculated as a change in the Poynting flux across the resonance layer, has been obtained in each simulation, and it shows a very strong scaling with growth rate / beam power (Fig.EP-9c). The best fit with the power law gives $\Delta S \sim (\gamma/\omega_{ci})^5$, implying that the energy loss at the resonance scales as a fifth power of the beam ion density (or the beam power). The strong scaling could be explained, if one assumes that the power absorbed at the resonance is proportional to the change in the CAE energy $P=2\gamma \int (\delta B)^2/4\pi \, d^3x \sim \gamma^5$. These results suggest that the energy channeling mechanism might play a significant role in the NSTX-U due to higher projected beam powers, provided that the CAEs are still unstable for larger toroidal field values (i.e. smaller values of v_{beam}/V_A parameter).

Beam-driven, high frequency compressional (CAE) and global (GAE) Alfvén eigenmodes have been linked to anomalous electron temperature profile flattening at high beam power in NSTX [EP-11]. A large set of linearized, 3D MHD-δf particle simulations using the HYM code [EP-12] have been conducted in order to investigate CAE and GAE stability for a wide range of beam parameters [EP-13], see Fig. EP-10. These simulation results have been analyzed and compared with analytic studies and a new, extensive experimental survey of NSTX discharges [EP-14][EP-15]. A detailed understanding of CAE/GAE excitation is vital to predicting (and ultimately controlling) their effects on plasma confinement. The central pitch variable ($\lambda_0 = \mu B_0 / E \approx (V_\perp^2 / V^2)(B_0 / B)$) and normalized injection velocity (V_b/V_A) are varied in a realistic beam-generated equilibrium fast ion distribution. λ_0 is scanned from 0.1 – 0.9 (typical NSTX values: 0.5 – 0.7) for V_b/V_A = 2.5 – 6.0 and toroidal mode numbers |n| = 1 – 16.

CAE are found to be the most unstable mode only when $V_b/V_A > 4$, whereas GAE can be excited for smaller injection velocities. This compares favorably with experimental observations where GAE are more ubiquitous [EP-15], and also implies significantly reduced CAE activity for NSTX-U due to its larger nominal toroidal field. The CAE seen in these simulations are all co-propagating, whereas the CAE observed in experiment are a mix of co- and counter-propagating. Theory suggests that co-CAE can be more unstable than counter-CAE even in the moderate frequency band ($< 0.4\omega_{ci}$) where they are missing in experiment [EP-16]. Moreover, these linear simulations find both co- and counter-propagating GAE, while co-GAE are rarely analyzed in the experimental literature. The co-GAE are most unstable for very tangential injection (λ_0 = 0.1 – 0.5), and switch to cntr-GAE as the most unstable mode as the beams become more perpendicular (λ_0 = 0.5 – 0.9). Of all the modes (co-CAE, cntr-GAE, co-GAE), these co-GAE modes have the largest growth rates, motivating their further experimental and theoretical analysis.
Unexpectedly, both the co- and cntr-GAE frequencies show a linear dependence on the injection velocity that can shift the mode frequency by up to a factor of 2. Increasing V_b/V_A consistently decreases the frequency of the cntr-GAEs and increases the frequency of the co-GAEs. This result is somewhat counterintuitive since these modes have previously been regarded as MHD modes, whose intrinsic properties should be independent of the fast ion distribution. Nevertheless, the Doppler-shifted cyclotron resonance condition and simplified shear Alfvén dispersion qualitatively captures this behavior. There is also preliminary experimental confirmation of this trend, as the amplitude-weighted average mode frequency of the full CAE/GAE mode spectrum taken from 1000+ time slices (173 separate NSTX discharges) also tends to decrease as V_b/V_A increases [EP-15]. Since these spectra are suspected to be largely composed of counter-GAE, this analysis is consistent with the simulation results. A more detailed comparison of the individual experimental and simulation modes is planned for the near future to more accurately probe this trend and others.

3. Development of theoretical and numerical tools for improved simulations of EP interaction with instabilities

Most results shown in this section are based on data from a L-mode NSTX scenario featuring robust toroidal Alfvén eigenmode activity, see Fig. EP-11. Several toroidal Alfvén eigenmodes (TAEs) are unstable following injection of 2MW NB power. Toroidal mode numbers are n=2-6, with dominant n=3,4 modes. Shortly after the NB is turned on, modes show small amplitude bursts and frequency chirps $\delta f/f<10\%$. The fast ion population increases in time, resulting in a stronger drive for the modes. Eventually, a strong burst of TAE activity (a so-called *avalanche*) occurs around t~480ms, which leads to large losses of fast ions from the core plasma.

The growth of TAEs driven unstable by energetic particles up to saturation has been investigated with the guiding center code ORBIT for L-mode NSTX scenarios [EP-18]. Numerical eigenfunctions (computed through the NOVA code) and a numerical EP distribution are used to make detailed comparison with the experiment. Two innovations are introduced. First, a very noise free means of obtaining the mode-particle energy and momentum transfer is introduced, and secondly, a spline representation of the actual beam particle distribution is used.

A δf formalism has been implemented in ORBIT to solve the drift kinetic equation in the presence of Alfvén modes and to advance the mode amplitudes and phases in time. The initial distribution f0, inferred from TRANSP, is assumed to be a steady state EP distribution in the absence of the modes, and f = f0 + δf describes the particle distribution in the presence of the modes. The analysis is applied to cases exhibiting saturated mode amplitudes at a well defined mode frequency, although the formalism can also describe mode chirping.

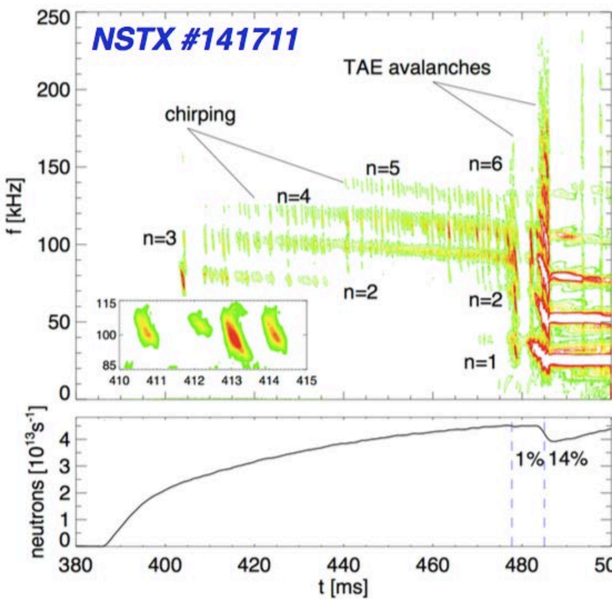

Figure EP-11: *(Top) Fluctuation spectrum for NSTX #141711. (Bottom) Measured neutron rate, showing sudden drops associated with strong bursts of TAE activity.*

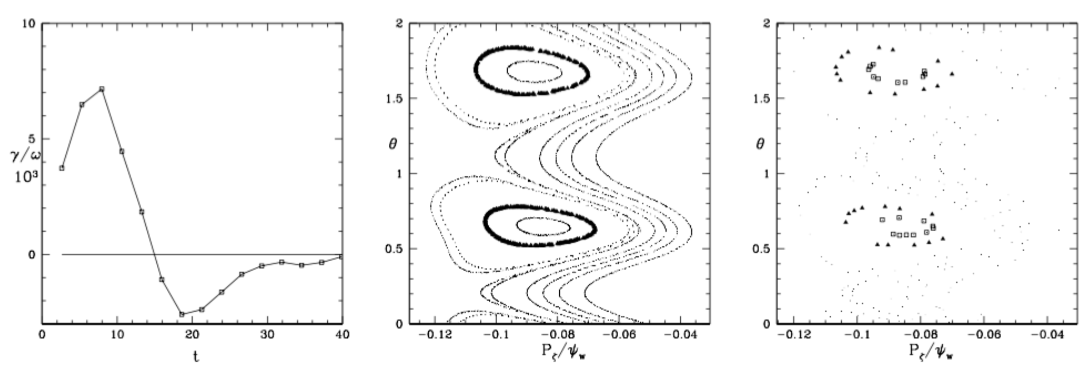

Figure EP-12: *γ/ω versus time, Poincaré plots with 1000 transits and 40 transits. In one bounce time the distribution in an island is flattened, and if the amplitude is fixed and there are no collisions or slowing down of particles, causing them to enter or leave resonance, the mode drive stops.*

The variables determining mode growth and saturation are the drive, given by partial derivatives of f and the slowing down and collision frequencies and the damping. Growth is determined by an imbalance between the rate at which free energy is available at the mode resonances and the mixing rate. Mode saturation occurs when the resonant islands grow to a point where these rates are balanced. Saturation occurs because the mixing rate increases with island size and eventually equals the energy source rate, allowing a local flattening of the distribution within the island and eliminating the mode drive as shown in Fig. EP-12.

For this study, the evolution of each mode was carried out separately, so there was no mode-mode interaction in these simulations. The simulations included pitch angle scattering and slowing down with time scales of 200 msec. The initial growth rate is given in the first 50 transits, and by 300 transits the growth rates for most modes have dropped to very small values. In this case the transit time is about three microseconds. An example of the time evolution of individual modes for NSTX discharge #141711 is shown in Fig. EP-13. 200,000 marker particles are used in the simulation. All modes evolve to stable saturated levels. The final time for these simulations, equal to 5 msec, corresponds to a small fraction of a collision time.

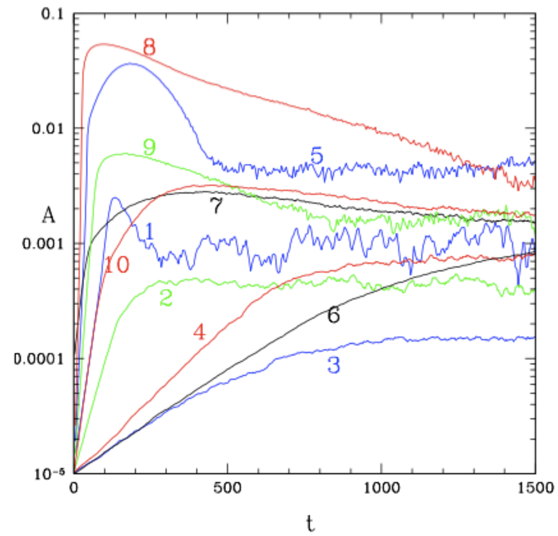

Figure EP-13: *An example of time evolution of individual modes using NOVA damping rates with collision time of 200 msec. Shown is the amplitude vs time, with time in units of toroidal transits.*

A second approach has been developed over the past few years to incorporate EP transport effects by instabilities in time-dependent integrated simulation codes such as TRANSP. The resulting reduced model (dubbed "kick model") has been implemented in the NUBEAM module of TRANSP. During FY-16, the model has been improved to include the effects of a finite electrostatic potential on EP orbits and energy. This is important for plasmas featuring values of EP potential energy associated to the underlying electrostatic potential as high as 15-20 keV, which is a considerable fraction of the typical NB injection energy of 80-90 keV. In addition, the kick model has been integrated within NUBEAM to treat EP transport on the same collisional time-scales as other "classical" effects such as slowing down and pitch angle scattering. Mapping of EP orbits from real to phase space has been also improved with respect to earlier implementation of the model.

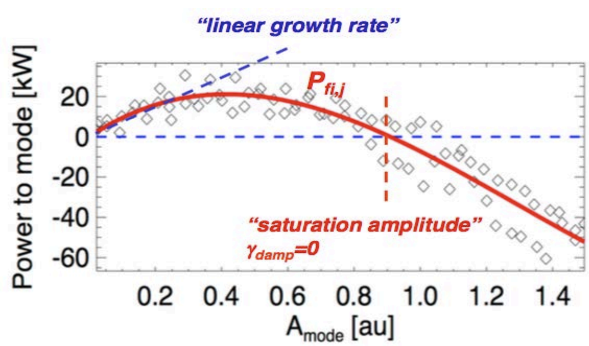

Figure EP-14: *Illustration of the method used to infer "linear" growth rate and mode saturation amplitude from the TRANSP/kick model analysis. Growth rate is computed from the derivative of the power transferred from the fast ions to the mode as the amplitude vanishes. Saturation amplitude is identified as the finite amplitude at which the net power transfer vanishes, indicating that growth and damping rates compensate each other.*

Recent applications of the kick model have focused on developing a procedure to compute mode stability and infer saturation amplitudes from the coupled TRANSP/kick model analysis [EP-19]. Similarly to the ORBIT analysis presented above, the kick model analysis is based on the evolution equation for the mode amplitude, whose growth is the result of the competition between drive from the EP population and damping. Drive is computrom the power transferred from the EP to the modes, which is calculated in NUBEAM (see Fig. EP-14). The procedure provides two important quantities: (i) "linear" growth rate in the limit of vanishing mode amplitude, and (ii) saturation amplitude such that drive and damping compensate each other. For this analysis, the only damping mechanism included comes from flattening of the EP distribution around resonances in phase space. The total damping is therefore under-estimated, which results in an upper limit for the computed saturation amplitudes.

Kick model results of the stability and saturation of TAEs for NSTX discharge #141711 are shown in Fig. EP-15. Mode structure for about 50 TAEs with toroidal mode number n=1-8 are first selected from NOVA calculations. The resulting transport probability matrices, computed through ORBIT, are then used in TRANSP/NUBEAM to assess mode stability and saturation amplitude. Overall, the analysis predicts an unstable TAE spectrum peaked at n=2-3, consistent with the experiment. The inferred mode amplitudes are $\delta B/B \sim 10^{-3}$, which is also a reasonable estimate compared to previous studies. As for the ORBIT analysis of the same discharge discussed above, a strongly unstable n=1 TAE is predicted but not observed in the experiment. This is arguably due to the destabilization of a lower-frequency n=1 kink mode in the real case, which is not included in the present analysis and can compete with the n=1 TAE.

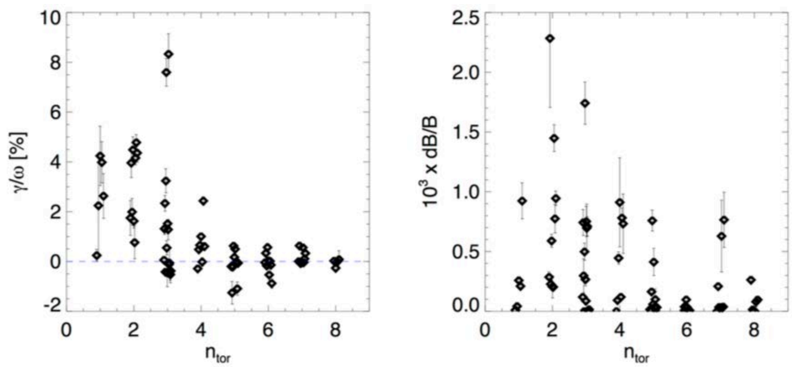

Figure EP-15: *TRANSP/kick model results of "linear" growth rate and saturation amplitude for NSTX #141711.*

Results from the TRANSP/kick model analysis have been compared with those from a model (CGM) based on the assumption of a "critical gradient" in EP space that sets the saturated AE amplitude and EP transport levels [EP-20]. This concludes a work started in FY-15

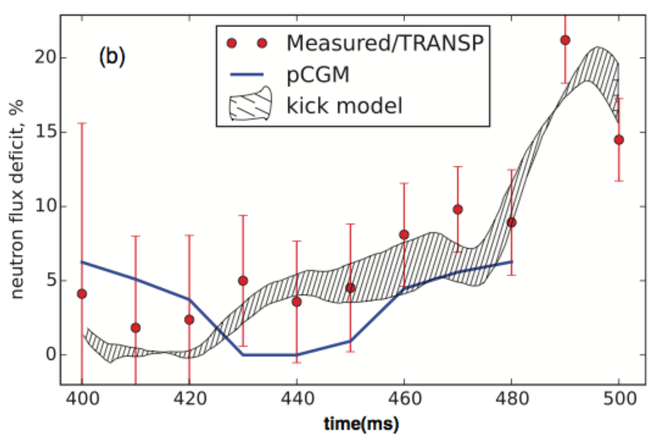

Figure EP-16: *Neutron deficit as computed by the TRANSP code for NSTX #141711. It compares the deficit with the predictions by the CGM and with the analysis of the kick model within the error bars. At t=480 ms a TAE avalanche occurs (cf. Figure EXP-SCEN), for which regime the validity of the CGM model is questionable.*

targeting the validation of predictive models for EP profile relaxation in burning plasmas, based on the comparison of model's predictions with NSTX and DIII-D data.

The main results are shown in Fig. EP-16, where the predicted deficit in neutron rate with respect to "classical" simulations (i.e., without additional transport by instabilities) is compared with experimental results for scenarios with strong AE activity.

In the application of perturbative version of CGM (pCGM) to the NSTX data, a version of the model based on the normalization of the AE growth rates to NOVA-K computed increments was used. The normalization constants are derived using the TAE mode structures at four/five radial points, r/a~0.1, 0.3, 0.5, 0.7 and 0.9. The radii are chosen by finding the locations of the maximum values of the growth rates of TAEs peaked at those radii. Between those locations, a linear interpolation formula was used. An analytic expression for growth and damping rates is employed outside that range. Figure EP-16 presents the results of the model predictions against the NSTX data. Considering experimental uncertainties in the absolute calibration of the neutron detectors, the pCGM predictions are within the error bars of the measurements. In addition, Fig. EP-16 compares pCGM computed neutron deficit with the one inferred from the experiments using the TRANSP/kick model approach described above. The later comparison shows the same level of agreements, i.e. within the error bars of the modeling. Overall, the pCGM validation exercise against the NSTX experimental results looks promising and warrants a confidence in its possible predictions for burning plasmas. The validating exercise ensures that the quasi-linear approach targeted within PPPL is an appropriate method for future research in the EP area.

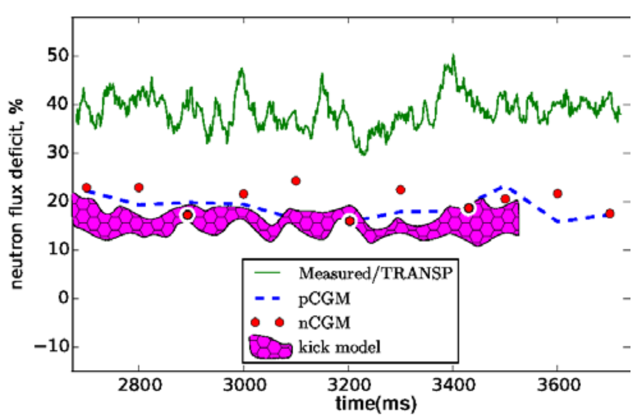

Figure EP-17: Comparison of the nCGM, nCGM and the kick models for DIII-D test case, discharge #153072. The deficit is compared with the experimentally obtained deficit using classical computations by the TRANSP code. All three models give the same discrepancy for the deficit, which is about 2 times smaller than the computed using TRANSP.

The perturbative approach adopted in the CGM (pCGM) model cannot be applied reliably to plasmas that feature large AE growth rates, such as typical DIII-D plasmas. Under those conditions, pCGM can under-predict the neutron deficit by up to a factor ~2. The question emerges whether the model is applicable, since earlier studies suggest that non-perturbative explanations should be brought [EP-21]. A new non-perturbative version of CGM (nCGM), is developed to account for the non-perturbative excitation of various modes including TAEs when their drive is strong [EP-20]. The HINST code (HIgh-N STability code, [EP-22][EP-23]) is available for that purpose and is applied. The code solves the system of relevant equations for AE modes in the ballooning variable to find the mode structure and its net growth rate non-perturbatively. HINST cannot be applied to NSTX because of its low aspect ratio. However it is applied to DIII-D plasma where the drive reaches $\gamma/\omega \sim 0.3$ locally and the application of the perturbative NOVA-K results is questionable. HINST computed net growth and damping rate are used for nCGM normalization where the linear interpolation was used again between the computed values of the growth rates. Twenty radial points are used by HINST computations and provide the growth and damping rates normalization points. Beam ion neutron flux deficit profiles are computed by the 1.5D code, which are plotted in Fig. EP-17. The results of the DIII-D validation show that the predictions of both pCGM and nCGM are close to each other. Another conclusion is that p,nCGMs are in agreement with the kick model computations shown in Fig. EP-17 [EP-20].

It should be noted that results from all three models discussed above postulate the existence of modes that saturate at well-defined amplitudes. As can be seen in Fig. EP-11 for a L-mode NSTX discharge, this may not be the case in real discharges: mode amplitude can vary in time, with features characteristic of a bursting/chirping non-linear regime, so that the concept of a stationary saturated amplitude may need to be replaced by that of a time-averaged amplitude with time-dependent oscillations. Predicting in which regime – stationary vs. bursting/chirping – the instabilities will develop is therefore critical for reliable predictions.

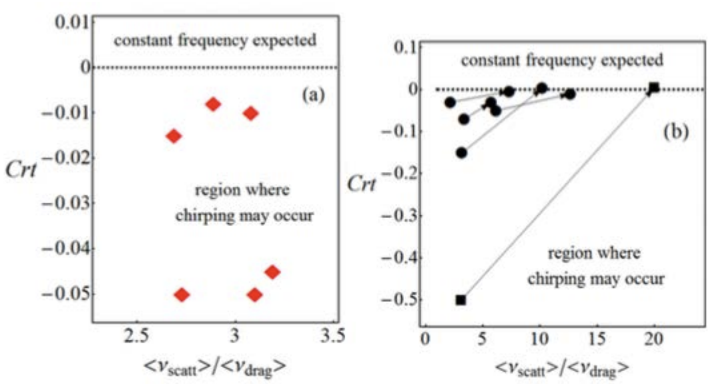

Figure EP-18: *Numerical values for the figure of merit Crt as a function of $<v_{scatt}>/<v_{drag}>$ for AE modes in (a) NSTX and (b) DIII-D. Negative values of Crt indicate that conditions for the insurgence of chirping modes are satisfied. Arrows indicate the change in the prediction as scattering from micro-turbulence is included. For the NSTX cases, the points hardly move upon the addition of spatial diffusion to collisional scattering. (Figure from Ref. [EP-24]).*

An improved criterion for prediction of the insurgence of bursting/chirping AEs has been developed in FY-16 [EP-24] and validated against NSTX and DIII-D experiments. The new criterion generalizes the approach used by Lilley, *et al* [EP-25] that indicates whether marginally unstable Alfvénic modes, destabilized by energetic particles, are more likely to chirp or more likely to remain as steady oscillations. The model indicates that stochasticity (e.g. from enhanced scattering of fast ions) promotes steady, fixed-frequency behavior, while drag (e.g. from slowing down) promotes chirping. It is often essential to use the detailed criterion, rather than an approximate form, to obtain a criterion that agrees with experimental data. Hence, the NOVA and NOVA-K eigenmode codes are used to calculate mode structure, the wave-particle interaction strength and the pitch angle and drag contributions from the resonant regions of phase space. Scattering of EPs due to micro-turbulence is also a significant stochastic diffusion process to consider even though the macroscopic EP equilibrium distribution is hardly affected by ion micro-turbulence. In addition, TRANSP is used to infer the ion micro-turbulent diffusion rate. Since the micro-turbulent space scale is typically much less than the energetic particle Larmor radius, the large energetic particle orbit has substantially less diffusion from this turbulence than the background plasma. A gyro-kinetic theoretical model [EP-26] is used to estimate this reduction. In NSTX, the contribution from the micro-turbulence interaction with fast ions is found to be insignificant. As a result, the generalized chirping criterion for NSTX experiments predicts that chirping should arise for the shots that were analyzed, cf. Fig. EP-18. This prediction is in agreement with the experimental observation in NSTX [EP-27]. In DIII-D, ion micro-turbulence is often at a high enough level so that induced stochastic diffusion from ion micro-turbulence needs to be accounted for. This contribution is typically large enough to prevent chirping from arising. However, the few cases that chirping is observed on DIII-D correlates closely with a marked reduction in the experimental ion micro-turbulence. Thus, this theory together with the observed data, appears to answer a puzzle as to why chirping is so rarely observed in D-III-D and so ubiquitous in NSTX. It provides important elements for predicting which of the two extreme scenarios is most likely to be relevant for the character of the energetic particle transport – stationary vs. bursting/chirping modes.

References

[EP-1] A. Bortolon et al., Phys. Rev. Letters **110** (2013) 265008

[EP-2] G. J. Kramer et al., Plasma Phys. Control. Fusion **58** (2016) 085003

[EP-3] F. Wang et al., Nucl. Fusion (submitted 2016).

[EP-4] N. N. Gorelenkov et al., Nucl. Fusion **43**, 228 (2003)

[EP-5] E. D. Fredrickson, et al., Phys. Plasmas **20**, 042112 (2013)

[EP-6] H. Smith, et al., PPCF **51**, 075001 (2009)

[EP-7] N. A. Crocker, *et* al, Nucl. Fusion **53**, 043017 (2013)

[EP-8] E.V. Belova, et al., Phys. Plasmas **7**, 4996 (2000).

[EP-9] E.V. Belova, et al., Phys. Rev. Lett. **115**, 015001 (2015).

[EP-10] E.V. Belova, et al., to be submitted to Phys. Plasmas (2016).

[EP-11] D. Stutman, et al., Phys. Rev. Lett. 102, 115002 (2009).

[EP-12] E.V. Belova, et al., Phys. Plasmas **7**, 4996 (2000).

[EP-13] J. Lestz, et al., Bull. Am. Phys. Soc. **60**, 146 (2015).

[EP-14] E. Fredrickson et al, Nucl. Fusion **52**, 043001 (2012).

[EP-15] S. Tang, et al., Bull. Am. Phys. Soc. **60**, 148 (2015).

[EP-16] V.S. Belikov, et al., Phys. Plasmas **10**, 4771 (2003).

[EP-17] D. Liu et al, Rev. Sci. Instrum. **87**, 11D803 (2016).

[EP-18] R. B. White et al., Plasma Physics Control. Fusion (in press 2016).

[EP-19] M. Podestà et al., presented at US Transport Task Force Meeting, Denver CO (March 2016)

[EP-20] N. N. Gorelenkov et al., Nucl. Fusion **56** (2016) 112015

[EP-21] Z. Wang et al., Phys. Rev. Lett. **111**, 145003 (2013).

[EP-22] C. Z. Cheng et al., Nucl. Fusion **35**, 1639 (1995).

[EP-23] C. Z. Cheng and N. N. Gorelenkov, Phys. Plasmas **11**, 4784 (2004).

[EP-24] V. N. Duarte, *Prediction of nonlinear evolution character of Energetic Particle driven instabilities*, Phys. Rev. Letters (submitted 2016)

[EP-25] M. K. Lilley et al., Phys. Rev. Letters **102** (2009) 195003

[EP-26] W. Zhang et al., Phys. Rev. Letters **101** (2008) 095001

[EP-27] M. Podestà et al., Nucl. Fusion **52**, 094001 (2012).

III. Integrated Scenarios Research Highlights

The integrated scenarios group is tasked with understand the following elements within the NSTX-U program:

- ST startup & ramp-up,
- HHFW heating and current drive,
- neutral beam current drive,
- axisymmetric plasma control,
- fully non-inductive plasma scenarios, including non-inductive ramp-up, and
- integration of the above elements amongst themselves, and with the scientific understanding achieved in the other science groups.

As in FY-15, the science group is led by Stefan Gerhardt (PPPL), with Roger Raman (U. of Washington) as the deputy. The science group is divided into three topical science groups (TSGs), as follows in the list below. This leadership is the same as in FY-15.

A. The **Solenoid Free Plasma Startup** (SFPS) TSG is tasked with understanding solenoid free startup-up and ramp-up. The TSG leader is Dennis Mueller (PPPL) with Roger Raman as the deputy. Fatima Ebrahimi (Princeton University) acts as the theory and modeling representative.

B. The **Wave Heating and Current Drive** (WHCD) TSG is tasked with understanding the physics and technology of HHFW, ECH, and potentially EBW, in the unique plasma conditions and geometry of the ST. The group is led by Rory Perkins (PPPL), with Joel Hosea (PPPL) as the deputy. Nicola Berteli (PPPL) is the theory and modeling representative, and Paul Benoli (MIT) is the university representative.

C. The **Advanced Scenarios and Control** (ASC) TSG is tasked with understanding axisymmetric plasma control, scenarios with very high non-inductive current fraction or very long pulse, and discharge scenario development in general. The TSG leader is Devon Battaglia (PPPL), with Stefan Gerhardt as the deputy. Francesca Poli (PPPL) is the theory/modeling representative, and Prof. Egemen Kolemen (Princeton University) is the University representative.

A. Solenoid-Free Start-up and Ramp-up TSG Research Highlights

A.1: Hardware Updates

Significant progress was made on preparing the CHI hardware for operations. This includes testing the CHI capacitor bank into a dummy load and installation of the high-speed vessel voltage instrumentation. The final major hardware installation required for CHI was the fast gas injection system. While the injection valves themselves were mounted on the machine, the fill-system was not completed when the run was brought to a premature end. This comparatively minor task was on schedule to be completed by the end of the run, and will be completed during the outage between the FY-16 and FY-17 run.

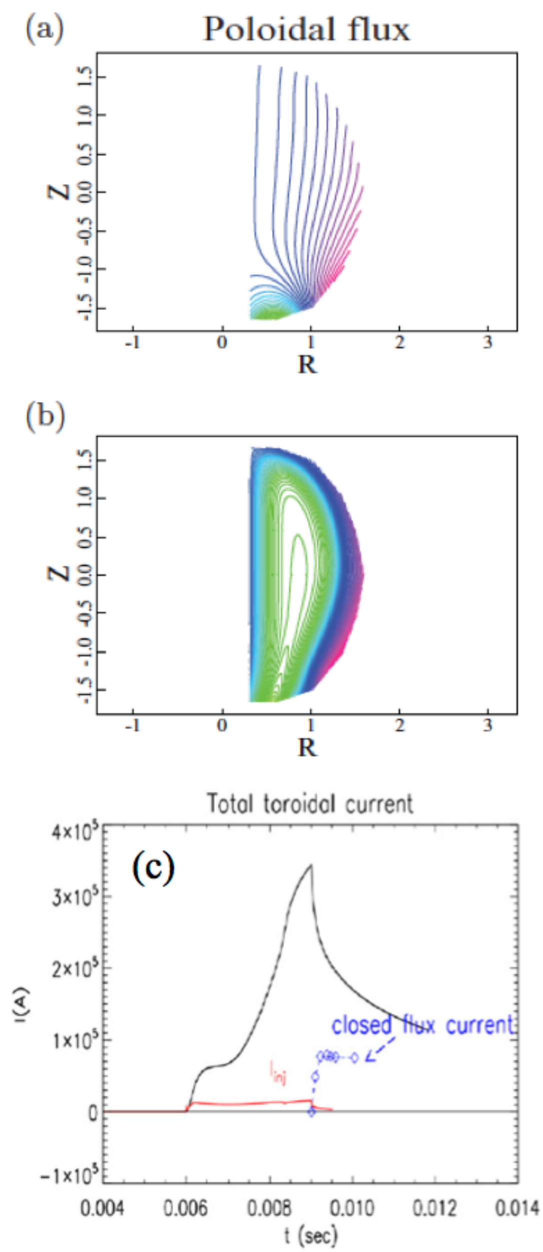

Figure IS-SFPS-1: No currents in the flux shaping coils. (a) Initial injector flux at t=0, (b) at t=9ms and (c) toroidal plasma current (black), the injector current (red), and the closed flux current magnitude (blue).

See the facility chapter of this report for more information on the CHI hardware for NSTX-U.

A.2: NIMROD Simulations

Recent NIMROD simulations by F. Ebrahimi (PU) in the NSTX-U geometry have obtained very high levels of closed flux for CHI initiation in the NSTX-U geometry [IS-1].

An example of a simulation that obtained low levels of closed flux is shown in Fig. IS-SFPS-1. Helicity injection in these simulations starts by applying a constant voltage to the inner and outer divertor plates at t=6 ms. In the absence of current in the flux shaping coils (PF2L and PF1aL), the initial poloidal flux shown in frame a) is generated with the primary injector coil (PF1cL). Plasma and poloidal flux expand into the device as shown in frame b). As the injector voltage is turned off at **t**=9 ms (decay phase), oppositely-directed field lines in the injector region are pushed together to reconnect and closed flux surfaces are formed. A small volume of closed poloidal flux is formed during the decay phase and open field lines carry most of the current. For this case, the total generated toroidal current is over 300 kA; however, only a small fraction of it, about 10– 30% of the current is on closed field lines as shown in frame c).

An example of a simulation which obtained high levels of flux closure is shown in Fig. IS-SFPS-2. In this simulation, currents are also driven in the injector flux shaping coils (PF2L and PF1aL) to bring the injector flux footprints closer together. To obtain a narrow injector flux footprint, the currents in the flux shaping coils should be in the opposite direction of current in the primary injector flux coil. The current in the injector coil is in the same direction as the plasma direction. As the injector flux footprint is made narrower, the force balance now requires a larger injector current, because the field line tension increases. This is seen in the simulations in Fig. IS-SFPS-2, where an injector current of 16 kA is needed for the wide footprint case (Fig. IS-SFPS-1) whereas a higher injector current of 34 kA is now needed for the narrow flux footprint case. The magnitude of the injector flux for the two cases of wide and narrow flux footprint are 70 mWb and 75 mWb, respectively. For simulations with narrow flux footprint, after the flux expands and fills up the vessel, a forced Sweet–Parker type reconnection is induced by reducing the injector voltage and current to zero. A much larger volume of flux closure is now formed as shown in frame a). Poloidal flux within the last closed flux surface is 40 mWb and, depending on the initial poloidal coil currents, is about 60– 70% of the injector flux. In this simulation, due to narrow injection flux footprint width and the availability of more reconnecting flux in a narrow region, most of the oppositely directed open field lines close. During the decay

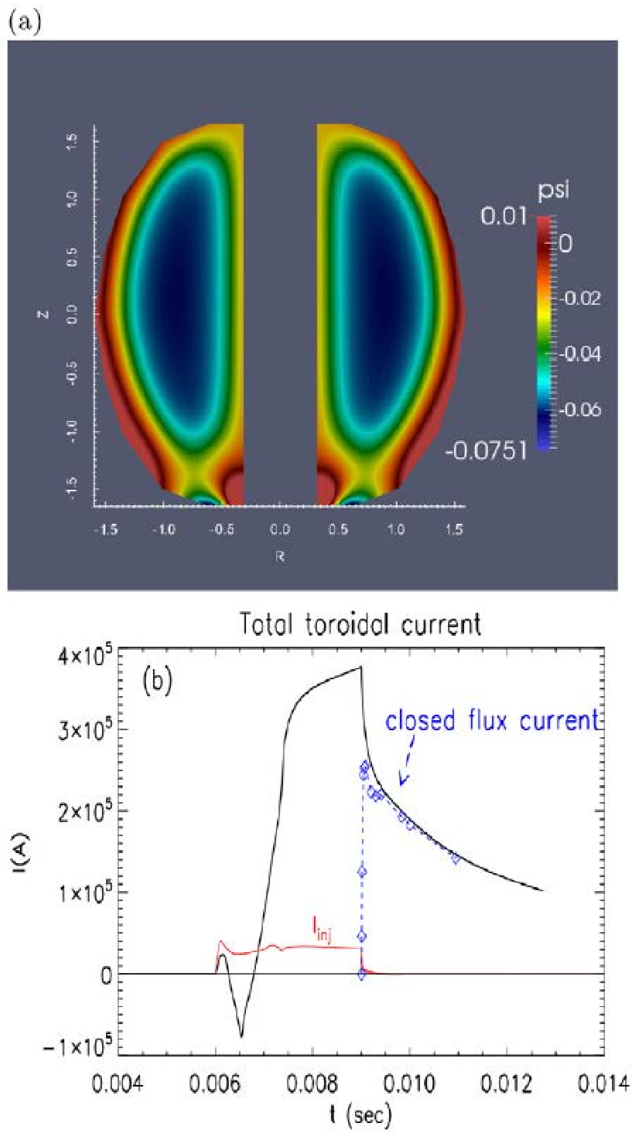

Figure IS-SFPS-2: *With currents driven in the flux shaping coils. (a) Poloidal flux at t = 9.8ms. (b) Toroidal plasma current, injector current (red), and closed flux currents (blue).*

phase, when the injector voltage is off, as the total current starts to resistively decay, almost all of the total current is found to in the closed flux region (with a large closed-flux current of about 240 kA), as seen in frame b).

We therefore find that the volume of closed flux surfaces and the closed-flux current with strong flux shaping coils are much larger than the case without flux-shaping coils. The maximum of closed flux current without the shaping coils is only 20– 30% of the total toroidal current and is about a third of the case with flux shaping coils.

We should note that the maximum 240 kA closed flux current with strong flux shaping coils is obtained using 140 kA·turns current in the primary injector flux coil PF1cL. Increasing the current in this coil to the full 318 kA· turns limit should generate more than 400 kA of closed flux current.

These simulations also show that the closed flux generation following injector voltage and current reduction can occur both during plasmoid mediated reconnection (described in the 2015 annual report) or the simpler Sweet-Parker type reconnection (described in the 2014 annual report). More details are provided in Reference [IS-1].

A transient CHI discharge has two primary phases. The first is the actively driven phase, a 1-2ms period on NSTX, during which the magnetic bubble is grown into the vessel. The bubble growth is programmed such that as the plasma fills the vessel, the energy in the driving capacitor bank is simultaneously depleted, so that the injector current is reduced to zero. During the second phase, because the substantially reduced injector current is no longer able to satisfy the requirement for injecting flux, the injected poloidal flux already in the vessel closes in on itself to generate a closed flux configuration. It had been previously postulated that some flux closure, although not necessary during the driven phase, might occur even during the actively driven phase. Interestingly the simulations reported above [IS-1] show this happing during the very early driven phase.

In a different set of NIMROD simulation (by B. Hooper, LLNL) the electron temperature was increased from the nominal 25eV (corresponding to present experimental condition) to 100eV. In addition the system was strongly driven by ensuring that the applied voltage for the 100eV simulations is the same as that for the 25eV simulations. Experimentally, this is an over-driven system because at the higher temperatures less applied voltage is needed to maintain the appropriate injector current requirement for transient CHI, and in addition, as described in the previous paragraph, for *transient* CHI, the injector current is reduced to zero as the plasma fills the vessel. Nevertheless, the simulation is applicable for the cases of *driven* CHI discharges. In these *driven* simulations a high poloidal mode number, n=1 instability is observed during the driven phase. In simulations for which the plasma temperature is low, the mode is coherent and has little effect on the injection. If the surface layer of the injected bubble rises to ~100eV or higher, the mode amplitude undergoes relaxation oscillations. During the relaxation events, magnetic flux closure regions seen during the injection phase of purely axisymmetric simulations do not occur.

With regard to publication, a paper describing the transient CHI configuration for a ST-FNSF was published [IS-2]. A paper describing the use of a transient CHI system to simplify the ST and AT reactor concepts was published [IS-3]. Finally, a paper describing modeling of the non-inductive ramp-up and sustainment on NSTX-U was published [IS-4]; some additional modeling on this topic is described in the ASC section of this report.

A.3 CHI on QUEST

Transient CHI experiments on QUEST will test a new CHI electrode configuration that may be easier to implement on a fusion reactor. The electrode configuration was described in the 2015 Annual report. Shown in Figure IS-SFPS-3 is the NSTX-sized CHI capacitor bank undergoing commissioning tests at the QUEST facility. All CHI systems needed to enable transient CHI capability have now been tested at QUEST. Initial experiments are planned for later in this calendar year.

Transient CHI studies on QUEST will address aspects of transient CHI development that may not be possible on NSTX-U, or may be too expensive to implement on NSTX-U. Therefore, these studies directly support CHI research on NSTX-U. The key objectives of CHI studies on QUEST are:

1) Study transient CHI operation using metal electrodes (as planned for on NSTX-U in future years)
2) Study the effect of high-power ECH heating of a CHI plasma (also directly in support of NSTX-U research)
3) Develop a new and alternate CHI electrode configuration that may easier to implement on fusion reactors, and even on other present and future tokamaks [IS-2,IS-3].

Figure IS-SFPS-3: The Univ. of Washington designed and built QUEST CHI capacitor bank (30 mF, 2kV) undergoing commissioning tests at the QUEST facility in Kyushu University during March 2016.

References

[IS-1] F. Ebrahimi and R. Raman, Large-volume flux closure during plasmoid-mediated reconnection in coaxial helicity injection, Nuclear Fusion (Letter) **56** (2016) 044002

[IS-2] R. Raman, T. Brown, L.A. El-Guebaly, T.R. Jarboe, B.A. Nelson, J.E. Menard**,** Design Description for a Coaxial Helicity Injection Plasma Start-up System for a ST-FNSF, Fusion Science and Technology **68**, 674 (2015)

[IS-3] R. Raman, T.R. Jarboe, J.E. Menard, M. Ono, G. Taylor, B.A. Nelson, D. Mueller, T. Brown, Simplifying the ST and AT Concepts, Journal of Fusion Energy, **35**, No. 1, 34-40 (2016)

[IS-4] F. Poli, R.G. Andre, N. Bertelli, S.P. Gerhardt, D. Mueller, and G. Taylor, Simulations of non-inductive current ramp-up and sustainment in the National Spherical Torus Experiment Upgrade, Nuclear Fusion **55** (2015) 123011

B. Wave Heating and Current Drive TSG Research Highlights

B.1: Advanced RF Modeling

Full wave simulations of fast wave efficiency and power losses in the scrape-off layer of tokamak plasmas in mid/high harmonic and minority heating regimes

2D AORSA full wave numerical analysis has been performed for “conventional” tokamaks with higher aspect ratios, such as the DIII-D, Alcator C-Mod, and EAST devices, in order to estimate the behavior of the RF power losses in “standard” geometry experiments, in similar or different heating regimes and to compare these with NSTX/NSTX-U results. DIII-D results are found to be in agreement with the results obtained for NSTX/NSTX-U and they are also in agreement with previous experimental observations [IS-5]. In contrast, numerical simulations for Alcator C-Mod and EAST, which operate with ICRH in the hydrogen minority regime in deuterium majority plasma, differ from the simulations results for NSTX/NSTX-U and DIII-D, which operate in the mid/high ICRH harmonic regime [IS-6]. Results in the minority heating regime are also consistent with the experimental data, which show a clear improvement in the ICRH performance when gas is injected in front of the ICRH antenna [IS-7]. Fig. IS-WHCD-1 shows that in C-MOD and EAST the SOL power loss is dramatically reduced with increasing electron density in front of the antenna, whereas the opposite trend is seen for the NSTX and DIII-D simulations.

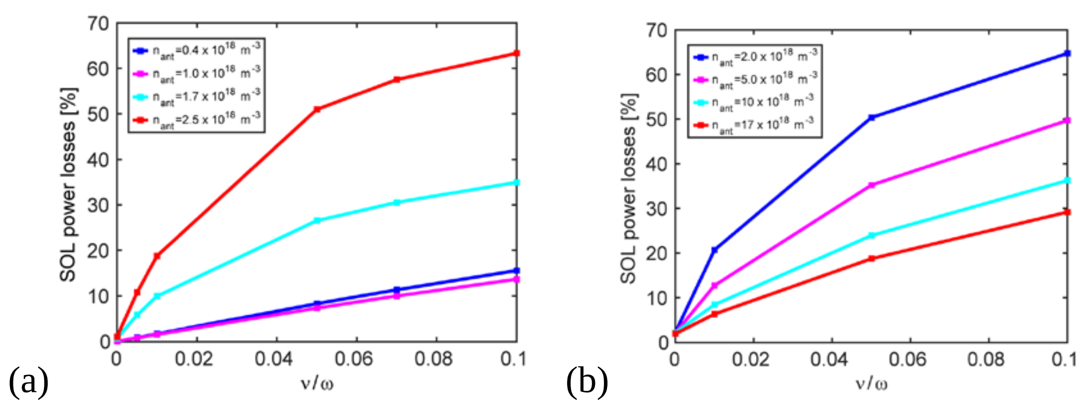

Figure IS-WHCD-1*. (a) Fraction of power lost to the SOL as a function of ν/ω for four different values of the electron density in front of the antenna n_{ant} = 0.4×10 ^{18} m^{-3}, 1.0×10^{18} m^{-3}, 1.7×10^{18} m^{-3}, and 2.5×10^{18} m^{-3} with toroidal mode number $n^{\phi} = -21$ for NSTX shot 130608. (b) Fraction of power lost to the SOL as a function of ν/ω for four different values of n_{ant} = 2.0×10 ^{18} m^{-3},5.0×10^{18} m^{-3}, 10×10^{18} m^{-3}, and 17×10^{18} m^{-3} with ω/2π = 80 MHz and n_{ϕ} = 10 for Alcator C-Mod case.*

Studies on the impact of the magnetic pitch angle on the behavior of the RF electric field and the associated power lost in the SOL in NSTX-/NSTX-U have been performed. Different NSTX-U magnetic equilibria have been generated by the stand-alone free-boundary equilibrium code ISOLVER for $B_{T,0}$ = 1 T and I_p = 0.5, 1.0, 1.6, and 2 MA. Figure IS-WHCD-2 shows the amplitude of the RF electric field for these cases with toroidal mode number $n_{\phi} = -21$ and density in front of the antenna $n_{ant} = 5.0\times10^{18}$ m^{-3}, a density at which the FW can propagate in the SOL region and large RF electric fields together with high SOL power losses have been found in the ‘standard’ NSTX-U with $B_{T,0}$ = 1 T and I_p = 1 MA (see figure 5 in [IS-8]). In figure IS-WHCD-2 one can note that with changing the magnetic pitch angle, the large high RF field amplitude in the SOL region is still present but the region with the strongest RF field amplitude moves down below the mid-plane as the plasma current is increased. These results seem to suggest that the magnetic pitch angle plays a significant role in the behavior of the RF field and the corresponding RF losses in the SOL. Results described in this Section are published in Bertelli et al, Nuclear Fusion 2016 [IS-9].

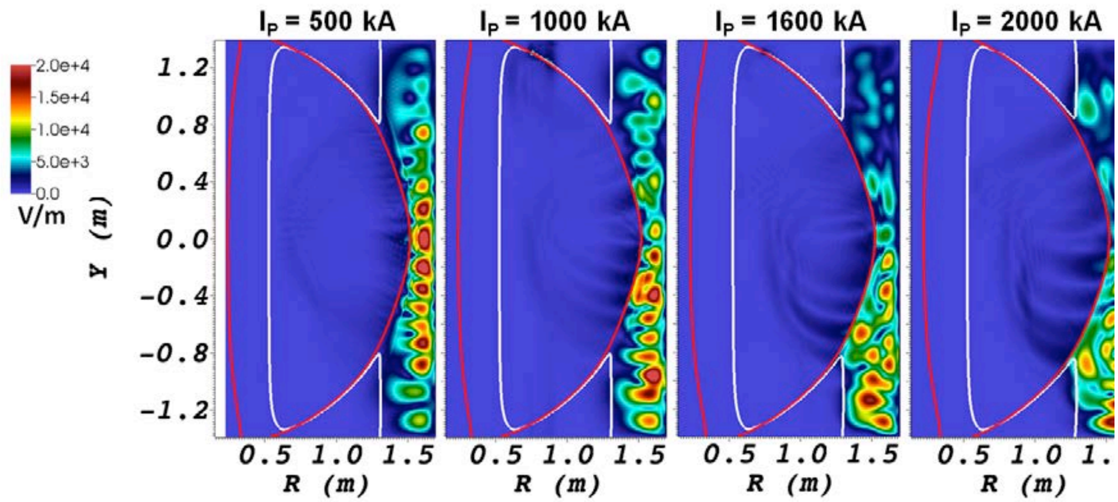

Figure IS-WHCD-2. Total electric field amplitude for different NSTX-U equilibria (generated by ISOLVER) with toroidal mode numbers $n_\phi = -21$, B_T = 1 T, different plasma currents (shown in the plots), and $n_{ant} = 5\times10^{18}\ m^{-3}$. The white and red curves indicate the FW cut-off layer and the LCFS, respectively.

The non-Maxwellian extension of the full-wave TORIC v.5 code in the high harmonic heating regime

As demonstrated in the NSTX and DIII-D experiments the interactions between fast waves and fast ions can be so strong that it can significantly modify the fast ion population from neutral beam injection (NBI). In fact, it has been found in NSTX that FWs can modify and, under certain conditions, even suppress the energetic particle driven instabilities, such as toroidal Alfvén eigenmodes (TAEs) and global Alfvén eigenmodes (GAEs) and fishbones [IS-10, IS-11, IS-12]. For these reasons, an extension of the full wave TORIC code to include non-Maxwellian ion effects in the HHFW regime has been implemented and tested. First, for the case of the thermal distribution function, the extended TORIC v.5 has been verified against the standard TORIC v.5 showing excellent agreement. Second, the bi-Maxwellian and slowing down analytical distributions have been implemented. With these inclusions it is seen that the total absorbed power by fast ions is insensitive to variations in the parallel electron temperature (with respect to the magnetic field), but varies with changes in perpendicular temperature. However, the absorption profile of the fast ions tends to be localized to the resonant layers for small parallel temperature (see Figure IS-WHCD- 3). Third, a comparison of the wave electric field and the power deposition profile with a slowing-down distribution has also been performed. Finally, the use of a “realistic” distribution function obtained by the Monte-Carlo NUBEAM code is underway. Tests and applications will be performed during FY2017.

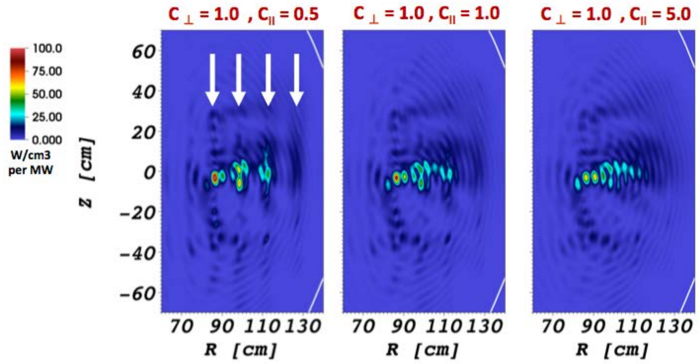

***Figure IS-WHCD-3**. Contour plots of the absorption by fast ions in a NSTX plasma for (a) $C_\perp = T_\perp/T = 1.0$ and $C_{||} = T_{||}/T = 0.5$ (b) $C_\perp = T_\perp/T = 1.0$ and $C_{||} = T_{||}/T = 1.0$, namely, the Maxwellian case, and (c) $C_\perp = T_\perp/T = 1.0$ and $C_{||} = T_{||}/T = 5.0$. $C_\perp$ and $C_{||}$ are parameters in the perpendicular [$v_{th,\perp} = \mathrm{Sqrt}(2C_\perp T(\psi)/m_D)$] and parallel [$v_{th,||} = \mathrm{Sqrt}(2C_{||}T(\psi)/m_D)$] thermal velocity, respectively, for fast ions species represented by a bi-Maxwellian distribution function . The white curve represents the last closed flux surface. The arrows on the left-most frame show the resonant layers.*

2D finite element full wave code

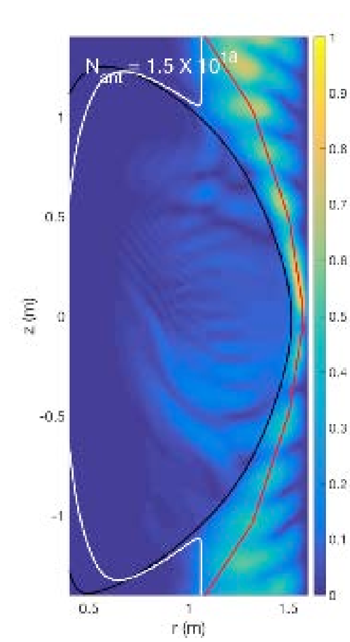

***Figure IS-WHCD-4**. Total electric field amplitude for $n_{ant} = 1.5 \times 10^{13} cm^{-3}$, n_{ant} is the density in front of the antenna), with toroidal mode numbers $n_\varphi = 12$. The white, black, and red curves indicate the FW cut-off layer, the LCFS, and vessel boundary, respectively.*

During FY2016, we started to collaborate with Dr. Eun-Hwa Kim (from the PPPL theory department) on the finite element 2D full-wave code (so called FW2D) [IS-13] to examine radio frequency (RF) waves in the scrape-off layer (SOL) of tokamaks. This wave code has been successfully applied to describe low frequency waves in planetary multi-ion magnetospheres, and the results include mode conversion at the ion-ion hybrid resonance, wave coupling near the crossover frequency, and magnetosonic wave propagation [IS-14, IS-15]. FW2D solves the cold plasma wave equations using the finite element method. One of the main advantage of this method is that the local basis functions can be readily adapted to boundary shapes and can be packed in such a way as to provide higher resolution in regions where needed. Therefore, this code is appropriate for carefully examining the wave propagation in the SOL region of a tokamak plasma (in particular, in NSTX-U), with realistic boundary shapes and arbitrary SOL density profiles (1D and 2D). In FY2016, as a first step, (i) we extended the code to be able to handle a toroidal magnetic field configuration; and (ii) we performed a few test runs for the NSTX case, similar to those conducted with the AORSA code [IS-8, IS-9]. An example is shown in Figure IS-WHCD-4. Additional benchmark activities will be performed in FY2016 together with some applications.

2: Ongoing Experimental Progress & Analysis

Recommissioning the HHFW System

Recommissioning the HHFW system was started in the previous fiscal year but was delayed due to a fault in the switching cabinet of HHFW system #5 upon failure of breaker Q6B5C to open. This occurred on January 5, 2016 and led to a lengthy repair/rebuild/replacement process to the crowbar circuit, breakers, and relays both in the HHFW systems and in the AC power yard. The modified system is improved and more resilient.

After corrective measures were implemented, vacuum conditioning commenced on all six sources. Conditioning was done mostly pair-wise: operating two adjacent sources (e.g. Sources 1 and 2, 3 and 4, or 5 and 6) while detuning the others from the resonant circuit. Every source was conditioned to at least 19 kV and for a duration of at least 100 ms. Based on past experience, these voltages in vacuum are sufficient to couple at least one to two megawatts of RF power to an NSTX-U plasma, and the entire system is ready for plasma conditioning.

HHFW Diagnostic Status

Two radial arrays of divertor Langmuir probes were installed to measure RF voltages in the divertor and sheath heat fluxes due to RF rectification. Probe circuitry was reviewed and built and is awaiting installation of the chassis in the test cell. An IR camera was acquired for monitoring heat loads to the antenna and antenna limiter; the magnetic shield has been fabricated, but the system was not installed during the campaign. The ORNL SOL reflectometer, to be used to acquire SOL density profiles in front on the antenna, has been reinstalled, and commissioning was begun. A midplane probe shaft, situated in the middle of the antenna, is being fitted with two Langmuir probes and double-Langmuir probe designed by ORNL. The probes and accompanying mechanical supports were designed and reviewed, and construction is nearly complete. Much of the installation work for a new fast color camera needed for monitoring arcs and plasma-antenna interactions was completed.

RF-Rectification during HHFW Power Ramp-up, and its Role in Heat Flux

Analysis of divertor Langmuir probes during HHFW heating is leading to important discoveries regarding radio-frequency (RF) rectification [IS-12]. Namely, the probes show the existence of rectified electron currents, which significantly increase the computed sheath heat flux. This discovery is important for NSTX in determining how the lost HHFW power is converted to a heat flux into the divertors, and it could have implications for ICRF antenna regarding antenna erosion, impurity production, and hot spot scaling. RF rectification has two aspects: an RF potential at the sheath entrance induces an increased average [rectified] electron current through the sheath, and then the plasma potential *may* rise to screen out the rectified current. It is frequently assumed in ICRF research that plasma potential rises to exactly cancel out the rectified current, but the rectified currents observed in the NSTX divertor Langmuir probes provide an instance where this is not the case.

These currents are indicated in Fig. IS-WHCD-5 by the change in probe floating potential (Fig. IS-WHCD-5a) without accompanying change in electron temperature or density (Fig. IS-WHCD-5b). Figure IS-WHCD-5c shows the computed RF potential, calculated assuming no change in plasma potential. We expect the RF potential to scale as the square root of applied HHFW power, and the first four data points do appear to follow this trend (solid lines in Fig. IS-WHCD-5d a and c). However, at higher HHFW power, the computed RF potential falls short of this trend, and we hypothesize that the plasma potential begins to rise, clamping the change in floating potential (and hence rectified current) at a fixed level. That is, the assumption that the plasma potential rises to screen the rectified current is likely only valid at large RF potentials, and the Langmuir probe data from the NSTX divertor may be showing the onset of this phenomena. To emphasize the importance of rectified currents, when these currents are accounted for in first-principle models for the heat flux to the tiles, we predict a sizeable enhancement for the heat flux in the presence of an RF field: for one case studied, the predicted heat flux doubles from 0.103 MW/m^2 to 0.209 MW/m^2. Figure IS-WHCD-5d shows the calculated heat flux to the probe under the two assumptions of rectified currents with no change in plasma potential and also for full-screened currents; it is clear that the former gives the larger heat flux, meaning that RF rectification is all the more likely to be playing a significant role in SOL losses of HHFW power in NSTX.

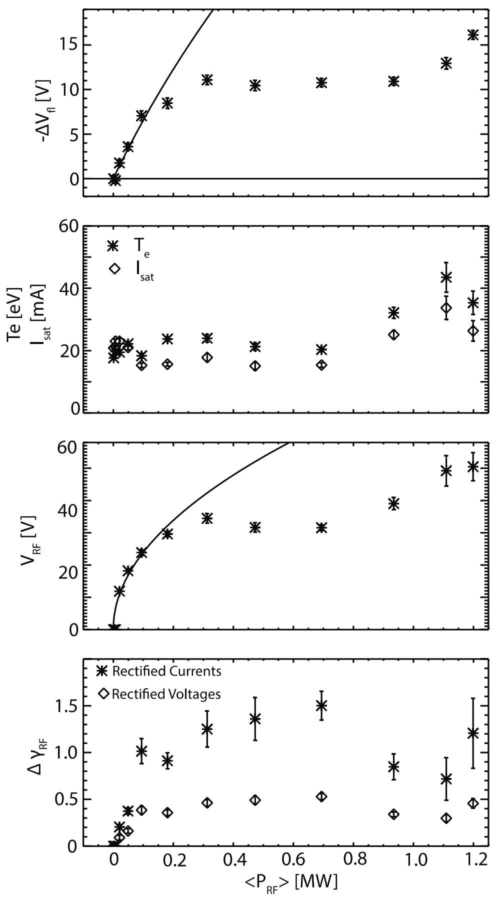

Figure IS-WHCD-5. *Probe characteristic and RF rectified quantities as a function of applied HHFW power for shot 141838 with no neutral beam injection. (top) Change in floating potential (2nd from top) Ion saturation and electron temperature; neither changes systematically with P_{RF} (2nd from bottom) RF potential calculated assuming no change in floating potential (bottom) heat flux to probe expressed as heat transmission coefficient, for both the assumption of fully rectified current and fully rectified voltages. The former gives the larger heat flux.*

Long-Pulse ICRH Heating for EAST

Our work in understanding RF rectification connects to our collaborative work on the EAST tokamak for the minority-heating regime. Fast-camera images show bands of light in the lower divertor region, similar to the spirals seen in the upper and lower divertors of NSTX (Fig. IS-WHCD-6). These bands move as the outer gap width is varied, again similar to the NSTX results [IS-17]. Divertor triple-probe arrays show a clear response to the applied ICRF power, and the change in floating potential appears to depend on whether the probes are magnetically connected to the antenna [IS-18]. We hope to further explore these features in an experimental proposal that was that allocated run-time but postponed due to machine conditions.

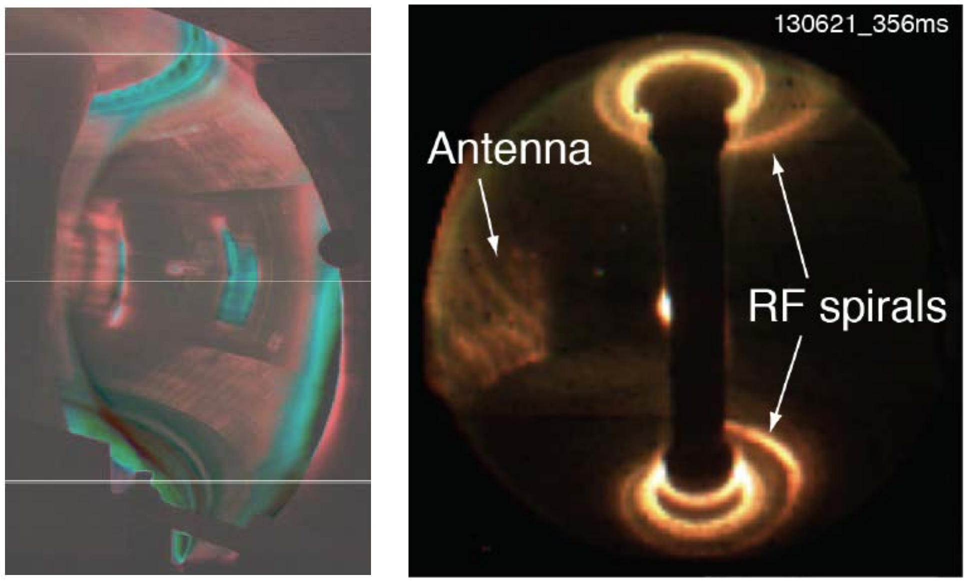

Figure IS-WHCD-6. *(Left) Fast-camera image of EAST shot at 3.525 s (with background subtraction at 3.190 s) for 1.7 MW applied ICRF power (0.73 MW estimated to couple to the core) with a 2 cm outer gap. The band of light on the bottom divertor is reminiscent of the spiral seen in NSTX during HHFW heating. (Right) Fast-camera image of NSTX for shot 130621 at 356 ms (no background subtraction).*

We also are engaged in discussion with staff from the Large Plasma Device at the University of California Los Angeles and also with B. LaBombard, D. Brunner, and A. Kwang of Plasma Science and Fusion Center concerning Langmuir probe response to RF application in their respective devices.

Annulus Resonances in Cylindrical Plasmas and Application to SOL Losses of HHFW Power

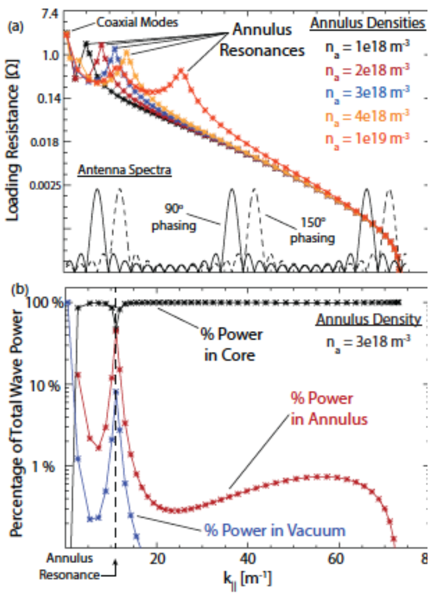

***Figure IS-WHCD-7**. (a) This figure shows that annulus resonances have the largest amplitude of all modes in the system. Each point is the loading resistance of an m = 2 mode; the different colors indicate different annulus densities n_a. The peak in loading seen for each annulus density is the annulus resonance; the parallel wavenumber $k_{||}$ of the resonance strongly depends on annulus density. Antenna spectra for model twelve-strap antenna with 21 cm inter-strap spacing and 90° and 150° phasing are plotted for reference. (b) This plots shows how the mode power is distributed spatially in the cylinder: core (black), annulus (red), and vacuum (blue) regions for the $n_a = 3 \times 10^{18}\ m^{-3}$ case of (a). Typical modes conduct the vast majority of the wave power in the core, but the annulus resonance shows an abrupt departure from this trend, with half the power being conducted in the relatively small edge*

A cold-plasma cylindrical model was previously developed using a low-density edge plasma to mimic the SOL of a tokamak. We identified a special class of modes, dubbed “annulus resonances,” that conducts a large fraction of the total wave power in the edge plasma. This year, we determined that these modes exist at wavenumbers such that a half radial wavelength fits into the edge plasma region, and they stand out from other modes not only in their large amplitude and unique radial distribution of Poynting flux (Fig. IS-WHCD-7), but they also appear to have a core fast-wave phase ninety-degrees out of phase with other modes [IS-19]. The modes are distinct from usual coaxial modes or surface modes and appear to be a new mode for fast waves in a bounded system. These results corroborate results drawn from the full-wave code AORSA, namely [IS-8, IS-9] that cavity-like modes are driving the SOL losses. These results also suggest that tailoring the outer gap size can influence the parallel wavenumber of these modes, possibly moving them off the antenna spectrum.

HHFW coupling during start-up plasmas, and the response of the outer gap to step-changes in plasma heating

Coupling HHFW power to the plasma depends strongly on the outer gap size, which can oscillate substantially both during the start-up phase and also in response to step changes to plasma heating. Both these features make it challenging to couple HHFW power to NSTX plasmas in general and especially to start-up plasmas.

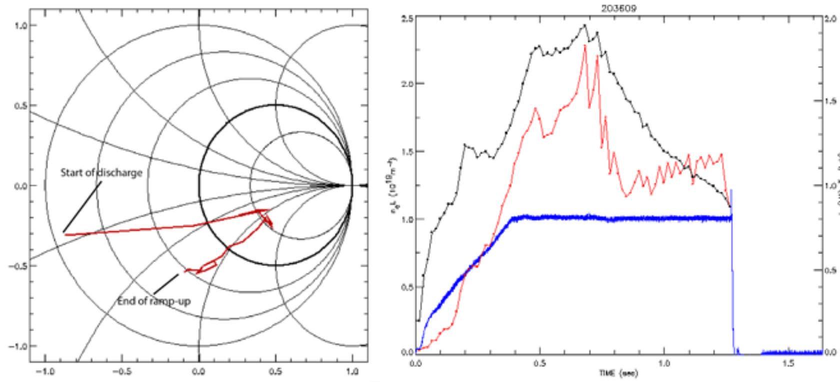

Figure IS-WHCD-8. *(Left) Reflection coefficient plotted on a Smith chart for single strap excitation during the ramp-up phase of shot 203609. Judicious adjustment of the matching circuit may transform these points closer to the match point at the center to permit coupling. (Right) Plasma current (blue), central electron temperature (red), and line-integrated electron density (black) for shot 203609.*

To assist in applying HHFW power during start-up, we are developing methods to apply low-power (2 W) 30 MHz power to the transmission line to test the antenna loading during NSTX-U operation. Figure IS-WHCD-8 shows an example of the trajectory of the complex reflection coefficient on a Smith chart during current ramp-up using a network analyzer. The modulus squared of this quantity is the fraction of reflected RF power: the outer circle indicates complete reflection, and the center represents a perfect match. Figure IS-WHCD-8 shows the substantial variations that occur as the density and outer gap evolve, which makes coupling HHFW power difficult during this phase. While this measurement needs to be improved to guarantee proper phasing at the antenna straps, it indicates a good starting point for determining how to configure the HHFW matching circuit to lower the reflection coefficient sufficiently to permit coupling during start-up.

When auxiliary plasma heating changes abruptly, the fractional change in stored energy can cause radial motion, which in turn can be detrimental to HHFW coupling. The changes in outer gap in NSTX-U can be different from those in NSTX due to the change in geometry (larger center stack radius changes plasma inductance) and the new start-up sequence. We have begun to study the outer gap oscillations using neutral beam heating as a proxy to HHFW heating. Figure IS-WHCD-9a shows that the onset of additional plasma heating can induce larger variations in the outer gap. However, it may be possible to minimize this effect by timing the auxiliary heating onset with a particular phase of the gap oscillation, or with the oscillations in the PF5 coil (Fig. IS-WHCD-9b), which is trying to control the outer gap. Alternatively, it may be possible to further optimize the outer gap control gains, in order to minimize these perturbations.

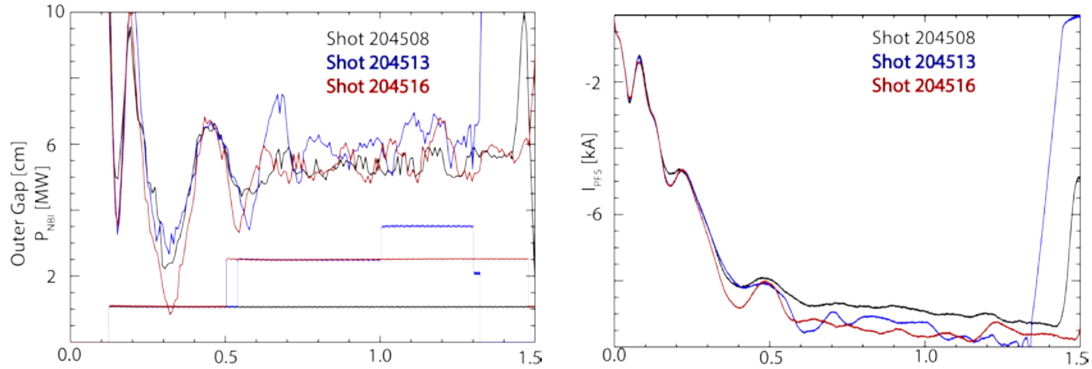

Figure IS-WHCD-9. *(Left) Outer gap values for L-mode discharges with different neutral beam waveforms. The outer gap has large oscillations and shot-to-shot variability during start-up. Also, step-changes in plasma heating induce larger gap oscillations as well. (Right) Current in the PF5 coil for the same set of shots; this coil is responsible for controlling the outer gap.*

Synthetic Aperture Microwave Imaging Diagnostic

A novel, proof-of-principle, Synthetic Aperture Microwave Imaging (SAMI) diagnostic, originally installed on the Mega-Amp Spherical Tokamak (MAST) at the Culham Centre for Fusion Energy, is now operational on NSTX-U. The diagnostic consists of an array of 8 independently-phased antennas. It operates at one of 16 frequencies in the range 10-34.5GHz at any one time. The operating frequency can be switched many times during a plasma pulse. This frequency range is chosen to cover the steep gradient region in the edge of H-mode plasmas. The antenna array is installed on the outboard midplane and has a wide field of view that extends over 80 degrees in the toroidal and poloidal direction. Consequently SAMI has a good view of the NSTX-U plasma. The imaging beam is steered in software after the plasma pulse to create an image of the emission surface. An active probing mode of operation is also used, where the plasma edge is illuminated with a monochromatic source and SAMI reconstructs an image of the Doppler back-scattered (DBS) signal. By assuming that density fluctuations extend along magnetic field lines, and knowing that the strongest back-scattered signals are directed perpendicular to the density fluctuations, SAMI's 2-D DBS imaging capability can be used to measure the pitch of the edge magnetic field. Preliminary magnetic field pitch angle measurements, obtained by SAMI on both MAST and NSTX-U, show encouraging agreement between SAMI and other independent measurements. Preliminary results on NSTX-U show the time evolution of the field pitch measured by SAMI just inside the last closed flux surface qualitatively follows estimates from EFIT, but are somewhat larger. While this discrepancy is currently unexplained, it is interesting to note that the MSE measurement on MAST, which is less well-resolved spatially than SAMI, also over-estimates the pitch angle compared to EFIT. MSE data has so far not been available on NSTX-U.

References

[IS-5] C. C. Petty *et al*, *Nucl. Fusion*, **39** (1999) 1421.
[IS-6] N. Bertelli *et al*, 25 IAEA FES Conf. (2014) TH/P4-14.
[IS-7] P. Jacquet *et al*, *Nucl. Fusion* **56** (2016) 046001.
[IS-8] N. Bertelli *et al*, *Nucl. Fusion* **54** (2014) 083004.
[IS-9] N. Bertelli *et al*, *Nucl. Fusion* **56** (2016) 016019.
[IS-10] E.D. Fredrickson *et al*, *Nucl. Fusion* **55** 013012 (2015).
[IS-11] M. Podestà *et al*, *Nucl. Fusion* **52** 094001 (2012).
[IS-12] W. W. Heidbrink *et al*, *Plasma Phys. Control. Fusion* **48** 1347 (2006).
[IS-13] J. R. Johnson, , E. Valeo, E.-H. Kim, and C. K. Philips (2012), PPPL technical report, 4743.
[IS-14] E.-H. Kim, and J. R. Johnson *Geophys. Res. Lett.*, **43** (2016) 13.
[IS-15] E.-H. Kim, J. R. Johnson, E. Valeo, and C. K. Phillips *Geophys. Res. Lett.*, **42** (2015) 5147.
[IS-16] R. J. Perkins *et al.*, *Nuclear Materials and Energy*, submitted.
[IS-17] R. J. Perkins *et al., Phys. Rev. Lett.* **104** (2012) 045001.
[IS-18] J. C. Hosea *et al.*, US-PRC Workshop 2016.
[IS-19] R. J. Perkins *et al., Phys. Plasmas* **23** (2016) 070702.

C. Advanced Scenarios and Control TSG Research Highlights

C.1 Summary of Milestone R16-3

The milestone R16-3 is titled "*Develop the physics and operational tools for obtaining high-performance discharges in NSTX-U*". The report associated with the completion of this milestone details much of the relevant ASC work for this fiscal year, and the interested reader is referred to that report. Key highlights include the following.

- rtEFIT was commissioned for NSTX-U. This includes a new multi-threading option that allows vessel and coil currents to be fit in realtime.
- ISOFLUX shape control was commissioned for NSTX-U. This includes a new closed loop inner-gap control algorithm.
- Improvements were made to the vertical control algorithm, including both additional sensors and improved numerical details.
- Error field control strategies have been developed, which improved the discharge performance.
- The Digital Coil Protection System (DCPS) supported routine operations.
- A plasma shutdown scheme, based on a state machine and controlling all NSTX-U actuators in a synchronized way, has been implemented and used.
- L-mode scenarios have been developed that exceed in duration the longest discharges ever taken on NSTX.
- H-mode plasma scenarios have been developed, with values of β_N exceeding the no-wall β_N limit.

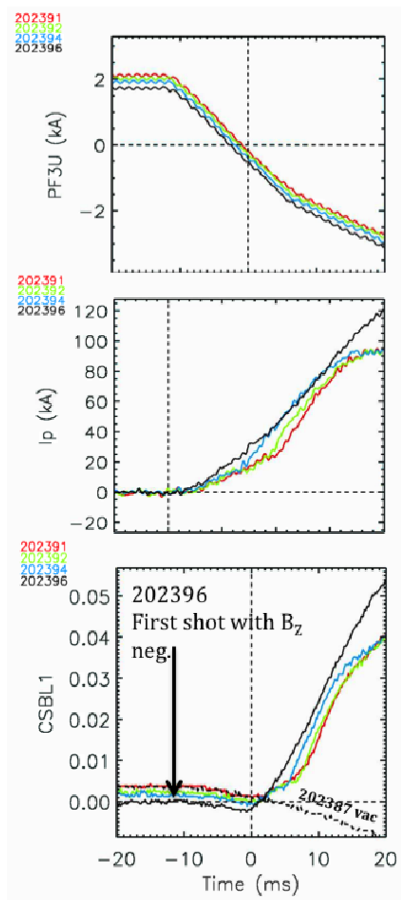

Figure IS-ASC-2*: PF3U coil current, plasma current and magnetic flux through a flux loop around the center column near the midplane. Timing of the startup moves earlier as the nulling field from PF3 is reduced.*

C.2 Inductive startup scenario development for NSTX-U

All discharges in the FY16 experimental campaign on NSTX-U were initiated using ohmic induction with either an 8 kA or 20 kA pre-charge of the ohmic solenoid. The 8kA ohmic precharge scenario is similar to the inductive startup scenario used on NSTX and was used to produce the first plasma on NSTX-U (see FY15 report).

XMP-101 (Inductive startup scenario development for NSTX-U) was completed over the first few days of FY16 operations. One result was the timing of the breakdown and start of the plasma current rampup was tuned to begin near t = 0 by scanning the magnitude of the nulling field from the PF3 coils. Figure IS-ASC-1 shows a scan of the PF3 current evolution used to produce the first plasma (red line) to an optimized scenario (black line). Calculations of the field evolution using the LRDFIT code are not in full agreement with the observations, as those calculations indicate discharge 202391 (red line) provides the optimum null timing; reconciling the calculation of the field null timing with the experimental observations is on-going work.

The LRDFIT calculations are in agreement with the observation that the field null has a reduced vertical extent on NSTX-U compared to NSTX as measured by fast-framing cameras. Figure IS-ASC-2 shows LRDFIT calculations of the axisymmetric breakdown parameter

$$\frac{V_{loop} I_{TF}}{\pi R^2 \left(B_\theta + \langle B_{\theta,NA} \rangle\right)}$$

averaged over 2 ms where B_θ is the axisymmetric poloidal magnetic field and $\langle B_{\theta,NA} \rangle$ is the toroidal average of the non-axisymmetric component of the poloidal magnetic field (i.e error field); note that only the top half of an up-down symmetric field null is shown in each frame. Figure IS-ASC-2a is a calculation for NSTX assuming $\langle B_{\theta,NA} \rangle$ is 4G in order to produce a breakdown parameter in the range of 1 V MA/ m^2 G. This magnitude of the toroidally averaged error field is consistent with measurements and simulations of the error field due to tilting of the ohmic solenoid at maximum current. Figure IS-ASC-2b is a calculation for NSTX-U that matches the 8kA ohmic pre-charge scenario that uses a larger toroidal field rod current and loop voltage than compared to NSTX. The breakdown region has a similar radial extent, but a smaller vertical extent and a smaller maximum value of the breakdown parameter. Reducing the non-axisymmetric fields in the calculation (figure IS-ASC-2c) achieves a match with the maximum magnitude to the NSTX calculation. The results from XMP-101 found that the loop voltage required with 8 kA of ohmic pre-charge and $N_{TF}I_{TF}$ = 3.0 MA·turns on NSTX-U was below 3V (2.5 – 2.8V was typical), which may suggest that non-axisymmetric fields at breakdown have been reduced compared to NSTX. This is consistent with measurements showing the ohmic solenoid tilting is significantly reduced on NSTX-U.

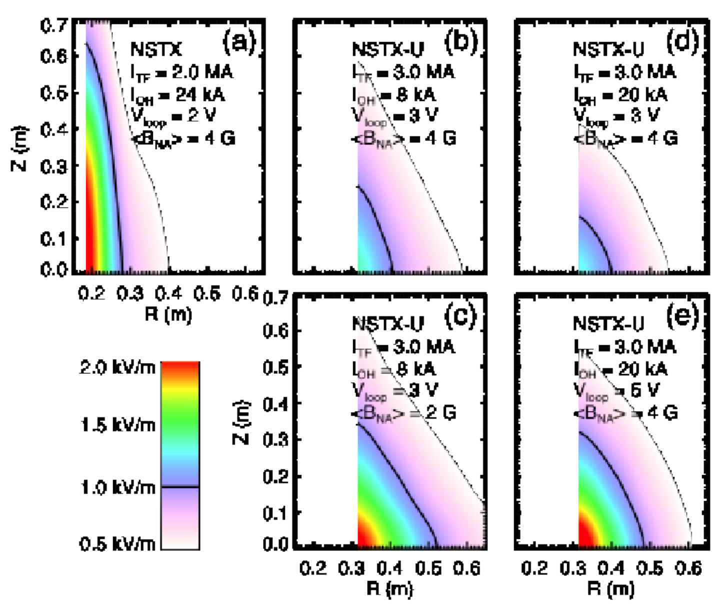

Fig. IS-ASC-2: *Contours of the average breakdown parameter for the first 2ms as calculated by LRDFIT for (a) NSTX and (b-e) NSTX-U.*

XMP-101 also established a breakdown scenario using a 20 kA ohmic precharge (the maximum solenoid current permitted for FY16). This scenario maximizes the volt-seconds available to maintain the plasma current, and thus was the primary startup scenario for most of the campaign. More loop voltage was needed for this scenario, consistent with LRDFIT calculations that indicate the vertical extent of the poloidal field null is reduced with larger ohmic precharge (figure IS-ASC-2d). Increasing the loop voltage at breakdown increases the magnitude of the breakdown parameter without much change to the shape of the field null (figure IS-ASC-2e). Experiments found that breakdown with the 20 kA ohmic pre-charge required about one extra loop voltage compared to the 8 kA pre-charge cases.

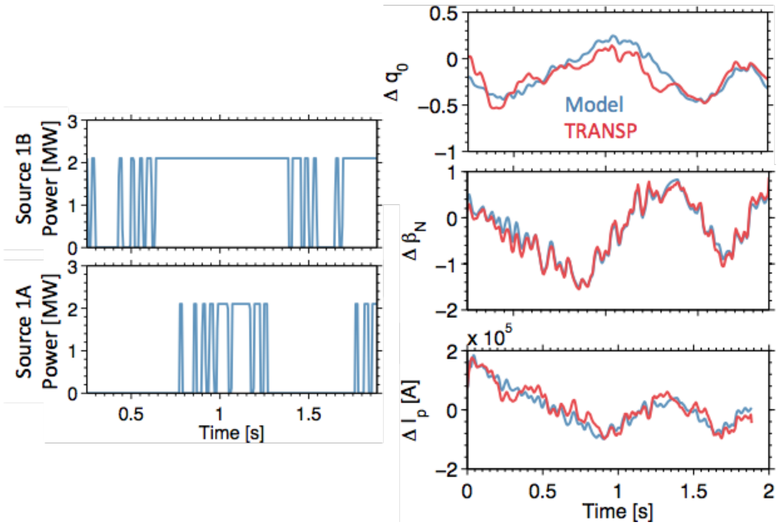

***Fig IS-ASC-3**: Beam modulations used during model comparison (left) and comparison of simplified linear model to TRANSP results (right).*

The 20 kA pre-charge scenario was successful in supporting experiments in FY16 (for example, see figure R16-3-1 in Milestone R(16-3) summary), however some work remains in optimizing the current ramp up in the first 10 ms of the discharge, which will be pursued during FY17 operations. Also, the breakdown scenarios required the PF3L current to be more negative than the PF3U current in order to center the magnetic field null in the vacuum vessel. The magnitude of the up-down asymmetry is not reproduced in LRDFIT calculations, and the source of this discrepancy is under investigation. Work will also continue on developing breakdown scenarios at lower toroidal fields. Most discharges in FY16 operated with $N_{TF}I_{TF}$ ~ 3.0 MA·turns (~83 kA per turn for 0.62 T on-axis), however work was done under XMP-101 to demonstrate breakdown over a range of rod currents as low as $N_{TF}I_{TF}$=1.6 MA·turns (~45 kA per turn or 0.35T on-axis) using the 8kA ohmic precharge scenario.

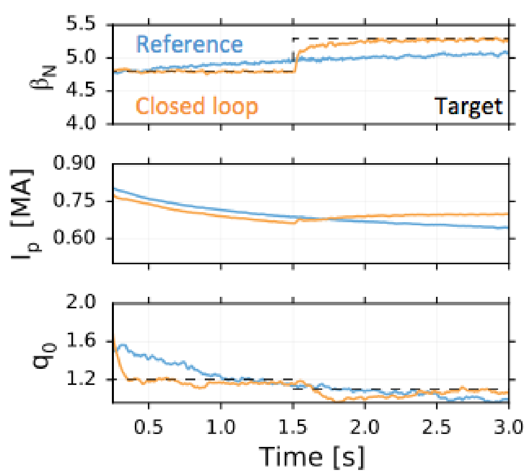

***Fig. IS-ASC-4**: Comparison of closed loop tracking results with reference simulation. In the closed loop simulation, beam power was used to control β_N and plasma boundary mid-plane outer gap size was used to control q_0.*

C.3 Control and Scenario Modelling

Study of Feedback Control of Non-Inductive Scenarios

In preparation for experimental studies of non-inductive scenarios on NSTX-U, TRANSP has been used to study the response of potential scenarios to disturbances in density, confinement, and profile shapes. A series of simulations has also been used to study the effect of possible actuators for controlling the scenario, including individual beam powers and the plasma shape. The simulation results were used to create a linearized dynamic model for the response of the stored energy, plasma current, and central safety factor to the actuators. The ability of the model to predict the output of the system during a simulation with modulated beam power is shown in Figure IS-ASC-3. The simplified model was used to study potential feedback control algorithms to improve system response time and track different targets for the model outputs. A recently developed framework for feedback control simulations in TRANSP has been used to study the effectiveness of the proposed control algorithms at tracking targets and rejecting disturbances. A demonstration of tracking step targets for the normalized plasma beta and central safety factor using the beam power and outer gap as actuators is shown in Figure IS-ASC-4.

TRANSP-based Trajectory Optimization of the Current Profile Evolution to Facilitate Robust Non-inductive Ramp-up in NSTX-U

Initial progress towards the design of non-inductive current ramp-up scenarios in the National Spherical Torus Experiment Upgrade (NSTX-U) has been made through the use of TRANSP predictive simulations [IS-4]. The strategy involves, first, ramping the plasma current with high harmonic fast waves (HHFW) to about 400 kA, and then further ramping to 900 kA with neutral beam injection (NBI). However, the early ramping of neutral beams and application of HHFW leads to an undesirably peaked current profile making the plasma unstable to ballooning modes. A collaboration between Lehigh (W. Wehner and E. Schuster) and PPPL (F. Poli) sponsored by the DOE SCGSR program[1] involves building an optimization-based control approach to improve on the non-inductive ramp-up strategy. The project aims to combine the TRANSP code with an optimization algorithm based on sequential quadratic programming to search for time evolutions of the NBI powers, the HHFW powers, and the line averaged density that define an open-loop actuator strategy that maximizes the non-inductive current while satisfying constraints associated with the current profile evolution for MHD stable plasmas.

The project also involves control oriented modeling of the current profile evolution in NSTX-U to combine the open-loop control approach described above with model-based feedback control to improve reproducibility of the non-inductive ramp-up strategy. To model the current profile evolution, empirical correlations are combined with first-principles laws to arrive at a control-oriented model, which captures the dominant physics necessary for model-based control design. The feedback controller is based on a model predictive control approach. The primary advantage of this approach is that it allows for explicit incorporation of constraints associated with the plasma state. This opens the possibility for the controller to maximize the non-inductive current fraction in a fashion that restricts the controller from driving the plasma outside of stability limits.

[1] http://science.energy.gov/wdts/scgsr/

HHFW modeling in TRANSP

Following the implementation and validation of the GENRAY-CQL3D workflow in TRANSP for Lower Hybrid calculations in TRANSP, we have undertaken the extension of the treatment of Fokker-Planck species in CQL3D/TRANSP to ions for application of HHFW in NSTX-U. The work is being done in collaboration with R. Harvey and Yu Petrov at COMPX. This way, the GENRAY-CQL3D interface allows a self-consistent treatment of interactions between RF and fast-ions from Neutral Beams, although with a model for NBI (FREYA) that is more simple that NUBEAM. This tool – which will provide an additional comparison with TORIC and NUBEAM - is presently under test and is not available to users yet.

EC/EBW modeling with Fokker-Planck treatment in TRANSP

EC wave propagation in plasmas can be approximated with linear ray tracing trajectories. However, at the low densities in the start-up and in the early ramp-up phase, Fokker Planck treatment is deemed necessary, because nonlinear effects become important. The GENRAY-CQL3D interface in TRANSP has been extended to the EC waves to allow for more consistent simulations in this phase of both EC absorption as well as EBW conversion.

Snowflake Divertor Control

A new algorithm has been implemented within the ISOFLUX shape control category of the NSTX-U plasma control system to enable realtime feedback control of snowflake divertor (SFD) magnetic configurations. The algorithm, defined by Patrick Vail, a PU graduate student advised by Prof. Egemen Kolemen, locates the position of two proximate x-points using data from rtEFIT and regulates the magnetic configuration by computing a set of current requests for a combination of the PF-1a, PF-1b, PF-1c, and PF-2 coils. A simple graphical user interface allows the physics operator to program target values for the parameters that determine the x-point positions and to use a set of numerical weights that define the relative importance of each parameter in the control. The implementation of the SFD control within ISOFLUX has been verified through both offline simserver simulations and testing on the realtime hardware. The algorithm will be used for realtime control of SFD configurations during the next NSTX-U run campaign.

Model Predictive Control of the Current Profile in NSTX-U

The availability of new diagnostics capabilities and additional heating and current-drive sources motivates the development of more advanced control algorithms for current profile regulation in NSTX-U. The work carried out by the Lehigh University Plasma Control Group has focused on the development of model-based current profile control algorithms to make use of these new diagnostics and actuation capabilities to their fullest. A feedforward + feedback control scheme [IS-20, IS-21] for the regulation of the current profile has been recently proposed by embedding a control-oriented plasma-response model [IS-22] into the control design process. The performance of this combined control approach, which uses sequential quadratic programming (SQP) for optimal feedforward design and linear quadratic integral (LQI) control for optimal feedback design, has been successfully assessed in closed-loop TRANSP simulations as the last testing stage before experimental implementation.

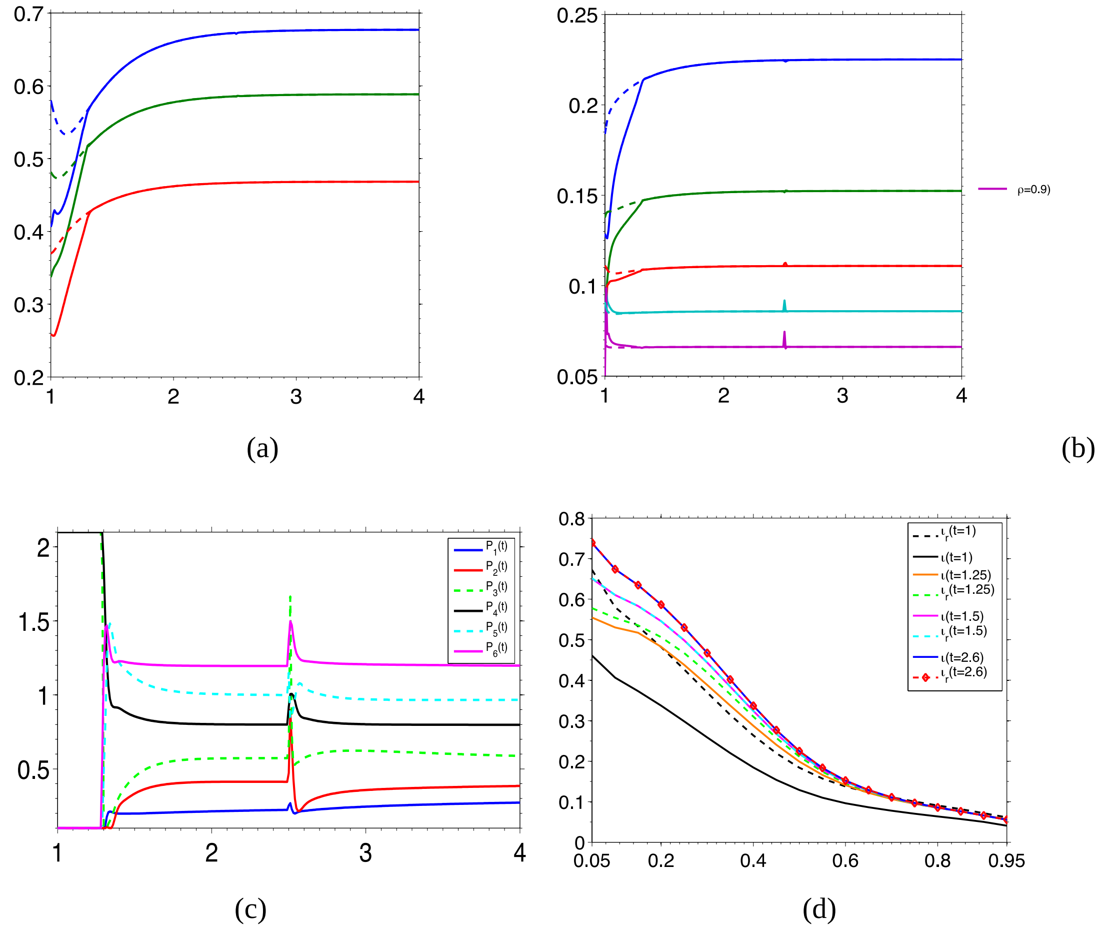

Figure IS-ASC-5: *MPC simulation results: (a)-(b) time evolution of the actual (solid) and target (dashed) iota profile at selected spatial locations, (c) beam powers, (d) actual and target iota profiles at selected instants of time.*

As a continuation of the effort towards advanced scenario planning and control, recent work carried out by members of the Lehigh University Plasma Control Group focuses on the development of a model predictive control (MPC) strategy to regulate the rotational transform (iota) profile around a desired target profile for the first time in NSTX-U [IS-23, IS-24]. One of the advantages of MPC over LQI optimal control is its capability to explicitly handle actuator and plasma-state constraints, eliminating in this way the need for an anti-windup compensator. Moreover, MPC is proactive in the sense that it recalculates the optimal actuator trajectory in real time at each time step by measuring the plasma present state, taking into account input and plasma-state constraints, predicting future plasma states based on a plasma response model, and minimizing a user-defined cost functional. Therefore, MPC has a great potential for achieving current-profile regulation as tight as allowed by the available actuation while avoiding MHD instabilities by imposing adequate plasma-state constraints. An integrator is embedded in this work into the standard MPC formulation to account for various modeling uncertainties and external disturbances. The effectiveness of the proposed MPC algorithm in regulating the current profile in NSTX-U has been initially demonstrated in closed-loop nonlinear control-oriented simulations. Figure IS-ASC-5 shows results from a simulation study where the goal is to track a target iota trajectory while rejecting perturbed initial conditions and constant input disturbances, which are added starting at t = 2.5 s. Neutral-beam powers, line-averaged electron density, and total plasma current are used as actuators. Fig. 1(a) and Fig. 1(b) compare the controlled iota evolution in time with its target at different locations in space. Fig. 1(c) shows the controlled beam powers, which react to the input disturbance added at t = 2.5 s. Finally, the controlled iota profile is compared in Fig. 1(d) to its target at different instants of time. The MPC algorithm is ready for further simulation tests in TRANSP before moving to experimental testing.

REFERENCES

[IS-20] Z.O. Ilhan, W. Wehner, J. Barton, E. Schuster, D. Gates, S. Gerhardt and J. Menard, "First-Principles-Driven Model-Based Optimal Control of the Current Profile in NSTX-U", *IEEE Multi-Conference on Systems and Control*, Sydney, Australia, September 21-23, 2015, pp. 1303-1308.

[IS-21] Z.O. Ilhan, W.P. Wehner, E. Schuster, M.D. Boyer, D.A. Gates, S. Gerhardt and J. Menard, "Performance Assessment of Model-Based Optimal Feedforward and Feedback Current Profile Control in NSTX-U using the TRANSP Code", *57th Division of Plasma Physics (DPP) Annual Meeting of the American Physical Society (APS),* Savannah, Georgia, USA, November 16-20, 2015.

[IS-22] Z. Ilhan, J.E. Barton, E. Schuster, D.A. Gates, S.P. Gerhardt and J.E. Menard, "Physics-based control-oriented modeling of the current density profile evolution in NSTX-Upgrade", *29th Symposium on Fusion Technology (SOFT),* Prague, Czech Republic, September 5-9, 2016.

[IS-23] Z.O. Ilhan, W.P. Wehner and E. Schuster, "Model Predictive Control with Integral Action for the Rotational Transform Profile Tracking in NSTX-U", *IEEE Multi-Conference on Systems and Control*, Buenos Aires, Argentina, September 19-22, 2016.

[IS-24] Z.O. Ilhan, W.P. Wehner, E. Schuster and M.D. Boyer, "Model Predictive Control with Integral Action for Current Density Profile Tracking in NSTX-U", *58th Division of Plasma Physics (DPP) Annual Meeting of the American Physical Society (APS)*, San Jose, California, USA, October 31-November 4, 2016.

Papers Published by NSTX-U Researchers (Oct. 2015 - Sept. 2016)

1. KAYE SM, Abrams T, Ahn J-W, et al.
   An overview of recent physics results from NSTX
   NUCL. FUSION 55 104002 (October 2015)

2. KIM K, Ahn J-W, Scotti F, et al.
   Ideal plasma response to vacuum magnetic fields with resonant magnetic perturbations in non-axisymmetric tokamak
   PLASMA PHYS. CONT. FUSION 57 104002 (October 2015)

3. LAZERSON SA, Park J-K, Logan N, et al.
   Numerical optimization of three-dimensional coils for NSTX-U
   PLASMA PHYS. CONT. FUSION 57 104001 (October 2015)

4. RAMAN R, Brown T, El-Guebaly LA, et al.,
   Design description for a co-axial helicity injection plasma startup system for a ST-FNSF
   FUSION SCI. AND TECHNOLOGY 68 674 (October 2015)

5. WANG W, Ethier S, Ren Y, et al.,
   Identification of new turbulence contributions to plasma transport and confinement in spherical tokamak regime
   PHYS. PLASMAS 22 102509 (October 2015)

6. REN, Y. et al.,
   Fast response of electron-scale turbulence to auxiliary heating cessation in National Spherical Torus Experiment
   PHYS. PLASMAS 22 110701 (November 2015)

7. RAMAN R, Jarboe TR, Menard JE, et al.,
   Fast time response electromagnetic disruption mitigation concept
   FUSION SCI. AND TECHNOLOGY 68 797 (November 2015)

8. RYUTOV DD and Soukhanovskii VA
   The snowflake divertor
   PHYS. PLASMAS 22 110901 (November 2015)

9. WANG W, Ethier S, Ren Y, et al.,
   Distinct turbulence sources and confinement features in Spherical Tokamak plasma regime
   NUCL. FUSION 55 122001 (December 2015)

10. BERKERY JW, Sabbagh SA, Bell RE, et al.,
    Modifications to ideal stability by kinetic effects in NSTX
    NUCL. FUSION 55 123007 (December 2015)

11. POLI FM, Andre RG, Bertelli N, et al.
Simulations of non-inductive current rampup and sustainment in the National Spherical Torus Experiment Upgrade
NUCL. FUSION 55 123011 (December 2015)

12. SHAING KC, Ida K and Sabbagh SA
Neoclassical plasma viscosity and transport processes in non-axisymmetric tori
NUCL. FUSION 55 125001 (December 2015)

13. RUIZ RUIZ J, Guttenfelder W, White AE, et al.
Stabilization of electron-scale turbulence by electron density gradient in National Spherical Torus eXperiment
PHYS. PLASMAS 22 122501 (December 2015)

14. MUNOZ BURGOS J, et al.,
Applications of advanced kinetic collisional radiative modeling and Bremsstrahlung emission to quantitative impurity analysis on NSTX
PHYS. PLASMAS 22 123301 (December 2015)

15. SCOTTI F. and Soukhanovskii VA
A dual wavelength imaging system for plasma-surface interaction studies on the National Spherical Torus Experiment Upgrade
REV. SCI. INSTRUMENTS 86 123103 (December 2015)

16. SOUKHANOVSKII V. A. and Xu, X
Tokamak Power Exhaust with the Snowflake Divertor: Present Results and Outstanding Issues, J Fusion Energ (2016) 35:31-33 DOI 10.1007/s10894-015-9999-z

17. SKINNER CH, Capece AM, Roszell, et al.
Spreading of lithium on a stainless steel surface at room temperature
J. NUCL. MATERIALS 468 26 (January 2016)

18. HART CA, Skinner CH, Capece AM, et al.
Sorption of atmospheric gases by bulk lithium metal
J. NUCL. MATERIALS 468 71 (January 2016)

19. BERTELLI N, Jaeger EF, Hosea JC, et al.
Full wave simulations of fast wave efficiency and power losses in the scrape-off layer of tokamak plasmas in mid/high harmonic and minority heating regimes
NUCL. FUSION 56 016019 (January 2016)

20. ABRAMS T, Jaworski MA, Chen M, et al.,
    Suppressed gross erosion of high-temperature lithium via rapid deuterium implantation
    NUCL. FUSION 56 016022 (January 2016)

21. RAMAN R, Jarboe TR, Menard JE, et al.
    Simplifying the ST and AT Concepts
    J. FUSION ENERGY, 35 34 (February 2016)

22. MEDLEY S, Liu D, Gorelenkova MV, et al.
    Implementation of a 3D halo neutral model in the TRANSP code and application to projected NSTX-U plasmas
    PLASMA PHYS. AND CONT FUSION 58 025007 (February 2016)

23. GOUMIRI I, Rowley C, Sabbagh S, et al.
    Modeling and control of plasma rotation for NSTX using Neoclassical Toroidal Viscosity and Neutral Beam Injection
    NUCLEAR FUSION 56 036023 (March 2016)

24. ZWEBEN S, Myra J, Davis W, et al.
    Blob structure and motion in the edge of NSTX
    PLASMA PHYS. AND CONT FUSION 58 044007 (April 2016)

25. SMITH, D., Fonck RJ, McKee GR, et al.
    Evolution patterns and parameter regimes in edge localized modes on the National Spherical Torus Experiment
    PLASMA PHYS. CONTROLLED FUSION 58 045003 (April 2016)

26. BANERJEE S, Diallo A and Zweben SJ
    Observation of quasi-coherent edge fluctuations in Ohmic plasmas on NationalSpherical Torus Experiment
    PHYS. PLASMAS 23 044502 (April 2016)

27. GUTTENFELDER, W, Kaye SM, Ren Y, et al.,
    Quasi-linear gyrokinetic predictions of the Coriolis momentum pinch in National Spherical Torus Experiment
    PHYS. PLASMAS 23 052508 (May 2016)

28. MUNOZ-BURGOS JM, Agostini M, Scarin P, et al.
    Evaluation of thermal helium beam and line-ratio fast diagnostic on the National Spherical Torus Experiment-Upgrade
    PHYS. PLASMAS 23 053302 (May 2016)

29. PODESTA M, Gorelenkova M, Fredrickson ED, et al.
Phase space effects on fast ion distribution function modeling in tokamaks
PHYS. PLASMAS 23 056106 (May 2016)

30. EBRAHIMI F and Raman R
Large-volume flux closure duringplasmoid-mediated reconnection in coaxialhelicity injection
NUCLEAR FUSION 56 044002 (April 2016)

31. HEIDBRINK W, Ruskov E, Liu D., et al.,
Analysis of fast-ion Dα data from the National Spherical Torus Experiment
NUCL. FUSION 56 056005 (May 2016)

32. LUNSFORD R, Bortolon A, Roquemore AL, et al.,
Lithium granule ablation and penetration during ELM pacing experiments at DIII-D
FUSION ENG. AND DESIGN (In press – available online May 2016)

33. RAMAN R, Pluckett G, Lay W-S
Massive Gas Injection Valve Development for NSTX-U
IEEE Transactions on Plasma Science (May 2016)

34. STOLTZFUS-DUECK T,
Parallel electron force balance and the L-H transition
PHYS. PLASMAS 23 054505 (May 2016)

35. FERRARO NM, et al.
Multi-region approach to free-boundary three-dimensional tokamak equilibria and resistive wall instabilities
PHYS. PLASMAS 23 056114 (May 2016)

36. FRERICHS H, Waters I, Schmitz O, et al.,
Exploration of magnetic perturbation effects on advanced divertor configurations in NSTX-U
PHYS. PLASMA 23 062517 (June 2016)

37. DAVIS WM, Tchilinguian GJ, Carroll T, et al.,
Control and data acquisition upgrades for NSTX-U
FUSION ENG. AND DESIGN (In press – available online June 2016)

38. CARLSSON JA, Wilson JR and Hosea JC,
Phase coherence of parametric decay modes during high-harmonic fast-wave heating in the National Spherical Torus Experiment
PHYS. PLASMA 23 062519 (June 2016)

39. COURY M, Guttenfelder W, Mikkelsen DR, et al.,
Linear gyrokinetic simulations of microinstabilities within the pedestal region of H-mode NSTX discharges in a highly shaped geometry
PHYS. PLASMA 23 062520 (June 2016)

40. MAINGI R, Canik JM, Bell RE, et al.,
Effect of progressively increasing lithium conditioning on edge transport and stability in high triangularity NSTX H-modes
FUSION ENG. AND DESIGN (In press – available online)
http://www.sciencedirect.com/science/article/pii/S0920379616304550

41. ONO M, et al,
Liquid lithium applications for solving challenging fusion reactor issues and NSTX-U contributions
FUSION ENG. AND DESIGN (In press – available online)
http://www.sciencedirect.com/science/article/pii/S0920379616304604

42. PERKINS RJ, Hosea JC and Bertelli N,
Resonance in Fast-Wave Amplitude in a Low-Density Peripheral Plasmas
PHYS. PLASMAS **23**, 070702 (July 2016)

43. PODESTA M, Gorelenkova M, Fredrickson ED, et al.
Effects of energetic particles phase space modifications by instabilities on integrated modeling
NUCL. FUSION **56** 112005 (July 2016)

44. WELLER M, et al.,
Three new extreme ultraviolet spectrometers on NSTX-U for impurity monitoring
REV. SCI. INST. **87**, 11E324 (2016) (August 2016)

45. KRAMER GJ, Bortolon, A, Ferraro NM, et al.,
Mitigation of Alfvenic activity by 3D magnetic perturbations on NSTX
PLASMA PHYS. AND CONT FUSION 58 085003 (August 2016)

46. IZACARD O
Kinetic corrections from analytic non-Maxwellian distribution functions in magnetized plasmas
PHYS. PLASMA 23 082504 (August 2016)

47. N.N. Gorelenkov, W.W. Heidbrink, G.J. Kramer et al.,
Validating predictive models for fast ion profile relaxation in burning plasmas
Nucl. Fusion **56** (July 2016) 112015

48. N. N. Gorelenkov
Ion Cyclotron Emission Studies: Retrospects and Prospects
Plasma Physics Reports **42**, (October 2016) 430.

49. J. C. Hillesheim, et al., “Intermediate-k density and magnetic field fluctuations during inter-ELM pedestal evolution in MAST,” Plasma Phys. Control. Fusion, vol. 58, no. 1, pp. 014020–1–14, Nov. 2015. *(Work funded by UCLA NSTX grant for MAST collaboration)*

Book Chapters Published by NSTX-U Researchers

50. MAINGI, R., Chapter 3 entitled “Plasma Exhaust” in "Magnetic Fusion Energy: From Experiments to Power Plants”, G. Neilson Editor, Elsevier, Woodhead Publishing, June 2016

51. KAYE, S.M. , Chapter 11 entitled “National Spherical Torus eXperiment” in "Magnetic Fusion Energy: From Experiments to Power Plants”, G. Neilson Editor, Elsevier, Woodhead Publishing, June 2016

Forthcoming Papers (as of 9/8/16)

52. MENARD JE, Brown T, El-Guebaly L, et al.,
Fusion Nuclear Science Facilities and Pilot Plants Based on the Spherical Tokamak
NUCLEAR FUSION 56 106023 (October 2016)

53. Van EDEN GG, Reinke ML, Peterson BJ, et al.,
Design and characterization of a prototype divertor viewing infrared video bolometer for NSTX-U
REV. SCI. INST. 87 11D402 (November 2016)

54. BEDOYA F, Allain JP, Kaita R, et al.,
Unraveling wall conditioning effects on plasma facing components in NSTX-U with the Materials Analysis Particle Probe (MAPP)
REV. SCI. INST. 87 11D403 (November 2016)

55. PETERSON BJ, Sano R, Reinke ML et al.,
Preliminary design of a tangentially viewing imaging bolometer for NSTX-U
REV. SCI. INST. 87 11D410 (November 2016)

56. SOUKHANOVSKII V et al.,
Real-time radiative divertor feedback control development for the NSTX-U tokamak using a vacuum ultraviolet spectrometer
REV. SCI. INST. 87 11D605 (November 2016)

57. LIU D, Heidbrink WW, Tritz K, et al.
Compact and multi-view solid state neutral particle analyzer arrays on National Spherical Torus Experiment-Upgrade

REV. SCI. INST. 87 11D803 (November 2016)

58. SCOTT E, et al.,
FIReTIP design and installation for NSTX-U
REV. SCI. INST. 87 11E114 (November 2016)

59. MUNOZ BURGOS JM, Barubui T, Schmitz O, et al.,
Time dependent analysis of visible helium line-ratios for electron temperature and density diagnostic using synthetic simulations on NSTX-U
REV. SCI. INST. 87 11E502 (November 2016)

60. WANG Zhehui, Lunsford R, Mansfield DK, Nichols, JH, Existing and new applications of micropellet injection (MPI) in magnetic fusion, J PLASMA PHY., Volume 82, Issue 2, article id. 615820202 11E502 (April 2016)

61. WANG Zhehui, Liu Q, Waganaar, W, Fontanese J, James D, Munsat, T., Four-dimensional (4D) tracking of high-temperature microparticles, REV. SCI. INST. 87 11D601 (June 2016)

Papers Recently Accepted for Publication (as of 9/8/16)

62. WHITE R, Gorelenkov N, Gorelenkova M,
Saturation of Alfvén modes in tokamaks
PLASMA PHYS. AND CONT FUSION (2016)

63. ZHOU M and White R,
Collisional dependence of Alfvén mode saturation in tokamaks
PLASMA PHYS. AND CONT FUSION (2016)

64. SCOTTI F, et al.,
Diagnostics for molybdenum and tungsten erosion and transport in NSTX-U
REV. SCI. INST. (2016)

Papers Submitted for Publication (as of 9/8/16)

65. SZALKOWSKI GA, Darrow DS and Cecil FE
Design and construction of Faraday cup ion detectors using thin film deposition
Submitted to REV. SCI. INSTRUM. (2015)

66. DARROW D., et al.,
Optimization of the angular orientation for a fast ion loss detector in a tokamak
Submitted to REV. SCI. INSTRUMENTS (2015)

67. SOUKHANOVSKII V, et al.,

Developing snowflake divertor physics basis in the DIII-D, NSTX and NSTX-U tokamaks aimed at the divertor power exhaust solution
Submitted to IEEE TRANS ON PLASMA SCI (2015)

68. CANAL GP, Ferraro NM, Evans TE, et al.,
M3D-C1 simulations of the plasma response to non-axisymmetric magnetic perturbations in the NSTX-U snowflake divertor, Submitted to NUCLEAR FUSION (2016)

69. MYRA JR, Russell DA and Zweben SJ,
Theory based scaling of edge turbulence and implications for the scrape-off layer width
Submitted to PHYS. PLASMA (2016)

70. WANG F, Fu GY and Shen W
Nonlinear Fishbone Dynamics in Spherical Tokamaks
Submitted to NUCLEAR FUSION (2016)

71. PODESTA M and Bell RE
Initial operation of the NSTX-Upgrade real-time velocity diagnostic
Submitted to PLASMA PHYS. AND CONT FUSION (2016)

72. FLESCH K, et al.,
Development of miniaturized, spectroscopically assisted Penning gauges for fractional helium and hydrogen neutral pressure measurements
Submitted to REV. SCI. INST. (2016)

73. SCHWARTZ J, et al.
Reconstruction of main ion velocity in the divertor by multiple impurity velocity measurements
Submitted to REV. SCI. INST. (2016)

74. VANN R, et al.,
Preliminary measurements of the edge magnetic field pitch from 2-D Doppler backscattering in MAST and NSTX-U
Submitted to REV. SCI. INST. (2016)

75. STOTLER DP, et al.,
Kinetic neoclassical calculations of impurity radiation profiles
Submitted to J. NUCL. MAT. AND ENERGY (2016)

76. SKINNER C, et al.,
Advances in boronization on NSTX-Upgrade
Submitted to J. NUCL. MAT. and ENERGY (2016)

77. MAINGI R, Kaita R, Scotti F, et al.,

Elimination of Inter-discharge Helium Glow Discharge Cleaning with Lithium Evaporation in NSTX, Submitted to J. Nucl. Mat. and Energy (2016)

78. PERKINS RJ, Hosea JC, Jaworski MA, et al.,
The Role of Far-Field RF Sheaths in SOL Losses of HHFW Power on NSTX, and Implications for Near-Field Studies of ICRF Antennae
Submitted to J. Nucl. Mat. and Energy (2016)

79. FIL A, Kolemen E, Bortolon A, et al.,
Modeling of Lithium Granule Injection in NSTX with M3D-C1
Submitted to J. Nucl. Mat. and Energy (2016)

80. SCOTTI F, et al.,
Toroidal asymmetries in impurity influxes in NSTX
Submitted to J. Nucl. Mat. and Energy (2016)

77. V. N. Duarte, H. L. Berk, N. N. Gorelenkov et al.,
Prediction of Nonlinear Evolution Character of Energetic-Particle-Driven Instabilities
Submitted to Phys. Rev. Letters.

Invited / Oral Talks at Scientific Conferences (Oct. 2015 - Sept. 2016)

Second IAEA Technical Meeting on Divertor Concepts, Sept. 29-Oct. 2 in Vienna, Austria.

1. R. Goldston (PPPL) "The Lithium Vapor Box Divertor"
2. V. Soukhanovskii (LLNL) "Developing Snowflake Divertor Physics Basis in the DIII-D, NSTX and NSTX-U Tokamaks Aimed at the Divertor Power Exhaust Solution"
3. R. Maingi (PPPL) "Lithium and liquid metal studies at PPPL."
4. D. Majeski (PPPL) "Concepts for fast flowing liquid lithium walls and divertors."

18th International Spherical Torus Workshop (ISTW-2015) and 2015 US-Japan Workshop on ST Plasmas, Princeton University, 3-6 November 2015

5. Stefan Gerhardt (PPPL) “NSTX-U Facility and Project Plans”
6. Jonathan Menard (PPPL) "Overview of Research Plans for NSTX Upgrade"
7. Joon-Wook Ahn (ORNL) "Relation of pedestal stability regime to the behavior of ELM heat flux footprints in NSTX-U and DIII-D"
8. Devon Battaglia (PPPL) "Bifurcation to Enhanced Pedestal H-mode on NSTX"
9. Nicola Bertelli (PPPL) "Full Wave Simulations of Fast Wave Scrape-off Layer Losses of NSTX/ NSTX-U in Mid/High Harmonic Regime and a Comparison with C-Mod/EAST in the Minority Heating Regime"
10. Fatima Ebrahimi (Princeton University) "Reconnection physics and fast flux closure during simulations of Coaxial Helicity Injection in NSTX/NSTX-U"
11. Eric Fredrickson (PPPL) "Suppression of TAE and GAE with HHFW heating"
12. Heinke Frerichs (UW-Madison) "Overview of edge modeling efforts for advanced divertor configurations in NSTX-U with magnetic perturbation fields"
13. Stephen Jardin (PPPL) "3D Modeling of NSTX Vertical Displacement Events with M3D-C1"
14. S.A. Sabbagh (Columbia U.) “Global MHD Mode Stabilization and Control for Disruption Avoidance”
15. Rajesh Maingi (PPPL) "Effect of Lithium on the Edge Plasma in NSTX and NSTX-U"
16. Jonathan Menard (PPPL) "Configuration Studies for Next-Step Spherical Tokamaks"
17. Rory Perkins (PPPL) "Field-Aligned SOL Losses of HHFW Power and RF Rectification in the Divertor of NSTX"
18. Francesca Poli (PPPL) "Towards fully non-inductive operation in NSTX-U"
19. Roger Raman (Univ. Washington) "Coaxial Helicity Injection and Disruption Mitigation Studies in Support of NSTX-U, ST-FNSF, and ITER"
20. Yang Ren (PPPL) "Studies of NSTX L and H-mode Plasmas with Global Gyrokinetic Simulation"

25th International Toki Conference in Toki, Japan, November 3 – 6, 2015.

21. Masa Ono (PPPL) “Spherical Tokamaks and Fusion Energy Development Path”

57th Annual APS-DPP meeting held in Savannah, Georgia on November 16 – 20, 2015.

22. D.A. Gates (PPPL) "The tokamak density limit: A thermo-resistive disruption mechanism"
23. M. Podesta (PPPL) "Phase space effects on fast ion transport modeling in tokamaks"
24. J-K. Park (PPPL) "Torque-consistent 3D force balance and optimization of non-resonant fields in tokamaks"
25. S.A. Sabbagh (Columbia U.) "Global MHD Mode Stabilization and Control for Tokamak Disruption Avoidance"
26. N.M. Ferraro (PPPL) "Free-Boundary 3D Equilibria and Resistive Wall Instabilities with Extended-MHD"

20th MHD Stability Control Workshop, November 22-24 (2015), Princeton Plasma Physics Laboratory, Princeton, NJ

27. Mark Boyer (PPPL) "TRANSP testing of feedback control algorithms for stored energy, safety factor, and plasma current in non-inductive scenarios in NSTX-U"
28. Zhirui Wang (PPPL) "Computation of Resistive/Relaxed Perturbed Equilibria with RPEC and resistive DCON"
29. Alan Glasser (U. Washington) "Implementation of Linear Neoclassical Inner Region Model in the DCON Package"
30. Steve Jardin (PPPL) "3D Modeling of NSTX VDEs and other disruptions with M3D-C1"
31. Steve Sabbagh (Columbia U.) "Global MHD Mode Stabilization for Tokamak Distruption Avoidance - Linear vs. Non-linear Considerations"
32. Jack Berkery (Columbia U.) "Modifications to Ideal Stability by Kinetic Effects for Distruption Avoidance"
33. Roger Raman (U. Washington) "Outstanding Issues for ITER and FNSF, NSTX-U Plans and Key Contributions to Disruption Mitigation"
34. Jong-Kyu Park (PPPL) "Kinetic plasma response and stability modeling with general perturbed equilibrium code"

10th Asia Plasma & Fusion Association Conference (APFA), December 14-18 (2015), Gandhinagar, India

35. Nicola Bertelli (PPPL), "Fast Wave Scrape-off Layer Losses of Tokamak Plasmas in Minority, Mid/High Harmonic, and Helicon Heating Regimes"

US-Japan MHD Workshop on "Fundamental understanding of 3-D magnetic field effects for optimization of fusion devices" – NIFS, Toki, Japan March 7-9, 2016

36. Jong-Kyu Park (PPPL) "Self-consistent NTV with force balance and how to systematically optimize 3D fields and NTV in tokamaks"
37. Clayton Myers (PPPL) "A multi-machine analysis of non-axisymmetric and rotating halo currents"
38. Nathaniel Ferraro (PPPL) "Extended-MHD Modeling of Resistive Wall Instabilities"

Workshop on RF-only ST plasma confinement, sustainment, and interaction with wall materials, March 24-25 (2016), Kyushu University, Japan

39. R. Raman (U. Washington), “CHI System Design and Plans on NSTX-U and QUEST”

US Transport Task Force meeting on March 28 – April 1 in Denver, CO

40. John Canik (ORNL) “Simulations of electron-scale turbulence in NSTX pedestals”
41. Yang Ren (PPPL) “Studies of NSTX L and H-mode Plasmas with Global Gyrokinetic Simulation”
42. Walter Guttenfelder (PPPL) “Analysis and prediction of momentum pinch in spherical tokamaks”
43. Travis Gray (ORNL) “Effect of Collisionality and Detachment Onset on the Scrape-off Layer Heat Flux Profiles in NSTX”
44. James Myra (Lodestar) “Scaling of edge turbulence properties and implications for the SOL width”
45. Mario Podesta (PPPL) “Inferring AE amplitudes from wave/particles power balance in a reduced EP transport model”
46. Juan Ruiz Ruiz (MIT) “Stabilization of Electron-Scale Turbulence by Electron Density Gradient in NSTX”

EC-19 Joint workshop on Electron Cyclotron Heating/ECE, Ahmedabad, India, April 4-7

47. Francesca Poli (PPPL) "Electron Cyclotron power management in ITER, from the commissioning phase to the demonstration baseline"

19th International Conference on Atomic Processes in Plasmas 4-8 April 2016, Paris

48. Vlad Soukhanovskii (LLNL) “Near-infrared spectroscopy of tokamak divertor plasmas”

International Sherwood Fusion Theory Conference 4-6 April 2016, Madison WI

49. Fatima Ebrahimi (Princeton University) **“**Physics of plasmoid-mediated reconnection and flux closure in simulations of Coaxial Helicity Injection”
50. V. N. Duarte (San Paulo U) “Realistic characterization of chirping instabilities in tokamaks”

22nd International Plasma-Surface Interactions Conference in Rome, Italy, May 30-June 3

51. M. Jaworski (PPPL) "Liquid metals as PFCs: progress and prospects."
52. M. Reinke (ORNL) "Expanding the role of impurity spectroscopy for investigating the physics of high-Z dissipative divertors."
53. J-W. Ahn (ORNL) "Effect of pedestal stability regime on the behavior of ELM heat flux footprints in NSTX and DIII-D."

US-Japan Workshop on RF Heating Physics, May 18-20 (2016), Toyama, Japan

54. Gary Taylor (PPPL) "Generation of Non-Inductive Plasmas with 30 MHz and 28 GHz Heating in NSTX-U"
55. Joel Hosea (PPPL) "HHFW far field rectification heat deposition via the SOL on NSTX and NSTX-U"
56. Nicola Bertelli (PPPL) "Full-wave simulations of HHFW and IC minority heating regimes with non-Maxwellian distributions"

21st Topical Conference on High Temperature Plasma Diagnostics, June 5-9, Madison, WI

57. "Investigation of ELM evolution patterns with beam emission spectroscopy measurements on NSTX-U" by D. Smith (University of Wisconsin-Madison)
58. "Synthetic aperture microwave imaging of the plasma edge in MAST and NSTX-U" by R. Vann (University of York)
59. Multi-energy SXR cameras for magnetically confined fusion plasmas" by L. Delgado-Aparicio (PPPL)

18th International Congress on Plasma Physics, June 27-July 2, 2016 in Kaohsiung, Taiwan

60. Jon Menard (PPPL) “Key physics issues and opportunities for next-step spherical torus devices”
61. Jack Berkery (Columbia University) “Kinetic resistive wall mode stabilization physics in tokamaks”
62. Yang Ren (PPPL) “Recent progress in understanding electron thermal transport in NSTX and NSTX-U”
63. Ahmed Diallo (PPPL) “Development of medium and fast burst laser systems for laboratory and fusion plasmas”

43rd EPS Conference on Plasma Physics, held July 4-8 in Leuven, Belgium

64. S.A. Sabbagh (Columbia University) - 2016 Landau-Spitzer Award lecture “Establishing a verified understanding of kinetic MHD theory to determine global mode stability in tokamak plasmas”

IEA Workshop: Theory and Simulation of Disruptions, PPPL, July 20-22, 2016

65. S.A. Sabbagh (Columbia University) “Disruption Event Characterization of Global MHD Modes in NSTX and Plans for Instability Avoidance in NSTX-U”
66. D. Pfefferlé (PPPL) “Magnetomechanics of Vertically Displacing Plasmas”
67. N. Ferraro (PPPL) “Extended-MHD Modeling of Tokamak Disruptions and Resistive Wall Modes with M3D-C1”

Fusion Materials / Plasma Wall Interactions, July 25-29, 2016 at UT Knoxville and ORNL

68. C. Kessel (PPPL) "FNSF/Design Team Overview and Material R&D Needs"
69. M. Jaworski (PPPL) "Liquid Metals as Plasma Facing Components: Progress and Prospects"
70. C. Skinner (PPPL) PPPL Institutional Overview including results from NSTX, LTX and Surface Science
71. M. Jaworski (PPPL) "International Collaborations and Device Exploitation"
72. R. Majeski (PPPL) "Deployment Issues in Flowing Liquid Plasma Facing Material systems"

22nd Topical Meeting on the Technology of Fusion Energy, August 21-25, 2016 in Philadelphia, PA

73. Devon Battaglia (PPPL) "Overview of Initial Operation on NSTX-U"
74. Jonathan Menard (PPPL) "Studies of Next-Step Spherical Tokamaks Using High-Temperature Superconductors"
75. Laila A. El-Guebaly (University of Wisconsin) "ST-Based Fusion Nuclear Science Facility: Breeding Issues and Challenges of Protecting HTS Magnets"
76. Dang Cai (PPPL) "Boronization System for the NSTX-Upgrade Fusion Device"

US-Japan Compact Toroid Workshop, Irvine, CA, Aug. 22-24

77. Walter Guttenfelder (PPPL) "Transport at high beta in spherical tokamaks"
78. Roger Raman (University of Washington) "Overview of transient CHI plasma start-up research in NSTX-U"

Seminars and Colloquia by NSTX-U Researchers

1. Jon Menard (PPPL) presented "Progress and plans for NSTX Upgrade and prospects for next-step spherical tori" at the APS Mid-Atlantic Section Morgantown, WV on 10/24/2015

2. Jack Berkery (Columbia U.) presented "Progress and Plans for NSTX Upgrade and Kinetic Resistive Wall Mode Stability" at the University of Washington on 10/26/2015

3. Clayton Myers (PPPL) presented "Laboratory study of ideal MHD solar instability eruption mechanisms " at MIT / PSFC on 10/30/2015

4. Clayton Myers (PPPL) presented "Bringing the Cosmos Down to Earth: Studying Astrophysical Processes in Laboratory Experiments" at The College of New Jersey on 11/03/2015

5. R. Raman, University of Washington (Plasma Seminar), Seattle, WA, "Disruption mitigation for tokamak reactors and mitigation plans on NSTX-U", 7 December (2015)

6. Rajesh Maingi (PPPL) presented "Effect of low-Z impurities on H-mode pedestal structure, performance, and ELMs" at the ITER international school on pedestal physics, Dec. 14-18, 2015, at USTC in Hefei, China

7. Mike Jaworski (PPPL) presented " NSTX-U upgrade plan for liquid-metal plasma-facing components" at General Atomics on 1/17/2016

8. Rajesh Maingi (PPPL) presented "Lithium and liquid metal studies at PPPL" at General Atomics on 1/17/2016

9. Dick Majeski presented "Lithium walls and enhanced tokamak performance" at General Atomics on 1/17/2016

10. Walter Guttenfelder (PPPL) presented "Progress, challenges & plans in transport research in NSTX-U" at UCLA on 2/11/2016

11. Mike Jaworski (PPPL) presented "Overview of liquid and solid PFC research for fusion energy at PPPL" at the National Energy Technology Lab on 2/18/2016

12. Robert Kaita (PPPL) "The Dusty Road to Fusion: Addressing First Wall Erosion in the National Spherical Torus Experiment Upgrade" at Baylor University in Waco, TX on April 5, 2016

13. Rajesh Maingi (PPPL) presented "Effect of low-Z impurities on edge plasma performance and stability in tokamaks" at the Princeton Univ. graduate seminar series on April 4 and April 11, 2016

14. Rajesh Maingi (PPPL) presented “Lithium and liquid metal studies at PPPL: an introduction” at Oak Ridge National Laboratory on 4/13/2016

15. Mike Jaworski (PPPL) presented " NSTX-U upgrade plan for liquid-metal plasma-facing components" at Oak Ridge National Laboratory on 4/13/2016

16. Dick Majeski presented “Lithium walls and enhanced tokamak performance” at Oak Ridge National Laboratory on 4/13/2016

17. Jack Berkery (Columbia U.) presented "Progress and Plans for NSTX Upgrade and Kinetic Resistive Wall Mode Stability" at the Georgia Institute of Technology on 4/14/2016

18. Jack Berkery (Columbia U.) presented " Progress and Plans for NSTX Upgrade and Kinetic Resistive Wall Mode Stability " at Auburn University on 4/15/2016

19. R. Lunsford (PPPL) "Skipping Rocks off the Sun: Taming fusion plasma eruptions through controlled microgranule injection" at the inaugural Princeton Research Day on May 5th, 2016

20. Walter Guttenfelder (PPPL) gave a talk to the Cranbury Presbyterian Senior Breakfast club on May 26 titled "Containing a star on earth: PPPL and the promise of fusion energy".

21. Neal Crocker (UCLA) delivered a talk on July 12, in the 2016 REU Faculty Seminar series for participants in the NSF Research Experiences for Undergraduates (REU) program at UCLA.

22. Masa Ono (PPPL) “NSTX-U status and plans” at the Center for Plasma-Material Interactions (CPMI), University of Illinois – Champaign campus on July 21, 2016.

23. Rajesh Maingi (PPPL) presented a seminar "The effect of lithium on Edge Plasma Performance and Stability in NSTX" at the University of Illinois – Champaign on Aug. 4, 2016

24. E. Kolemen (Princeton University) presented “Controlling Fusion Power” at MIT on September 16th, 2016.

25. E. Kolemen (Princeton University) presented an invited keynote seminar at the Taming the Flame; Divertor Detachment Control in Tokamaks September 23rd, 2016.

Major Awards by NSTX-U Researchers

- Professor Rob Goldston (Princeton University) was awarded the 2015 Nuclear Fusion Award. The award recognizes Prof. Goldston's paper which describes a new model for estimating the width of the scrape-off layer — the hot plasma that is exhausted in fusion facilities called tokamaks — as the most outstanding paper published by the journal in 2012.

- Jack Berkery and Steve Sabbagh (NSTX-U Team collaborators – Columbia University), along with colleagues Yueqiang Liu (CCFE) and Holger Reimerdes (EPFL), were awarded the 2016 Landau-Spitzer Award, presented jointly every two years by the American and European Physical Societies (APS and EPS). The Award is given to an individual or group of researchers for outstanding theoretical, experimental, or technical contribution(s) in plasma physics, and for advancing the collaboration and unity between the European Union and the United States. The research for which the award was given comprises nearly a decade of published effort on kinetic resistive wall mode theory validation and understanding, which included experiments from NSTX and DIII-D.

- Stefan Gerhardt (PPPL) was awarded the Fusion Power Associates 2016 Excellence in Fusion Engineering Award in recognition many scientific contributions, including recent work on predicting plasma disruptions, which will provide major benefit to ITER and other major fusion experiments, and for leadership provided for the successful completion and soperations of the NSTX-U experiment at PPPL.

- Egemen Kolemen (Princeton University) received the DOE Early Career Award for "Physics-Based Real-time Analysis and Control to Achieve Transients-Free Operations for the ITER Era".

Hosted / Organized Meetings and Workshops

1. NSTX-U researchers organized and hosted the 18th International Spherical Torus Workshop (ISTW-2015) and 2015 US-Japan Workshop on ST Plasmas, Princeton University, 3-6 November 2015

2. The PPPL theory department organized the IEA Workshop on the Theory and Simulation of Disruptions held at PPPL July 20-22, 2016.

3. PPPL played a major role in organizing the 22nd Topical Meeting on the Technology of Fusion Energy, August 21-25, 2016 in Philadelphia, PA

4. PPPL hosted the 20th Workshop on MHD Stability Control, November 22-24, 2015 (J-K. Park, M. Okabayashi and E. Kolemen)

NSTX-U PPPL Employee FY16 Leadership in Venues Outside of PPPL

1. Bell, R., Expert, ITPA Diagnostics Topical Group
2. Darrow, D., Chair, ITPA Diagnostics, Fusion Products Working Group
3. Darrow, D., Expert, ITPA Diagnostics Topical Group
4. Diallo, A., Expert, ITPA Pedestal and Edge Physics Topical Group
5. Ferraro, N., Expert, ITPA Pedestal and Edge Physics Topical Group
6. Ferraro, N., Treasurer, Sherwood Fusion Theory Conference Executive Committee
7. Fredrickson, E., Member, ITPA Energetic Particle Physics Topical Group
8. Gates, D.A. IAEA-US and International Paper Section Committee (2016)
9. Gerhardt, S., Member, ITPA Integrated Operating Scenarios Group
10. Gerhardt, S. Leader, ITPA MDC WG-6
11. Gorelenkov, N., Leader, USBPO Energetic Particles Topical Group
12. Gorelenkov, N., Member, ITPA Energetic Particle Physics Topical Group
13. Guttenfelder, W., Member, ITPA Transport and Confinement Topical Group
14. Hosea, J., Co-chair, US-Japan RF Physics Workshop
15. Hosea, J., Member, US ITER IO Red Team Review Panel to prepare for DOE's determination of the Project’s readiness for Critical Decision 2 and 3, Approval of Performance Baseline and Approval of Start of Construction
16. Jaworski, M., Member, ITPA scrape-Off-Layer and Divertor Topical Group
17. Kaye, S., Expert, ITPA Transport and Confinement Topical Group
18. Kaye, S., Member, U.S. Transport Task Force Steering Committee
19. Kaye, S., Member, U.S. Burning Plasma Organization Research Council
20. Kaye, S., Coordinator, International H-mode Database Update Task (ITPA)
21. Kaye, S., Panel Member, FES Integrated Modeling Workshop
22. Kolemen, E., Assistant Professor, Princeton University
23. Kolemen, E., Member, ITER Plasma Control System design review committee
24. Kolemen, E., Local Organizer MHD Control Workshop at Princeton
25. Kolemen, E., Keynote Speaker “Taming the Flame” Workshop
26. Maingi, R., Chair, ITPA Pedestal and Edge Physics Topical Group
27. Maingi, R., Expert, ITPA Diagnostics Topical Group
28. Maingi, R., Expert, ITPA Divertor and SOL Topical Group
29. Maingi, R., Member, ITPA Coordinating Committee
30. Maingi, R., Leader, FES-sponsored community-led PMI strategic workshop activity
31. Maingi, R., Technical Program Committee Member, of the H-mode Workshop
32. Maingi, R., Invited participant in the ITER Research Plan Workshop, July 25-29, 2016
33. Menard, J., Chair, Local Organizing Committee for 18th International Spherical Torus Workshop
34. Menard, J., Co-chair, International Advisory Committee for China Fusion Engineering Test Reactor (CFETR)
35. Menard, J., Member, Executive Committee of IEA Implementing Agreement for Cooperation on Spherical Tori
36. Menard, J., Member, Culham Centre for Fusion Energy Advisory Committee
37. Menard, J., Member, MAST Upgrade project review committee

38. Menard, J., Member, Research Councils UK Fusion Advisory Board
39. Menard, J., Expert, ITPA MHD, Disruptions and Control Topical Group
40. Menard, J. Member, ITER Plasma Control System design review committee
41. Menard, J., Chair, U.S. DOE FES Fusion Facility Coordinating Committee
42. Menard, J., Member, Princeton University C7 Committee
43. Ono, M., Member, APS DPP Program Committee 2015
44. Ono, M., Member, ISTW Program Committee 2015
45. Ono, M., Member, International Toki Conference Program Committee 2015
46. Ono, M., Member, International Symposium of Liquid Metal Applications Program Committee
47. Ono, M., Member, All-About-Divertor Symposium Program Committee 2016
48. Ono, M., Member, ICPP Program Committee 2016
49. Ono, M. , Associate Editor, Journal of Fusion Energy
50. Park, J-K., Committee Member, Workshop on MHD Stability Control
51. Park, J-K., MDC-19 Leader, ITPA MHD, Disruption and Control Topical Group
52. Park, J-K., Deputy Leader, MS Topical Science Group, NSTX-U Team
53. Park, J-K., NTV Sub-Task Force Leader, KSTAR Team
54. Park, J.K., Lecturer, Princeton University
55. Podesta, M., Member, ITPA Energetic Particle Physics Topical Group
56. Podesta, M., Member, TTF Executive Committee 2015
57. Podesta, M., Member of the Editorial Advisory Board of Review of Scientific Instruments
58. Poli, F., Deputy Leader, BPO Topical Group on Integrated Scenarios
59. Poli, F., Member, US ITPA-IOS
60. Poli, F. Member, TTF Executive committee 2015
61. Poli, F., Panel Member, FES Integrated Modeling Workshop
62. Poli, F., Panel Member, FES-ASCR Exascale workshop
63. Poli, F., PI of ITER Task Agreement on EC modeling and applications
64. Ren, Y., Expert, ITPA Transport and Confinement Topical Group
65. Skinner, C., Expert, ITPA Diagnostics Topical Group
66. Stratton, B., Member, ITPA Diagnostics Topical Group
67. Stratton, B., Deputy Group Leader, USBPO Diagnostics
68. Taylor, G., Expert, ITPA Diagnostics Topical Group

65. Wang, W. X., Secretary/Treasurer, Executive Committee of Sherwood Conference
66. Wang, W. X., Member, IAEA FEC 2016 U.S. Paper Selection Committee

NSTX-U Collaborator Institutions

Number	Institution	Country
1	College of William and Mary	USA
2	Columbia University	USA
3	CompX	USA
4	Florida International University	USA
5	General Atomics	USA
6	Idaho National Laboratory	USA
7	Johns Hopkins University	USA
8	Lawrence Livermore National Laboratory	USA
9	Lehigh University	USA
10	Lodestar Research Corporation	USA
11	Los Alamos National Laboratory	USA
12	Massachusetts Institute of Technology	USA
13	Nova Photonics, Inc	USA
14	Oak Ridge National Laboratory	USA
15	Old Dominion University	USA
16	Princeton University	USA
17	Purdue University	USA
18	Sandia National Laboratory	USA
19	Tech-X Corporation	USA
20	University of California - Davis	USA
21	University of California - Irvine	USA
22	University of California - Los Angeles	USA
23	University of California - San Diego	USA
24	University of California, Space Sciences Laboratory	USA
25	University of Colorado	USA
26	University of Illinois	USA
27	University of Maryland	USA
28	University of Rochester	USA
29	University of Tennessee	USA
30	University of Texas	USA
31	University of Washington	USA
32	University of Wisconsin	USA
33	University of Costa Rica	Costa Rica
34	Institute of Plasma Physics-Czech Republic	Czech Republic
35	Hiroshima University	Japan
36	Japan Atomic Energy Agency	Japan
37	Kyoto University	Japan
38	Kyushu University	Japan
39	NIFS National Institute for Fusion Science	Japan
40	Niigata University	Japan
41	University of Hyogo	Japan
42	University of Tokyo	Japan
43	FOM Institute DIFFER	Netherlands
44	ASIPP - Institute of Plasma Physics - Chinese Academy Of Sciences	P.R. China
45	Ioffe Physical-Technical Institute	Russia
46	TRINITI - Troitskii Institute of Innovative & Thermonuclear Research	Russia
47	KAIST - Korea Advanced Institute of Science and Technology	South Korea
48	NFRI - National Fusion Research Institute	South Korea
49	Seoul National University	South Korea
50	Ulsan Science Institute of Science & Technology	South Korea
51	Institute for Nuclear Research-National Academy of Science	Ukraine
52	Culham Centre for Fusion Energy	United Kingdom
53	Tokamak Energy	United Kingdom
54	University of York	United Kingdom